

**Basalt Genesis Across the Solar System:  
Observational and Experimental Studies of Shergottite and Eucrite Meteorites**

by

Nicholas Castle

A thesis submitted in partial fulfillment of the requirements for the degree of

Doctor of Philosophy

Department of Earth and Atmospheric Sciences

University of Alberta

©Nicholas Castle, 2017

## **Abstract**

This thesis consists of three projects based on exploring igneous processes on two parent bodies: the HED (howardite-eucrite-diogenite) parent body and Mars. The HED parent body is an asteroidal parent body (possibly Vesta) that differentiated rapidly in the early solar system; Mars is a planet with an extensive geologic history and active igneous processes from the beginning of the solar system through the present. Similar experimental, analytical, and conceptual techniques were used between the projects, creating a unified theme despite the differences in petrogenesis on the two parent bodies.

This first project examines the petrology of the Tissint meteorite, an olivine phyric shergottite fall belonging to the depleted geochemical trend of Martian basalts. Tissint is one of very few shergottites with a near-liquid composition, allowing for the calculation of a robust parental liquid composition. Mineral assemblages in Tissint are consistent with two different oxygen fugacities ( $fO_2$ s), QFM-3.5 for the early-formed olivine-spinel-pyroxene mineral assemblage, and QFM-1.4 for the late-formed titanomagnetite-ilmenite mineral assemblage. Geothermometer/oxybarometer (GTOB) estimates and MELTS calculations were compared to experimental results; GTOB estimates tend to overestimate temperatures by 100-150°C, but  $fO_2$  estimates were close to experimental settings, and the crystallization curve produced by MELTS was close to the experimentally derived crystallization curve. MELTS was used to estimate the maximum extent of auto-oxidation of the Tissint magma to ~0.8 log units, far short of the 2.1 derived from GTOB estimates, leading to the conclusion that Tissint had undergone an oxidation event during petrogenesis. This is the first time the phenomenon has been

observed in a depleted shergottite, providing insights into volatiles in the Martian interior. The liquid line of descent demonstrates that QUE 94201, a basaltic shergottite, could be derived from a Tissint-like magma; however, both Shergotty and Zagami, also basaltic shergottites, could not. Further, the parental composition for EETA79001, another olivine-phyric shergottite, could not be derived from a Tissint-like magma, suggesting that there is additional magmatic variety within each of the textural types.

The second project aims to determine the mechanism by which Cr in olivine was overprinted in experiments on the Tissint parental composition that were subjected to oxidation during crystallization (hybrid  $fO_2$  experiments). Chromium profiles in the Tissint shergottite are similar to the experimentally-derived overprinted olivine, and not to the olivine produced by cooling rate experiments without an oxidation event. Several variants of the original hybrid experiment were performed, each allowing evaluation of a different proposed mechanism. The diffusion length scale was found to be too short to cause the change in Cr observed in the experiments. Although oxidation-induced peritectic resorption of olivine, forming pyroxene, is expected during oxidation of the Tissint liquid during cooling, the large degree of resorption required to account for the overprinting was not observed. Oxidation-induced exsolution of spinel from olivine appears consistent with the observed overprinting, and occurs on a length scale closer to the diffusion length scale. An experiment doped with V demonstrated that V behaves similarly to Cr during the experiment; Co and Ni are also suspected to behave similarly to Cr, partitioning into spinel during exsolution, but additional experimentation is required to confirm.

The third project involved partial melting of a zoned eucrite, NWA 7035, to provide an experimental test of the hypothesis that the incompatible trace-element (ITE) enrichment of the Stannern trend (ST) can be formed from the main group trend (MGT) by mixing with such a partial melt. A zoned eucrite was selected for experimentation because it represents an unmetamorphosed igneous sample, similar to what is expected in a primitive eucritic crust on the HED parent body. Partial melts of NWA 7035 have an ITE enrichment capable of creating a ST-like rare earth element composition from a MGT composition, but would have an accompanying enrichment in both Sc and Fe that is incompatible with derivation of the ST from a MGT magma. A larger plagioclase component in melting, either from a longer duration equilibration time or a higher plagioclase fraction in the melting crust, may resolve the Sc enrichment. The drop in Mg# might be countered by starting with a more magnesian composition of eucrite, but additional experiments on such a composition are required to evaluate.

## **Preface**

Chapter 2 of this thesis has been published as N. Castle and C. D. K. Herd “Experimental Petrology of the Tissint Meteorite: Redox Estimates, Crystallization Curves, and Evaluation of Petrogenetic Models” in the journal *Meteoritics and Planetary Science*, vol. 52, issue 1, 125-146. I was responsible for the design and execution of the research agenda, the data collection and analysis, and was lead author in writing the publication. C. D. K. Herd was the supervisory author, was involved in concept formation and discussion, and contributed substantially to editing of the manuscript. Minor edits have been made in the chapter version in response to defense committee comments. The supplemental tables included in the publication have been included as Appendix 1.

The remainder of the thesis is original work by Nicholas Castle, and has not been previously published.

## **Dedication**

For Mom, who has been there for me from scraped knees, now through a PhD. I'm glad that my eccentricities make you proud.

## **Acknowledgements**

There are many people to whom I am indebted for their support during the graduate program that lead to this thesis. Foremost of these is my dad, who has been my sounding board, support, and inspiration from the very beginning – thank you dad, for everything that you do!

I would like to thank Tony Irving for introducing me to the world of meteoritics. I hope and strive to be as much of a well-spoken, polite, rabble-rouser as you manage to be. Thank you for your encouragement.

I owe a great deal to the many people who have lent me their technical expertise over the course of these projects, from Scott Kuehner who taught me to use the microprobe, to Ilona Ranger and Andrew Locock who helped me collect the brunt of my research data, Nathan Gerein who patiently lead me through SEM analysis, Guangcheng Chen who collected the bulk trace-element composition of NWA 7035, and Andy DuFrane who helped me run the laser and process the data from LA-ICP-MS.

I would also like to thank my adviser, Chris Herd, for not just patiently, but enthusiastically, helping me through this program. Your encouragement, mentorship, and technical instruction have shaped me into the scientist I am today. Thank you for believing in me.

Many thanks to my defense committee: Tom Chacko, Bob Luth, Graham Pearson, James Brennan, and Chris Herd. I really did mean it when I said it was a pleasure.

And finally, I would like to thank my wife, Maria Castle. Thank you for being crazy enough to come alongside a graduate student studying rocks in space. You make each day a little more wonderful than the one before.

## Table of Contents

<b>Abstract</b> .....	<b>ii</b>
<b>Preface</b> .....	<b>v</b>
<b>Dedication</b> .....	<b>vi</b>
<b>Acknowledgements</b> .....	<b>vii</b>
<b>Table of Tables</b> .....	<b>x</b>
<b>Table of Figures</b> .....	<b>xi</b>
<b>Chapter 1: Introduction to the Thesis</b> .....	<b>1</b>
<b>1.1: Introduction to Mars</b> .....	<b>2</b>
<b>1.2: Introduction to the HED parent body and Vesta</b> .....	<b>6</b>
<b>Chapter 2: Experimental Petrology of the Tissint Meteorite</b> .....	<b>26</b>
<b>2.1 Introduction</b> .....	<b>26</b>
<b>2.2 Methods</b> .....	<b>28</b>
2.2.1 Experiments and Quantitative Analysis .....	28
2.2.2 Calculated Estimates and MELTS .....	31
<b>2.3 Results</b> .....	<b>34</b>
2.3.1 Experimental Results .....	34
2.3.2 Oxygen Fugacity.....	38
2.3.3 MELTS Model Validation.....	40
<b>2.4 Discussion</b> .....	<b>40</b>
2.4.1 The nature of oxidation events in Martian magmas.....	40
2.4.2 Cr in olivine and oxygen fugacity.....	42
2.4.3 Magmagenesis and the Martian mantle.....	48
2.4.4 Chemical relations between textural types.....	49
<b>2.5 Conclusions</b> .....	<b>51</b>
<b>Chapter 3: The Mechanism Behind Overprinting from Oxidation in the Tissint Meteorite</b> .....	<b>66</b>
<b>3.1 Introduction</b> .....	<b>66</b>
<b>3.2 Methods</b> .....	<b>67</b>
<b>3.3 Experimental Agenda</b> .....	<b>70</b>
<b>3.4 Results</b> .....	<b>72</b>
<b>3.5 Discussion</b> .....	<b>73</b>
3.5.1 Cr behavior and diffusion rates in olivine.....	73
3.5.2 Oxidation and the olivine peritectic reaction.....	76
3.5.3 The chromite exsolution model .....	78
3.5.4 Implications for Tissint petrogenesis.....	82
3.5.5 Implications for shergottite petrogenetic interpretation .....	83
<b>3.6 Conclusions</b> .....	<b>85</b>

<b>Chapter 4: Partial Melting of the Zoned Eucrite Northwest Africa 7035: Implications for Eucrite Petrogenesis.....</b>	<b>104</b>
<b>4.1 Introduction .....</b>	<b>104</b>
<b>4.2 Methods.....</b>	<b>107</b>
<b>4.3 Results .....</b>	<b>110</b>
<b>4.4 Discussion .....</b>	<b>113</b>
4.4.1 Major-element geochemical description of melting.....	114
4.4.2 Trace-element description of melting and the Stannern trend .....	116
4.4.3 Metasomatism .....	119
<b>4.5 Conclusions.....</b>	<b>120</b>
<b>Chapter 5: Summary, Conclusions, and Further Study.....</b>	<b>140</b>
<b>5.1 Summary, and questions for further study of the Tissint meteorite .....</b>	<b>140</b>
<b>5.2 Summary, and questions for further study of eucrites.....</b>	<b>141</b>
<b>References.....</b>	<b>143</b>
<b>Appendix 1 – Supplemental information from Tissint experimental petrology .....</b>	<b>156</b>
<b>Appendix 2 – X-Ray maps from cooling rate experiments.....</b>	<b>173</b>
<b>Appendix 3 – NWA 7035 glass trace-element compositions .....</b>	<b>182</b>

## Table of Tables

Table 2.1: Experimental parameters and summarized results.....	53
Table 2.2: Meteorite whole rock (WR) and parental compositions.....	54
Table 2.3: Experimental glass compositions.....	55
Table 3.1: Tissint bulk compositions.....	87
Table 3.2: Experimental run parameters .....	88
Table 3.3: Experimentally produced mineralogy and textures .....	89
Table 3.4: Average experimental glass compositions.....	90
Table 3.5: Representative olivine analyses.....	91
Table 3.6: Representative pyroxene analyses .....	93
Table 3.7: Average experimentally produced oxide compositions .....	95
Table 4.1: Experimental parameters, melt observations .....	122
Table 4.2: Average glass compositions from partial melting experiments .....	123
Table 4.3: NWA 7035 mineral compositions .....	125
Table 4.4: NWA 7035 bulk composition from solution ICP-MS.....	126
Table A1.1: Calculated modal abundances from isothermal experiments at QFM-3.2 .....	157
Table A1.2: Calculated modal abundances from isothermal experiments at QFM-1 .....	158
Table A1.3: Isothermal experiment average chromite analysis .....	159
Table A1.4: Isothermal experiment average titanomagnetite analysis .....	160
Table A1.5: Isothermal experiment average olivine analysis.....	161
Table A1.6: Isothermal experiment average pyroxene analysis .....	163
Table A1.7: Isothermal experiment average plagioclase analysis .....	164
Table A1.8: Isothermal experiment average glass analyses .....	165
Table A1.9: Cooling rate experiment average glass analyses .....	167
Table A1.10: Example Tissint mineralogy and olivine-spinel-pyroxene geothermometer/oxybarometer results.....	168
Table A1.11: Example Tissint mineralogy and titanomagnetite-ilmenite geothermometer/oxybarometer results.....	169
Table A1.12: Laboratory-GTOB comparison.....	170
Table A1.13: Cr partitioning behavior calculated from experimental olivine and glass .....	171
Table A3.1: Full collection of trace-element compositions measured in glasses from partial melting of NWA 7035.....	183

## Table of Figures

<b>Figure 1.1:</b> Evidence for the Martian origin of the Martian meteorites (from Treiman et al., 2000). The plot contrasts the measured composition of the Martian atmosphere (Owen, 1992; Owen et al., 1977) against the composition of trapped gasses in EETA79001 (Pepin and Carr, 1992).....	12
<b>Figure 1.2:</b> Oxygen isotope compositions of Martian meteorites (MFL), angrites (AFL), and eucrites (EFL) relative to the terrestrial fractionation line (TFL). This figure is from Greenwood et al. (2005).....	13
<b>Figure 1.3:</b> Visual depiction of the disequilibrium in Fe-Mg space between olivine cores and the bulk composition indicating that most shergottites have undergone a substantial degree of mineral accumulation. This figure is from Filiberto and Dasgupta (2011).....	14
<b>Figure 1.4:</b> Composite figure that shows the correlation of enrichment in two isotopic decay systems (Sm-Nd and Rb-Sr) and trace-elements (rare earth elements, REEs, shown). This figure is from Shearer et al. (2013) based on the original from Symes et al. (2008).....	15
<b>Figure 1.5:</b> Example isochron age calculations from mineral separates of a basaltic shergottite (Nyquist et al., 2009a).....	16
<b>Figure 1.6:</b> Measured and calculated isotopic composition for whole-rock Nd in a variety of SNC meteorites based on a two stage fractionation model. This figure is from a review by Mezger et al. (2013), and is an update of an earlier figure by Borg et al. (2003).....	17
<b>Figure 1.7:</b> Correlation between oxygen fugacity and chemical type for the two main shergottite textural types. This figure is an update of Castle and Herd (2017), modified to show the estimates for LAR 12095, and based off of the original figure from Herd (2003) who first described the relation between enrichment and oxidation in shergottite magmas. ....	18
<b>Figure 1.8:</b> Polygonal surface consistent with disruption caused by magmatic intrusion from below (from Dundas et al., 2016).....	19
<b>Figure 1.9:</b> Evidence for the formation of eucrite Asuka 881394 while $^{26}\text{Al}$ was still active (from Nyquist et al., 2003).....	20
<b>Figure 1.10:</b> HED meteorite oxygen isotope systematics (from Greenwood et al., 2016).....	21
<b>Figure 1.11:</b> Schematic diagram of three models for the structure of the HED parent body and the relation between eucrites and diogenites (from Shearer et al., 2010).....	22
<b>Figure 1.12:</b> Norm projection of eucrite liquids with liquidus boundaries (from Stolper, 1977). ....	23
<b>Figure 1.13:</b> Schematic diagram of eucrite pyroxene compositions.....	24
<b>Figure 1.14:</b> Modeling results from Barrat et al. (2007) where the Stannern trend is conceptualized as the result of mixing a main group trend magma with a low degree partial melting of a eucritic crust.....	25
<b>Figure 2.1:</b> Shergottite whole-rock La/Yb plotted against $f\text{O}_2$ . ....	56

<b>Figure 2.2:</b> Various calculations relating to oxygen fugacity from the Tissint meteorite, experiments, and the MELTS models. ....	57
<b>Figure 2.3:</b> A: Fe-Mg exchange between olivine and liquid. B: Comparison between olivine and pyroxene equilibrium observed in Tissint isothermal experiments and the expected equilibrium calculation from the literature (Longhi and Pan, 1989).....	58
<b>Figure 2.4:</b> BSE images of S54 (1240°C) and S40 (1200°C), both at QFM-3.2.....	59
<b>Figure 2.5:</b> Phase abundances, as a function of temperature, calculated from a chemical mass balance, for both QFM-3.24 (A) and QFM-1 (B).....	60
<b>Figure 2.6:</b> Comparison between experiment settings and GTOB calculation results for the Ol-Sp-Px GTOB. ....	61
<b>Figure 2.7:</b> Comparison between MELTS simulations and experimental results. ....	62
<b>Figure 2.8:</b> A: regression relation between olivine composition (Fo) and $D_{Cr}$ . B: comparison of calculated and measured compositions for both olivine and glass produced in isothermal experiments.. ....	63
<b>Figure 2.9:</b> Olivine zoning profiles from cooling rate experiments (a: S58, b: S50), natural olivines from Tissint (c), and the hybrid experiment (d: S64). ....	64
<b>Figure 2.10:</b> Schematic ternary phase diagram after Stolper et al. (1979). ....	65
<b>Figure 3.1:</b> Backscatter electron images of typical mineral textures.....	97
<b>Figure 3.2:</b> $Cr_2O_3$ vs Mg# for olivine profiles from Tissint experiments.....	99
<b>Figure 3.3:</b> Variation between Ni content and Mg# in S75 olivine. ....	100
<b>Figure 3.4:</b> Pyroxene compositional range from reducing (circles) and hybrid (diamond) cooling rate experiments (S75, triangles).....	101
<b>Figure 3.5:</b> Spinel compositional range from reducing (circles) and hybrid (diamonds) cooling rate experiments.....	102
<b>Figure 3.6:</b> Selected x-ray maps of olivines from hybrid and reducing cooling rate experiments.....	103
<b>Figure 4.1:</b> BSE photo mosaic of NWA 7035 thin section.....	128
<b>Figure 4.2:</b> Pyroxene compositions from traverses of NWA 7035; each color represents a separate traverse of a different pyroxene grain. ....	129
<b>Figure 4.3:</b> BSE images of several features observed in melting experiments.....	130
<b>Figure 4.4:</b> A: High-Fe mesostasis in NWA 7035 located near ferroan pyroxene rims. B: Fine-grained intergrowth of fayalite, anorthite, ferroan-augite, silica, and oxides resulting from breakdown of a metastable ferripigeonite or pyroxferrite composition. ....	131
<b>Figure 4.5:</b> Rare earth element trends of each of the experimentally derived partial melts. ....	132
<b>Figure 4.6:</b> Pyroxene compositional ranges from three experiments in both major and minor elements. Glass compositions are also included. ....	133
<b>Figure 4.7:</b> CIPW norm projection of the melt composition with increasing degree of melting for normative plagioclase (anorthite + albite + orthoclase), pyroxene (diopside + hypersthene), and quartz.....	134
<b>Figure 4.8:</b> Stolper's projection of the silica, forsterite, and fayalite components of eucritic melts (see text for projection details), modified from Stolper (1977). ....	135

<b>Figure 4.9:</b> Best-fit rare earth element compositions for mixtures of the experimentally derived melt compositions with the Juvinas bulk composition to generate a Stannern-like composition.....	136
<b>Figure 4.10:</b> Partial mixing models for the experimentally-derived melt compositions with the Juvinas bulk composition of Barrat et al. (2007).....	137
<b>Figure 4.11:</b> Partial mixing models for experimentally-derived melt compositions with the Juvinas bulk composition of Barrat et al. (2007).....	138
<b>Figure 4.12:</b> BSE photomicrograph of a Fe-rich vein and surrounding metasomatized pyroxene in experiment B (1040°C).....	139
<b>Figure A1.1:</b> Comparison between oxide pairs and the equilibrium model of Bacon and Hirschmann (1988) for Mg-Mn equilibrium.....	172
<b>Figure A2.1:</b> X-Ray maps of an olivine grain in S48, the cooling rate experiment under reducing conditions from 1375-1225°C. ....	174
<b>Figure A2.2:</b> X-Ray maps of an olivine grain in S50, the cooling rate experiment under reducing conditions from 1375-1100°, oxidized at 1150°C.....	175
<b>Figure A2.3:</b> X-Ray maps of a pyroxene grain in S50, the cooling rate experiment under reducing conditions from 1375-1100°C. This series was collected on a pyroxene grain, rather than centered on an olivine grain as the rest of the figures in this appendix.....	176
<b>Figure A2.4:</b> X-Ray maps of a mixture of olivine and pyroxene grains in S58, the cooling rate experiment under reducing conditions from 1375-1000°C.....	177
<b>Figure A2.5:</b> X-Ray maps of an olivine grain in S64, the hybrid cooling rate experiment from 1375-1100°, oxidized at 1200°C.....	178
<b>Figure A2.6:</b> X-Ray maps of an olivine grain in S68, the hybrid cooling rate experiment from 1375-1100°, oxidized at 1150°C.....	179
<b>Figure A2.7:</b> X-Ray maps of an olivine grain in S69, the hybrid cooling rate experiment from 1375-1200°, oxidized at 1200°C, then held for 24 hrs.....	180
<b>Figure A2.8:</b> X-Ray maps of an olivine grain in S75, a hybrid cooling rate experiment from 1375-1100°, oxidized at 1200°C. This experiment was performed using a synthetic composition doped with 1% each NiO and V <sub>2</sub> O <sub>5</sub> .....	181

## **Chapter 1: Introduction to the Thesis**

Broadly, the subject of this thesis is the formation, evolution, and continuing igneous processes that formed and shaped the solid bodies in the solar system using the tools and techniques of experimental petrology. As this is a very broad subject, a narrower subset was chosen where individual meteorites could be used to test specific theories related to the igneous evolution of a parent body. Two bodies were chosen for study: Mars, and the HED parent body. These two bodies represent contrasting examples of basalt genesis. An extensive literature exists related to both of these bodies, creating a fertile field for targeted experimental studies to evaluate existing hypotheses. Although basalts were studied from both bodies, the geologic histories leading to each suite of meteorites are highly dissimilar: Mars is a planet with an extensive, and potentially ongoing, volcanic history, whereas the HED parent body, which may or may not be the asteroid Vesta but is certainly a small asteroidal body, was only geologically active in the earliest part of solar system history. As a result, shergottites (Martian basalts) represent relatively recent geologic activity based on conventional mantle melting processes, whereas eucrites (asteroidal basalts from the HED suite) are among the oldest materials in the solar system and are likely the direct products and differentiates of an evolving magma ocean. The projects related to these two parent bodies have used igneous meteorites to examine the primordial differentiation that resulted in crust and mantle formation, as well as further details of their igneous petrogenesis.

Experiments in this study relied heavily on the use of 1-bar gas-mixing furnaces. Although pressure is a major variable in terrestrial igneous petrology, and has been shown to greatly influence the evolution of a magma, its effect is much more minimal in planetary studies. The Earth is one of the two largest solid bodies in the solar system, the other being Venus, so it has a relatively high pressure gradient with depth; most other parent bodies have a substantially lower pressure gradient with depth. For example, the central pressure of Vesta is calculated to be no more than approximately 4 kbar, a pressure corresponding to only ~15 km depth in the Earth. As a trade off to not being able to control pressure, the advantage of 1-bar gas-mixing experiments is the ability to

readily, and precisely, control the oxygen fugacity ( $fO_2$ ) of the experimental system. Whereas terrestrial basaltic systems tend to have a relatively restricted range of  $fO_2$ , likely reflecting the vigorous convection of the terrestrial mantle, planetary basalts form from various parent bodies over a wide range of  $fO_2$ s, likely due to the heterogeneity of oxidation in the solar nebula, and can even exhibit a wide range of  $fO_2$ s within a suite (e.g. shergottites).

## **1.1: Introduction to Mars**

Shergottites are basaltic achondrites, differentiated igneous meteorites dominated by pyroxene and plagioclase. A subset of shergottites contain impact glasses that trapped atmospheric gases (e.g. EETA 79001); these trapped gases are a close match for the Martian atmospheric composition in both major-elements and isotopic ratios (Fig. 1.1), and so the shergottite parent body has been identified as Mars (Becker and Pepin, 1984; Bogard and Johnson, 1983; Bogard et al., 1984; Ott, 1988). Geochemical arguments relate shergottites to Nakhilites and Chassignites - pyroxenites and dunites, respectively - leading to a collective reference to the SNC meteorites as the Martian meteorites (McSween, 1994; Treiman et al., 2000); both terms are commonly used to reference a range of Martian meteorites beyond the strict S-N-C types (e.g. including NWA 7034/7533, which is an ancient breccia; Agee et al., 2013; Hewins et al., 2016; Humayun et al., 2013). Of the three main SNC types, shergottites are by far the most numerous, making up approximately 80% of the Martian meteorite collection (Irving, 2017), and all three fall along a common mass-dependent oxygen isotope fractionation line, significantly separated from the terrestrial fractionation line (e.g. Greenwood et al., 2016, and references therein) (Fig. 1.2). Despite being basalts, presumably either erupted or shallowly emplaced on Mars, most have undergone a substantial degree of olivine accumulation (Filiberto and Dasgupta, 2011; Shearer et al., 2008). The degree of accumulation is frequently estimated using the Fe-Mg disequilibrium between the bulk composition and olivine cores, where the equilibrium olivine-liquid distribution coefficient ( $K_d$ ) is known to be 0.30-0.33 (Fig. 1.3; Filiberto and Dasgupta, 2011).

Shergottites are subdivided into a number of types based on texture or composition. Based on texture, there are four shergottite types: the olivine-phyric shergottites (Ol-phyric) are characterized by an olivine megacryst assemblage; the pyroxene-phyric shergottites (Px-phyric) are characterized by a pyroxene megacryst assemblage; the poikilitic shergottites, sometimes referred to as lherzolithic shergottites, contain olivine oikocrysts poikilitically enclosed by orthopyroxene; the basaltic shergottites lack a significant megacryst assemblage, but are instead dominated by a plagioclase-pyroxene groundmass. All four textural types are typically regarded as separate magma compositions, meaning that one type is not believed to evolve into another (e.g. Bridges and Warren, 2006; McSween, 1994), based on the wide and overlapping ranges in typical geochemical indicators of magmatic maturity (e.g. Mg#, the molar ratio of Mg/Fe+Mg). Based on incompatible trace-element (ITE) abundances, the shergottites are additionally subdivided into three chemical types: the enriched, intermediate, and depleted types. Trace-element and radiogenic isotope compositions correlate, showing the same sense of enrichment or depletion (Fig. 1.4), however, the geochemical types do not correlate with the textural types as examples of most of the geochemical types can be found within each of the textural types (Shearer et al., 2013; Shearer et al., 2008; Symes et al., 2008). The correlation of radiogenic systems with ITE variation indicates that these reservoirs represent long-term reservoirs that have existed without intermixing until sampled to form the various shergottite magmas (e.g. Borg and Draper, 2003; Borg et al., 1997).

As a whole, shergottites represent fairly recent Martian magmatism, but provide insights into Mars' ancient past. Isotopic compositions of mineral separates from individual shergottite meteorites plot along isochron lines consistent with ages ranging from as old as 600 Ma to as young as 160 Ma (Fig. 1.5) indicating a young igneous age (Borg and Draper, 2003; Borg et al., 1997; Borg et al., 2003; Nyquist et al., 2009a). Contrasting this, whole-rock isotope ratios from a range of shergottites spanning all three chemical types fall along an isochron line consistent with a 4.52 Ga origin (Fig. 1.6; Borg and Draper, 2003; Debaille et al., 2007). The whole-rock isochron is not believed to represent a magmatic age, but rather the age of differentiation of the source reservoirs that gave rise to the chemical diversity later sampled by shergottite magmas (Borg et al.,

2003); as this differentiation event is nearly as ancient as Mars itself, it is believed that this represents the primordial silicate differentiation from the early magma ocean (e.g. Borg and Draper, 2003; Debaille et al., 2007).

Oxygen fugacity ( $fO_2$ ) plays an important role in the petrogenesis of shergottites. Shergottite magmas, and their likely mantle source compositions, range over approximately 4 log units of  $fO_2$  (e.g. Basu Sarbadhikari et al., 2009; Goodrich et al., 2003; Herd, 2003; Peslier et al., 2010). The oxidation state of a magma changes the stable mineral assemblage, not just in terms of the abundance and composition of minor oxides, but also in terms of the dominant mineral assemblage (e.g. oxidizing conditions favor pyroxene over olivine, see Ch.2 or Castle and Herd, 2017). The oxidation state of shergottite magmas correlates both with the degree of enrichment, where enriched magmas are more oxidized than depleted magmas, and with textural type, where, for any given degree of enrichment, basaltic shergottites are more oxidized than Ol-phyric shergottites (Fig 1.7; Herd et al., 2002a; Wadhwa, 2001). A subset of Ol-phyric shergottites have been shown to have undergone oxidation during their crystallization history, e.g. the enriched shergottites NWA 1068 (Herd, 2006) and LAR 06319 (Peslier et al., 2010), as well as the intermediate shergottite NWA 6234 (Gross et al., 2013). This oxidation is generally tracked using geothermometer/oxybarometer (GTOB) estimates calculated from the temperature and oxidation dependent equilibrium of oxide assemblages, like the olivine-spinel-pyroxene (Ol-Sp-Px) GTOB (Sack and Ghiorso, 1991a; Wood, 1991), which records early magmatic conditions, or the titanomagnetite-ilmenite (Tmt-Ilm) GTOB (Ghiorso and Sack, 1991; Ghiorso and Evans, 2008), which records late magmatic conditions. A potential mechanism for causing this oxidation is volatile loss, where a reduced gas escapes leaving a more oxidized residuum (Shearer et al., 2013); good potential examples for volatiles in shergottite magmas are based on C, S, and Cl species. Previous studies have only demonstrated this oxidation in enriched or intermediate Ol-phyric shergottites, leading to the suggestion that volatile content is related to the enriched geochemical reservoir (Herd, 2003), a conclusion that this work has contested (Castle and Herd, 2017; see Ch.2).

The exact nature and origin of the enriched and depleted geochemical reservoirs on Mars is still a matter of discussion, but several things are known. As the whole-rock

isochron indicates that the geochemical reservoirs are primordial, there are two likely physical locations for these reservoirs: the enriched reservoir may be the ancient Martian crust, believed to have formed as the surface quench of a Martian magma ocean (e.g. Herd et al., 2002a); or it may be the last-gasp of a crystallizing magma ocean (e.g. Herd, 2003), similar to the model for the origin of lunar KREEP (e.g. McKay and Weill, 1976, 1977). In both models the depleted reservoir is likely the dominant mantle composition, made depleted relative to the bulk silicate Mars by the extraction of the enriched reservoir. The oxidized nature of the enriched reservoir is consistent with either model (e.g. Herd et al., 2002a; Wadhwa, 2001), and volatiles could be accounted for in either model. Given that Mars has never experienced plate tectonics or crustal recycling, it is easy to conceptualize the crust as the enriched reservoir because it is likely to be an enriched reservoir that has persisted from the earliest differentiation of Mars. Arguing against a crustal assimilation model, it is difficult to create a geochemical model where assimilation leads to an increased ITE composition without an accompanying systematic alteration of the major-element composition. Further, it would be an extraordinary coincidence if every Martian basalt thus far measured assimilated the identical altered crustal component required to generate the proportional shift observed in REEs, Sm-Nd and Rb-Sr isotopic composition, and  $fO_2$  (see Herd, 2003 for a more detailed discussion). Physically, assimilation of crustal blocks into surface lava flows has been inferred using satellite observations of the Martian surface (Fig. 1.8; Dundas et al., 2016), supporting the notion that enrichment from a crustal component has occurred in some Martian magmas; however, presently there is no way of determining if these magmas are represented within the shergottite suite. Given the geochemical difficulty in the crustal assimilation model for the enriched reservoir, this study makes the assumption that both the enriched and depleted reservoirs are present in the mantle.

This study begins by tracing the igneous history of a depleted, olivine-phyric shergottite, Tissint, by examining the liquid line of descent. The results of isothermal experiments, simulating the equilibrium crystallization curve of the meteorite, allows us to examine the  $fO_2$  evolution of the meteorite, and to draw conclusions about the nature of volatiles in the depleted Martian geochemical reservoir. The implications of this investigation, discussed in Chapter 2, revise our understanding of shergottite petrogenesis

by presenting evidence that volatiles are not linked to geochemical reservoir. The chemical evolution of a crystallizing Tissint magma also shows that it can be related to the composition of some, but not all, basaltic shergottites, and cannot be related to some olivine-phyric shergottite compositions; this suggests that there are further subdivisions within the shergottite textural types based on plausible magmatic relations.

In the process of examining the effect of a change in  $fO_2$  on a crystallizing Tissint magma, it was discovered that the oxidation event overprinted the zoning profile of Cr in olivine. Chapter 3 follows a further investigation of the phenomenon, aiming to describe the mechanism by which Cr profiles in olivine were overprinted, and, in so doing, help constrain what other elements may be similarly affected. The combined observations of these two studies (Ch.2 and 3) presents a plausible resolution of a long-standing conflict in the literature, where different techniques came to opposite conclusions about whether olivine grains in NWA 1068/1110 were phenocrystic or xenocrystic (Herd, 2006; Shearer et al., 2008).

## **1.2: Introduction to the HED parent body and Vesta**

The HED meteorite suite is composed of three sets of related meteorite types, the howardites, eucrites, and diogenites. Eucrites are mafic rocks defined by a subequal assemblage of low-calcium pyroxene (pigeonite) and anorthitic plagioclase. Diogenites are ultramafic rocks, classically defined as nearly pure orthopyroxenites, but more recently expanded to include increasing olivine abundances up to and including dunites (Beck and McSween Jr, 2010; Beck et al., 2011). Howardites are highly variable breccias defined as containing a somewhat arbitrary minimum of 10% each eucritic and diogenitic clasts/fragments. It is the close association of eucrites and diogenites in howardites that lead to their classification as a suite of related meteorite types. In terms of collections, eucrites are the most abundant differentiated, or achondrite, meteorite type.

HED meteorites are among the oldest differentiated materials in the solar system, and so provide valuable insight into the earliest stages of accretion and differentiation. Mineral separates of eucrites commonly yield crystallization ages older than 4.5 Ga (e.g. Nyquist et al., 1997; Nyquist et al., 2003; Nyquist et al., 1986). Ar-Ar ages are generally

much younger, ranging between 4.5 and 3.5 Ga (e.g. Bogard and Garrison, 2003; Nyquist et al., 1997), consistent with a substantial period of impact activity resetting the Ar systematics around that time. A number of studies have shown evidence that some eucrites formed while a number of short-lived radionuclides were active (Fig. 1.9), e.g.  $^{26}\text{Al}$ ,  $^{146}\text{Sm}$ , and  $^{53}\text{Mn}$  (Lugmair and Shukolyukov, 1998, 2001; Mittlefehldt et al., 1998; Nyquist et al., 2009b; Nyquist et al., 2003; Schiller et al., 2010). The  $^{182}\text{Hf}$ - $^{182}\text{W}$  isotope system, which tracks the timing of core formation, shows that the HED parent body had formed a core by  $4563.2 \pm 1.4$  Ma, within the first 5 Ma of the solar system (Kleine et al., 2004; Quitté et al., 2000). All of this evidence leads to the conclusion that the HED parent body accreted rapidly in the early solar system, differentiated to form a core, mantle, and crust, and then was geologically dead, excepting impact processes, within the first few 10s of millions of years of the birth of the solar system.

Most HED meteorites fall along a single mass-dependent oxygen isotope fractionation line, often referred to as the HED fractionation line (Fig. 1.10). Typically, eucrites have the highest  $^{18}\text{O}$  content and the diogenites the lowest. A number of eucrites are referred to as anomalous either because they fall off of the line with regard to  $^{17}\text{O}$  (e.g. Ibitira; Mittlefehldt, 2005) or because they are substantially lower in  $^{18}\text{O}$  content than more typical eucrites (e.g. NWA 1240; Scott et al., 2009). Although the common association along a single mass dependent fractionation line is often cited as evidence of origin on a single parent body, it is more rigorous to instead infer that meteorites off of this line are unlikely to originate on the same parent body (Clayton and Mayeda, 1983; Greenwood et al., 2016) unless a likely mechanism can be identified that would cause a large mass-independent shift in oxygen isotopes. The concept that common oxygen isotope compositions do not require a common origin can be somewhat trivially demonstrated, as mesosiderites, silicate inclusions in IIIAB irons, and some pallasites fall along, or very near to, the HED fractionation line, but none of them are presently believed to originate on the HED parent body (Greenwood et al., 2016; McSween et al., 2013; Mittlefehldt, 2015). In the case of the mesosiderites this is a recent realization, based largely on the idea that the mesosiderites represent reassembled fragments of a disrupted parent body whereas the HED parent body is believed to be intact (McSween et al., 2013). The existence of anomalous eucrite compositions suggests that the HED parent

body may not have been a unique body but instead the product of a common differentiation process (e.g. Wiechert et al., 2004), although the concept of multiple HED parent bodies is still considered highly controversial (Ruzicka, personal communication; Mittlefehldt, personal communication).

In terms of structure of the parent body, eucrites are thought to represent the planetary crust, diogenites either a crustal cumulate or residual mantle, and howardites the impact breccia and regolith near the surface of the body (Fig. 1.11). Howardites, as fragmental breccias, are most likely the result of impact bombardment on an airless body. In many cases impactor material is preserved as xenolithic clasts in howardites, typically IIIAB iron or CM chondrite fragments although other types have been described (Metzler et al., 1995; Wilkening, 1973). The typical low degree of shock preserved in HED meteorites argues for their origin on a small body (most do not contain maskelynite, although a rare few have been described). Some howardites show both chemical and physical indicators of interaction with the solar wind (e.g. glass spherules, Ni enrichment; Cartwright et al., 2013; Warren et al., 2009) consistent with a true regolith, although not one as texturally mature as the Lunar regolith. A typical howardite contains a ratio of approximately 2-1 eucritic to diogenitic material, leading to the conclusion that eucrites dominate the surface of their parent body (e.g. Warren et al., 2009). As basalts and gabbros from a short-lived body, eucrites make sense as an early-formed crust of the parent body, whether as a crustal lid on a magma ocean or as a partial-melting extract from an ultramafic mantle (Wilson and Keil, 1996). Diogenites, as the less common component of howardites, are consistent with either a deeper layer of the HED parent body where their low relative abundance is the result of a lower fraction of impact events sampling deeply enough to access diogenites (De Sanctis et al., 2012; Righter and Drake, 1997; Ruzicka et al., 1997), or as a less commonly formed material, potentially an ultramafic cumulate from the magma that formed the eucrites (Shearer et al., 2010).

Historically, there have been two conflicting models for the origin of the HED suite; however, at present their formation from a magma ocean is the preeminent model. To briefly summarize the less-favored model, referred to as the partial melting model, eucrites are an extracted liquid from a primitive (that is, chondritic) mantle, leaving behind a diogenitic residue. The principal evidence for the partial melting model is the

clustering of eucrite compositions around a compositionally-constrained melting point ("pseudotectic" Stolper, 1975, 1977); this composition is not a composition that a fractionally crystallizing liquid is bound to, and is not a composition that a range of potential source compositions would even pass through during fractional crystallization, but is the major-element melt composition from a wide range of plausible source compositions until melting exhausts one of the major mineral phases (Fig. 1.12). Further, in support of the partial melting model, it was demonstrated that melting an LL chondrite under reducing conditions can produce a eucrite-like liquid while leaving behind a diogenite-like orthopyroxene composition (Jurewicz et al., 1995). In contrast, the magma ocean model for HED petrogenesis is favored primarily because of the chemical homogeneity of these meteorites in a number of trace-element and isotopic systems (Greenwood et al., 2005; Mittlefehldt and Lindstrom, 2003). Formation from a magma ocean requires that the clustering around the pseudotectic composition be purely coincidental. Computational models have been performed, with varying degrees of success, which suggest that both eucrites and diogenites could crystallize from a plausible parental composition (Grove and Bartels, 1992; Righter and Drake, 1997; Ruzicka et al., 1997). A more recent, and more detailed, study by Mandler and Elkins-Tanton (2013) uses MELTS (Asimow and Ghiorso, 1998; Ghiorso and Sack, 1995) to calculate the range of plausible liquid evolutions that could generate both eucrites and diogenites from a magma ocean; they conclude that the most likely model is a 60-70% equilibrium crystallization of a mantle from the magma ocean (which is not represented in our meteorite collections), and that both eucrites and diogenites form from the extracted residual liquid as fractional crystallization products. A recent review paper by Mittlefehldt (2015) provides a more detailed discussion of HED petrology, geochemistry, etc., for the interested reader.

The focus of my research in the HED suite has been the eucrite meteorites. Eucrites are basalts and gabbros, and preserve a fundamental dichotomy between meteorites with a liquid-like bulk composition, referred to as the basaltic eucrites (previously the non-cumulate eucrites), and meteorites that have undergone some degree of accumulation, the cumulate eucrites (sometimes erroneously referred to as gabbroic eucrites as not all gabbros are fractionated from their source liquids). The two can often

be distinguished based on texture, but, more rigorously, cumulate eucrites (CE) are identified based on mineral or bulk compositional features consistent with mineral accumulation; for example, cumulate eucrites typically have more magnesian compositions with cumulate rare earth element (REE) patterns (Hsu and Crozaz, 1997; Pun and Papike, 1995; Pun et al., 1997). Basaltic eucrites are divided into three groups based on whole-rock or pyroxene chemistry (Ahrens, 1970; Mittlefehldt and Lindstrom, 2003; Stolper, 1977): the main group trend (MGT), the Nuevo Laredo trend (NLT), and the Stannern trend (ST). The MGT is the most common eucrite composition, and is believed to reflect the composition of the liquid from which all eucrites are derived (Mittlefehldt and Lindstrom, 1997). The NLT is a ferroan evolution of the MGT, consistent with its formation from fractional crystallization of a MGT magma, roughly complementary to the CE composition. The ST has the same major-element composition as the MGT, but is enriched in incompatible trace-elements (ITE), for example La. A complication in working with the igneous petrology of eucrites is that the majority of eucrites have undergone varying degrees of metamorphism that has typically homogenized the pyroxene composition (Fig. 1.13), even though many preserve igneous textures (Takeda and Graham, 1991; Yamaguchi et al., 1996); eucrites that have not undergone this homogenization are referred to as zoned or unequilibrated eucrites. On top of their metamorphic homogenization, most eucritic pyroxenes have exsolved from a, presumably homogeneous, pigeonite composition into high and low-Ca pyroxene lamellae, making determination of the original pyroxene composition difficult (e.g. Mayne et al., 2009). These sub-solidus processes make interpretation of the igneous evolution of these meteorites difficult, and typically model dependent.

An advantage of the partial melting model over the magma ocean model is the difficulty encountered in generating the Stannern trend from a magma ocean. In the partial melting model, the ST is simply the result of lower degrees of partial melt, which would generate the same bulk composition but with a higher fraction of ITEs as additional melting does not shift the melt from the pseudotectic composition, but does dilute the ITEs that preferentially move into the magma (Stolper, 1975, 1977). From a liquid, it is difficult to generate an ITE enrichment without concurrently altering the major-element composition, complicating the magma ocean model. A number of models

have been proposed (e.g. in situ crystallization, Barrat et al., 2000; melt capture disequilibrium, Treiman, 1996) but the most successful so far is a modification of a combined assimilation and fractional crystallization model (AFC, after DePaolo, 1981) where a low degree partial melt of a preexisting MGT eucrite is mixed with a crystallizing MGT liquid (Fig. 1.14; Barrat et al., 2007). This study aims to experimentally investigate a potential source of such a partial melt by performing partial melting experiments on a zoned eucrite; the results are discussed in Chapter 4.

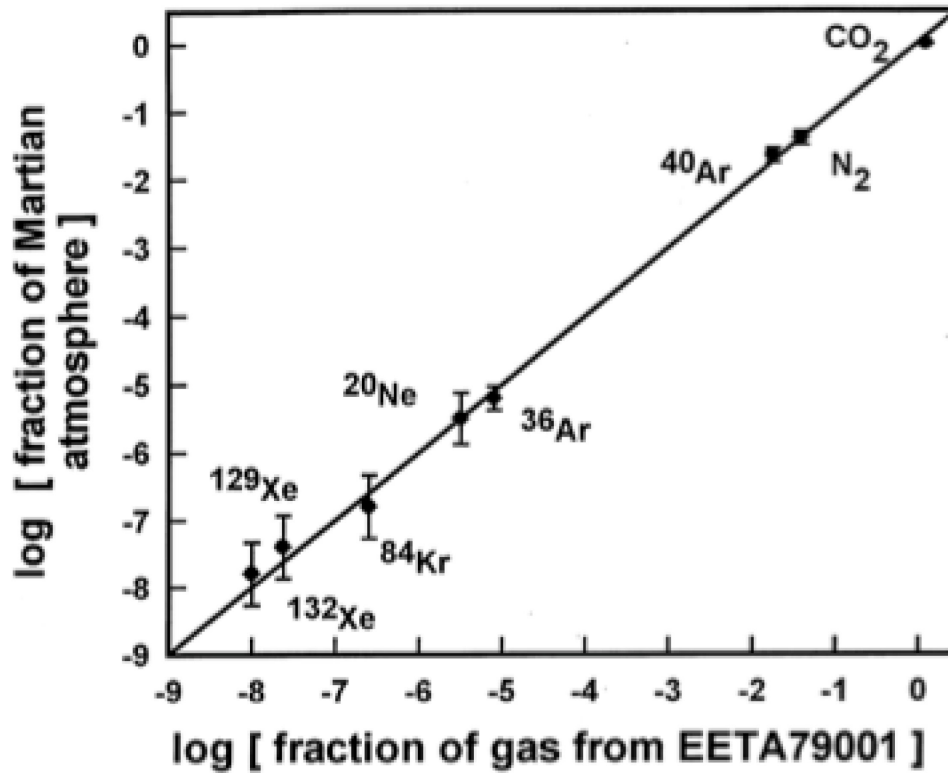


**Figure 1.1:** Evidence for the Martian origin of the Martian meteorites (from Treiman et al., 2000). The plot contrasts the measured composition of the Martian atmosphere (Owen, 1992; Owen et al., 1977) against the composition of trapped gases in EETA79001 (Pepin and Carr, 1992).

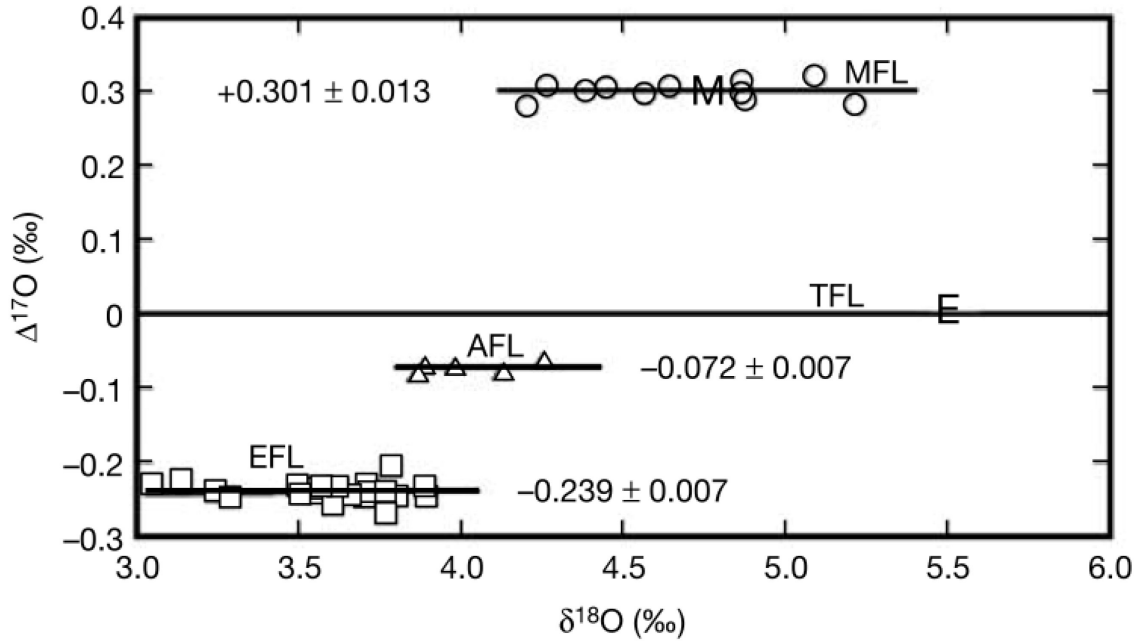


**Figure 1.2:** Oxygen isotope compositions of Martian meteorites (MFL), angrites (AFL), and eucrites (EFL) relative to the terrestrial fractionation line (TFL). Each mass-dependent fractionation line, horizontal lines with constant  $\Delta^{17}\text{O}$ , is believed to represent a different parent body, although it is possible for two separate parent bodies to fall along the same fractionation line. This figure is from Greenwood et al. (2005).

# Bulk composition

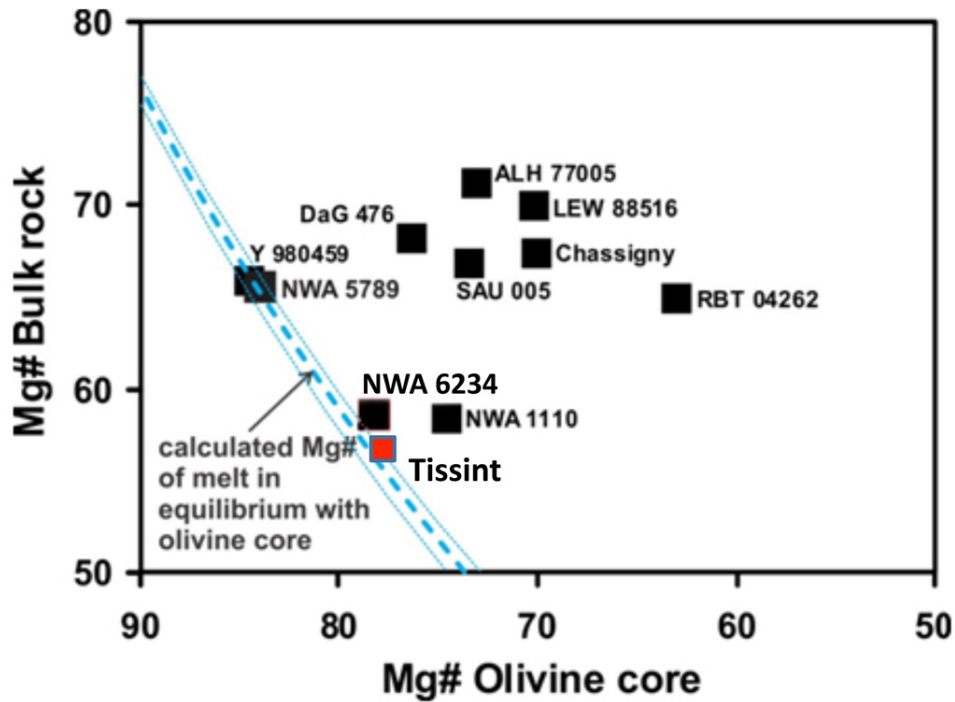


**Figure 1.3:** Visual depiction of the disequilibrium in Fe-Mg space between olivine cores and the bulk composition indicating that most shergottites have undergone a substantial degree of mineral accumulation. The dark line shows the calculated equilibrium line based on a  $K_d$  of 0.35 (Filiberto and Dasgupta, 2011). The further to the right points lie (towards lower Mg#, or Fo, of olivine) relative to the equilibrium line, the larger the degree of disequilibrium, and therefore the larger the degree of olivine accumulation the meteorite has undergone. This figure is modified from Filiberto and Dasgupta (2011) with data from Gross et al. (2013) and Herd et al. (2013).

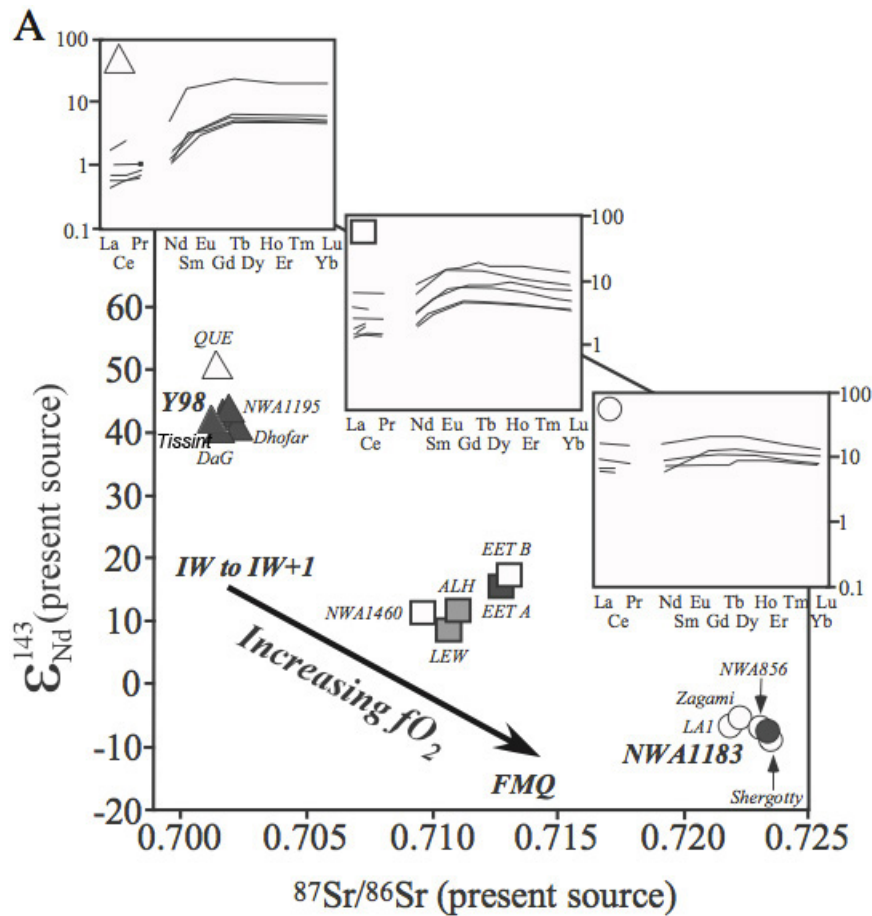


**Figure 1.4:** Composite figure that shows the correlation of enrichment in two isotopic decay systems (Sm-Nd and Rb-Sr) and trace-elements (rare earth elements, REEs, shown). Multiple shergottite textural types are in each reservoir, here shown as different shades of gray, indicating that the geochemical reservoirs do not correlate with textural type. The separation of the types may reflect three distinct reservoirs, or may be due to undersampling of a mixing curve between the enriched and depleted end members. This figure is from Shearer et al. (2013) based on the original from Symes et al. (2008) and has been modified to show the Tissint isotopic composition from Brennecka et al. (2014).

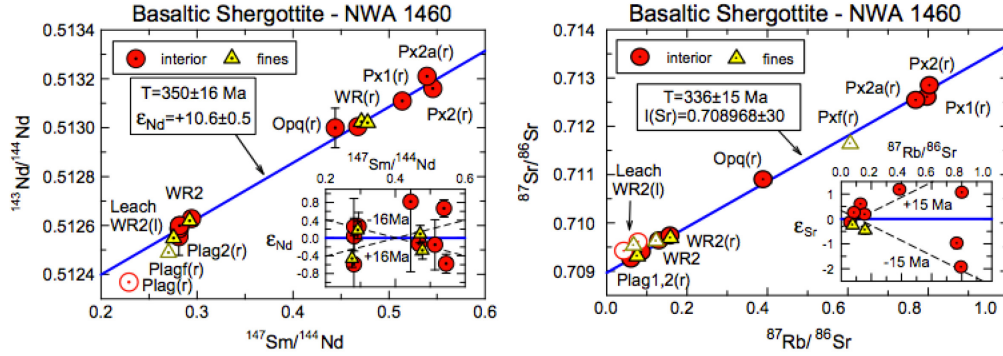


**Figure 1.5:** Example isochron age calculations from mineral separates of a basaltic shergottite (Nyquist et al., 2009a). In a number of cases, like the one shown here, ages calculated from multiple isotope systems are in agreement, lending confidence to the conclusion that the mineral separates reflect a relatively young igneous age for the meteorites studied. There are indications of a contaminant in some of the plagioclase separates shown here, likely terrestrial contamination in the Rb-Sr system and inadvertent inclusion of fusion crust with the Sm-Nd analysis, demonstrating the level of care that must be taken when obtaining isotopic ages; the interested reader is referred to the more detailed discussion in Nyquist et al. (2009a).

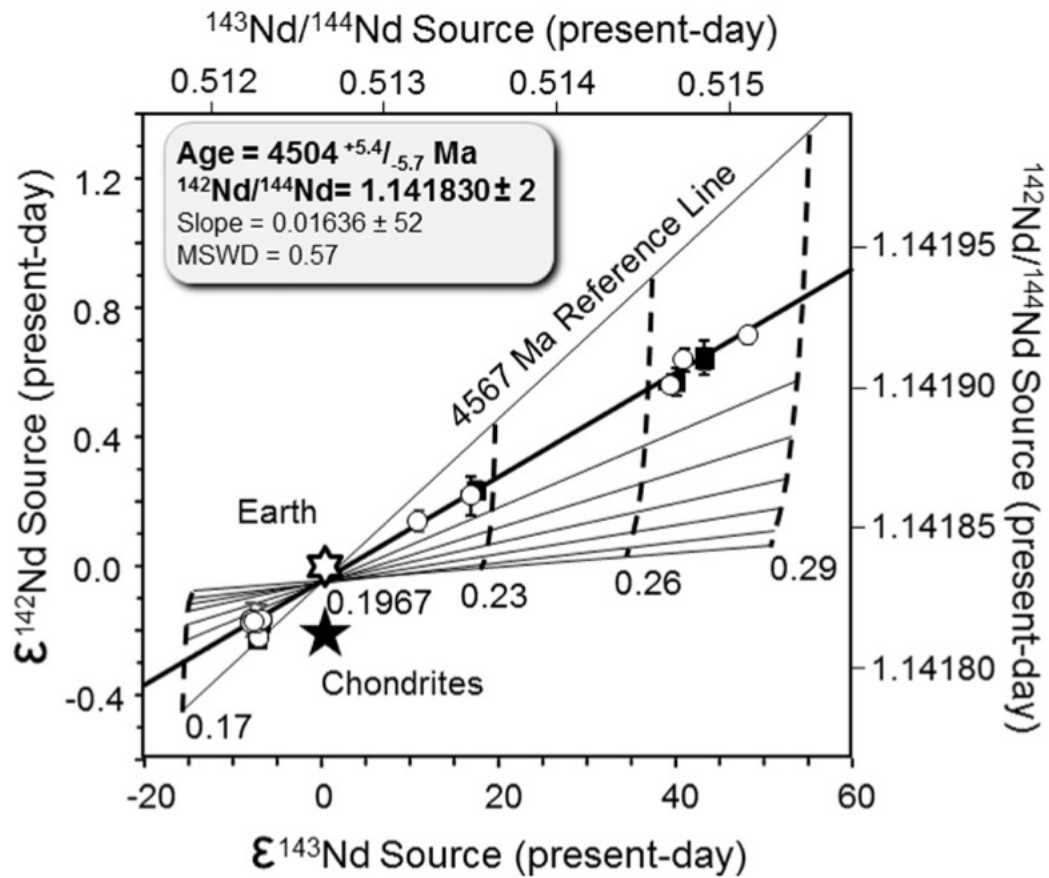


**Figure 1.6:** Measured and calculated isotopic composition for whole-rock Nd in a variety of SNC meteorites based on a two stage fractionation model. The three chemical types of shergottites (enriched, intermediate, and depleted) fall within reasonable agreement with a differentiation event segregating the three reservoirs very early in the history of Mars. This figure is from Borg et al. (2016).

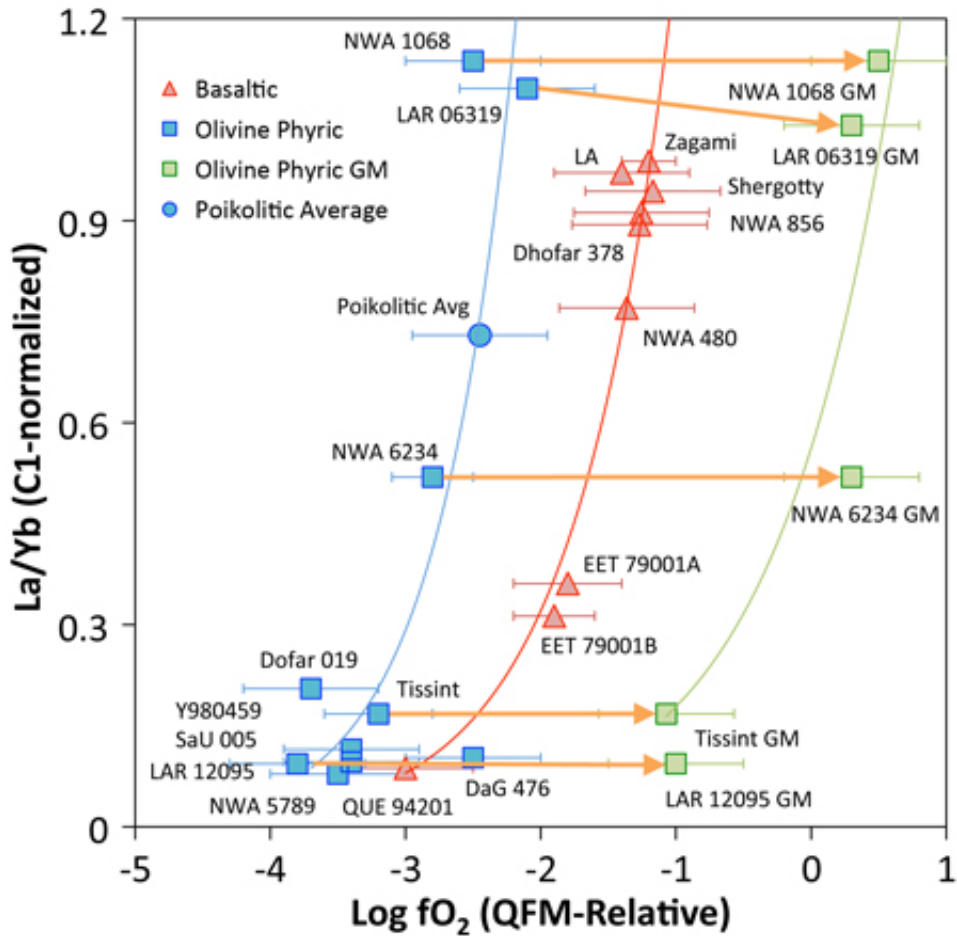


**Figure 1.7:** Correlation between oxygen fugacity and chemical type for the two main shergottite textural types; samples from the enriched reservoir (highest La/Yb ratio) formed under more oxidizing conditions than the depleted or intermediate reservoirs (middle and lowest La/Yb ratios, respectively), and the basaltic shergottites (red) formed under more oxidizing conditions than the olivine-phyric shergottites (blue), but all fall along a sensible regression curve relating the degree of enrichment to the oxidation. A separate curve (green) is shown for the subset of olivine-phyric shergottites that preserve a groundmass assemblage that has been shown to have formed under more oxidizing conditions than the early mineral assemblage. This figure is an update of Castle and Herd (2017), modified to show the estimates for LAR 12095, and based on the original figure from Herd (2003) who first described the relation between enrichment and oxidation in shergottite magmas.

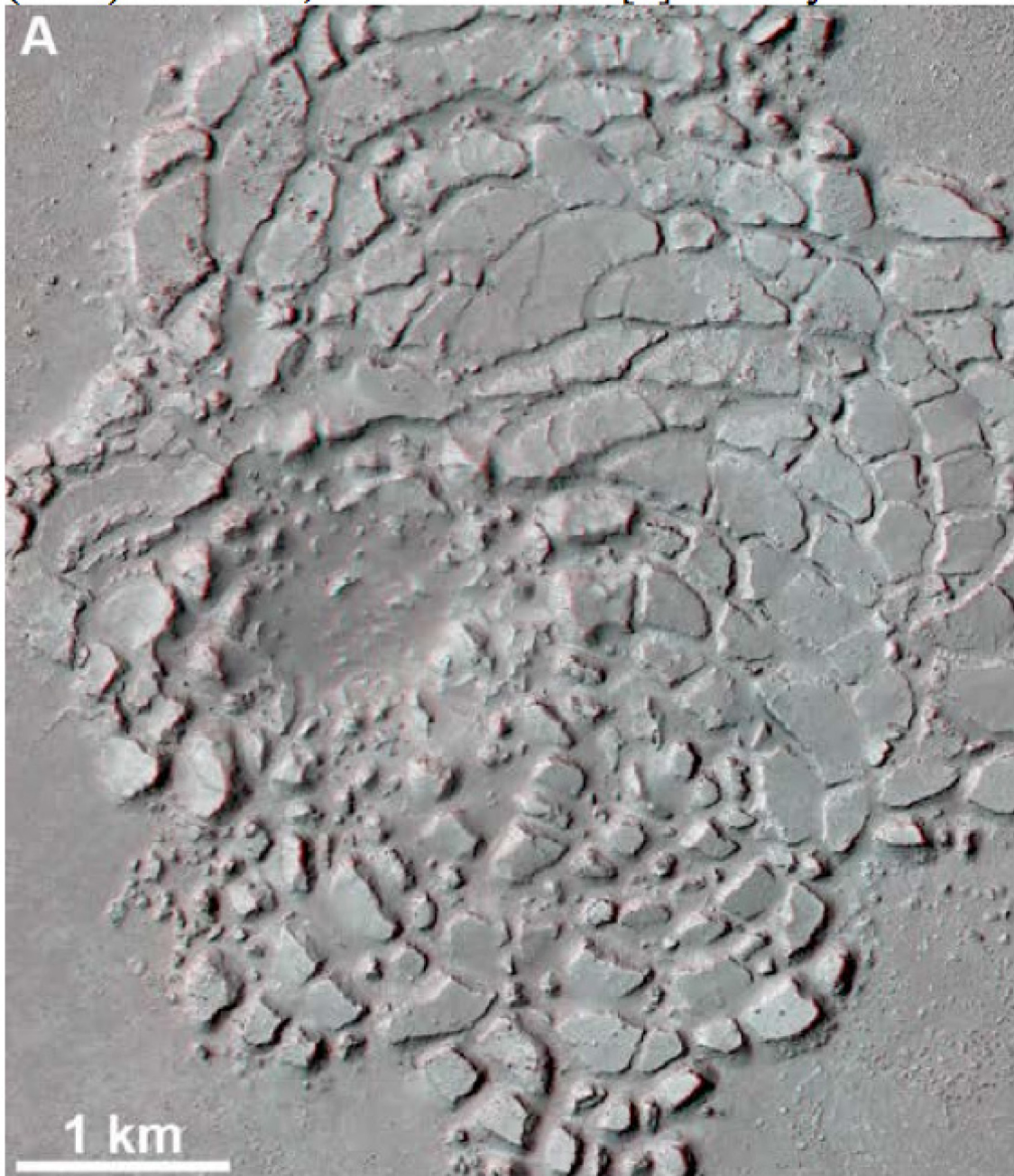


**Figure 1.8:** Polygonal surface consistent with disruption caused by magmatic intrusion from below (from Dundas et al., 2016). This sort of observation suggests that at least some Martian magmas did incorporate crustal blocks during emplacement.

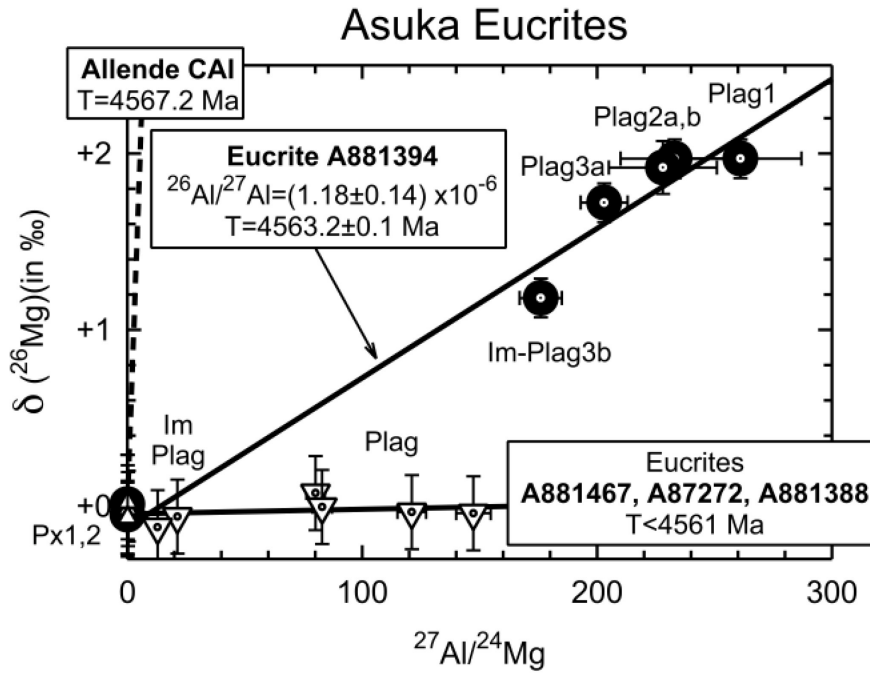


**Figure 1.9:** Evidence for the formation of eucrite Asuka 881394 while  $^{26}\text{Al}$  was still active (from Nyquist et al., 2003). Although many eucrites formed after  $^{26}\text{Al}$  was depleted, some eucrites formed while it was still active, making eucrites some of the oldest basalts in the solar system.

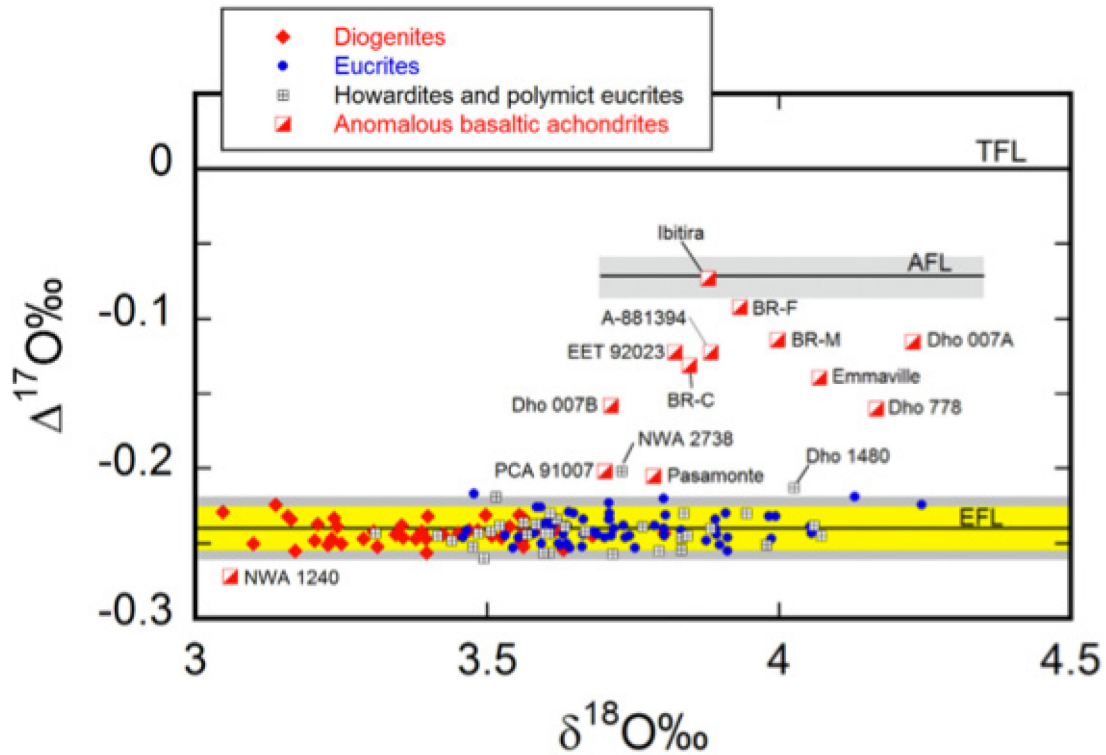


**Figure 1.10:** HED meteorite oxygen isotope systematics (from Greenwood et al., 2016). ‘Anomalous basaltic achondrites’ is the designation given by Greenwood et al. for eucrites (and one diogenite) with oxygen isotope compositions inconsistent with the inferred eucrite fractionation line (EFL). The EFL is also known as the HED fractionation line as it is typically calculated from the mass-dependent variation of the majority of howardites, eucrites, and diogenites measured, not just eucrites. The angrite fractionation line (AFL) and terrestrial fractionation line (TFL) are included for reference.

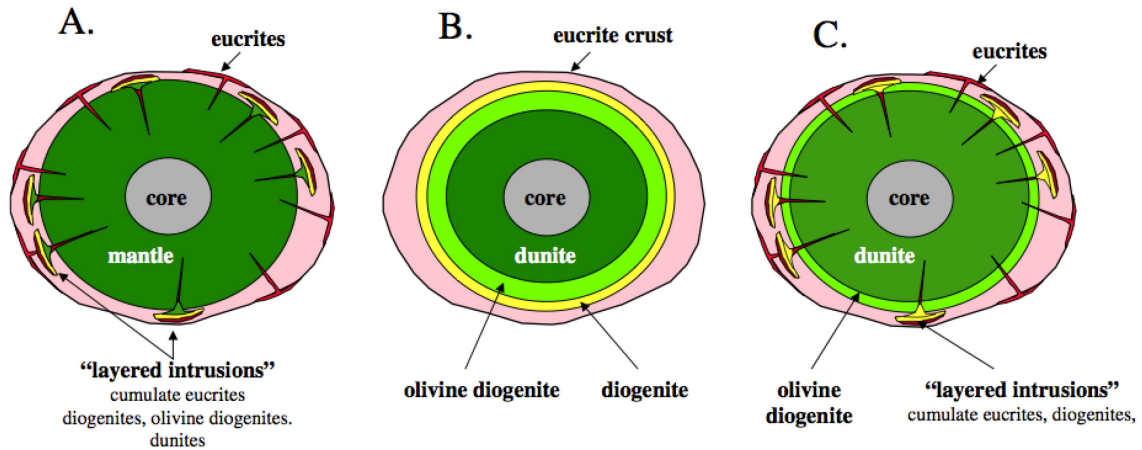


**Figure 1.11:** Schematic diagram of three models for the structure of the HED parent body and the relation between eucrites and diogenites (from Shearer et al., 2010). The typical orthopyroxenite diogenites may or may not be related to olivine diogenites or dunites, and either may be formed as ultramafic cumulates from magmatism or as part of the mantle remaining after melt extraction. The basaltic eucrites are believed to be the crust of the body, but their relation to cumulate eucrites or diogenites is less certain. The models presented are: A) a layered volcanism model, where all observed igneous compositions from HEDs are the result of magmatic differentiation processes; B) a layered formation model resulting from crystallization of a magma ocean where the most mafic composition is at the bottom; and C) a hybrid model where olivine diogenites and orthopyroxenite diogenites do not share a common origin, but are mantle residuum and ultramafic cumulate, respectively.

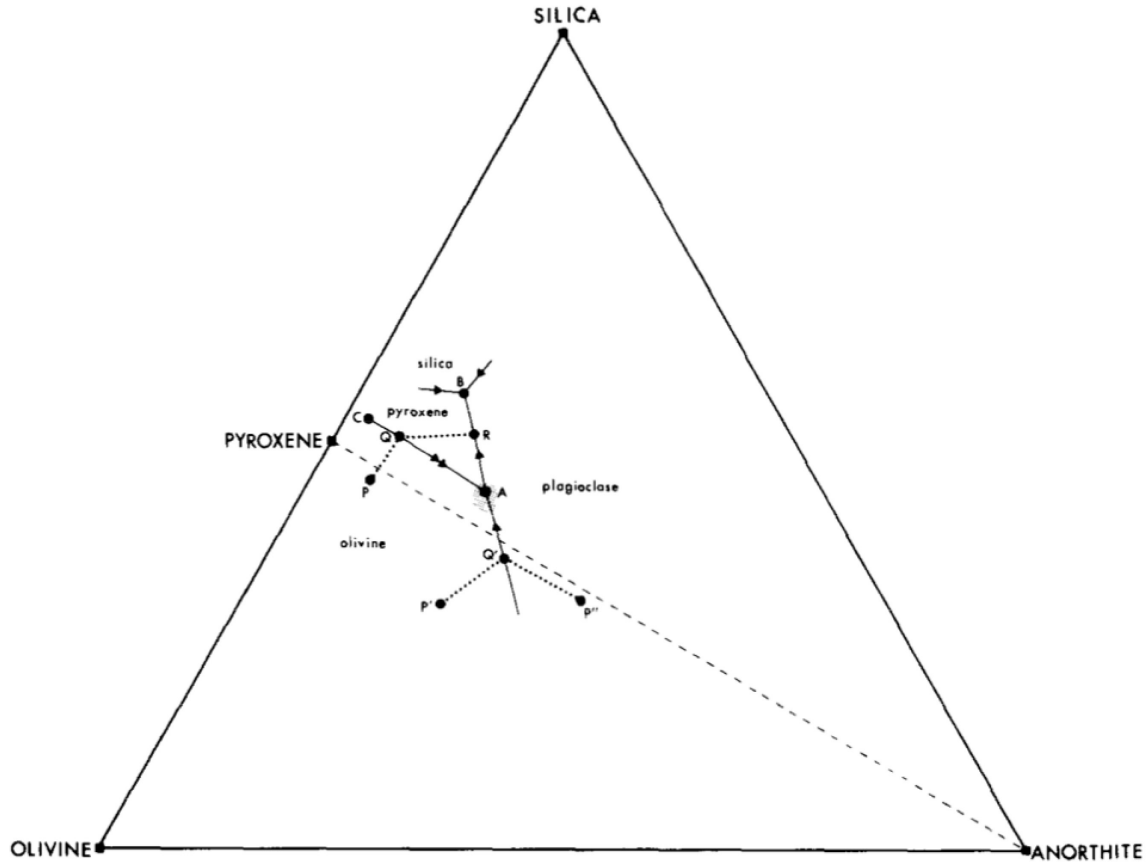


**Figure 1.12:** Norm projection of eucrite liquids with liquidus boundaries (from Stolper, 1977). Composition A, the composition that the basaltic eucrites cluster around, is the “pseudotectic” composition from melting of a mantle with olivine, plagioclase, and pyroxene. Fractional crystallization of a magma with a composition proximal to P’ or P” will pass through A, but will not be bound to it, suggesting that either eucrites are a partial melting composition, or that they coincidentally cluster around the pseudotectic composition. A liquid with a composition proximal to P will only encounter point A if the liquid is crystallizing under equilibrium conditions; a fractional path will not intersect point A.

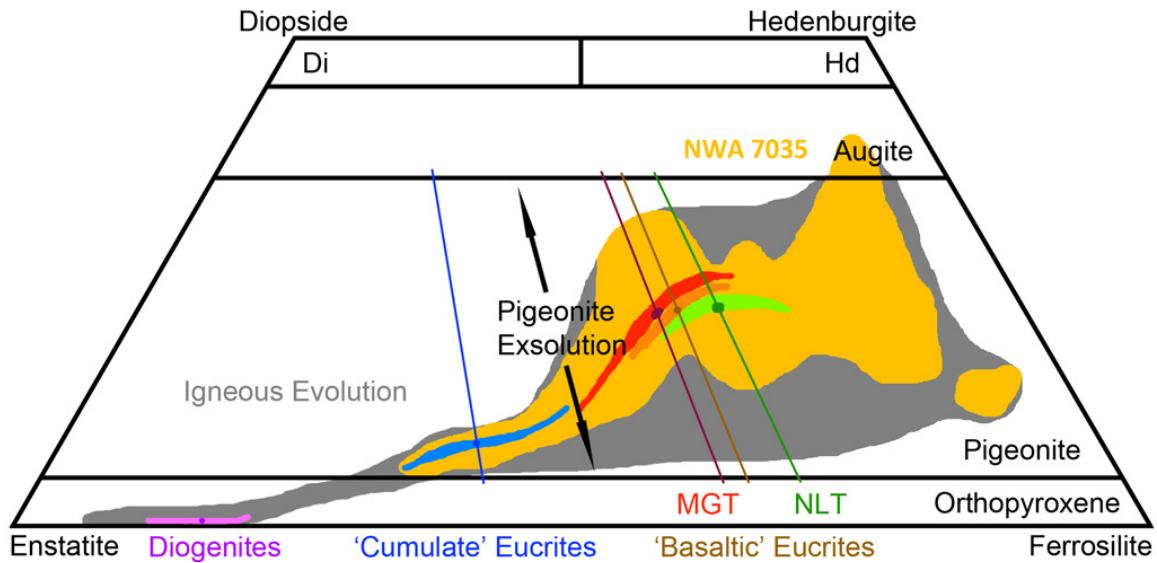


**Figure 1.13:** Schematic diagram of eucrite pyroxene compositions. The gray field is a hypothetical full range of magmatic pyroxenes resulting from fractionation of a primary eucrite magma. The colored fields are hypothetical subsets of fractionation preserved in each of the different eucrite chemical types (MGT, NLT, and CE) and diogenites. Metamorphism would reduce the observed range of pyroxene compositions to a single point, as shown within each colored field. Sub-solidus exsolution of augite from pigeonite hosts results in a sub-vertical range in pyroxene composition, and is schematically drawn for each colored “average” composition. The large orange field is the approximate range of pyroxene observed in the unequilibrated eucrite NWA 7035, the sample selected for study as representative of a primitive eucritic crust on the HED parent body, which belongs to the Pasamonte trend of zoned eucrites.

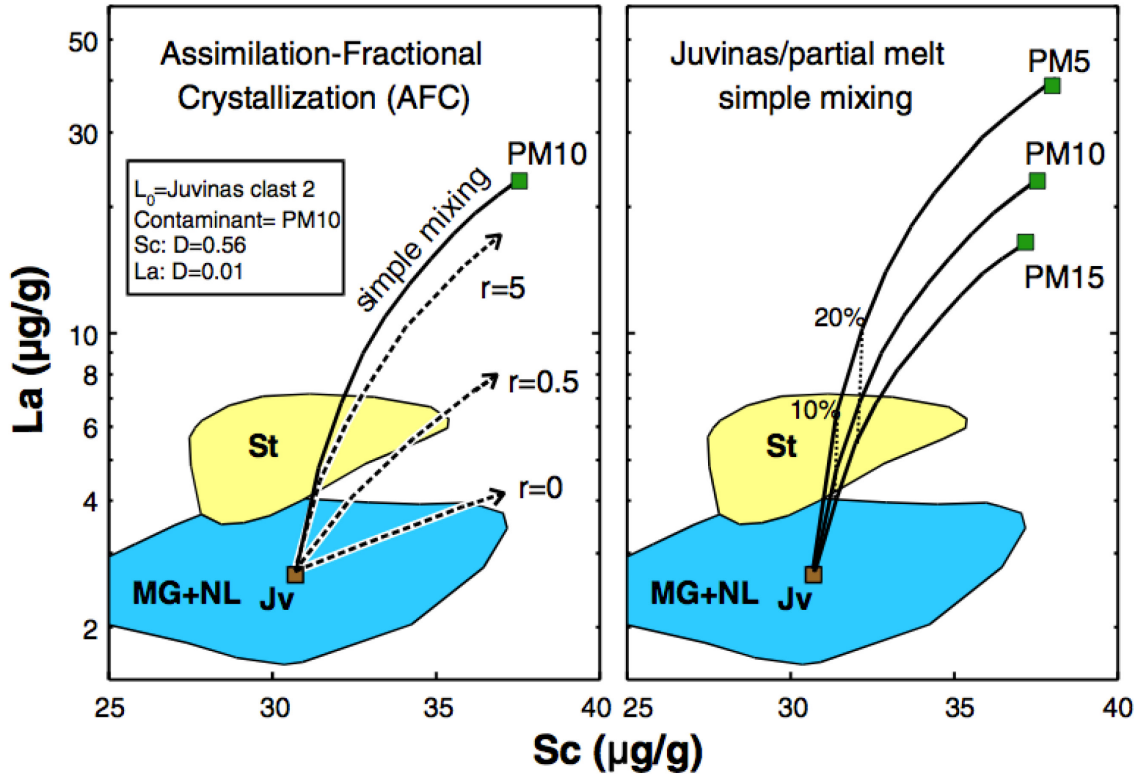


**Figure 1.14:** Modeling results from Barrat et al. (2007) where the Stannern trend is conceptualized as the result of mixing a main group trend magma with a low degree partial melting of a eucritic crust. Simple mixing is contrasted with a combined model incorporating fractional crystallization (AFC; after DePaolo, 1981); in this model “r” is the ratio of ‘assimilating’ material to crystallizing material. PM5, PM10, and PM15 are calculated 5, 10, and 15% partial melts of the Juvinas bulk composition.

## Chapter 2: Experimental Petrology of the Tissint Meteorite

### 2.1 Introduction

Basalts, as the least modified products of mantle melting, are probes of planetary interiors and allow the investigation of igneous processes such as magma-genesis. Shergottites, which are Martian basalts and the most common Martian meteorite type, provide a window into the interior of Mars, offering insights into igneous processes on another planet. The shergottite suite is divided into four types based on texture and phenocryst composition: olivine-phyric (porphyritic with olivine as the main phenocryst); pyroxene-phyric (orthopyroxene phenocrysts), poikilitic (also known as lherzolithic, characterized by pyroxene oikocrysts enclosing olivine phenocrysts); and basaltic (subequal pyroxene and plagioclase in a non-porphyritic texture) (e.g., Bridges and Warren, 2006; McSween, 1994). These textural divisions do not appear to be related by fractional crystallization; all four overlap in terms of major-element compositions and ratios, e.g., Fe/Mg. Thus, the shergottites represent a variety of parental magma compositions and degrees of fractionation.

Shergottites are also subdivided into enriched, intermediate, and depleted types based on incompatible trace-element concentrations (e.g., review by Papike et al., 2009). This is particularly obvious in light rare earth elements (L-REE) where the enriched type shows a flat rare earth element pattern and the depleted type shows L-REE depletion. There is no correlation between these chemical groups and the textural groups; however there is a correlation with radiogenic isotope compositions that show the same sense of enrichment and depletion (Shearer et al., 2008; Symes et al., 2008). As a whole, the suite shows a bulk-rock Rb-Sr and Sm-Nd isochron consistent with an age of ~4.5 Ga; however, individual meteorites have mineral isochrons with ages between 160 and 600 Ma (Borg and Draper, 2003; Borg et al., 1997; Borg et al., 2003; Nyquist et al., 2009a). The 4.5 Ga age is thought to reflect the formation of enriched and depleted mantle reservoirs early in Mars' history, which have been subsequently tapped at various times between 160 and 600 Ma to form the shergottites (Borg et al., 2003). The depleted and

enriched reservoirs must have formed by  $\sim 4.52$  Ga and remained largely unmixed until magma formation, most likely as mantle reservoirs, resulting from the rapid differentiation of a primordial magma ocean (e.g. Borg and Draper, 2003; Debaille et al., 2007), rather than assimilation of a crustal component into melts from a homogeneous mantle. The latter model is challenged in particular by the difficulty in creating a crustal composition that can be readily assimilated to form the trace-element patterns without a corresponding major-element change, as well as by the extraordinary coincidence required for every Martian basalt to assimilate the identical composition of altered crust required to generate the proportional shift in REEs, Sm-Nd and Rb-Sr isotopic composition, and  $fO_2$  (Herd, 2003).

Oxygen fugacity ( $fO_2$ ) is an important variable in basaltic systems. A correlation between  $fO_2$  and incompatible element enrichment among the shergottites indicate that the depleted reservoir is reduced and the enriched reservoir is oxidized (Herd et al., 2002a; Wadhwa, 2001). In detail, it appears that while the depleted shergottites all formed under similarly reduced conditions, the enriched shergottites formed under a range of oxidized conditions that seem to vary with textural type (Fig. 2.1). Superimposed on these trends, some olivine-phyric shergottites record an  $fO_2$  increase during crystallization, likely due to volatile loss during eruption (Shearer et al., 2013). Previous observations have shown  $fO_2$  change during crystallization primarily in enriched shergottites, e.g. NWA 1068 (Herd, 2006) and LAR 06319 (Peslier et al., 2010), as well as in the NWA 6234 intermediate shergottite (Gross et al., 2013), leading to the conclusion that volatile content is tied to the enriched reservoir.

Tissint is a Martian meteorite that was observed to fall over Morocco on July 18, 2011. Specimens were collected while fresh from the Sahara desert. Texturally, Tissint has abundant subhedral to anhedral olivine megacrysts in a fine-grained groundmass of mixed pyroxene and plagioclase with lesser olivine (Balta et al., 2015; Chennaoui Aoudjehane et al., 2012). It has undergone substantial shock, converting the plagioclase into maskelynite and locally generating shock glass as veins and patches. Based on bulk-rock chemistry, Tissint belongs to the depleted group of shergottites from both incompatible trace-element abundances (e.g. L-REEs) and radiogenic isotope compositions (e.g. Rb-Sr and Sm-Nd) (Balta et al., 2015; Brennecka et al., 2014).

Radioisotope ages from mineral separates show Tissint to be among the oldest shergottites with a crystallization age of 574 Ma (Brennecka et al., 2014). Previous work has shown that Tissint has undergone a minimal degree of mineral accumulation, unlike most shergottites which have undergone significant (>20%) mineral accumulation (McSween and Treiman, 1998) allowing for a robust parental melt calculation (Herd et al., 2013).

Consistent with the depleted shergottite trend, Tissint has a reduced initial magmatic  $fO_2$ . Estimates vary, but are in the range of 2 to 4 log units below the quartz-fayalite-magnetite (QFM) buffer (Balta et al., 2015; Herd et al., 2013). The current work reproduces and refines these estimates by applying the olivine-spinel-pyroxene geothermometer/oxybarometer (GTOB), which is based on a thermodynamic calculation of mineral equilibrium (Ballhaus et al., 1991; O'Neill, 1987; Sack and Ghiorso, 1989, 1991a, b, 1994a, b, c; Wood, 1991), to a large dataset of Tissint mineral chemistry. We further extend the existing GTOB estimates by examining the late magmatic  $fO_2$  utilizing the ilmenite-titanomagnetite GTOB, which relies on a similar thermodynamic calculation (Ghiorso and Evans, 2008). The application of both GTOBs allows for an assessment of  $fO_2$  change during crystallization, allowing a test of the hypothesis that oxidation during crystallization, and potentially volatile content, is tied to the enriched reservoir. Further, this work experimentally determines the liquid line of descent of the Tissint magma under both equilibrium and quasi-fractional crystallization, and examines the role of oxygen fugacity in its chemical evolution.

## **2.2 Methods**

### *2.2.1 Experiments and Quantitative Analysis*

Petrologic experiments were performed in GERO high-temperature vertical-tube furnaces in the High Temperature Planetary Petrology Laboratory at the University of Alberta (UAlberta). The parental-liquid composition of Tissint is derived from Herd et al. (2013); these authors considered the degree of olivine accumulation (~5%, based on Fe-Mg disequilibrium between olivine cores and the bulk rock) and adjusted the bulk

composition accordingly. The parental composition was synthesized from pure oxide powders, twice melted in a Pt-crucible above the liquidus, quenched, and ground in an agate mortar and pestle to ensure homogeneity. First and second quench glass compositions were determined by electron microprobe analysis (EMPA) to verify the synthetic composition. Experimental charges consisted of 100-150 mg of synthetic Tissint parental-liquid composition powder pressed into pellets. Charges were suspended on Re-wires under reducing conditions in the furnace as per the method of Borisov and Jones (1999). Polyvinyl alcohol (PVA) was used during sample loading to secure the pellet to the wire. Oxygen fugacity was controlled using a CO-CO<sub>2</sub> gas mixture, with the flow rate controlled by Vernier valves. The oxygen fugacity of the gas mixture was determined in the effluent using a zirconia cell suspended in a DelTech reference furnace at constant temperature, similar to the methodology used at the NASA Johnson Space Center Experimental Petrology Lab; redox potentials were calculated using the Gas.bas program (Jurewicz et al., 1993) that uses the Nernst equation to calculate  $f_{O_2}$ . Reference gas mixtures were used to verify the calibration of the zirconia cell. Effluent from the furnace flowed through a silica wool trap that was periodically checked for the presence of graphite – none was found. Oxygen fugacity was calculated and reported relative to the QFM buffer model of Wones and Gilbert (1969).

In an attempt to fully characterize the chemical and petrologic evolution of the Tissint meteorite, several rounds of experiments were performed (Table 2.1). The most extensive series of experiments was a set of isothermal experiments performed under reducing conditions (3.2 log units below the QFM buffer, or QFM-3.2). To examine the effect of redox on mineral equilibria, a less extensive series of isothermal experiments was performed at more oxidizing conditions (QFM-1). In all isothermal experiments, experimental charges were held above the liquidus for  $\geq 1$  hr, then rapidly dropped (set as 999.9°C/hr) to the target temperature and held for the reported duration of the experiment. Temperature was measured throughout with a type-B (Pt30Rh-Pt6Rh) thermocouple, calibrated against the melting point of Au. The CO-CO<sub>2</sub> gas mixture was calibrated for the target temperature and not readjusted for the super-liquidus soak. To examine the effect of fractional crystallization, a series of cooling rate experiments was performed. Each of these experiments had a constant cooling rate of 1°C/hr for the

duration of the experiment after a >1hr super-liquidus soak. As the offset between the furnace set-point and the sample temperature is not constant, the absolute cooling rate for each experiment is slightly below 1°C/hr. For each cooling rate experiment, the gas mixture was set for an  $fO_2$  of QFM-3.2 at the midpoint temperature. This resulted in a small relative shift in the activity of oxygen, both in an absolute and in a QFM-relative sense, over the course of the experiment (see Fig. 2.2). An additional experiment was used to investigate the effect of an abrupt redox change during cooling. In this case the initial  $fO_2$  was set to QFM-3.2 for the midpoint of the initial cooling portion (1375-1200°C), and the final  $fO_2$  set to QFM-1 for the midpoint of the final cooling portion (1200-1100°C). All experiments were terminated by removal from the furnace and quenching in air. In cooling rate experiments all samples were quenched within 1hr of reaching the target temperature.

Chemical analyses were performed on phases within three thin sections of Tissint (MET11640/2-2-1/TEP, MET11640/2-3-2/TEP, and MET11640/2-3-4/TEP from the University of Alberta Meteorite Collection) as well as on phases in experimental run charges, including: olivine (Ol), pyroxene (Px), plagioclase (Pl), spinel (Sp) (chromite [Chr] and titanomagnetite [Tmt]), ilmenite (Ilm), and glass (Gl). In Tissint, Ol and Px were analyzed for comparison with the chemical range reported in the literature (Balta et al., 2015; Chennaoui Aoudjehane et al., 2012), and for use in  $fO_2$  estimates. Oxide phases (Chr, Tmt, and Ilm) were analyzed for use in estimating the  $fO_2$  of the primitive (Ol-Sp-Px) and late stage (Ilm-Tmt) magmas. Fe(II)/Fe(III) contents of oxide phases were calculated by charge balance. All minerals and glasses produced in experiments (synthetic phases) were analyzed to characterize the evolution of the melt and to check geothermometry/oxybarometry (GTOB) calibration.

Mineral compositions were determined by electron microprobe analysis (EMPA) using the JEOL 8900 electron microprobe at UAlberta. Natural samples were analyzed for Si, Ti, Al, Cr, V, Fe, Mn, Mg, Ni, Ca, Na, K, S, and P. A subset of natural oxides were also analyzed for Zr and Zn. Synthetic samples were analyzed for all elements in the synthesis: Si, Ti, Al, Cr, Fe, Mn, Mg, Ca, Na, K, and P. All samples were calibrated with well-characterized standards. All glass and Pl analyses were conducted with a beam diameter of 10  $\mu\text{m}$ ; all other mineral analyses were performed with a focused or 2  $\mu\text{m}$

beam diameter. Most analyses were conducted with a 15 nA beam current and a 15 kV accelerating voltage. A subset of the natural Ol and Px were analyzed with a 20 nA beam current and 20 kV accelerating voltage to improve minor-element counting statistics; no significant compositional differences were observed with the change in beam current or accelerating voltage. Peak count times varied between 20-60 sec, depending on the required precision, but were typically 30 sec; backgrounds were each measured for half the peak count time. Standardization was performed under identical conditions to the mineral/glass analyses.

Errors are reported as 1 standard error, calculated as standard deviation divided by the square root of the number of values included (n) in the reported average, to reflect the confidence of the mean value, except where otherwise noted. In GTOB estimates, n is the number of vetted calculations; in EMPA analyses n is the number of measured values. Standard deviation, rather than standard error, is reported when comparing values with a natural range (e.g. An content of Pl from experiments compared with natural Pl, and Mg# of Ol or Px between isothermal experiments, cooling rate experiments, and natural samples).

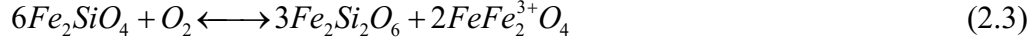
### 2.2.2 Calculated Estimates and MELTS

Temperature and  $fO_2$  were calculated using two GTOB methods. The olivine-spinel-pyroxene (Ol-Sp-Px) GTOB was used to estimate the  $fO_2$  of the early liquid (Ballhaus et al., 1991; O'Neill, 1987; Sack and Ghiorso, 1989, 1991a, b, 1994a, b, c; Wood, 1991). The Ol-Sp-Px GTOB operates around the two mineral equilibria:



The first reaction (2.1) describes the oxidation-induced breakdown of olivine into spinel and a silica polymorph (e.g. quartz), described here for pure iron end-members. The second reaction (2.2) shows the subsequent reaction of olivine with the surrounding

liquid to generate pyroxene, again described here for the pure iron end-members. The combination of the two reactions reduces to the FFM buffer (Mattioli and Wood, 1988):



The titanomagnetite-ilmenite (Tmt-Ilm) GTOB was used to estimate the  $fO_2$  of the late liquid (Ghiorso and Sack, 1991; Ghiorso and Evans, 2008). All calculations were performed on the OFM-Research computational thermodynamics server (ctserver.ofm-research.org). Natural samples contain both assemblages; all but one experiment lacked Ilm, although Chr and Tmt were often present. As natural samples contain zoned silicates and a range of oxide compositions, several selection criteria were developed to improve the likelihood of equilibrium assemblages. For the Ol-Sp-Px GTOB the most magnesian Px composition was used; an Ol Fe/Mg ratio in equilibrium with the Px was calculated using an Ol-Px Fe-Mg exchange  $K_d$  of 1.2 (Longhi and Pan, 1989) based on the exchange reaction between Fe- and Mg-end-members:

$$K_d^{Ol-Px} = \frac{[Fe]_{Ol} [Mg]_{Px}}{[Fe]_{Px} [Mg]_{Ol}} \quad (2.4)$$

where  $[Fe]_{Ol}$  is the concentration of Fe in Ol, etc.; note that the  $K_d$  is only calibrated for Ca-free Px compositions and is likely to change at higher Ca-content. A matching Ol composition from the observed zoning was used. As Chr and Px stabilize at approximately the same temperature in the Tissint magma, Chr compositions with the lowest Ti content, highest Cr#, and highest Mg# were selected on the assumption that they represent the most primitive compositions, following the criteria of Goodrich et al. (2003). For the Tmt-Ilm GTOB, high Ti Ilm and low Cr Tmt were selected. Furthermore, only Tmt-Ilm pairs were used that fall within Mg-Mn equilibrium based on a  $K_d$  of 1.23 (Bacon and Hirschmann, 1988):

$$K_d^{Tmt-Ilm} = \frac{[Mg]_{Tmt} [Mn]_{Ilm}}{[Mg]_{Ilm} [Mn]_{Tmt}} \quad (2.5)$$

for the equilibrium exchange of Mg and Mn between spinel (e.g. magnetite, or Tmt) and rhombohedral oxide (Ilm). The Mg-Mn equilibrium calculation is not a guarantee of equilibrium, but is the best available selection criterion when determination of equilibrium from petrography is equivocal. The presence of Ol+Sp+Px in experimental charges enabled evaluation of the Ol-Sp-Px GTOB; the absence of Ilm in most experimental charges precluded evaluation of the Tmt-Ilm GTOB, or an intercalibration check between the GTOBs.

Mineral modes were calculated in synthetic samples by chemical mass balance. The chemical mass balance was performed using the mineral and glass compositions from each experimental charge by generating the weighted average that mostly closely approaches the parental melt composition, where the weighting factors are the mineral abundances. To estimate the material loss from chemical volatilization expected over an analytical run, an experimental charge was held above the liquidus for 28.2 hrs at QFM-3.2 and then analyzed after quenching. The resulting glass showed a significant Na loss, but otherwise was in reasonable agreement with the synthesis composition. Increased  $fO_2$  appeared to enhance the loss of Na from the sample, but most samples at low  $fO_2$  showed no signs of Na-loss.

The MELTS software package was used in multiple ways in this study (Asimow and Ghiorso, 1998; Ghiorso and Sack, 1995; Gualda et al., 2012). The MELTS simulations were used to help develop the experimental plan; ultimately, however, experiments were used to evaluate the MELTS model. Multiple versions of the MELTS software package were used, including both the basic MELTS package (V5.0.0, revision 1.13) and rhyoliteMELTS (V1.0.1), based on the recommendations of the developer (Ghiorso, personal communication). Thermal step sizes were varied from 1°C to 0.01°C without significant differences in the result; reported simulations were all run at 1°C per step. Pressure was kept at 1 bar for all calculations for best comparison to laboratory results. Oxygen fugacity was run over a wide range, from QFM-5 to QFM+2, both as a constant (buffered conditions) and as a variable with a set initial value (auto-oxidation). Reported crystallization curves are for the set initial condition of QFM-3, the closest whole-number value to the early magmatic estimate from the Tissint meteorite.

## 2.3 Results

### 2.3.1 Experimental Results

Isothermal experiments yielded a generalized crystallization sequence consistent with typical basalt evolution as well as the sequence inferred from petrography (e.g. Balta et al., 2015) (Tables A1.1-A1.2). The liquidus phase was Ol (first appearing at 1363°C), as expected by the presence of large Ol crystals in the natural sample. In terms of silicate phases, Px is the second phase to form (1240°C), followed by Pl (1100°C). The first oxide appearance (Sp) is concurrent with Px under reducing conditions (1240°C), but is already present in the highest temperature experiment under oxidizing conditions (1275°C), before Px is stabilized. Initially, Sp is a high Cr, low Ti composition (Chr; initially Mg# 32.3±0.2, Cr# 82.8±0.7, TiO<sub>2</sub> 1.3±0.1wt%, where Cr# = Cr/Cr+Al; Table A1.3). At lower temperatures, Sp splits into a higher Ti composition (Mg# 11.7±0.1, Cr# 63±1, TiO<sub>2</sub> 13.0±0.2wt%) coexisting with the low Ti, high Cr composition (Mg# 18.0±0.2, Cr# 81±2, TiO<sub>2</sub> 3.1±0.3wt%; Table A1.3-A1.4). For ease of reference, the higher Ti Sp composition is referred to as Tmt, although its composition is intermediate between the Tmt and Chr end-member compositional ranges. In the lowest temperature experiments Sp exists solely as Tmt. Although the last phase that crystallized in the experiments was Pl, the high P content of the residual glasses suggests that a phosphate would form at lower temperature. Ilm was never formed in isothermal experiments; this may be due to a kinetic impediment to Ilm formation or a low Ti activity. The reducing and oxidizing experimental series both reproduce this crystallization sequence and are primarily distinguished by the increased fraction of Px in the solid in the oxidizing experimental series.

To examine the validity of our suite of isothermal experiments, two chemical exchange systems were examined to determine if our results are consistent with having achieved equilibrium: the partition coefficient (D) for Fe-Mg exchange between Ol and liquid, and the Ol-Px exchange coefficient (K<sub>d</sub>) for Fe-Mg equilibrium. The value of D<sub>Fe/Mg</sub> was assumed to be insensitive to Ol composition, an assumption supported

empirically by previous studies (Longhi and Pan, 1989) and corroborated by our experimental results (Fig. 2.3a). As  $D_{\text{Fe/Mg}}$  does not appear to be sensitive to  $f\text{O}_2$ , both datasets were combined to yield  $0.353 \pm 0.005$  for the partition coefficient. This value is indistinguishable from the literature value of 0.35 (Filiberto and Dasgupta, 2011). The Ol-Px  $K_{\text{d}_{\text{Fe-Mg}}}$  was calculated under the assumption that it is invariant with mineral composition; no attempt was made to determine a Ca-dependence on the exchange as the Ca-content of experimental Px was typically low. The best fit of the Fe/Mg ratio between Ol and Px yields a Kd of  $1.31 \pm 0.04$ . This value is in reasonable agreement with the existing literature value of 1.2 (Longhi and Pan, 1989). It is likely that the Kd is biased towards lower Mg# Ol at lower temperatures due to the comparatively slow rate of equilibration of major-elements in Px, artificially increasing the slope of the best-fit line from partial Px-liquid disequilibrium. Both the literature and the experimentally derived values for Kd have been shown, along with experimental data, in Mg# space (Fig. 2.3b). The general agreement of these two fundamental chemical exchange relationships demonstrates that our experimental method yields results that are consistent with those from other shergottite compositions, and indicates that our experiments achieved equilibrium.

Experimental results are consistent with a peritectic forming the first Px by reaction of Ol and liquid. Two main lines of evidence support the presence of a peritectic reaction: a sharp decrease in the abundance of Ol at the initial appearance of Px (Table A1.1-A1.2), and a change in crystal habit where previously euhedral Ol becomes embayed (hopper) after the appearance of Px (Fig. 2.4). The peritectic reaction does not go to completion, leaving stable Ol in the solidus assemblage (Fig. 2.5). Reducing conditions impede the peritectic reaction, even allowing Ol to increase in abundance during Px formation after an initial drop in abundance. Oxidizing conditions enhance the peritectic reaction, decreasing the amount of Ol in the final assemblage. This difference suggests that the Tissint bulk composition is close to a peritectic composition, and that the  $f\text{O}_2$  driven breakdown of Ol to Px may play a significant role in the evolution of these magmas.

The experimentally-produced mineral chemistry compares favorably with that observed in Tissint (Table A1.3-A1.7). The highest-temperature Ol formed at  $1363^\circ\text{C}$

(Table A1.5) with a Mg# of  $78.8 \pm 0.2$  ( $n=8$ ; standard deviation) after a calculated 1 wt% mineral crystallization under reducing conditions (QFM-3.2). This is more ferroan than the reported typical range in Tissint of 80-81 (Balta et al., 2015), but not substantially so. The first appearance of Px under reducing conditions is between 1250 and 1240°C (Table A1.6). At 1240°C Px has a Mg# of  $75.5 \pm 0.1$  ( $n=12$ ; standard deviation). This is slightly more magnesian than the typical Px core at Mg# 73.7 (Balta et al., 2015). The first appearance of Px is compositionally consistent with pigeonite, rather than orthopyroxene, with a Wo component of  $3.24 \pm 0.05$  ( $n=12$ ; standard deviation), similar to natural mineral observations where the lowest Wo content was reported at 4.2-5 (Balta et al., 2015; Chennaoui Aoudjehane et al., 2012).

Plagioclase (Pl) chemistry is significantly impacted by  $fO_2$ . The first appearance of Pl under reducing conditions is at 1100°C with An  $80 \pm 1$  ( $n=12$ ; standard deviation), changing to An  $76 \pm 2$  ( $n=10$ ; standard deviation) by 1080°C (Table A1.7). Under oxidizing conditions Pl is significantly more calcic at An  $99.2 \pm 0.1$  ( $n=11$ ; standard deviation; 1100°C). All of these Pl analyses are substantially more calcic than observed in the natural sample, which ranges over An 69-50 (Balta et al., 2015; Chennaoui Aoudjehane et al., 2012). Given the observed Na-loss in the experimental blank, it is likely that the low Ab content in Pl is due to Na-volatilization from the system, although results do not correlate well between isothermal run duration and low Na content in the residual glass. High  $fO_2$  isothermal experiments have very little Na present in the glass, likely due to enhanced volatilization of Na, but potentially due to increased compatibility of Na in Px at higher  $fO_2$ , an effect likely to be enhanced by the increased abundance of Px at higher  $fO_2$ .

Cooling rate (CR) experiments yielded broadly similar results to isothermal experiments, although several key differences were observed. The largest difference between the two types of experiments was, unsurprisingly, in how ferroan the magma, and the resulting mineralogy, became (Table A1.3-A1.9). Cooling rate experiments are designed to simulate fractional crystallization by preserving mineral zones, but are not fully fractional as some chemical exchange occurs over the course of the experiment. This is similar to how natural samples evolve as they cool, but is not fully described by Rayleigh fractionation. The result is that mineral cores generally re-equilibrate, and re-

equilibrate to an increasing extent over longer experiments. Isothermal experiments generated Ol with Mg# starting at 78.8 and evolving to 51.3 by 1078°C. The most magnesian cores in Ol from CR experiments had a Mg# of approximately 78, marginally more ferroan than in the most primitive isothermal experiments. In the CR experiment that covered the same temperature range as the isothermal experiments (1375°C-1100°C), Ol rim compositions were comparable to the most ferroan Ol observed in isothermal experiments (Mg# 54 from CR, Mg# 54.5 from 1100°C in isothermal experiments). Natural Ol zones observed in Tissint range from Mg# 81.2 in megacryst cores to Mg# 27.6 in megacryst rims, with a typical high Mg# interior of 78.7 (Balta et al., 2015); the zoned Ol compositions from the 1375-1000°C CR experiment ranged from Mg# 74.3 in Ol cores to Mg# 27.6 in Ol rims, comparable to natural samples.

Pyroxene showed a similar trend to olivine. Isothermal experiments generated Px starting at  $\text{En}_{73.0}\text{Fs}_{23.8}\text{Wo}_{3.2}$  (1240°C, QFM-3.2) and evolving to a mixture of low- and high-Ca Px of  $\text{En}_{60.2}\text{Fs}_{31.3}\text{Wo}_{8.5}$  and  $\text{En}_{40.7}\text{Fs}_{33.3}\text{Wo}_{26.0}$  respectively (1078°C, QFM-3.2). Reducing and oxidizing isothermal experiments produced similar Px compositions. The 1375-1100°C CR experiment generated Px beginning at  $\text{En}_{58.8}\text{Fs}_{33.4}\text{Wo}_{7.8}$  and evolving to a mixture of low- and high-Ca Px of around  $\text{En}_{51.1}\text{Fs}_{37.9}\text{Wo}_{11.0}$  and  $\text{En}_{43.7}\text{Fs}_{38.0}\text{Wo}_{18.3}$  respectively. It is likely that the Px rims are not pure analyses, artificially averaging high- and low-Ca Px, resulting in intermediate Ca-contents and Mg#s in both sets of evolved Px. Natural Px ranges from  $\text{En}_{70.6}\text{Fs}_{25.2}\text{Wo}_{4.2}$  to  $\text{En}_{28.7}\text{Fs}_{63.8}\text{Wo}_{7.5}$ , with the highest Ca Px of  $\text{En}_{47.2}\text{Fs}_{21.2}\text{Wo}_{31.6}$  (Balta et al., 2015); the Px compositions in the 1375-1000°C CR experiment ranged from  $\text{En}_{64.8}\text{Fs}_{29.9}\text{Wo}_{5.3}$  to  $\text{En}_{26.9}\text{Fs}_{48.6}\text{Wo}_{24.5}$  (although considerable variation in the Ca-content of the most evolved Px was observed), with a highest-Ca Px of  $\text{En}_{38.9}\text{Fs}_{29.0}\text{Wo}_{32.1}$  (although high-Ca Px was observed over a considerable range of En, from  $\text{En}_{50.3}\text{Fs}_{31.2}\text{Wo}_{18.5}$ , increasing to  $\text{En}_{44.2}\text{Fs}_{28.8}\text{Wo}_{27.0}$ , etc.). Within reasonable experimental error, these results show that isothermal and quasi-fractional (cooling rate) experiments are consistent in both Ol and Px compositions, and that the natural samples are consistent with a slow (~1 °C/hr) cooling of the parental composition from the liquidus to ~1000°C.

### 2.3.2 Oxygen Fugacity

Oxygen fugacity estimates differ between early- and late-formed assemblages in Tissint (Table A1.10-A1.11). The Ol-Sp-Px GTOB yielded QFM-3.49 ( $\pm 0.04$ ,  $n=52$ ), the Tmt-Ilm GTOB QFM-1.4 ( $\pm 0.1$ ,  $n=29$ ), in both cases after selective filtering of the data based on the following criteria (Fig. 2.2). First, the range of associated temperature estimates from both GTOBs, 753-1542°C using the unfiltered Ol-Sp-Px data, is implausible. Thus, plausible temperatures were selected from the Ol-Sp-Px GTOB results to be within 950-1400°C. The lower temperature bound is a generous overestimate of low temperature Sp stability, where the stable oxide is observed to switch from Tmt to Ilm in CR experiments terminating at 1100°C and 1000°C, respectively. The upper bound is based on the temperature of Sp saturation in reduced Iso experiments, 1240-1250°C, plus the typical thermal overestimate from the Ol-Sp-Px GTOB of 150°C (see below). The result narrows the range of temperatures to 971-1384°C with an average of 1130°C ( $\pm 20$ ,  $n=52$ ). After selecting from Tmt-Ilm mineral pairs consistent with Mg-Mn equilibrium (Fig. A1.1) the calculated temperature range is 891-1498°C with an average of 1120°C ( $\pm 30$ ,  $n=29$ ). Neither set of GTOB results shows an obvious correlation between temperature and  $fO_2$ , so we conclude that the temperature range has little influence on the  $fO_2$  estimate (see calibration notes below for additional details). The preliminary  $fO_2$  estimate for Tissint was QFM-3.24 (Castle and Herd, 2014), leading to the slightly more oxidizing conditions in the experimental series. The recorded difference between early and late magmatic redox conditions suggests that Tissint experienced a  $\sim 2.1 \pm 0.1$  log unit change in oxygen fugacity. There is a higher uncertainty in the redox change calculation than is reflected in the direct propagation of errors due to a lack of sufficient intercalibration experiments between the two GTOBs (Herd, 2008), making the preferred uncertainty  $2.1 \pm 0.5$  log units.

It is important to determine the most primitive Ol and Px compositions as GTOB estimates that use the Ol-Sp-Px GTOB have a significant sensitivity to the Ol-Px pairs utilized (Table A1.10). The most primitive natural Px observed in this study was  $En_{68.5}Fs_{25.6}Wo_{5.8}$ , with a Mg# of 72.8. The calculated Ol in equilibrium with this composition has a Mg# of 68.8 from a Kd of 1.2 (Longhi and Pan, 1989). Under reducing

conditions, the equilibrium pair observed at 1240°C (first appearance of Px in isothermal study) is Px with  $\text{En}_{73.0}\text{Fs}_{23.7}\text{Wo}_{3.2}$  (Mg# 75.5) and Ol with Mg# 70.2. This compositional pairing is consistent with a  $K_d$  of 1.2. The temperature of first appearance of Px is not as well constrained under oxidizing conditions, but the highest temperature Px observed (1200°C) was  $\text{En}_{67.4}\text{Fs}_{27.7}\text{Wo}_{4.9}$  (Mg# 70.9), coexisting with Ol of Mg# 66.5, also consistent with a  $K_d$  of 1.2. At 1200°C, the only statistically significant chemical difference in Ol and Px between the reducing and oxidizing experimental assemblages is a slightly higher Wo content (5.9) in the Px formed under reducing conditions, suggesting that the natural samples have undergone a low degree of chemical re-equilibration from the initial mineral cores. Although the experimentally produced first Ol-Px equilibrium pair is more magnesian than the natural Px cores, the difference is consistent with re-equilibration over ~40°C of fractional crystallization, and therefore unlikely to result in a substantial error in the GTOB calculation.

The reliability of the GTOB estimates was checked against laboratory experiments from the Tissint simulant compositions by applying the Ol-Sp-Px GTOB to crystals in the isothermal experimental runs (Fig. 2.6, Table A1.12). When multiple Sp populations were present, the high- and low-Ti Sp were run separately using the same Ol and Px pairs. The lack of experimentally generated Ilm precluded use of the Tmt-Ilm GTOB. Estimates were made for the most ferroan set, the most magnesian set, the average mineral compositions, and for random sets of all three based on an arbitrary ordering. Although the absolute oxygen fugacity was sensitive to the temperature reported, the oxygen fugacity relative to a standard buffer (e.g., QFM) remained relatively constant (Fig. 2.6b), and oxygen fugacity estimates were consistent with experimental settings within experimental error. In contrast, estimates from Ol-Sp-Px geothermometry tended to overestimate the temperature, typically by 100-200°C (Fig. 2.6a). The thermal overestimate observed here should broaden the criteria applied to Ol-Sp-Px GTOB results where thermally unreasonable results are typically discarded; however the lack of apparent correlation between QFM-normalized  $f\text{O}_2$  estimates and temperature suggests that exclusion of the estimates with the highest temperature will not alter the average  $f\text{O}_2$  estimate. Intriguingly, elevated Ti content in the Sp seems to have

minimal effect on the reliability of the estimate, suggesting that both primitive Chr and Tmt may be used in the estimate.

### *2.3.3 MELTS Model Validation*

A comparison of results from MELTS modeling with the experiments shows that MELTS models generally predict higher temperatures. For example, the MELTS liquidus is 10-25°C higher than that found experimentally. Similarly, Px forms ~20°C lower than predicted by MELTS. The MELTS solidus is around 1110°C, whereas isothermal experiments show it to be below 1080°C, likely near 1060°C. None of these are major differences and are unlikely to invalidate computational thermal models utilizing MELTS.

MELTS model mineral abundances are generally in reasonable agreement with experimentally derived crystallization curves (Fig. 2.7). One discrepancy is that MELTS tends to over-stabilize Ol. A substantial excess in Ol in the MELTS model relative to experimental results is most apparent under oxidizing conditions where ~20% more of the system is calculated to be Ol than was produced experimentally. This is likely to generate problems when the MELTS model is used to simulate Martian magma compositional evolution, but may not preclude its use as long as this discrepancy is accounted for when interpreting the model results.

## **2.4 Discussion**

### *2.4.1 The nature of oxidation events in Martian magmas*

The observation of a redox change during magmatic evolution preserved in the Tissint meteorite alters the basic model for Martian magmatism. Previously, only olivine-phyric shergottites belonging to the enriched chemical suite had shown this  $fO_2$  change (e.g., LAR 06319; NWA 1068/1110), and it was thought that this indicated a higher volatile content in the enriched magma to allow this change, or alternatively, mixing of magmas from oxidized and reduced sources (Herd, 2006; Peslier et al., 2010).

Observation of the same phenomenon in a depleted shergottite suggests that this may be a more common feature of Martian magmatism, and thus a more broadly applicable mechanism. Finding a substantial  $fO_2$  change in a depleted shergottite strongly suggests that if the  $fO_2$  change is related to volatile content then there is no relationship between volatile content and the chemical groupings of the shergottites into enriched and depleted groups (e.g. McCubbin et al., 2012).

The possible boundary conditions can tell us more about the recorded  $fO_2$  change in Tissint. In any chemical system there are two end-member boundary conditions: closed system evolution or open system evolution. In terms of oxygen fugacity, this develops into three end-member scenarios: 1) externally buffered evolution, where open system interaction dictates the redox state of the magma over the entire evolution, fixing it at a constant potential, 2) closed system evolution, where auto-oxidation changes the redox state of the magma as oxidized or reduced ions are preferentially partitioned into solid phases, or 3) an external control, where open system chemical exchange dictates a redox change outside of the expected chemical evolution. Buffered systems are common for laboratory studies as they allow oxygen fugacity to be studied as an independent variable, assessing how it affects the system. If the natural system evolved as a buffered system, then the oxygen fugacity estimates from the early and late magmatic assemblages should match; they do not, but instead show more than 2 log units of oxidation relative to the QFM buffer. A model is required to assess whether the magma evolved as a closed system, or if an external control is required to account for the oxidation change.

One potential model for auto-oxidation is provided by MELTS. The MELTS software can estimate auto-oxidation by running a simulation from a chosen oxygen fugacity without a set buffer. One problem with the MELTS calculation is that it does not calculate a Ol-Px peritectic reaction. Previous work has shown that this can be an  $fO_2$  driven breakdown of Ol (Mattioli and Wood, 1988; Wood, 1991); our work supports this by demonstrating that the reaction favors Px formation at higher  $fO_2$ . Consequently, although MELTS can calculate the  $fO_2$  change from auto-oxidation, the result of the calculation should be treated as an upper bound on the estimate. Simulations suggest that the magnitude of auto-oxidation increases as a function of initial oxygen fugacity, ranging from 0.66 log units for QFM-4 to 0.96 log units for QFM-2. Averaging the

results from QFM-3 and QFM-4 gives an estimated  $fO_2$  change of 0.7 log units for starting conditions around QFM-3.5, the best estimate of the natural magma starting  $fO_2$  (Fig. 2.2). Given that the natural system recorded a  $2.1 \pm 0.5$  log unit change, we conclude that there was an open system control.

There has already been a considerable work evaluating open system controls on the redox state of Martian magmas (e.g. Shearer et al., 2013). A likely scenario for open system control is degassing resulting in a net oxidation of the residuum. Oxides of S, Cl, and C are the most likely gases in such a mechanism, and each is thought to be able to cause an approximate 0.5 log unit change in the residual magma in shergottite parental liquids (Shearer et al., 2013). As the late-stage  $fO_2$  is greater than 1 log unit beyond the modeled oxidation change from auto-oxidation, it is likely that multiple gases would be required to account for the high degree of oxidation recorded in the Tissint meteorite.

An alternative model, within the open system requirement, is the assimilation of small amounts of a highly oxidized material. A commonly proposed material for this scenario is the Martian crust. A difficulty in rationalizing an assimilation model is that even small amounts of assimilated material should still generate a systematic major-element change in the resulting magma, and none has yet been observed (see Herd, 2003 for a more detailed discussion).

#### *2.4.2 Cr in olivine and oxygen fugacity*

Redox sensitive trace-elements in mineral zones can be utilized to examine the evolution of magmatic  $fO_2$ . One such element is Cr: under redox conditions of IW to QFM, magmatic Cr changes from being dominated by  $Cr^{2+}$  to  $Cr^{3+}$  (Berry and O'Neill, 2004; Hanson and Jones, 1998; Roeder and Reynolds, 1991; Schreiber and Haskin, 1976). This in turn changes the compatibility of Cr in Ol as  $Cr^{2+}$  is typically more compatible in Ol than  $Cr^{3+}$ . Although in theory this redox-sensitive behavior enables the use of Cr in Ol as a quantitative redox indicator, in practice the Cr-profile of Ol tells more about the stability of Sp than about the  $fO_2$  of the melt as the majority of Cr in Tissint is found in Chr. However, experiments demonstrate that a qualitative approach is still possible, as outlined below.

Isothermal experiments allow for a detailed examination of how Cr content in olivine and glass are related (Fig. 2.8). The concentration of Cr in Ol initially increases with continuing fractionation as Ol is the only solid phase, and Cr is behaving incompatibly, increasing the concentration in the liquid as Ol forms (Fig. 2.8b; Table A1.5, A1.8). The increase of Cr content in the olivine levels off as Cr gradually becomes more compatible in Ol, then abruptly drops when Sp forms (1250-1240°C), lowering the Cr content of the melt. The concentration then gradually lowers, despite an increasing compatibility of Cr in Ol (Fig. 2.8a), because of the decreasing concentration of Cr in the liquid due to crystallization of Sp and, to a lesser extent, Px. A major difference between the reducing and oxidizing isothermal series is the temperature at which Sp is stabilized (Table A1.1-A1.2). At QFM-3.2, Sp is stabilized between 1240-1250°C, while at QFM-1 Sp is stable in the highest temperature experiment at 1275°C. The result is a much earlier drawdown of Cr in the liquid under oxidizing conditions (Fig. 2.8b). Furthermore, the Cr content of the liquid is lower after Sp stabilization at QFM-1 because a higher fraction of the Cr in the liquid is Cr<sup>3+</sup>, which is preferentially partitioned into the Sp. The relationship between  $fO_2$  and the temperature of Sp saturation allows for a qualitative estimate of the  $fO_2$  from the profile of Cr content in Ol. If the Ol crystallized in the absence of Sp (e.g., lower  $fO_2$ ), then the Cr-content of the Ol is expected to increase; once Sp is stable, Cr in Ol would decrease, regardless of  $fO_2$ .

Spinel saturation experiments, and therefore the qualitative estimate of  $fO_2$ , depend significantly on the starting Cr content, which determines the timing of spinel saturation. If the starting Cr content (the assumed parental melt composition) is underestimated, then Sp will saturate at lower temperature in the experiments relative to the natural sample. In the synthesis of the Tissint parental melt composition, a conservatively high Cr content was estimated by assuming no Cr was present in the accumulated Ol. Furthermore, petrographic examination of the Tissint meteorite shows that Sp formed late relative to Ol as Sp is never included in Ol cores, and only rarely present in Ol rims. This presents a conundrum, as both petrographic and experimental results show that Ol in Tissint formed in the absence of Sp, but the profile of Cr in Tissint Ol suggests that the Ol formed after Sp saturation (Fig. 2.9c). In the following section, we

examine the behavior of Cr in Ol and the liquid in more detail in order to address this conundrum.

In order to calculate equilibrium liquid compositions from olivine in natural or experimental (cooling rate) cases we established the relationship between  $D_{Cr}$  and Fo content in Ol in Tissint (Table A1.13). There are two end-member methods for this calculation, which we applied (Fig. 2.8).  $D_{Cr}$  was determined experimentally for olivine from isothermal experiments; the only limitation of this method occurs when the Cr-content of both the olivine and the liquid approach the method detection limit (MDL).  $D_{Cr}$  was also calculated from the liquid composition and known experimental conditions ( $fO_2$  and temperature) based on the parameterization of Hanson and Jones (1998). In this parameterization,  $D_{Cr(III)}$  depends entirely on the polymerization and long-range silica structure in the magma (typically discussed as the ratio of non-bridging oxygen vs. tetrahedral oxygen, or NBO/T) according to the relationship  $D_{Cr(III)} = -0.39 \text{ NBO/T} + 1.29$ .  $D_{Cr(II)}$  depends entirely on the temperature according to the relationship  $\ln D_{Cr(II)} = 6600 / T(K) - 4.48$ . The ratio  $Cr^{2+}/Cr^{3+}$  depends on the absolute oxygen fugacity according to  $\log (Cr^{2+}/Cr^{3+}) = -0.275 \log (fO_2) - 2.598$ . Both methods are in agreement at higher Fo content (Fig 2.8a), where the Cr-content is still high compared to MDL, so the calculated  $D_{Cr}$  was used for the regression. The resulting relationship, specific to the Tissint parental composition, is  $D_{Cr} = -0.0285 \text{ Fo} + 2.84$  ( $R^2 = 0.995$ ). Figure 2.8b shows the result of calculating both the olivine composition from the liquid using  $D_{Fe/Mg} = 0.35$  and the calculated  $D_{Cr}$  for each glass, and the liquid composition calculated from each olivine using the Fo- $D_{Cr}$  regression relationship (from Fig 2.8a). As the calculated results are comparable to the experimental results, we assert that the regression relationship is an adequate representation of Cr-partitioning behavior in Tissint liquids.

Isothermal and cooling rate experiments at QFM-3.2 reproduced similar zoning profiles for Cr in Ol, as shown in a plot of  $Cr_2O_3$  vs. Fo (Fig. 2.9, a & b), but with some important differences. Olivine core Mg# becomes lower with increasing experiment duration, as can be seen by comparing the highest Mg# Ol compositions from the 1375-1100°C and 1375-1000°C runs (S50 and S58, respectively). The peak Cr content of all three CR runs was highest in the run that halted before Sp and Px saturation (S48; not shown), suggesting that diffusion lowers the Cr-content of the Ol zones as Cr is removed

from the liquid. The biggest difference between the CR and isothermal runs is how abruptly the Cr-content decreases. A likely explanation for this difference is a kinetic difficulty in precipitating Sp, potentially causing it to form later in kinetically driven experiments (e.g. CR or fractional crystallization) than in isothermal experiments, resulting in a lag in Cr drawdown over the experiment.

The hybrid experiment attempts to examine how the olivine zoning profile changes if the oxygen fugacity is changed during crystallization, as results suggest occurred in the natural sample. In the experiment, the  $fO_2$  was shifted from QFM-3.2 during the initial cooling of the sample (1375-1200°C) to QFM-1 for the final cooling (1200-1100°C). The expectation is that the Ol profile should show an abrupt drop in Cr content after the shift for two reasons: the higher  $fO_2$  favors additional Sp formation, lowering the Cr remaining in the melt, and the higher  $fO_2$  decreases the fraction of Cr that is  $Cr^{2+}$ , effectively lowering the  $D_{Cr}$  of Ol. However, this is not what is observed in the experiment. Instead, the Cr content, although higher, parallels the results of the isothermal experiments run at QFM-1 (Fig 2.9d); in effect, the initial record of olivine formation and the associated Cr increase with cooling at QFM-3.2 has been overwritten.

Several details help to explain both the lack of sudden change in the Ol Cr zones and the overprinting of the initial Ol Cr profile in the hybrid experiment. The first detail is that the abundance of Cr in Ol is controlled primarily by the stability of Sp, not by  $D_{Cr}$ . At 1200°C, the temperature at which the  $fO_2$  was changed,  $D_{Cr(II)}$  and  $D_{Cr(III)}$  are similar (1.0 and 0.73-0.76, respectively) as calculated by the regressions from Hanson and Jones (1998) (Table A1.13). So, although the shift in  $fO_2$  changes the Cr in the system from 72% to only 40%  $Cr^{2+}$ , the total  $D_{Cr}$  only changes from 0.93 to 0.84. As this is a small change in  $D_{Cr}$ , it cannot be responsible for the lower Cr abundance in Ol under oxidizing conditions. Instead, the formation of additional Sp lowers the abundance of Cr in the liquid, resulting in a lower concentration of Cr in the Ol. In the scenario in which Sp has not yet formed, the drop in Cr would be a slow process, as seen in the contrast between Ol Cr profiles in isothermal and CR experiments; however, as Sp had already nucleated in the hybrid experiment the drop may have been more abrupt. Nevertheless an abrupt drop in Cr in the liquid does not explain why there is no abrupt drop in Cr in the Ol profile.

The  $fO_2$  sensitivity of the peritectic reaction may provide some insight into how the Ol Cr profile was overprinted. In the isothermal experiments at 1200°C, Ol represents 20% of the system under reducing conditions and 14% under oxidizing conditions; thus, the change in  $fO_2$  results in a 30% reduction in the abundance of Ol (Table A1.1-A1.2). This  $fO_2$ -driven resorption may erase the record of high Cr in Ol, but only if the peak Cr content, the bump in the Ol Cr profile, is within the outer 30% of the Ol. The percentage of Ol resorbed could be increased either by lowering the temperature of the oxidation event, or by increasing the  $fO_2$  of the oxidation event, but neither of these scenarios is relevant to the hybrid experiment. As the record of pre-Sp saturation peak Cr in Ol is not within the last 30% of Ol formed in the hybrid experiment, resorption alone cannot explain how the Ol profile was overprinted.

Because the peritectic resorption of the Ol alone cannot remove evidence of pre-Sp saturation Cr content in Ol, diffusion of Cr in Ol must play a role in causing the overprinting. A peculiar feature of the zoned Ol in the hybrid experiment is that, although the Cr-concentration is slightly higher, it parallels the oxidized isothermal experiments, suggesting that the Ol formed entirely under Sp-saturated conditions, which we know was not the case from CR experiments. If rapid diffusion of Cr out of the olivine were responsible for modifying the concentration, then the characteristic bump in Cr content from pre-Sp saturation Ol, observed in both the reducing isothermal and CR experiments, should still be seen in the profile of the hybrid experiment, albeit at reduced concentration. The absence of this feature in the Ol Cr profile in the hybrid experiment leads us to conclude that diffusion alone cannot explain the overprinting event.

A combination of resorption and diffusion may offer an explanation of how the overprinting occurred. Peritectic resorption of Ol increases the Mg# of the liquid, as the Px formed from the reaction is more ferroan than the Ol being replaced, while simultaneously exposing higher Mg# Ol in the outermost rim of the residual Ol. This resorption also exposes higher-Cr Ol to the liquid while the liquid Cr content is dropping from increased formation of Sp. Both the Fe-Mg co-exchange and Cr-diffusion coefficients have been studied for a range of Ol compositions under a variety of conditions (Buening and Buseck, 1973; Chakraborty, 1997; Ito and Ganguly, 2006; Oeser et al., 2015; Sio et al., 2013), and although the Fe-Mg coexchange is typically faster than

Cr diffusion, the actual rate of Fe-Mg exchange is likely to be slower than Cr-diffusion in this case. This is because during the peritectic resorption the Mg# disequilibrium between Ol and liquid is minimized as both are increasing in Mg# (albeit likely at different rates) and the Cr disequilibrium is increasing as Cr is drawn down in the liquid while increasingly Cr-rich zones of the Ol are exposed. This increased compositional contrast may allow diffusion to remove Cr from the outer layers of the residual Ol while allowing very little Fe-Mg exchange with the Ol cores.

Natural olivine compositions follow the curve established for the oxidizing isothermal experiments, overprinting the likely initial profile in Cr. The early-formed Ol-Sp-Px GTOB estimates show that the initial Tissint liquid had a reduced  $fO_2$ , while the late-formed Tmt-Ilm GTOB shows the final liquid was oxidized. Despite the initial reducing conditions, the Cr content drops sharply, paralleling the oxidizing curve. The initial increase in Cr expected by incompatible behavior in the Ol is not observed. This demonstrates that although the Ol-Sp-Px assemblage did not reequilibrate, the Cr in the Ol did.

If the Cr in Ol profile was overprinted by an oxidation event, as our results suggest, this raises the possibility that other elements are affected, with implications for other olivine-phyric shergottites. One example is Northwest Africa (NWA) 1068/1110. Herd (2006) suggested that olivine megacrysts in NWA 1068/1110 were xenocrystic because they formed under substantially more reducing conditions than the groundmass (QFM-2.5 and QFM+0.5, respectively) based on calculations using the Ol-Sp-Px and Tmt-Ilm GTOBs. The anhedral nature of the olivine cores support this assumption (Barrat et al., 2002b), demonstrating that they were unstable in the magma. In contrast, Shearer et al. (2008) concluded that the olivine cores were in equilibrium with the melt on the basis of trace-elements (Co and Ni), having formed under oxidizing conditions, and were therefore likely phenocrysts. The results of our study suggest that NWA 1068/1110 initially crystallized under reducing conditions, forming the early Ol-Sp-Px assemblage, then experienced an oxidation event that destabilized some of the olivine, resulting in its anhedral character and overprinting the trace-element profile of the residual cores, rationalizing the observations of Shearer et al. (2008). Thus, olivine formed under reduced conditions may appear oxidized in multiple chemical systems.

The potential for overprinting of Ol chemical zones calls into question techniques that rely on chemical zoning in Ol for interpretation of shergottite petrogenesis. Our results suggest that attempts to track magmatic  $fO_2$  during crystallization using chemical zoning of redox-sensitive elements in Ol may be in error. Peritectic resorption, along with the potential for reequilibration of remnant Ol cores, calls into question arguments about the phenocrystic vs xenocrystic nature of Ol in shergottite magmas, particularly when such estimates are based on redox sensitive or Sp compatible elements in Ol. This may have further implications into calculated parental melt compositions and liquid lines of descent, potentially impacting our understanding of the Martian mantle, but further research is required to determine to what extent other elements are affected.

#### *2.4.3 Magma-genesis and the Martian mantle*

In an effort to compare the Tissint bulk composition and fractionation products, mineral norms were calculated for each of the experimentally produced liquids according to the CIPW method (Cross et al., 1902). One observation from this calculation is that Ol is normative only in the glasses produced at high temperature under reducing conditions. This is consistent with the experimental observation that Ol is stable for the initial evolution of the melt but becomes unstable at lower temperatures where it increasingly converts to Px.

To a first order, the chemical difference between the basaltic and Ol-phyric shergottites is well demonstrated by the CIPW norms of the bulk compositions (Fig. 2.10). Unsurprisingly, Ol-phyric shergottites have a much more Ol-normative composition than basaltic shergottites. In bulk chemistry, basaltic shergottites often have a more calcic, or, broadly, higher alkali, composition. How this difference arises might be explained by one of several possible mechanisms, relying either on differences in magma-genesis (e.g. differences in source mineralogy, the extent of melting, or the depth of melting), or differences in magma evolution (e.g. fractional crystallization, or assimilation mechanisms). If the difference is due to magma-genesis, then the magmas are fundamentally different. Fundamentally different magmas can be generated in one of two ways: variations in the source mantle composition, or variation in the magma-genesis

process. Both of these end-member scenarios are likely present in any two magma-genesis events, so the real question is which of these two is the dominant process, if the magmas are fundamentally different.

The homogeneity of the Martian mantle is a matter of debate (Agee and Draper, 2004; Blinova and Herd, 2009; Borg and Draper, 2003). Significant uncertainty exists in whether the relatively small, and biased, sample suite represented by the shergottite meteorites may be used to constrain the homogeneity of the Martian mantle (e.g. McCoy et al., 2011; Walton et al., 2008). Geochemical models from the shergottite suite show that there must be at least two, distinct, sources within the Martian mantle that give rise to the depleted and enriched shergottite suites (e.g., Blinova and Herd, 2009; Borg and Draper, 2003; Debaille et al., 2007). Geophysical models add useful constraints, but are inconclusive with regard to the major-element homogeneity of the mantle (Kiefer, 2003). They do, however, demonstrate how a mixed, but heterogeneous, Martian mantle could be generated and still preserve the chemical distinctions observed within the Shergottite suite.

Assuming a relatively homogeneous major-element composition for the Martian mantle, the differences between the various primitive shergottite melt types may be analogous to the terrestrial distinction between alkalic and tholeiitic magmas. Near surface melts of the terrestrial mantle generate low alkali magmas (tholeiitic basalts); at greater depths, mantle melts become increasingly silica undersaturated (alkalic basalts), resulting in a higher relative alkali content of the basalt (Kushiro, 1968). A benefit of this model is that it does not require significant differences in the mantle composition to generate the observed variation in basalt chemistry. Instead, this model makes depth the key determinant. This model also does not preclude the different trace-element reservoirs, and, in the scenario of a heterogeneous mantle, allows for both the depleted and enriched mantle reservoirs to be tapped at different depths, generating the various shergottite textural types.

#### *2.4.4 Chemical relations between textural types*

The shergottite textural types are typically regarded as originating from fundamentally different magmas. This means that while fractional crystallization is regarded as a mechanism to change magma composition within each textural type, little work has been done examining if fractional crystallization can cross textural types. It is intriguing that the experimental glasses from the Tissint parental composition begin in the Ol-phyric field and progresses through the basaltic shergottite parental melt field in multiple chemical systems (Fig. 2.10). A particularly good example of this is the glass produced under reducing conditions at 1140°C which is a very close match, in both major and minor-elements, for the whole-rock composition of QUE 94201 (Kring et al., 2003; Mikouchi et al., 1998) (Table 2.2 and 2.3). In detail, QUE 94201 is lower in SiO<sub>2</sub> and higher in TiO<sub>2</sub>, but these differences are relatively minor, and may be due to analytical limitations. The coincidence of these compositions is significant because QUE 94201 is a rapidly quenched, near-liquidus, basaltic shergottite composition. Although the two meteorites are not part of the same igneous event (they differ in igneous age by ~270 Ma), we can conclude that some basaltic shergottites whose bulk compositions represent parental melts may be the fractionation products of Ol-phyric shergottite magmas, consistent with inferences made by other workers (e.g., Rapp et al., 2013).

Comparing glass compositions with meteorite compositions is not without pitfalls, however. Another good example of similar compositions is between the Tissint experiments and both the Shergotty and Zagami meteorites. The experimental glass produced under reducing conditions at 1240°C is a close match to the Shergotty whole-rock composition, excepting a lower alkali content (Na<sub>2</sub>O, K<sub>2</sub>O, and CaO are low; FeO and MgO are reciprocally higher; Table 2.2 and 2.3) (Stolper and McSween Jr, 1979). This is the bulk composition of Shergotty, not the parental liquid composition, which makes the similarity coincidental, as the Shergotty meteorite is a cumulate. Multiple estimates of the Shergotty parental liquid composition have been made, the most recent by Hale et al. (1999), and where the Tissint liquid line of descent crosses the Mg# of the calculated parental composition the liquids differ in most major- and minor-element concentrations.

There are several examples where this comparison simply fails. One example is the parental composition of the EETA 79001 (lithology A) meteorite, referred to as the

‘Eg’ composition (Herd et al., 2002b; Longhi and Pan, 1989; McSween Jr and Jarosewich, 1983; Warren et al., 1999). At high temperature (1363-1280°C) the Tissint glasses pass through the SiO<sub>2</sub> and Mg# range of the Eg composition. The Tissint glasses are significantly more mafic, demonstrating a significant deficiency in CaO, Na<sub>2</sub>O, TiO<sub>2</sub>, and Al<sub>2</sub>O<sub>3</sub>, with an accompanying surplus in FeO, MnO, MgO, and Cr<sub>2</sub>O<sub>3</sub>. If the calculated Eg parental melt composition is correct, then the discrepancy demonstrates that these are very different magmas, despite being of the same textural type. Thus, we conclude that there is considerable chemical variation in the primitive mantle melts that form the shergottites.

The destabilization of Ol during crystallization may explain why Ol is seldom euhedral in shergottites, and why Ol is rarely present in the groundmass (e.g., Barrat et al., 2002b; Basu Sarbadhikari et al., 2009). If the peritectic relation of Ol-Px is sensitive to  $fO_2$ , as our results suggest, then any increase in  $fO_2$  after initial Ol formation could result in resorption of Ol, generating anhedral Ol phenocrysts. This may also alter trace-element patterns in the, now anhedral, Ol, making it appear xenocrystic, as residual cores will not match outer zones if they are large enough to avoid overprinting by the peritectic reaction. If the  $fO_2$  change is related to gas escape during eruption, as previous work suggests that it may be (Shearer et al., 2013), then a small  $fO_2$  change would impede Ol formation in the groundmass while a large change would prevent it entirely. A much larger  $fO_2$  change may even cause the complete resorption of Ol phenocrysts, making an Ol-phyric shergottite bulk composition appear basaltic.

## 2.5 Conclusions

The presence of a substantial change in  $fO_2$  over the course of magmatic crystallization has now been observed in Tissint, a depleted member of the Ol-phyric shergottite suite, arguing for the presence of significant volatiles in both the enriched and depleted shergottites. A change in oxygen fugacity has a significant impact on trace-element zones in olivine via  $fO_2$  driven peritectic resorption of the olivine. Experiments show that this effect can overprint original magmatic zoning of Cr in olivine. The potential for  $fO_2$  change as a common phenomenon in shergottite magmas calls into

question the use of trace-elements, particularly redox sensitive trace-elements, in olivine as tracers of magmatic evolution. This may impact the interpretation of shergottite olivines as phenocrysts vs. xenocrysts, as well as calculations of parental magma compositions. Peritectic resorption of olivine, as a result of a rapid increase in  $fO_2$ , may also explain why olivine is seldom observed in the groundmass of olivine-phyric shergottites and why olivine megacrysts are typically anhedral. Overprinting of chemical zones in early-formed Ol after an oxidation event may reconcile conflicting interpretations of olivine cores in NWA 1068/1110 (Herd, 2006; Shearer et al., 2008).

Basaltic and olivine-phyric shergottites appear to be most readily distinguished, at a bulk chemical level, by their alkali content. This distinction may be similar to the terrestrial tholeiitic and alkalic basalts, where depth of formation, rather than mantle heterogeneity, causes the compositional differences. Experimentally produced glasses highlight the potential for some basaltic shergottite compositions to be derivatives of Ol-phyric shergottite magmas (e.g. QUE 94201 which has a bulk composition similar to an experimentally produced glass from the Tissint parental composition);  $fO_2$  driven resorption of Ol may further enhance this possibility by removing the characteristic Ol megacrysts from an otherwise Ol-phyric shergottite, resulting in its classification as a basaltic shergottite. The Tissint liquid line of descent does not correlate well with all other Ol-phyric shergottites (e.g., it has significant overlap with the liquid line of descent for Yamato 980459, but no overlap with the parental composition of EETA 79001), indicating that there is still substantial variation in Ol-phyric source magmas.

**Table 2.1:** Experimental parameters and summarized results

ID	Mass (g)	$fO_2$ (QFM)	Temp* (°C)	Duration** (Hr:Min)	Iso/CR	Mineralogy
S38	0.1251	-3.24	1375	28:12	Iso	Glass only
S43	0.1223	-3.24	1363	27:20	Iso	Ol
S45	0.1210	-3.24	1363	124:44	Iso	Ol
S52	0.1062	-3.24	1362	190:44	Iso	Ol
S42	0.1268	-3.24	1280	40:47	Iso	Ol
S44	0.1211	-3.24	1250	118:31	Iso	Ol
S54	0.1008	-3.24	1240	188:07	Iso	Ol, Chr
S46	0.1200	-3.24	1225	179:48	Iso	Ol, Px, Chr
S40	0.1248	-3.24	1200	60:24	Iso	Ol, Px, Chr
S39	0.1207	-3.24	1140	49:10	Iso	Ol, Px, Chr
S49	0.1216	-3.24	1100	70:36	Iso	Ol, Px, Pl, Chr, Tmt
S55	0.1006	-3.24	1078	284:43	Iso	Ol, Px, Pl, Tmt
S63	0.1003	-1.0	1275	86:03	Iso	Ol, Chr
S60	0.0998	-1.0	1200	134:56	Iso	Ol, Px, Chr
S62	0.1012	-1.0	1100	185:53	Iso	Ol, Px, Pl, Chr, Tmt
S48	0.1234	-3.24	1375-1225	156:15	CR	Ol
S50	0.1021	-3.24	1375-1100	292:00	CR	Ol, Px, Chr
S58	0.1040	-3.24	1375-1000	403:54	CR	Ol, Px, Pl, Ilm
S64 <sup>†</sup>	0.1008	-3.24 -1.0	1375-1200 1200-1100	292:12	CR	Ol, Px, Chr

\* In isothermal (Iso) experiments this is the hold temperature. In cooling rate (CR) experiments, this is the temperature range. CR experiments were set to a cooling rate of 1°C/hr, but due to the temperature dependency of the offset between the sample temperature and the instrument set temperature the true cooling rates were lower (0.96-0.92°C/hr). All samples started with a >1hr soak at 1375°C.

\*\* The reported duration is from when samples were set to cool to when they were removed. In isothermal experiments, this time began when the furnace was set to cool the sample at the maximum cooling rate of the furnace. At the longest, the cooling to the target temperature was accomplished within ~30 min in isothermal experiments. In CR experiments, the samples were removed within 1hr of achieving the target temperature.

<sup>†</sup> S64 was run from 1375-1200°C at QFM-3.24, and from 1200°C-1100°C at QFM-1 in an attempt to recreate the observed mineralogy/textures of the Tissint meteorite. This is the ‘hybrid’ experiment.

**Table 2.2:** Meteorite whole rock (WR) and parental compositions

Type	Tissint		QUE 94201	EETA79001A	“Eg”
	WR	Parental	WR	WR	Parent
Reference	Herd et al., 2013	Herd et al., 2013	Kring et al., 2003	Warren et al., 1999	Herd et al., 2002
SiO <sub>2</sub>	46.2	47.2	47.02	50.49	49.0
TiO <sub>2</sub>	0.63	0.67	1.84	0.7	1.7
Al <sub>2</sub> O <sub>3</sub>	4.86	5.20	11.1	5.86	7.4
Cr <sub>2</sub> O <sub>3</sub>	0.41	0.44	1.39		0.15
FeO	21.2	21.6	18.5	18.53	18.4
MnO	0.52	0.56	0.451	0.49	0.52
MgO	17.1	16.0	6.1	14.59	11.5
CaO	6.5	7.0	11.1	7.4	9.2
Na <sub>2</sub> O	0.72	0.77	1.64	0.795	0.9
K <sub>2</sub> O	0.02	0.02		0.04	
P <sub>2</sub> O <sub>5</sub>	0.48	0.51	2.05		1.2
Mg#	61.5	59.4	39.5	60.9	55.3
Exp-Glass	n/a	S38	S39	n/a	S52, S42

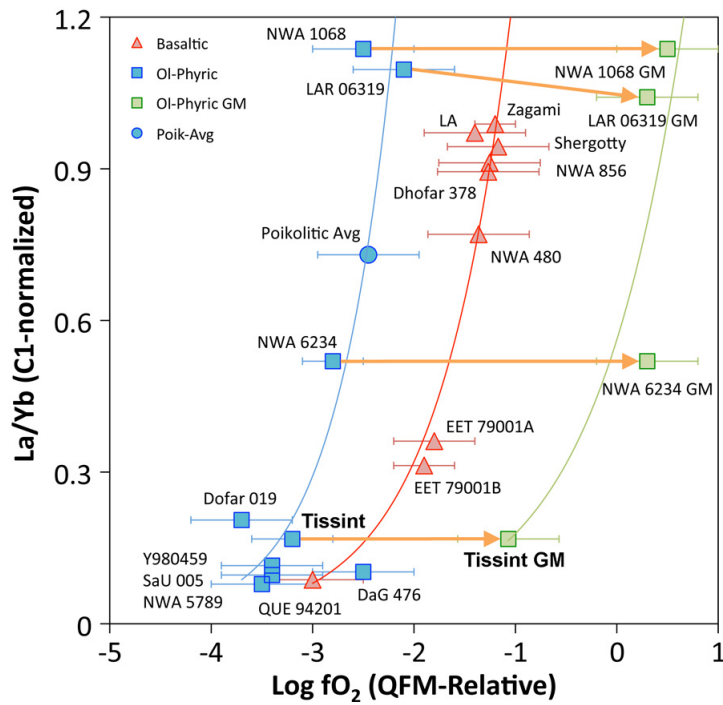
  

Chemical Textural	Shergotty		Zagami		Y 980459
	WR	Parent	WR	Parent	WR
Reference	Stolper and McSween, 1979	Hale et al., 1999	Stolper and McSween, 1979	McCoy et al., 1992	Symes et al., 2008
SiO <sub>2</sub>	50.4	50.9	50.8	50.7	48.79
TiO <sub>2</sub>	0.81	1.0	0.77	1.03	1.01
Al <sub>2</sub> O <sub>3</sub>	6.89	8.0	5.67	7.8	5.07
Cr <sub>2</sub> O <sub>3</sub>	0.21		0.30		
FeO	19.1	19.8	18.0	18.5	17.07
MnO	0.50	0.5	0.50	0.54	0.46
MgO	9.27	7.7	11.0	7.98	19.74
CaO	10.1	9.7	10.8	11.2	6.78
Na <sub>2</sub> O	1.37	1.5	0.99	1.64	0.71
K <sub>2</sub> O	0.16	0.2	0.14	0.18	
P <sub>2</sub> O <sub>5</sub>		0.9		0.71	
Mg#	49.0	43.5	54.7	46.1	69.6
Exp-Glass	S54	S40	S52, S42	S40	n/a

**Table 2.3:** Experimental glass compositions

Run	S52		S42		S54		S40		S39	
T	1362°C		1280°C		1240°C		1200°C		1140°C	
fO <sub>2</sub>	QFM-3.2		QFM-3.2		QFM-3.2		QFM-3.2		QFM-3.2	
n	8		8		9		8		17	
SiO <sub>2</sub>	47.46	±0.07	49.56	±0.02	48.64	±0.06	49.16	±0.05	48.96	±0.04
TiO <sub>2</sub>	0.71	±0.01	0.79	±0.01	0.91	±0.01	1.05	±0.01	1.32	±0.01
Al <sub>2</sub> O <sub>3</sub>	5.67	±0.01	6.50	±0.01	7.32	±0.01	8.46	±0.01	11.02	±0.02
Cr <sub>2</sub> O <sub>3</sub>	0.38	±0.01	0.39	±0.01	0.33	±0.01	0.22	±0.01	0.11	±0.01
FeO	21.56	±0.03	21.67	±0.04	21.48	±0.03	20.74	±0.05	18.77	±0.03
MnO	0.54	±0.01	0.56	±0.01	0.56	±0.01	0.51	±0.01	0.45	±0.01
MgO	14.77	±0.02	11.59	±0.04	10.01	±0.07	8.02	±0.03	5.91	±0.01
CaO	7.80	±0.02	8.80	±0.02	9.99	±0.04	10.97	±0.02	11.39	±0.01
Na <sub>2</sub> O	0.91	±0.02	0.51	±0.01	0.12	±0.01	0.77	±0.01	1.43	±0.01
K <sub>2</sub> O	<MDL		<MDL		<MDL		0.01	±0.01	0.02	±0.01
P <sub>2</sub> O <sub>5</sub>	0.05	±0.01	0.45	±0.01	0.53	±0.01	0.62	±0.01	0.86	±0.01
Mg#	55.0	±0.1	48.8	±0.2	45.4	±0.3	40.8	±0.2	35.9	±0.1
Most similar comp.	“Eg” Zagami WR		“Eg” Zagami WR		Shergotty WR		Shergotty/ Zagami Parent		QUE 94201	

MDL stands for method detection limit



**Figure 2.1:** La/Yb plotted against  $fO_2$ . While  $fO_2$  always increases as shergottites become more enriched, the basaltic (red triangles) and Ol-phyric (blue squares) shergottites follow different trends. A subset of Ol-phyric shergottites, including Tissint, show a substantially higher  $fO_2$  in the groundmass (green squares), representing late-stage oxidation of the magma. Meteorite trace-element compositions are from whole rock powders and  $fO_2$  estimates are from geothermometry/oxybarometry calculations (Barrat et al., 2002a; Barrat et al., 2002b; Basu Sarbadhikari et al., 2009; Chennaoui Aoudjehane et al., 2012; Filiberto et al., 2012; Goodrich et al., 2003; Gross et al., 2013; Gross et al., 2011; Herd, 2006; Herd et al., 2004; Laul et al., 1986; Peslier et al., 2010; Rubin et al., 2000; Wadhwa et al., 1994; Walton et al., 2012).

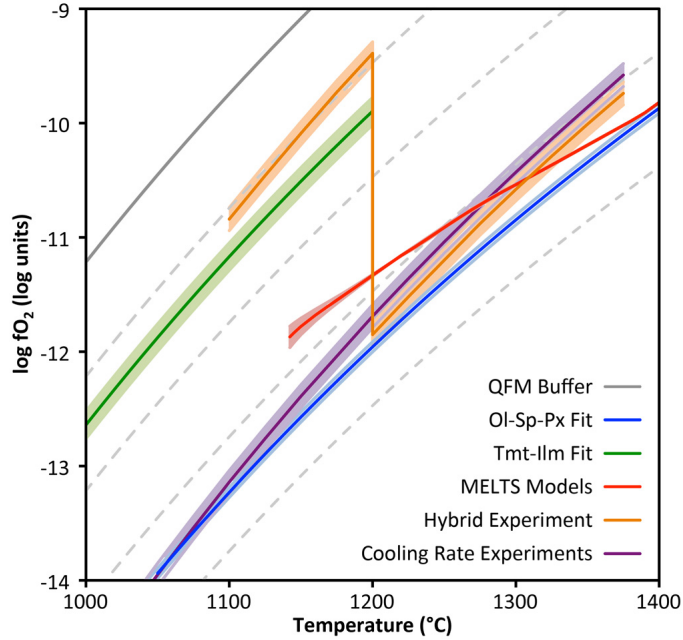


**Figure 2.2:** Various calculations relating to oxygen fugacity from the Tissint meteorite, experiments, and the MELTS models. The temperature dependence of the QFM buffer is shown for reference, along with log unit offsets (dashed gray lines). The early magmatic  $fO_2$  estimate from the Ol-Sp-Px GTOB is shown as a QFM-relative curve (blue); the late magmatic  $fO_2$  estimate from the Tmt-Ilm GTOB is shown similarly (green); error envelopes are standard errors from GTOB estimates. MELTS models were performed over a range of  $fO_2$ s to simulate auto-oxidation from a closed system evolution; the average of the output of two models, starting at QFM-3 and QFM-4, is shown (red); error bounds are from the QFM-3 and QFM-4 models. Cooling rate experiments were run with a set CO-CO<sub>2</sub> gas mixture, resulting in a variable  $fO_2$  over the course of the experiment (purple). Finally, a hybrid experiment was performed to simulate the  $fO_2$  change observed from the difference in the GTOB estimates in the Tissint meteorite by using a constant cooling rate (1°C/hr) and changing the gas mixture part way through the experimental run (orange). Error envelopes from both CR and hybrid experiments is an arbitrary  $\pm 0.1$  log unit laboratory reproducibility.

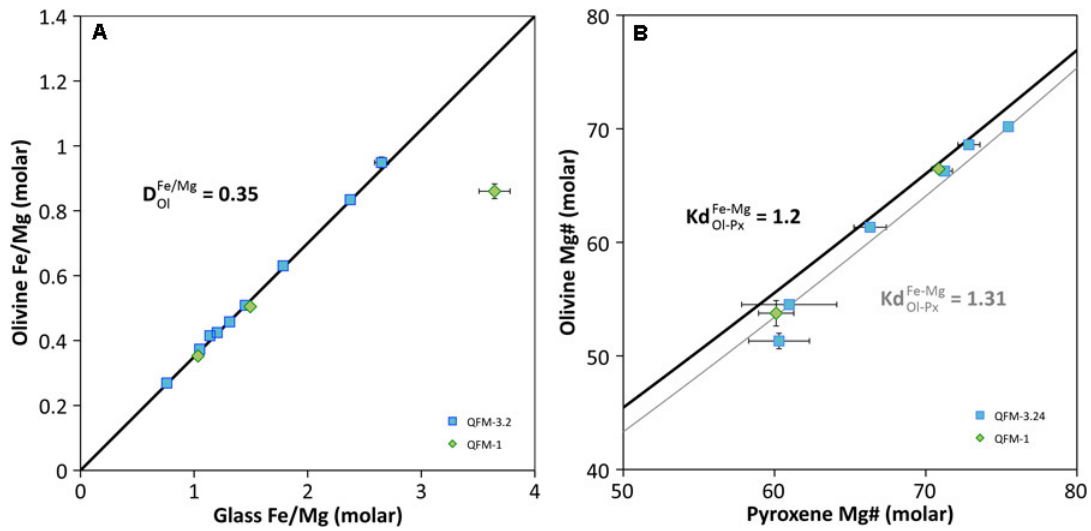


**Figure 2.3:** A: Fe-Mg exchange between olivine and liquid. Both oxidizing and reducing data are in agreement with the literature value of  $0.353 \pm 0.005$  (Filiberto and Dasgupta, 2011), excluding an outlier in the oxidizing dataset. B: Comparison between olivine and pyroxene equilibrium observed in Tissint isothermal experiments and the expected equilibrium calculation from the literature (Longhi and Pan, 1989). The best-fit  $Kd$  from isothermal experiments,  $1.31 \pm 0.04$ , is higher than the expected literature value of 1.2, but still within reasonable variation.

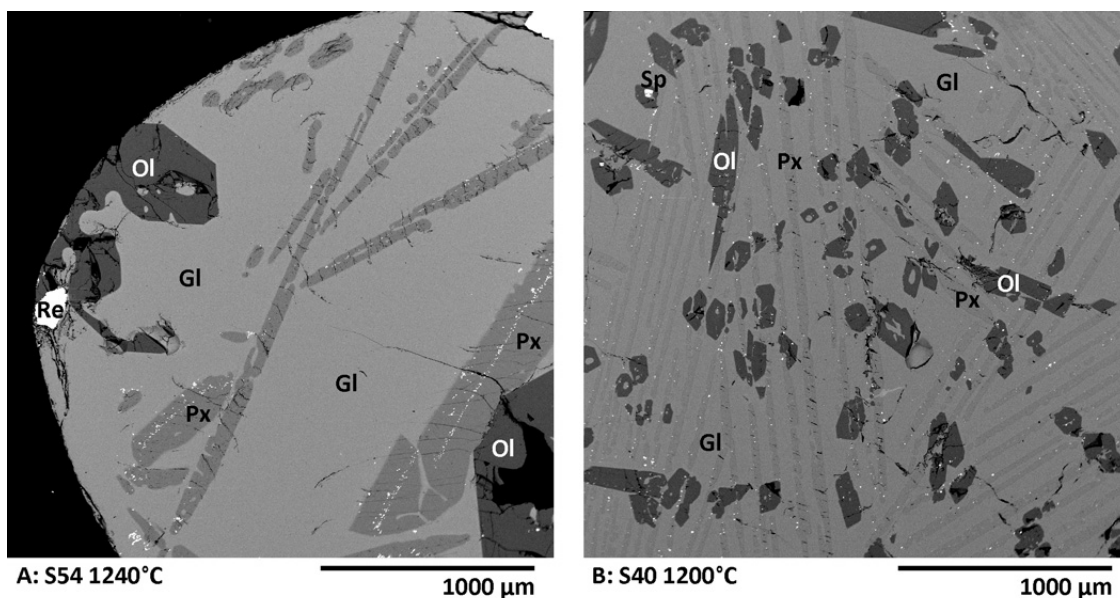


**Figure 2.4:** BSE images of S54 (1240°C) and S40 (1200°C), both at QFM-3.2. For reference, the peritectic reaction begins between 1250 and 1240°C. Symbols, from brightest to darkest, are rhenium-wire (Re), spinel (Sp), glass (Gl), pyroxene (Px), and olivine (Ol). S54 olivine is mostly euhedral, but shows some evidence of embayment (see left hand edge near the Re-wire). The lower temperature sample (S40) has a much more heavily resorbed texture with glass frequently contained inside olivine grains.

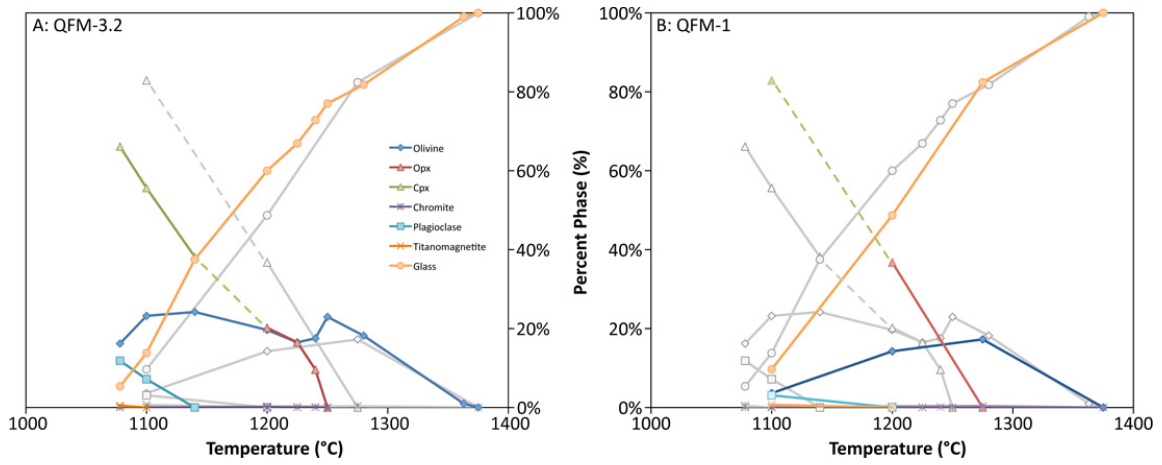


**Figure 2.5:** Phase abundances, as a function of temperature, calculated from a chemical mass balance, for both QFM-3.24 (A) and QFM-1 (B). Phases are as follows: glass (orange circles), Ol (blue diamonds), Opx (red triangles), Cpx (green triangles), Pl (light blue squares), Chr (purple asterisks), Tmt (orange crosses). In each diagram the other set of experiments are shown as gray symbols for comparison.

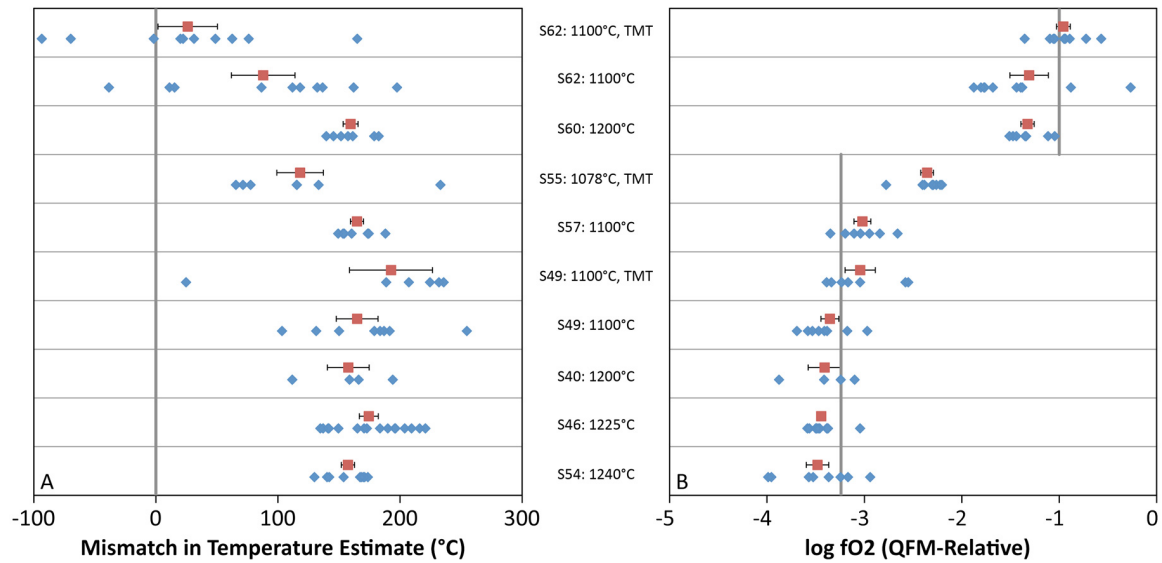


**Figure 2.6:** Comparison between experiment settings and GTOB calculation results for the Ol-Sp-Px GTOB. Horizontal lines separate experimental runs, or a change in Sp composition. Chr is the default Sp composition; higher Ti compositions are labeled as Tmt. Figure A is the difference between the GTOB derived temperature and the experimental set temperature. Figure B is the GTOB calculated oxygen fugacity relative to the QFM buffer compared to the experimentally set oxygen fugacities shown as a gray vertical line. Blue points are for individual GTOB calculation results. Red points are the average of all GTOB calculations for that dataset and include 1s standard errors about the mean.

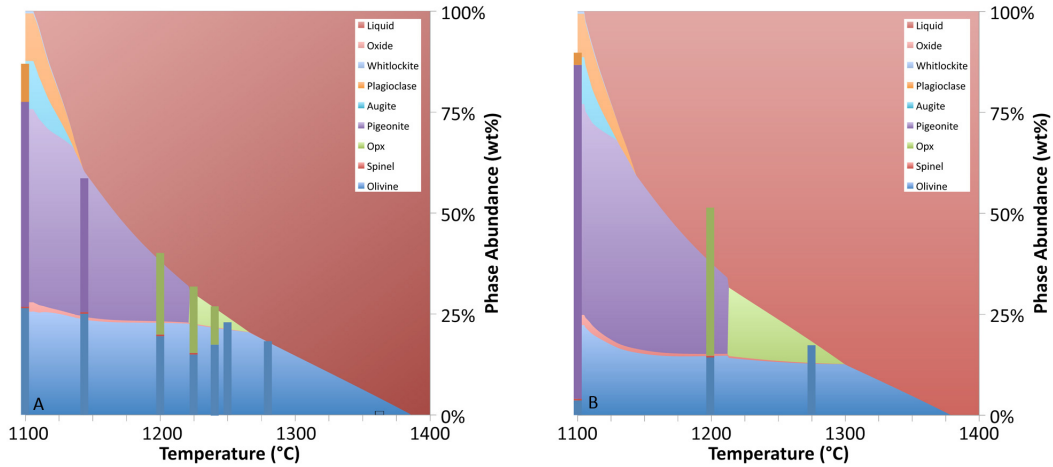


**Figure 2.7:** Comparison between MELTS simulations and experimental results. Smooth curves are MELTS simulations for buffered oxygen fugacities at QFM-3 (A) and QFM-1 (B). Temperature steps were set to 1°C, but results are consistent with 0.1°C calculations. Bar graphs are calculated phase abundances from mineral and glass chemistry from experiments at QFM-3.24 (left) and QFM-1 (right). The MELTS calculations are in relative agreement with experimental results, excepting that MELTS tends to overestimate temperatures.

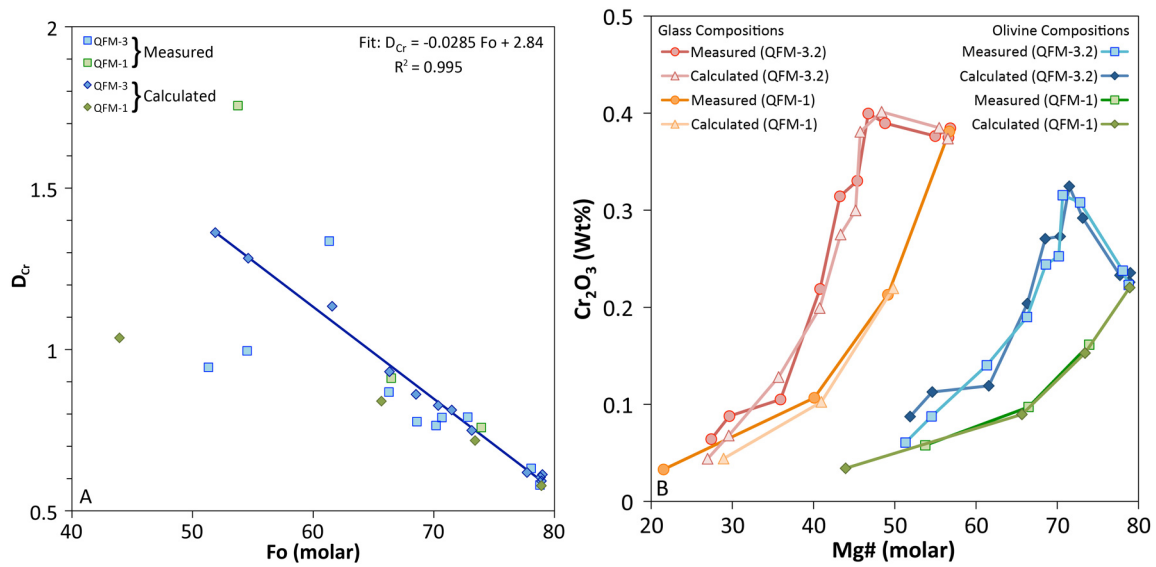


**Figure 2.8:** A: regression relation between olivine composition (Fo) and  $D_{Cr}$ . Data are for both reducing (blue) and oxidizing (green) isothermal experiments, and  $D_{Cr}$  was calculated both from measurements of experimentally produced glass and olivine (squares) and from parameterization of Cr behavior (diamonds). All four datasets are in reasonable agreement at high Fo, but  $D_{Cr}$  becomes suspect at lower Fo as Cr concentration in the glass and olivine both approach MDL. B: comparison of calculated and measured compositions for both olivine and glass produced in isothermal experiments. Measured olivines at QFM-3 (blue squares) and QFM-1 (green squares) compare favorably with olivine compositions calculated from equilibrium liquids (blue/green diamonds); similarly, measured liquid compositions from QFM-3 (red circles) and QFM-1 (orange circles) compare favorably with liquids calculated from olivine compositions (red/orange triangles) based on the linear relationship calculated between  $D_{Cr}$  and Fo (part A).

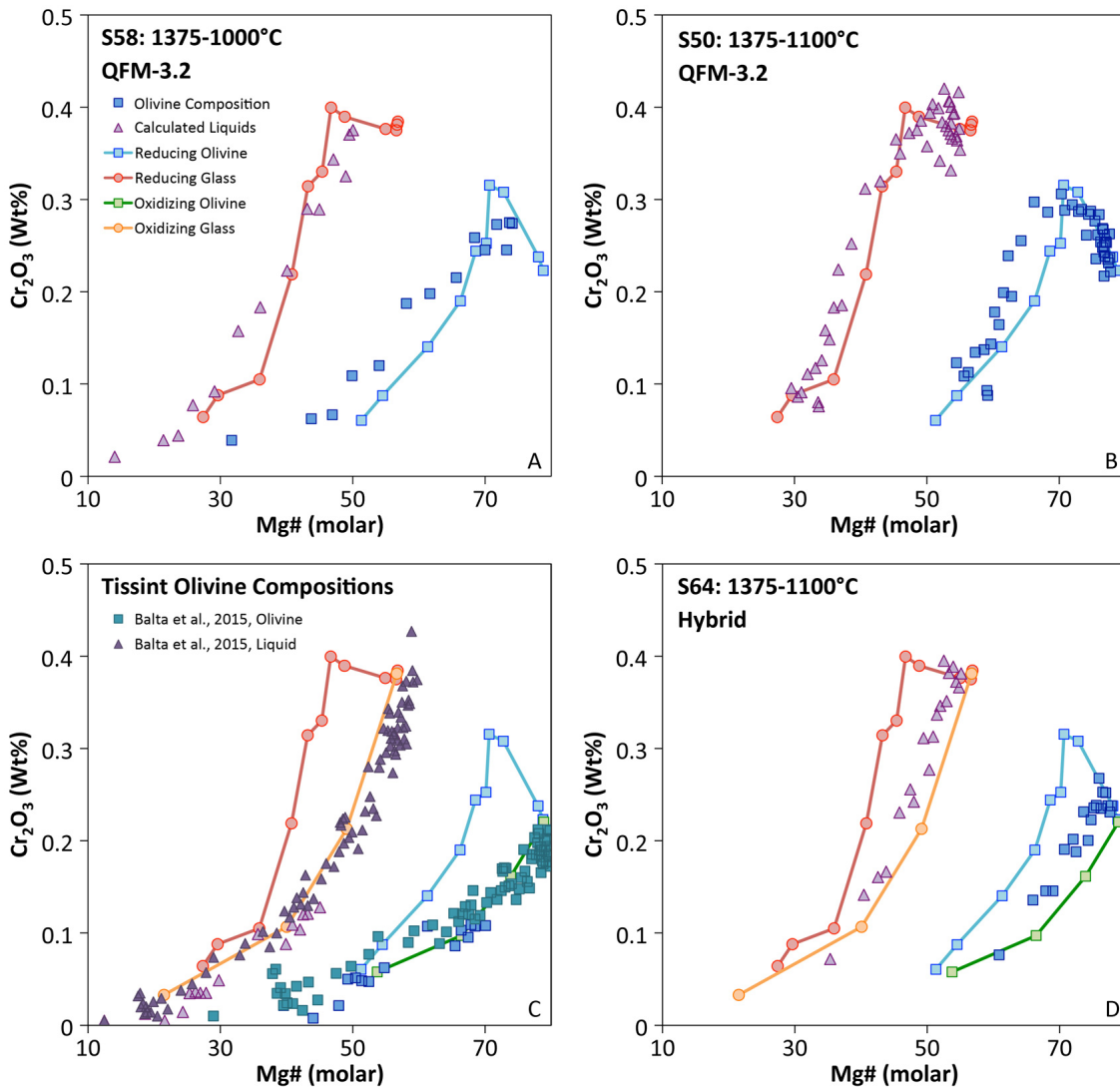


**Figure 2.9:** Olivine zoning profiles from cooling rate experiments (a: S58, b: S50), natural olivines from Tissint (c), and the hybrid experiment (d: S64). Each symbol represents three averaged analyses, ordered by decreasing Mg#, to reduce analytical scatter. Squares are measured olivine compositions (dark blue), along with the average results from isothermal experiments under reducing (light blue) and oxidizing (green) conditions for comparison. Triangles (purple) are liquid compositions calculated from olivine compositions based on  $D_{\text{Fe}/\text{Mg}} = 0.35$  and a calculated  $D_{\text{Cr}}$  from the fit of  $D_{\text{Cr}}$  vs. Olivine Mg# (see Fig. 8). For comparison, circles are measured glass compositions from isothermal experiments under reducing (red) and oxidizing (orange) conditions (from Fig. 8). Tissint olivine compositions are both new data (standard symbols) and data from Balta et al., 2015 (Balta, personal communication; teal squares and dark purple triangles). Notice how the Cr-content of the hybrid experiment closely parallels the results from the oxidizing isothermal experiments, despite  $\sim 2/3$  of the cooling having been under reducing conditions. Natural olivine samples show a similar trend, suggesting that they do not record the original zones, but reequilibrated after the shift in oxygen fugacity.

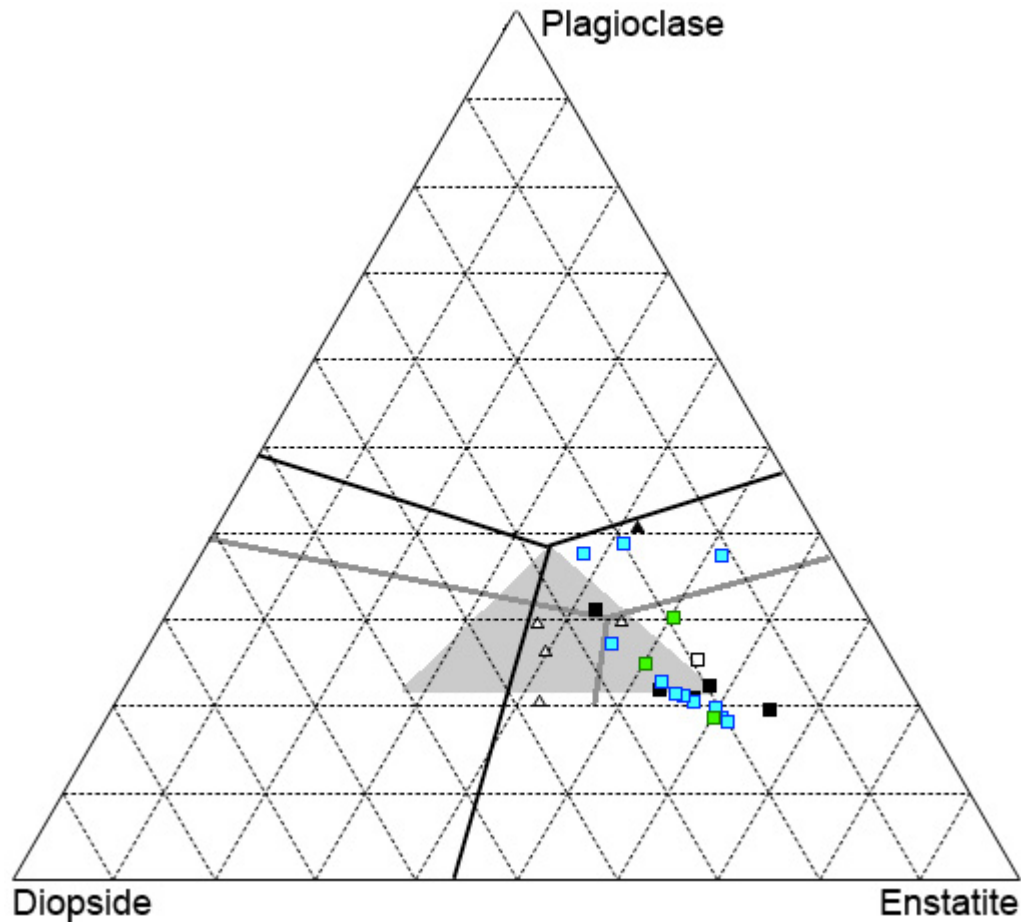


**Figure 2.10:** Schematic ternary phase diagram after Stolper et al. (1979). The shaded gray region is the permissible parental compositional range calculated by Stolper and McSween (1979) for the basaltic shergottites based on the Shergotty and Zagami meteorites. Tissint experiments at QFM-3.2 (blue) and QFM-1 (green) are shown in relation to Ol-phyric (squares) and basaltic (triangles) shergottite bulk (filled symbols) and estimated parental liquid (open symbol) compositions (Hale et al., 1999; Herd et al., 2002b; Kring et al., 2003; McCoy et al., 1992; Stolper and McSween Jr, 1979; Symes et al., 2008; Warren et al., 1999). Phase boundaries are schematically drawn for typical shergottite An content (~An55-75; black lines) and the Na-free system (An100; gray lines). Mineral abundances are calculated according to the CIPW norm from experimental glasses (Cross et al., 1902). Plagioclase is calculated as the combined CIPW norm of anorthite and albite. At high temperatures, under reducing conditions, the mineral norm contains olivine; at low temperatures the mineral norm contains quartz. At all temperatures apatite is calculated in the norm from the  $P_2O_5$  abundance, although the amount is negligible above 1100°C.

## **Chapter 3: The Mechanism Behind Overprinting from Oxidation in the Tissint Meteorite**

### **3.1 Introduction**

The shergottite suite of basaltic meteorites represents a window into the Martian mantle and offers insights into igneous processes on Mars. Texturally, the suite is divided into four types: olivine-phyric characterized by olivine megacrysts, pyroxene-phyric characterized by pyroxene megacrysts, poikilitic (also known as lherzolithic) characterized by olivine oikocrysts poikilitically enclosed by pyroxene megacrysts, and basaltic characterized by subequal amounts of pyroxene and plagioclase in the absence of olivine (e.g. Bridges and Warren, 2006; McSween, 1994). As the least chemically evolved group, the olivine-phyric shergottites offer the most direct window into the Martian mantle and the geochemical processes related to magma-genesis and volcanism on Mars (e.g. Bridges and Warren, 2006; McSween, 1994). Shergottites are also divided along geochemical lines based on a combination of radiogenic and incompatible trace-element abundances into the enriched, intermediate, and depleted types (e.g. Papike et al., 2009; Shearer et al., 2008; Symes et al., 2008). Radiogenic isotope compositions suggest that the chemical types reflect long-term reservoirs in the Martian mantle, potentially originating from differentiation of a Martian magma ocean (Borg and Draper, 2003; Borg et al., 1997; Borg et al., 2003; Debaille et al., 2007; Nyquist et al., 2009a; Shearer et al., 2008; Symes et al., 2008). Although it was believed that volatile content was likely to be related to the degree of enrichment in shergottite magmas (e.g. Gross et al., 2013; Herd, 2006; Peslier et al., 2010), our recent study has shown that Tissint, a depleted olivine-phyric shergottite, came from a magma which underwent the same scale of oxidation as enriched shergottites, implying that both enriched and depleted shergottites have undergone some degree of volatile degassing (Chapter 2; Castle and Herd, 2017).

Oxygen fugacity plays an important role in the evolution of a magma. A higher oxygen fugacity does not just result in a change in the minor-element chemistry of a magma by altering the stable composition of spinel, or other oxide minerals, but can

cause major-element and textural changes by altering the stability of major mineral phases. For example, in the case of the olivine-phyric shergottites, higher degrees of oxidation favor pyroxene over olivine in the stable mineral assemblage (Castle and Herd, 2017). A number of shergottites have been shown to oxidize during crystallization, ranging from enriched shergottites like NWA 1068/1110 and LAR 06319 (Herd, 2006; Peslier et al., 2010) to intermediate and depleted shergottites like NWA 6234 and Tissint (Balta et al., 2015; Gross et al., 2013), respectively, which should result in an oxygen-driven peritectic reaction as the oxidation event shifts stability from olivine to pyroxene. Texturally, resorption results in anhedral olivine phenocrysts, potentially explaining why anhedral olivine is ubiquitous in olivine-phyric shergottites (e.g. Barrat et al., 2002b; Basu Sarbadhikari et al., 2009). Oxygen-driven resorption may also provide an alternative explanation of why some olivine megacrysts do not appear to be stable in their host magmas, rather than the conventional xenocrystic assumption (for example, see the discussion of whether olivine megacrysts are phenocrysts or xenocrysts in NWA 1068/1110: Herd, 2006; Shearer et al., 2008).

A limited study on the effect of an oxidation event during petrogenesis of the Tissint meteorite by Castle and Herd (2017) noted that an increase in oxygen fugacity during crystallization can alter the existing trace-element record preserved in olivine by demonstrating that oxidation caused the overprinting of the Cr compositional profiles in olivine phenocrysts. This study aims to further investigate this effect by illuminating the mechanism, and to expand the discussion to other elements likely to be affected (or unaffected). This study combines results from Castle and Herd (2017) with results from new experiments to elucidate the effect of oxidation on the crystallization Tissint magma and, in particular, the record of that crystallization recorded in the olivine phenocrysts.

### **3.2 Methods**

This work utilizes a synthetic Tissint composition based on the parental-liquid composition calculated by Herd et al. (2013); the authors considered the degree of olivine accumulation (~5 wt% based on the degree of Fe-Mg disequilibrium between olivine cores and the bulk composition) and adjusted the bulk composition accordingly. The

synthetic composition was verified by electron microprobe analysis (EMPA) and is described in more detail by Castle and Herd (2017). For this study, a 1.9993 g split of the synthetic powder was doped with 19.7 and 19.8 mg (~1 wt% each) of NiO and V<sub>2</sub>O<sub>5</sub> powders to investigate the behavior of Ni and V in a subset of experiments; the doped powder was reground under acetone in an agate motor and pestle until homogeneous. The bulk composition of Tissint, the calculated parental liquid, the synthetic composition, and the doped composition are listed in Table 3.1.

This work is a continuation of the previous study of Castle and Herd (2017), incorporating both new experiments and new analysis of previously reported experimental results. Experiments, both the new set and the old, were performed at 1-bar in GERO high temperature vertical-tube furnaces in the High Temperature Planetary Petrology Laboratory at the University of Alberta (UAlberta) in a redox-controlled environment. A CO-CO<sub>2</sub> gas mixture was used to control the  $f_{\text{O}_2}$ , and the redox potential of the gas mixture was determined in the effluent using a zirconia cell suspended in a DelTech reference furnace at constant temperature. The reference potential of the zirconia cell was calculated using the Gas.Bas program (Jurewicz et al., 1993). Oxygen fugacity is calculated and reported relative to the QFM buffer model of Wones and Gilbert (1969). Samples consisted of 100 to 150 mg of synthetic powder pressed into pellets and suspended on Re-wire, similar to the method of Borisov and Jones (1999). Polyvinyl alcohol (PVA) was used to attach the sample pellets to the Re-wire, and care was taken to ensure that the PVA had evaporated before the sample was loaded into the furnace.

Previous work utilized isothermal experiments to determine the crystallization curve for Tissint under both reducing and oxidizing conditions (QFM-3.2 and QFM-1, respectively, both conditions being consistent with mineralogical observations of the Tissint meteorite), as well as cooling rate (CR) experiments to examine the effects of fractional crystallization. In previous work, a single CR experiment, the hybrid experiment, was performed where the oxygen fugacity was abruptly increased during crystallization to examine the effect of an oxidation event on Tissint's petrogenesis; the new experiments are additional variations of the original hybrid experiment, aiming to further explore the effect of an oxidation event. All CR experiments maintained a cooling

rate of 1°C/hr for the duration of the experimental cooling after a >1 hr super-liquidus soak. For each experiment, the gas mixture was set to an  $fO_2$  of QFM-3.2 for the midpoint temperature of the initial cooling, and an  $fO_2$  of QFM-1 for the midpoint temperature of the final cooling; this resulted in a small change in  $fO_2$  over the course of the experiment (see Castle and Herd, 2017, for additional details and discussion). All experiments were terminated by removal from the furnace, quenching in air, within 1 hr of the end of cooling, except S69 where the sample was intentionally held at constant end temperature for ~24 hrs. Experimental parameters are summarized in Table 3.2.

Chemical analyses were performed on phases within experimental charges, including: olivine (Ol), pyroxene (Px), plagioclase (Pl), spinel (Sp), and glass (Gl). Compositions were determined by electron microprobe analysis using the JEOL 8900 electron microprobe at UAlberta. All elements in the synthetic and doped synthetic compositions were analyzed in all samples: Si, Ti, Al, Cr, Fe, Mn, Mg, Ca, Na, K, and P, with Ni and V in the doped samples. All samples were calibrated with well-characterized standards. All glass and Pl analyses were conducted with a beam diameter of 10  $\mu\text{m}$ ; all other mineral analyses were performed with a focused or 2  $\mu\text{m}$  beam diameter. Analyses were conducted with a 15 nA beam current, and the majority with a 15 kV accelerating voltage with a minority at 20 kV. Peak count times varied between 20-60 sec, depending on the required precision, but were typically 30 sec; backgrounds were each measured for half the peak count time. Standardization was performed under identical conditions to the mineral/glass analysis. New analyses were performed on both the previously reported experimental samples (Castle and Herd, 2017) and samples from the new experiments.

Elemental maps and backscatter electron images (BSE) were collected using the Cameca SX100 electron microprobe at UAlberta. Elemental peaks were determined using well-characterized standards. Maps were generated for Si, Al, Cr, Fe, Mg, Ca, Na, and P on all samples; a subset was additionally mapped for either Ni and V or Ti and Mn. Maps were collected with a 20 nA beam current and a 20 kV accelerating voltage at a resolution of 1  $\mu\text{m}$ /pixel. Pixel dwell time was set to 20 ms, and a focused beam was utilized. Collection occurred over two successive passes.

Errors are reported as 1 standard error, calculated as standard deviation divided by the square root of the number of values included (n), in reported averages (e.g. glass

compositions). Errors are reported as 1 standard deviation on individual chemical analyses based on estimated analytical errors (e.g. representative olivine core/rim compositions). This difference arises from the difference in objective between comparing certainty in individual analyses to uncertainty in the confidence of a mean value. Elemental profiles of Ol were calculated by sorting analytical results by Mg#, then averaging sets of three successive analyses to help minimize the effect of analytical scatter, except where otherwise noted. For example, Cr in olivine is plotted where each composition represents the average of three successive Mg# olivine compositions from analysis, along with the average of the corresponding Cr<sub>2</sub>O<sub>3</sub> contents.

### **3.3 Experimental Agenda**

The original hybrid experiment (S64) was designed to reasonably capture the igneous evolution of the actual meteorite while remaining comparable to the standard cooling rate experiments. The temperature of oxidation was intentionally chosen based on petrographic observations of the Tissint meteorite. Oxygen fugacity estimates from oxybarometry show that the most primitive olivine-spinel-pyroxene mineral assemblage formed under reducing conditions; pyroxene and spinel were not observed in isothermal experiments until 1240°C under reducing conditions (spinel likely forms earlier under oxidizing conditions). The temperature of 1200°C was chosen for the experiments to allow a significant formation of both spinel and pyroxene before the system was oxidized. A change in oxygen fugacity is consistent with the proposed mechanism of oxidation - namely, gas escape during eruption or shallow emplacement. Although the natural sample had a higher cooling rate for the groundmass than for the olivine phenocrysts, the cooling rate was kept constant to enable a direct comparison with the purely reducing cooling rate experiments. The fact that the hybrid experiment produced olivine grains with a nearly identical Cr profile to natural samples, but distinct from the Cr profiles in purely reducing cooling rate experiments, lead to the concern that oxidation-induced overprinting of chemical zones in olivine may lead to erroneous interpretation of natural olivine compositions, and this extension of the earlier experimental study of the Tissint meteorite. The goal of each of the new variants of the

original hybrid experiment was to investigate one aspect of the overprinting in hopes of constraining the mechanism that caused it (Table 3.2).

Our early hypothesis suggested that resorption played an important role in the overprinting mechanism. For context, mass-balance calculations show a much lower abundance of olivine in the solid assemblage under oxidizing conditions than under reduced once pyroxene is stabilized (Fig. 2.5). At 1275°C, the olivine abundance is about the same under both reduced and oxidized conditions, but as temperature decreases so does the contrast in abundance: the oxidized sample had 27% less olivine than the reduced at 1200°C and 84% less at 1100°C, with an estimated drop of 67% at 1150°C. To emphasize the resorption process, one of the new hybrid experiments (S68) was conducted with the oxidation at lower temperature, 1150°C, to test whether a larger fraction of the present olivine would be destabilized by the oxidation event; all other variables were kept the same as the original experiment (1375-1100°C, 1°C/hr, etc.).

In order to directly access the effect of oxidation, one of the hybrid experiments was held at constant temperature after the oxidation (S69). Although a great deal of insight can be gleaned from isothermal experiments, calculations based on isothermal experiments assume that the system is allowed to reach equilibrium before examination; as cooling rate experiments are quasi-fractional crystallization experiments by design, this fundamental assumption is violated. Thus, although predictions can be made from isothermal experiments, these predictions need to be verified using cooling rate experiments. The disequilibrium created by oxidizing the system under isothermal conditions, therefore, needed to be verified using a cooling rate experiment. To this end, the original hybrid experiment was reproduced, but cooling halted after oxidation to avoid the effects of additional cooling; in this experiment (S69), the sample was held at constant temperature for 24 hrs to allow the system to respond to the oxidation.

As one of the goals of this investigation is to determine what other elements might be overprinted in olivine phenocrysts by oxidation, a final variant of the hybrid experiment (S75) was performed using a charged doped with two elements not present in the original synthesis: Ni and V. Nickel was chosen because, unlike every other minor-element included in the original synthesis, it is compatible in olivine, making it much more sensitive to changes in olivine abundance at low degrees of crystallization.

Vanadium was chosen because it is one of a small number of minor or trace-elements whose oxidation state changes significantly over the range of  $fO_2$  used in the experiments, making it an excellent indicator of altered behavior in response to oxidation during experimentation.

### 3.4 Results

All three experiments formed minerals and glass qualitatively similar to the original hybrid experiment, as can be seen in BSE images (Figure 3.1). Olivine produced was anhedral and normally zoned in BSE images. Pyroxenes produced were typically euhedral, and often accumulated along Ol edges, but are not included in Ol rims. Larger Px crystals suspended in the glass are typically elongate and incorporate significant glass, consistent with rapid growth, but preserve flat crystallographic faces on both internal and external faces. Pyroxenes also show patchy zoning, where individual crystals contain wide ranges of Mg# and Wo content in discrete patches, a feature also observed in the non-hybrid cooling rate experiments of Castle and Herd (2017). Coarse ( $>10 \mu\text{m}$ ) euhedral Sp crystals are present in the glass, and fine ( $<1 \text{ mm}$ ) Sp grains are present in Ol rims; in contrast, Sp was not present in Ol in any of the non-hybrid cooling rate experiments of Castle and Herd (2017). Plagioclase and ilmenite were not observed in the hybrid experiments presented here, nor in the study by Castle and Herd (2017); the only experiment that produced Pl and Ilm was the CR experiment to  $1000^\circ\text{C}$ , that also produced a silica phase (Castle and Herd, 2017). Mineralogy and textures are summarized for comparison in Table 3.3.

Mineral and glass compositions from all four hybrid experiments were broadly similar to one another and to the same from cooling rate experiments with comparable final temperatures (Tables 3.4-3.7). Glasses from S64, S68, and S75 are similar in most elements, and are most comparable to the cooling rate experiment over the same temperature range, S50. Similarly, the glass from S69 was most comparable to the cooling rate experiment over a similar temperature range, S48 (S69 ended at  $1200^\circ\text{C}$ , S48 at  $1225^\circ\text{C}$ ). Olivine chemical zones in all four hybrid experiments and all three cooling rate experiments overlap, excepting in Cr where the hybrid experiments are distinct

(Figure 3.2). S75 shows that Ni behaves similarly to Mg, decreasing from core to rim, but additional experimentation is required to address Ni behavior in detail (Figure 3.3). Pyroxene major-element evolution is similar in all of the cooling rate experiments, but varies in details between the various experiments (Figure 3.4). While all spinel compositions are intermediate between chromite and titanomagnetite (Figure 3.5), spinel is the most widely varied mineral composition between the experimental runs. Plagioclase and ilmenite were only observed in the lowest temperature cooling rate experiment (S58, 1000°C), so no comparison is available.

X-ray maps of olivine show the same sense of chemical zoning in all experiments (Appendix A2, Fig. A2.1-A2.8). Qualitatively, all olivine grains decrease in Mg from cores to rims while simultaneously increasing in Fe (Figure 3.6). Cr maps are not sensitive enough to show zoning patterns, but reveal the presence of sub  $\mu\text{m}$  chromites in the hybrid experiments. The S75 map of V highlights the presence of small ( $<10 \text{ nm}$ ) Sp grains in Ol rims, as V is preferentially included in Sp. The P map of S68 shows a feathery zoning pattern along what appear to be flat crystallographic faces internal to the anhedral Ol phenocrysts; faint parallel variations in the P map of S69 suggest a subtle version of this zoning near the limit of detection, but otherwise this feathered zoning is not apparent in any other mapped olivine. The feathered P zoning does not correlate with any other elemental variation.

A limitation of the experimental technique employed is that Ni preferentially partitions into the Re-wire during experimental heating. This is apparent in the bulk composition of the doped synthetic composition, where, although 1 wt% NiO was added in the synthesis, only 0.36% was measured in the glass (S76). It is likely that a larger portion of the Ni would be partitioned into the wire in a longer duration experiment (e.g. S75), adding uncertainty to interpretations based on Ni in the doped hybrid experiment.

## **3.5 Discussion**

### *3.5.1 Cr behavior and diffusion rates in olivine*

The simplest mechanism to overprint a mineral core is diffusion. One way to determine whether diffusion is an adequate mechanism to overprint olivine cores is to calculate a diffusion length scale for the experimental settings. A limitation of the diffusion length scale is that it is intended to estimate the distance over which a material would reach equilibrium; however, it does provide a means to assess the viability of the diffusion mechanism. In the fastest diffusing direction, parallel to the c-axis, the activation energy ( $E_a$ ) is  $299 \pm 14$  kJ/mol and the diffusion constant ( $D_0$ ) is  $6.65 (\pm 0.59) \cdot 10^{-7}$  m<sup>2</sup>/sec for Cr diffusion in olivine (Ito and Ganguly, 2006). Although it is likely that Cr(II) diffuses more rapidly than Cr(III) in olivine, based on the difficulty of substituting an  $M^{3+}$  cation into the olivine structure, no significant difference was determined for the diffusion rate between IW and IW+2, even though the  $Cr^{2+}/Cr^{3+}$  ratio should be significantly lower at IW+2 (IW is the iron-wüstite buffer, approximately the same as QFM-4; Ito and Ganguly, 2006). The change from IW to IW+2, although part of a log unit more reducing, approximates the redox change replicated under experimental conditions; therefore, the effect of changing  $fO_2$  can be neglected for the purposes of this calculation. After oxidation, the original hybrid experiment (Castle and Herd, 2017) was run for an additional 105 hrs. The diffusion length scale, a rule of thumb calculation for the length over which diffusion can equilibrate a system, can be calculated from the diffusion rate at a given temperature ( $D$ ) for a given duration ( $t$ ) by  $L = \sqrt{Dt}$ , where  $L$  is the length scale. As an upper limit on the diffusion, the diffusion length scale for olivine held at 1200°C for 100 hrs is approximately 2.4  $\mu$ m, more than two orders of magnitude smaller than the olivine grains produced experimentally (S48, the cooling rate experiment to 1225°C, produced a single large olivine grain with a distance of 500-800  $\mu$ m from core to rim, depending on the measurement direction. S48 is a reasonable proxy for pre-oxidation olivine grain sizes in the hybrid experiments). This shows that Cr diffusion in olivine is simply too slow for chemical exchange with the glass to explain the scale of Cr overprinting in olivine during any of the variants of the hybrid experiment.

Some level of diffusion of Cr out from olivine cores should occur based on the changes in the liquid chemistry in response to oxidation. Oxidizing a magma reduces the  $Cr^{2+}/Cr^{3+}$  ratio as Cr(II) is converted into Cr(III). It has been speculated that the presence of Fe in the system should reduce the magnitude of change in the Cr system by

preferentially stabilizing Cr(III) to lower  $fO_2$  (Schreiber and Haskin, 1976), but this effect was not observed in the study of Hanson and Jones (1998) where the relationship between total Cr and  $fO_2$  in a spinel-saturated system did not change with the introduction of Fe to the system. Using the Fe-free model of Hanson and Jones (1998), a model that reasonably approximates their results for both Fe-free and Fe-bearing systems, the  $Cr^{2+}/Cr^{3+}$  ratio should drop by 75% during the oxidation of the hybrid experiments. In percent species, at 1200°C (the temperature of most hybrid experiments) the system would have changed from 80.6% to 50.8% Cr(II); at 1100°C the calculated drop in the ratio is still 75%, although the calculated ratio is much higher at 1100°C, meaning that more Cr(II) should be present at 1100°C than at 1200°C under the same  $fO_2$ . By 1200°C, the Tissint magma is saturated in spinel, whether under reducing or oxidizing conditions, implying that the total activity of Cr(III) is buffered, so as Cr(III) is formed from Cr(II) more spinel precipitates in response, resulting in a lower total Cr in the liquid after oxidation. There is a corresponding effect on the Fe-Mg system, but it is negligible given the minor abundance of spinel formed relative to the abundances of Fe and Mg.

Oxidation also has a significant effect on the partitioning of Cr into olivine. Beyond the simple drop in Cr in the liquid lowering the equilibrium concentration in olivine, the shift in Cr oxidation state also affects the partition coefficient. The model of Hanson and Jones (1998) allows us to estimate  $D_{Cr(II)}$  and  $D_{Cr(III)}$ ; in their model,  $D_{Cr(II)}$  is primarily dependent on temperature at 1 bar, while  $D_{Cr(III)}$  is dependent on the polymerization of the melt (specifically, the ratio of non-bridging oxygens to tetrahedral oxygen, NBO/T, is used as the variable for melt chemistry. See Mysen, 1983 for more details on NBO/T). Using the temperature of the hybrid experiment and the glass compositions from isothermal experiments  $D_{Cr(II)}$  is calculated to be 1.0 and  $D_{Cr(III)}$  switches from 0.76 to 0.73 during oxidation; while this is only a modest change, the average partition coefficient depends on the ratio of  $Cr^{2+}/Cr^{3+}$ , so the average  $D_{Cr}$  coefficient decreases nearly 10% (from 0.95 to 0.87). The decrease in  $D_{Cr}$  is larger at lower temperatures, becoming a 15% drop in compatibility by 1100°C, so as the Cr abundance in the liquid is dropping Cr is simultaneously becoming less compatible in olivine, creating a diffusion gradient where Cr would eventually diffuse out of the olivine, given a sufficient duration before quenching.

### 3.5.2 Oxidation and the olivine peritectic reaction

An alternative to pure diffusion as the overprinting mechanism is diffusion assisted by resorption. In isothermal experiments, under both reducing and oxidizing conditions, the olivine abundance decreases after pyroxene forms indicating a peritectic reaction where olivine reacts with the liquid to form pyroxene as the liquid evolves. Therefore, in the context of increasing  $fO_2$  conditions one would expect a much larger resorption event as significantly less olivine is stable under oxidizing than reducing conditions once pyroxene is present. Resorption would reduce the size of olivine grains, shortening the diffusion length between olivine cores and the liquid. At the same time, the more primitive olivine compositions that are becoming exposed via resorption should have a higher Cr abundance, increasing the disequilibrium between olivine and liquid, and raising the rate of Cr diffusion.

The mineral abundance estimates from the isothermal experiments of Castle and Herd (2017) can be used to calculate an equilibrium estimate of the extent of olivine resorption as a function of temperature. As discussed earlier, at 1275°C, ~25°C above the temperature where pyroxene is stabilized under reducing conditions, the contrast in olivine abundance from mass balance calculations between the oxidizing and reducing isothermal experiments is minimal (~5%). By 1200°C, the temperature of oxidation in most of the hybrid experiments, the contrast has increased substantially (27%); as temperature decreases so does the contrast in olivine abundance, becoming as high as 84% by 1100°C (the contrast at 1150°C is estimated at 67%). Although this theoretical extent of resorption becomes quite substantial as temperature decreases, this will only occur if the system reaches equilibrium; cooling rate experiments are, by design, kinetically dominated experiments, not equilibrium experiments. As fractional experiments, the full extent of resorption is unlikely to be achieved, making these calculations an upper-bound estimate of the possible extent of olivine resorption.

Resorption rims should be apparent in olivine from hybrid experiments in elements that diffuse sufficiently slowly to preserve a compositional contrast. Of all of the elements included in the synthetic composition, P is the slowest diffusing element in

olivine. It also has the most predictable behavior, as the only mineral in Tissint in which P is compatible is merrillite (Balta et al., 2015), a phase that was never stabilized experimentally and is thought to be one of the last crystallizing phases; this means that P should monotonically increase in the liquid as crystallization proceeds. As a result, the P content of olivine grains in Tissint should gradually increase with decreasing Mg#. Unfortunately, the relative uncertainty associated with the measurement of P in olivine was large compared to the likely total variation, obscuring a relationship between P and Mg# in olivine profile compositions. Similarly, X-ray maps of P abundance had statistical noise that was larger than the total variation mapped in olivine grains which resulted in no discernable variation in P across olivine grains, except in S68 (discussed below). Further, no sharp contrast in abundance was mapped in any element in olivine, meaning that no evidence of a resorption rim was found in x-ray mapping. Three factors may explain the lack of observed resorption rims: 1) analytical uncertainty in elemental determinations and maps, 2) diffusion masking compositional contrasts, 3) a low degree of resorption, or a lack of resorption, achieved due to kinetic factors despite the prediction of substantial resorption based on equilibrium calculations. Whichever the explanation, the result is either that the degree of resorption achieved was low, or that the compositional contrast generated was low, meaning that resorption is not a viable mechanism to increase the diffusion rate to explain Cr overprinting in olivine.

Experiment S68, the lower temperature hybrid experiment, was the only experiment where a significant variation in the P content of olivine was mapped (Fig. 3.6F). Olivine cores in S68 show a gradual, and low magnitude, increase in P content, but olivine rims show a feathered zoning pattern where the P content oscillates between the highest and lowest concentrations observed in the olivine grain. Multiple orientations are observed with P zones occurring along straight edges, likely crystallographic faces, although the orientation of the P-rich zones were not determined to verify this hypothesis. If correct, the oscillatory zonation of P along crystallographic faces indicates that the olivine crystallized rapidly relative to the diffusion rate of P in the liquid. The only difference between S68 and the original hybrid experiment (S64) was the temperature of oxidation, where S68 was oxidized at 1150°C rather than at 1200°C. If, as implied by the discussion above, oxidation halts olivine growth or causes resorption, then the presence

of the oscillatory zoning pattern exclusively in the lower temperature experiment suggests that it formed in the olivine between 1150°C and 1200°C, as the oxidation of the sample would interrupt olivine growth and prevent its formation. This may provide an additional constraint for when the Tissint magma was oxidized, as similar oscillatory zoning was observed in the natural sample (Basu Sarbadhikari et al., 2016); however, it is unclear why a feathered P zoning pattern was not observed in X-ray maps of S50 and S58 (the cooling rate experiments to 1100°C and 1000°C, respectively). The potential to generate feathered zoning in olivine during monotonic cooling, particularly in the absence of similar variation in any other element, suggests that care must be taken if petrogenetic interpretations are made from the zoning of P in olivine in natural samples.

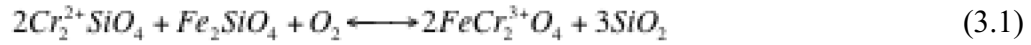
### *3.5.3 The chromite exsolution model*

To summarize the discussion so far, diffusion is a likely mechanism to cause overprinting of Cr within olivine, but the diffusion rate is much too slow for the Cr to diffuse out from an olivine core into the surrounding liquid. Although oxygen-driven resorption may help shorten the required diffusion distance while simultaneously enhancing the diffusion gradient, there is no evidence of resorption rims in olivine grains from hybrid cooling rate experiments. Because diffusion to the liquid is not an adequate mechanism, another mechanism must be identified. One possibility is the formation of an exsolved mineral phase, sequestering the Cr out of the olivine. Based on our observations, the phase responsible is chromite ( $\text{FeCr}_2\text{O}_4$ ).

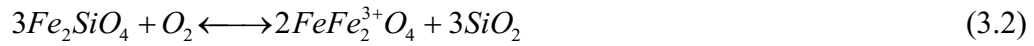
Chromium exists differently in the olivine structure depending on its charge (e.g. Papike et al., 2005). As a divalent cation, Cr(II) is directly substituted into the octahedral site. As a trivalent cation, Cr(III) generates a charge imbalance, requiring either a coupled substitution (e.g. with Al into the T site) or a vacancy substitution; this factor is likely why Cr(III) is less compatible in the olivine structure. When the system is oxidized, the Cr(II) in the olivine structure may convert to Cr(III), forcing a change in the olivine composition. An increase in oxidation state of Cr would have two effects: 1) as a less compatible species, Cr(III) is likely to be forced out of the olivine structure; 2) what additional Cr(III) is incorporated into the olivine structure would force out other M(II)

cations from the structure as there is nothing available to substitute into the olivine structure to establish a charge balance. Both changes would likely result in spinel exsolution, but via different mechanisms.

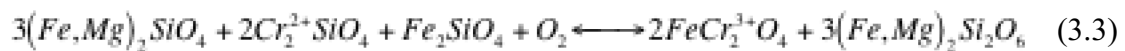
If Cr(III) is forced out of the olivine structure, then a breakdown of olivine, similar to the reaction that defines the QFM buffer, is likely. A potential reaction for this breakdown is:



where  $Cr_2SiO_4$  is the idealized composition of the Cr end-member olivine. For comparison, the QFM buffer reaction is:



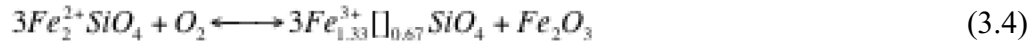
where olivine (fayalite) breaks down into spinel (magnetite) and quartz in the presence of excess oxygen. A major implication of this mechanism is that for every mol of spinel generated from olivine, 1.5 mol of silica should be generated. This mechanism is inconsistent with observations in that silica is not observed included in olivine; however, it is plausible that the silica inclusions are simply not resolved in microprobe BSE imaging. It is highly probable that silica excess from the olivine would result in pyroxene formation, rather than free silica, as the olivine composition is intermediate rather than the high-iron end member. Taking the intermediate composition into account the formula becomes:



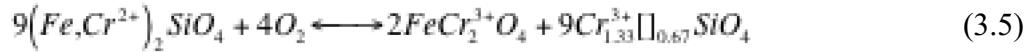
The resulting pyroxene would have a lower Mg# than the original olivine, as the Fe end member of olivine is preferentially converted into spinel, but the BSE image contrast difference between the original olivine and the newly formed pyroxene would be minimal. Further, as it should exsolve proximally to the spinel grains, the contrast

difference may be overwhelmed by the bright spinel. Alternatively, whether silica or pyroxene is formed, the grain size may simply be too small to resolve with the microprobe, requiring a higher resolution technique (e.g. TEM).

If Cr(III) is incorporated into the olivine structure during closed-system oxidation, rather than preferentially removed during olivine breakdown, then a more exotic mechanism is required. Laihunite, also known as oxy-fayalite, can be formed by oxidation of fayalite (Iishi et al., 1989):



In this reaction, the excess Fe is expelled from the M site, allowing the system to maintain charge balance as Fe(II) is converted into Fe(III), and results in the formation of hematite. Modifying this reaction to address the conversion of Cr(II) to Cr(III) in olivine, and the formation of spinel instead of a rhombohedral oxide (e.g. hematite), yields the potential reaction:



As with the earlier mechanism, we are not suggesting that pure Cr-olivine or oxy-Cr-olivine end members exist, but instead that they represent the portion of the solid solution participating in the reaction. This reaction is proposed, rather than a coupled substitution with the T site or similar, as the system is theorized as a closed system excepting the addition of oxygen from the oxidizing environment. This particular mechanism is compatible with observations in that it does not require an accompanying silicate to precipitate from the olivine; however, further analysis needs to be performed if it is to be verified as a potential mechanism to exsolve spinel from olivine. A limitation of this mechanism is that it only results in a relatively small drop in the concentration of Cr in the olivine as 4.5 mol of oxy-Cr-olivine must be generated for every mol of spinel, corresponding to a 33% drop in Cr-content. In contrast, the difference in Cr-content between reducing and oxidizing isothermal experiments is approximately 50%.

The clearest evidence for the exsolution of spinel from olivine is in the hybrid experiment with added V (S75). X-ray maps of an olivine grain in S75 reveal a substantial number of small spinel grains throughout, but preferentially located in the olivine rims. Although the grains were too small for quantitative analysis, energy dispersive spectroscopy (EDS) showed the spinel to be intermediate between chromite ( $\text{FeCr}_2\text{O}_4$ ) and coulsonite ( $\text{FeV}_2\text{O}_4$ ), strongly suggesting that V had behaved identically to Cr in the experimentally formed olivine. Although the abundance was substantially lower, small grains of spinel were subsequently observed in BSE images of olivine in each of the other hybrid experiments (S64, S68, S69), but not observed in olivine in the non-hybrid cooling rate experiments (S48, S50, S58); this difference demonstrates that the oxidation is what controls the formation of spinel from the olivine, as presented in the mechanisms above. The lack of accompanying silica or pyroxene suggests that the first mechanism is less likely, although the literature on oxidized olivine (laihunite, as the Fe end-member) suggests that experimental conditions were still too reducing to form significant quantities of oxidized olivine, as required by the second mechanism. However it forms, the typical spacing between mapped spinel grains in S75 is on the order of 10  $\mu\text{m}$ , which is much closer to the length scale of diffusion calculated for Cr diffusion at experimental conditions. The typical procedure for EMPA requires the user to avoid mineral inclusions to measure reliable mineral compositions, and data processing typically removes outliers; thus, the sequestering of Cr into spinel would result in the lower Cr abundance measured in olivine in the hybrid experiments, and accordingly in olivine in the Tissint meteorite.

It is likely that any other element strongly partitioned into spinel relative to olivine would be similarly modified by the exsolution, effectively overprinting the magmatic chemical zoning generated before the oxidation. As only a relatively small amount of spinel is typically formed, due to the low abundance of Cr in the Tissint magma, the accompanying enrichment in elements that strongly partition into olivine is negligible. Further, the direct evidence of this study only demonstrates the effect on redox sensitive elements strongly partitioned into spinel (Cr and V), so it is possible that the redox sensitivity is also required for an element to preferentially partition into the spinel.

### 3.5.4 Implications for Tissint petrogenesis

Three lines of evidence now suggest that the Tissint magma underwent an oxidation event. The most definitive is the geothermometry/oxybarometry calculations from mineral assemblages, which show a substantially more reduced  $fO_2$  for the early-formed olivine-spinel-pyroxene assemblage than the late-formed titanomagnetite-ilmenite assemblage (QFM-3.5 and QFM-1.4, respectively; Castle and Herd, 2017). Secondly, there is a textural argument, where the ubiquitously anhedral olivine phenocrysts and the lack of low Mg# minor grains of olivine in the groundmass (Balta et al., 2015; Basu Sarbadhikari et al., 2016) suggest that olivine was destabilized, and a likely mechanism is the oxidation of the magma (Castle and Herd, 2017). This study now adds the observation that a minor abundance of very small (<1-5  $\mu\text{m}$ ) spinel grains is likely the result of oxidation-induced exsolution of spinel from olivine, rather than incorporation of magmatic spinel.

Exsolution of spinel modifies the chemical profiles of olivine cores from their initial magmatic profiles, as discussed above. This effect was first observed in Cr, where the profile of olivine cores was modified in a hybrid experiment to resemble the expected profile formed exclusively under oxidizing (that is, spinel saturated) conditions, rather than preserving evidence of a transition (Castle and Herd, 2017). It is likely that other spinel-compatible elements are similarly modified by the exsolution; a tentative list of additional elements includes V, Ni, and Co, based on their relatively high compatibility in spinel over olivine (Herd et al., 2009; Righter et al., 2006), but further study is required to verify the behavior of these elements in the Tissint magma. It is unlikely that elements not preferentially partitioned into spinel would be significantly altered given the low abundance of spinel formed via exsolution. As a result, most elements in olivine profiles are unlikely to be modified, meaning that few assessments are likely to be affected.

The absence of coarse (>10  $\mu\text{m}$ ) spinel inclusions in olivine in Tissint is unusual among the olivine-phyric shergottites (Balta et al., 2015; Basu Sarbadhikari et al., 2016; Basu Sarbadhikari et al., 2009; Goodrich et al., 2003). Although it is commonly accepted that spinel is likely to be the liquidus phase in shergottite magmas (e.g. Goodrich et al.,

2003), the oxidation-induced exsolution mechanism suggests that it is not, an interpretation that is consistent with experimental results that show olivine stabilizes 125°C higher than spinel under the reducing conditions calculated from mineral equilibrium. This may be the result of Tissint, as a depleted olivine-phyric shergottite, being among the most reduced shergottites thus far described, as spinel saturation is suppressed under reducing conditions. The consistency of natural observations with experimental results demonstrates that the calculated parental composition did not have an artificially low Cr content, which is the alternate hypothesis for why spinel would be absent from olivine cores in the Tissint magma.

Peritectic resorption of olivine in response to oxidation of the magma likely occurred in the Tissint meteorite, but not to the full extent inferred from isothermal experimental results. The difference in olivine abundance between isothermal experiments under reducing and oxidizing conditions suggests that a large fraction (27-84%, the fraction increasing as temperature decreases from 1200°C to 1100°C) of the olivine could resorb, but the failure to detect resorption rims in hybrid experiments suggests that a much lower degree of resorption actually occurs. The lower degree of resorption is likely due to the kinetic-dominated (i.e. fractional), rather than ideal (i.e. equilibrium), nature of cooling rate experiments. At slower cooling rates, the behavior of the system would shift from kinetically-dominated towards ideal behavior, increasing the fraction of olivine that resorbs in otherwise similar experiments. At a minimum, oxidation of the magma halts the formation of olivine; however, the existence of anhedral olivine grains in all hybrid experiments, compared to the euhedral to subhedral nature of olivine in purely reducing cooling rate experiments over similar cooling intervals, supports that resorption does occur to some degree in the hybrid experiments.

### *3.5.5 Implications for shergottite petrogenetic interpretation*

A systematic model for the occurrence of spinel as the liquidus phase, rather than olivine, in olivine-phyric shergottites is still elusive. Within the shergottite suite, olivine-phyric shergottites are the most reduced textural type for any given degree of enrichment (Castle and Herd, 2017; Herd, 2003); as spinel saturation is suppressed under reducing

conditions it is counterintuitive that most olivine phyric shergottites have significant spinel inclusions in olivine phenocrysts. The lack of spinel incorporated in olivine, rather than exsolved from olivine, makes Tissint somewhat of an oddity among the shergottites. The lack of spinel is unlikely to be a result of chemical maturity as NWA 5789, another depleted olivine-phyric shergottite, has both a higher Mg# in olivine cores, indicating that it is from a more primitive magma, and spinel included in olivine phenocrysts (Gross et al., 2011; Irving et al., 2010); contrasting this, Y-980459, also a depleted olivine-phyric shergottite, has a very similar composition to NWA 5789, but lacks spinel inclusions in olivine (Usui et al., 2008). Rather than a fundamental mechanism generating this difference, it is likely that olivine-phyric shergottites are from magmas that are close to spinel saturation in T, P,  $fO_2$ , composition space, so minor variations in the source magma change the ordering of saturation.

As it appears that spinel grains incorporated into Tissint olivine phenocrysts are the result of oxidation induced exsolution of Cr from olivine grains, the presence of fine grained ( $< 10 \mu\text{m}$ ) spinel in olivine in other olivine-phyric shergottites may indicate that their magmas also underwent an oxidation event during crystallization. As many shergottites do not have multiple mineral assemblages conducive to estimating  $fO_2$ , this may provide a valuable petrologic indicator. However, as the majority of shergottites contain spinel inclusions in olivine phenocrysts, it may be difficult to determine if spinel exsolved from olivine as any exsolving spinel is likely to form as overgrowths on preexisting spinel; this may warrant a further high-resolution study of naturally formed spinel grains in olivine-phyric shergottites. It is also conceivable that some coarse spinel is not the result of inclusion during crystallization, but instead exsolved spinel that has coarsened due to relatively slow subsolidus cooling.

Castle and Herd (2017) discussed a conflict in the literature where different assessments had led to opposite conclusions on whether the olivine megacrysts in NWA 1068/1110 were phenocrysts or xenocrysts (Herd, 2006; Shearer et al., 2008). To summarize, Herd (2006) concluded that the olivine grains had to be xenocrysts since they were unstable in the groundmass liquid composition, evidenced by their anhedral nature, and had formed under more reducing conditions than the groundmass; Shearer et al. (2008) came to the opposite conclusion by noting that the trace-element composition of

the olivine cores (notably Ni and Co) is in equilibrium with the bulk composition, having also formed under oxidizing conditions. The proposed resolution was that the olivine formed as a phenocryst under reduced conditions, then, as the magma oxidized, the olivine was overprinted. The mechanism which we elucidate here - namely, oxidation induced spinel exsolution from olivine - would require that both Ni and Co either undergo a similar oxidation to Cr, driving their removal from olivine, or that they be strongly partitioned into spinel over olivine. As Ni and Co remain in the 2+ state over the typical range of  $fO_2$  of planetary basalts (e.g. Herd et al., 2009), the latter is more likely. Studies of Ni behavior in crystallizing basalts suggest that Ni is partitioned into spinel over olivine, as  $D_{Ni}(Sp)$  is 31-65 (Nielsen et al., 1994) and  $D_{Ni}(Ol)$  is 4-19 (Herd et al., 2009) (Nabelek 1980, Dale and Henderson 1972, Seifert et al. 1988). Cobalt does not have a clear partitioning driver as basalt studies result in similar partition values for  $D_{Co}(Sp)$  and  $D_{Co}(Ol)$  (Righter et al., 2006) (3.4 and 3.1, respectively; Paster et al. 1974; Lemarchand 1987). In any event, the mechanism appears consistent with the proposed resolution, that olivine in NWA 1068/1110 formed as a phenocryst assemblage and then was overprinted by the oxidation induced exsolution of spinel, but further study is required to address the applicability of the mechanism to Ni and Co to fully explain the observations.

### 3.6 Conclusions

Tissint is one of several olivine-phyric shergottites that have undergone an oxidation event during crystallization. Cooling rate experiments with a hybrid oxygen fugacity, where the system is oxidized part way through cooling to simulate the change in the natural sample, demonstrate that the record of Cr in olivine zones was substantially altered from the original profile: the modified profile appears as though the olivine formed under oxidizing conditions. Diffusive exchange with the surrounding liquid is too slow to cause the overprinting; a likely mechanism is the oxidation-induced exsolution of spinel from the olivine. Evidence to support oxidation-induced exsolution is the presence of fine ( $< 10 \mu m$ ) spinel grains in olivine rims exclusively in hybrid cooling rate experiments, where the sample was oxidized part way through cooling, similar to the

natural sample. The overprinting is likely to modify any element preferentially incorporated into spinel over olivine, or which is sensitive to changes in redox state over the interval of  $fO_2$  increase.

Feathered P zones were observed in a single hybrid experiment. Other experiments showed little variation in P content across olivine zones. Although intriguing, there is no apparent reason why that particular experiment should have generated a feathered zoning pattern while other experiments did not; as a result, the most plausible interpretation is that the occurrence in the mapped grain was coincidental, and that feathered zoning only occurs sporadically in cooling rate experiments, hybrid or otherwise. Further research is required if the significance is to be determined.

Overprinting of olivine cores resolves the debate over whether olivine megacrysts in NWA 1068/1110 are phenocrystic or xenocrystic. Olivine cores are phenocrysts, formed under reducing conditions, but exsolution of spinel grains after an oxidation event altered the profiles of Co and Ni in olivine rims, making the grains appear in equilibrium with the groundmass conditions, despite having formed under very different oxygen fugacities.

**Table 3.1:** Tissint bulk compositions

	Tissint <sup>1</sup>	Tissint Parental <sup>2</sup>	Synthetic Tissint <sup>3</sup>		Doped Tissint <sup>4</sup>	
n			16		4	
SiO <sub>2</sub>	46.2	47.2	47.65	±0.04	46.8	±0.1
TiO <sub>2</sub>	0.63	0.67	0.676	±0.007	0.644	±0.008
Al <sub>2</sub> O <sub>3</sub>	4.86	5.2	5.39	±0.01	5.21	±0.01
V <sub>2</sub> O <sub>3</sub>					0.838	±0.008
Cr <sub>2</sub> O <sub>3</sub>	0.41	0.44	0.38	±0.01	0.338	±0.006
FeO	21.2	21.6	21.99	±0.03	21.31	±0.03
NiO					0.361	±0.007
MnO	0.52	0.56	0.552	±0.005	0.775	±0.004
MgO	17.1	16	16.16	±0.03	14.9	±0.07
CaO	6.5	7	7.35	±0.01	7.41	±0.01
Na <sub>2</sub> O	0.72	0.77	0.133	±0.004	0.166	±0.009
K <sub>2</sub> O	0.02	0.02	<MDL		<MDL	
P <sub>2</sub> O <sub>5</sub>	0.48	0.51	0.348	±0.008	0.413	±0.002
Total			100.65	±0.05	99.1	±0.2
Mg#	61.5	59.4	56.7	±0.1	55.5	±0.3

<sup>†</sup> MDL stands for method detection limit.

<sup>1</sup> Bulk Tissint composition reported in Chennaoui Aoudjehane et al. (2012).

<sup>2</sup> Calculated Tissint parental composition reported in Herd et al. (2013).

<sup>3</sup> Synthetic Tissint composition reported in Castle and Herd (2017). Most experiments discussed in this study utilize this composition.

<sup>4</sup> Doped Tissint composition is the mixture of the synthetic Tissint composition mixed with 1 wt% each of NiO and V<sub>2</sub>O<sub>5</sub> powders, utilized to determine the behavior of Ni and V. The additional elements raised the liquidus temperature, so the glass was held at 1425°C for 1 hr to ensure complete melting.

**Table 3.2:** Experimental run parameters

Run	Mass (mg)	Temp <sup>1</sup> (°C)	$f_{O_2}$	Duration (hrs:min)	Notes	Phases
S48 <sup>2</sup>	123.4	1375-1225	QFM-3.2	156:15		Gl, Ol, Sp
S50 <sup>2</sup>	102.1	1375-1100	QFM-3.2	292:00		Gl, Ol, Px, Sp
S58 <sup>2</sup>	104.0	1375-1000	QFM-3.2	403:54		Gl, Ol, Px, Pl, Ilm
S64 <sup>2</sup>	100.8	1375-1200	QFM-3.2			Gl, Ol, Px, Sp
		1200-1100	QFM-1	292:12		
S68 <sup>1</sup>	101.4	1375-1150	QFM-3.2			Gl, Ol, Px, Sp
		1150-1100	QFM-1	291:02		
S69	107.6	1375-1200	QFM-3.2			Gl, Ol, Px, Sp
		1200	QFM-1	212:20	T-hold	
S75	100.5	1375-1200	QFM-3.2		Doped	Gl, Ol, Px, Sp
		1200-1100	QFM-1	292:01	V, Ni <sup>3</sup>	

<sup>1</sup>All experiments were set to a cooling rate of 1°C/hr for the duration of the experiment, except S69 where the temperature was held constant after oxidation (24:18 hold duration). The offset between furnace set point and sample temperature resulted in a slightly slower than 1°C/hr cooling rate (0.96-0.93°C/hr).

<sup>2</sup>S48, S50, S58, and S64 have been previously reported in Castle and Herd (2017).

<sup>3</sup>S75 was performed using a doped powder, including 1 wt% each of NiO and V<sub>2</sub>O<sub>5</sub>.

**Table 3.3:** Experimentally produced mineralogy and textures

	Olivine	Pyroxene	Plagioclase	Spinel	Silica	Ilmenite
S48	Euhedral			Euhedral		
S50	Subhedral	Euhedral		Euhedral		
S58	Anhedral	Euhedral	Euhedral		Euhedral	Euhedral
S64	Anhedral	Euhedral		Euhedral		
S68	Anhedral	Euhedral		Euhedral		
S69	Anhedral	Euhedral		Euhedral		
S75	Anhedral	Euhedral		Euhedral		

**Table 3.4:** Average experimental glass compositions

Run	S48	S50	S58
Oxidation <sup>1</sup>	CR	CR	CR
Quench <sup>2</sup>	1225°C	1100°C	1000°C
n	8	8	10
SiO <sub>2</sub>	49.64 ±0.04	50.7 ±0.1	42 ±0.5
TiO <sub>2</sub>	0.863 ±0.008	1.26 ±0.01	4.11 ±0.1
Al <sub>2</sub> O <sub>3</sub>	6.84 ±0.03	10 ±0.1	7.2 ±0.1
Cr <sub>2</sub> O <sub>3</sub>	0.397 ±0.01	0.1 ±0.01	0.008 ±0.004
FeO	21.38 ±0.04	20.21 ±0.07	30.9 ±0.6
MnO	0.569 ±0.007	0.516 ±0.007	0.6 ±0.01
MgO	9.68 ±0.03	3.42 ±0.04	0.28 ±0.02
CaO	9.47 ±0.01	12.02 ±0.01	11.06 ±0.04
Na <sub>2</sub> O	0.081 ±0.004	0.056 ±0.005	0.038 ±0.004
K <sub>2</sub> O	<MDL	<MDL	<MDL
P <sub>2</sub> O <sub>5</sub>	0.36 ±0.01	0.481 ±0.008	2.29 ±0.07
Total	99.28 ±0.06	98.8 ±0.1	98.53 ±0.07
Mg#	44.7 ±0.1	23.2 ±0.3	1.6 ±0.1

Run	S64	S68	S69	S75
Oxidation <sup>1</sup>	1200°C	1150°C	1200°C	1200°C
Quench <sup>2</sup>	1100°C	1100°C	1200°C	1100°C
n	9	5	8	8
SiO <sub>2</sub>	49.87 ±0.08	49.7 ±0.3	49.7 ±0.3	50.1 ±0.2
TiO <sub>2</sub>	1.33 ±0.01	1.29 ±0.03	0.99 ±0.01	1.35 ±0.01
Al <sub>2</sub> O <sub>3</sub>	10.75 ±0.03	10.6 ±0.2	7.95 ±0.07	10.83 ±0.06
V <sub>2</sub> O <sub>3</sub>				0.434 ±0.008
Cr <sub>2</sub> O <sub>3</sub>	0.051 ±0.009	0.037 ±0.006	0.134 ±0.007	0.05 ±0.007
FeO	20.6 ±0.07	20.4 ±0.1	21.3 ±0.1	20.08 ±0.07
NiO				0.016 ±0.002
MnO	0.495 ±0.008	0.495 ±0.003	0.557 ±0.003	0.484 ±0.005
MgO	3.41 ±0.02	3.81 ±0.05	7.98 ±0.07	3.68 ±0.03
CaO	12.12 ±0.02	12.18 ±0.02	10.82 ±0.03	11.81 ±0.02
Na <sub>2</sub> O	0.07 ±0.002	0.039 ±0.002	0.014 ±0.004	0.048 ±0.008
K <sub>2</sub> O	<MDL	<MDL	<MDL	<MDL
P <sub>2</sub> O <sub>5</sub>	0.488 ±0.008	0.57 ±0.01	0.39 ±0.009	0.58 ±0.02
Total	99.18 ±0.08	99.19 ±0.07	99.83 ±0.06	99.46 ±0.06
Mg#	22.8 ±0.1	25 ±0.3	40.1 ±0.4	24.6 ±0.2

<sup>1</sup> Purely reducing cooling rate experiments (non-hybrid experiments) did not have an oxidation event, so are labeled “CR.”

<sup>2</sup> All experiments were cooled at 1°C/hr and quenched on arrival at their quench temperature, except S69 that was held at 1200°C for ~24hrs.

**Table 3.5:** Representative olivine analyses

Run	S48		S50		S58			
Oxidation <sup>1</sup>	CR		CR		CR			
Quench <sup>2</sup>	1225°C		1100°C		1100°C		1000°C	
	Rim <sup>3</sup>		Core		Rim		Core	
							Rim	
SiO <sub>2</sub>	37.9		38.2		35.4		38.2	
TiO <sub>2</sub>	<MDL		<MDL		<MDL		0.03	
Al <sub>2</sub> O <sub>3</sub>	0.05		0.04		0.05		0.06	
Cr <sub>2</sub> O <sub>3</sub>	0.32		0.26		0.09		0.29	
FeO	27.6		20.6		39.3		23.5	
MnO	0.57		0.42		0.83		0.47	
MgO	33.7		40.7		25.9		38.1	
CaO	0.29		0.24		0.38		0.23	
Na <sub>2</sub> O	0.01		0.02		<MDL		0.01	
K <sub>2</sub> O	0.01		<MDL		<MDL		0.01	
P <sub>2</sub> O <sub>5</sub>	0.02		0.08		<MDL		0.03	
Total	100.4		100.6		101.9		100.9	
Mg#	68.5		77.8		54.0		74.3	

Run	S64		S68		S69		S75	
Oxidation <sup>1</sup>	1200°C		1150°C		1200°C		1200°C	
Quench <sup>2</sup>	1100°C		1100°C		1200°C		1100°C	
	Core		Rim		Core		Rim	
SiO <sub>2</sub>	38.5		36.2		38.1		36.1	
TiO <sub>2</sub>	0.02		0.05		<MDL		<MDL	
Al <sub>2</sub> O <sub>3</sub>	0.03		0.02		<MDL		0.04	
V <sub>2</sub> O <sub>3</sub>							0.17	
Cr <sub>2</sub> O <sub>3</sub>	0.26		0.04		0.25		0.14	
FeO	20.4		36.6		20.4		33.9	
NiO							0.77	
MnO	0.43		0.74		0.43		0.69	
MgO	40.4		27.0		40.8		28.5	
CaO	0.22		0.44		0.24		0.32	
Na <sub>2</sub> O	<MDL		<MDL		<MDL		<MDL	
K <sub>2</sub> O	<MDL		<MDL		<MDL		<MDL	
P <sub>2</sub> O <sub>5</sub>	0.18		0.02		0.08		0.06	
Total	100.4		101.2		100.3		99.8	
Mg#	77.9		56.8		78.1		60.0	

<sup>1</sup> Purely reducing cooling rate experiments (non-hybrid experiments) did not have an oxidation event, so are labeled "CR."

<sup>2</sup> All experiments were cooled at 1°C/hr and quenched on arrival at their quench temperature, except S69 that was held at 1200°C for ~24hrs.

<sup>3</sup> The core of S48 was never measured.

**Table 3.6:** Representative pyroxene analyses

Run	S50			S58		
Quench <sup>1</sup>	1100°C			1000°C		
Px <sup>3</sup>	High Mg#	Low Mg#	High Wo	High Mg#	Low Mg#	High Wo
SiO <sub>2</sub>	53.7	49.8	51.2	53.0	49.4	50.3
TiO <sub>2</sub>	0.16	0.25	0.31	0.09	1.10	0.55
Al <sub>2</sub> O <sub>3</sub>	0.81	1.25	1.58	0.59	1.77	3.02
Cr <sub>2</sub> O <sub>3</sub>	0.64	0.63	0.86	0.50	0.17	0.68
FeO	21.3	23.8	19.7	19.9	28.3	17.3
MnO	0.77	0.79	0.72	0.62	0.68	0.57
MgO	21.1	15.1	14.7	24.1	8.8	13.1
CaO	3.91	7.73	12.6	2.74	11.2	15.0
Na <sub>2</sub> O	0.02	0.02	<MDL	<MDL	<MDL	0.02
K <sub>2</sub> O	<MDL	0.02	<MDL	<MDL	0.007	<MDL
P <sub>2</sub> O <sub>5</sub>	<MDL	0.02	<MDL	<MDL	0.04	0.03
Total	102.4	99.4	101.6	101.6	101.3	100.7
En	58.8	44.5	42.2	64.8	26.9	39.0
Fs	33.3	39.2	31.7	30.0	48.5	28.9
Wo	7.8	16.3	26.0	5.3	24.5	32.1

Run	S64			S68		S69
Oxidation	1200°C			1150°C		1200°C
Quench <sup>1</sup>	1100°C			1100°C		1200°C
Px <sup>3</sup>	High Mg#	Low Mg#	High Wo	High Mg#	Low Mg#	Average
SiO <sub>2</sub>	53.2	52.0	50.9	52.2	50.7	52.8
TiO <sub>2</sub>	0.14	0.14	0.41	0.16	0.20	0.13
Al <sub>2</sub> O <sub>3</sub>	1.08	0.92	3.00	0.87	1.15	0.90
Cr <sub>2</sub> O <sub>3</sub>	0.57	0.34	0.77	0.80	0.52	0.66
FeO	18.5	21.2	17.6	19.9	22.9	18.9
MnO	0.64	0.69	0.61	0.64	0.75	0.61
MgO	25.1	19.4	16.7	21.8	17.4	23.5
CaO	2.79	6.49	11.0	3.17	5.96	2.47
Na <sub>2</sub> O	<MDL	<MDL	<MDL	<MDL	<MDL	<MDL
K <sub>2</sub> O	<MDL	<MDL	<MDL	<MDL	<MDL	<MDL
P <sub>2</sub> O <sub>5</sub>	0.02	0.02	<MDL	<MDL	0.02	0.02
Total	102.0	101.2	101.0	99.6	99.7	100.1
En	67.0	54.0	48.4	61.8	50.4	65.6
Fs	27.6	33.1	28.7	31.7	37.2	29.5
Wo	5.35	13.0	22.9	6.46	12.4	4.94

Run	S75		
Oxidation	1200°C		
Quench <sup>1</sup>	1100°C		
Px <sup>2</sup>	High Mg#	Low Mg#	High Wo
SiO <sub>2</sub>	51.2	50.1	49.7
TiO <sub>2</sub>	0.17	0.26	0.22
Al <sub>2</sub> O <sub>3</sub>	1.44	2.11	1.99
V <sub>2</sub> O <sub>3</sub>	0.90	1.53	1.57
Cr <sub>2</sub> O <sub>3</sub>	0.27	0.28	0.33
FeO	19.5	21.2	18.6
NiO	0.14	0.10	0.11
MnO	0.64	0.70	0.65
MgO	21.1	14.3	15.0
CaO	4.26	9.14	10.8
Na <sub>2</sub> O	<MDL	<MDL	<MDL
K <sub>2</sub> O	<MDL	<MDL	<MDL
P <sub>2</sub> O <sub>5</sub>	<MDL	0.02	<MDL
Total	99.7	99.7	99.0
En	60.1	43.6	45.1
Fs	31.2	36.3	31.4
Wo	8.73	20.1	23.5

<sup>†</sup> MDL stands for method detection limit.

<sup>1</sup> Quench temperature for each experiment in °C. All experiments were cooled at 1°C/hr and quenched on arrival at their quench temperature, except S69 that was held at 1200°C for ~24hrs.

<sup>2</sup> Representative analyses were picked from among the highest and lowest Mg# pyroxenes in each sample, as well as the highest Wo content pyroxene if it was different from the lowest Mg# pyroxene. No pyroxene was present in S48. Pyroxene chemical variation was under-constrained in samples S68, S69, and S75, so three representative pyroxene compositions were not always represented in the analytical dataset.

**Table 3.7:** Average experimentally produced oxide compositions

Run	S48	S50	S58 <sup>6</sup>
Oxidation <sup>1</sup>	CR	CR	CR
Quench <sup>2</sup>	1225	1100	1000
n	4	4	4
SiO <sub>2</sub>	0.1358 ±0.002	0.18 ±0.01	0.12 ±0.03
TiO <sub>2</sub>	1.24 ±0.02	1.41 ±0.02	51.62 ±0.19
Fe <sub>2</sub> O <sub>3</sub> <sup>3</sup>	1.32 ±0.16	0.67 ±0.05	1.71 ±0.11
Al <sub>2</sub> O <sub>3</sub>	6.33 ±0.04	6.42 ±0.09	0.22 ±0.03
Cr <sub>2</sub> O <sub>3</sub>	59.04 ±0.08	58.70 ±0.12	0.14 ±0.09
FeO	24.65 ±0.17	26.78 ±0.21	43.95 ±0.84
MnO	0.46 ±0.01	0.49 ±0.01	0.60 ±0.02
MgO	6.45 ±0.12	5.29 ±0.14	1.76 ±0.53
CaO	0.072 ±0.009	0.051 ±0.004	0.21 ±0.04
Na <sub>2</sub> O	0.019 ±0.007	0.016 ±0.002	0.026 ±0.004
K <sub>2</sub> O	<MDL	<MDL	<MDL
P <sub>2</sub> O <sub>5</sub>	0.014 ±0.009	<MDL	<MDL
Total	99.74 ±0.16	100.02 ±0.12	100.37 ±0.28
Mg# <sup>4</sup>	30.8 ±0.4	25.6 ±0.6	6.4 ±1.9
Chr <sup>5</sup>	83.34 ±0.09	82.72 ±0.11	
Ulvö <sup>5</sup>	3.33 ±0.06	3.78 ±0.07	
Spn <sup>5</sup>	13.33 ±0.08	13.50 ±0.17	

Run	S64	S68	S69 <sup>2</sup>	S75
Oxidation <sup>1</sup>	1200	1150	1200	1200
Quench <sup>2</sup>	1100	1100	1200	1100
n	8	4	6	8
SiO <sub>2</sub>	0.19 ±0.02	0.27 ±0.06	0.135 ±0.008	0.090 ±0.005
TiO <sub>2</sub>	1.38 ±0.08	1.89 ±0.19	1.47 ±0.07	1.80 ±0.10
Fe <sub>2</sub> O <sub>3</sub> <sup>3</sup>	4.93 ±0.27	4.5 ±0.6	5.38 ±0.22	4.1 ±0.3
Al <sub>2</sub> O <sub>3</sub>	7.50 ±0.49	9.4 ±1.1	7.01 ±0.13	4.64 ±0.09
V <sub>2</sub> O <sub>3</sub>				24.8 ±0.73
Cr <sub>2</sub> O <sub>3</sub>	52.7 ±1.1	47.7 ±2.4	52.9 ±0.5	32.1 ±1.3
FeO	27.0 ±0.3	28.4 ±1.3	25.30 ±0.18	28.7 ±0.5
NiO				0.145 ±0.005
MnO	0.494 ±0.003	0.590 ±0.005	0.602 ±0.003	0.537 ±0.009
MgO	5.21 ±0.07	4.7 ±0.8	5.99 ±0.19	3.95 ±0.25
CaO	0.11 ±0.02	0.21 ±0.03	0.136 ±0.026	0.072 ±0.019
Na <sub>2</sub> O	<MDL	<MDL	<MDL	<MDL
K <sub>2</sub> O	<MDL	<MDL	<MDL	<MDL
P <sub>2</sub> O <sub>5</sub>	<MDL	<MDL	<MDL	<MDL
Total	99.56 ±0.17	97.71 ±0.33	98.91 ±0.35	100.97 ±0.28
Mg# <sup>4</sup>	22.8 ±0.4	20.6 ±3.7	26.2 ±0.8	17.9 ±1.2
Chr <sup>5</sup>	79.2 ±1.4	73.1 ±3.2	80.0 ±0.4	75.4 ±0.9
Ulvö <sup>5</sup>	4.0 ±0.2	5.5 ±0.6	4.23 ±0.18	8.2 ±0.7
Spn <sup>5</sup>	16.8 ±1.2	21.4 ±2.6	15.81 ±0.29	16.35 ±0.25

<sup>†</sup> MDL stands for method detection limit.

<sup>1</sup> Temperature of oxidation for hybrid experiments in °C. Purely reducing cooling rate experiments (non-hybrid experiments) did not have an oxidation event, so are labeled “CR.”

<sup>2</sup> Quench temperature for each experiment in °C. All experiments were cooled at 1°C/hr and quenched on arrival at their quench temperature, except S69 that was held at 1200°C for ~24hrs.

<sup>3</sup> Fe<sub>2</sub>O<sub>3</sub> was calculated from mineral stoichiometry.

<sup>4</sup> Mg# was calculated as molar 100 \* Mg / (Mg + Fe<sub>T</sub>), where Fe<sub>T</sub> is the total iron.

<sup>5</sup> Chromite (Chr), ulvöspinel (Ulvö), and spinel (Spn) fractions were calculated based on the molar ratios Chr = 100 \* Cr / (Cr + 2Ti + Al), Ulvö = 100 \* 2Ti / (Cr + 2Ti + Al), Spn = 100 \* Al / (Cr + 2Ti + Al).

<sup>6</sup> S58 produced solely ilmenite, rather than a spinel. All other samples produced spinel as the sole stable oxide.

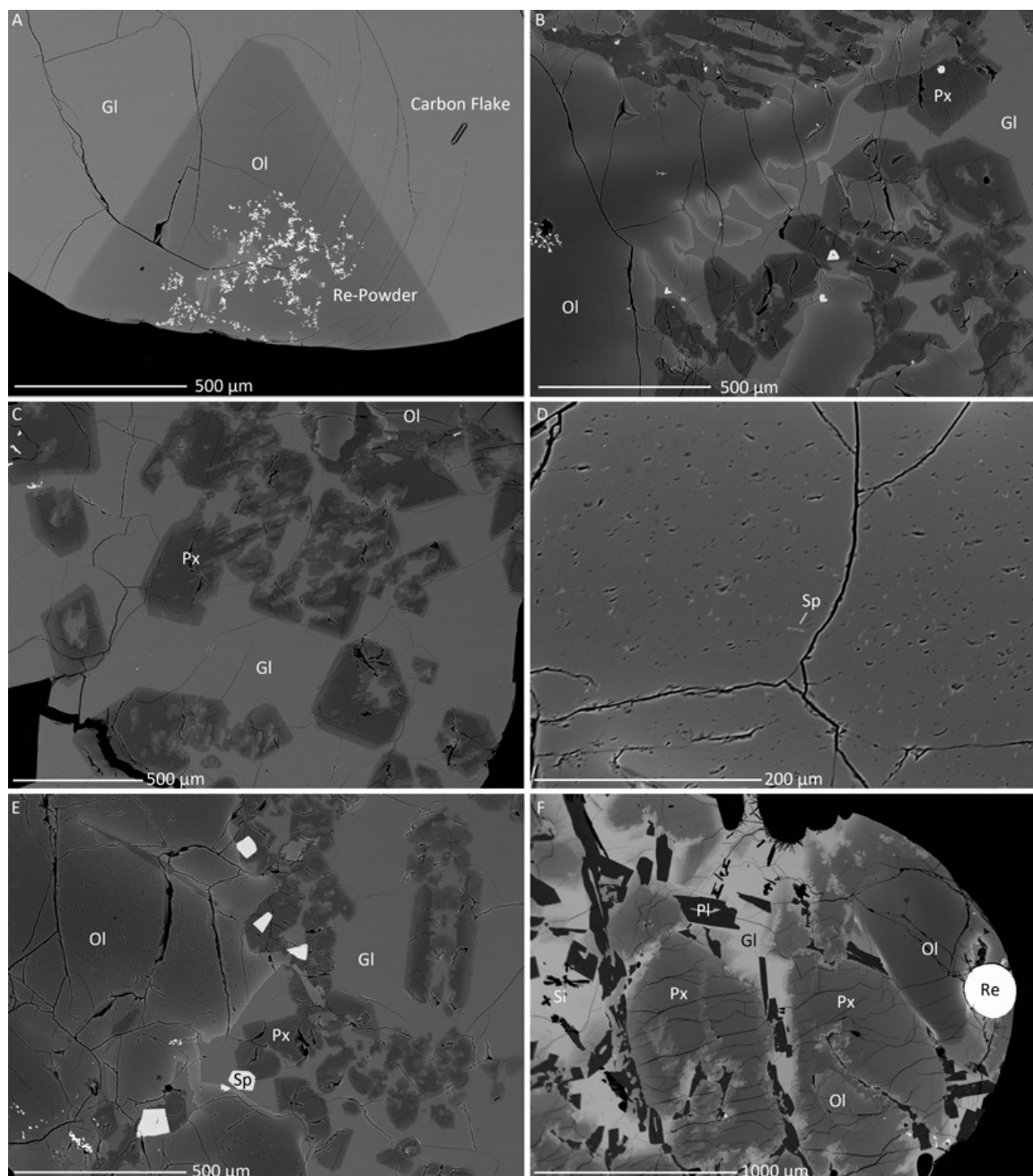


**Figure 3.1:** Backscatter electron images of typical mineral textures. A) Euhedral olivine in S48, one of the cooling rate experiments. B) Anhedral olivine in S64, one of the hybrid oxygen fugacity cooling rate experiments. C) Patchy pyroxene in S64. This particular image happens to catch the equant cross sections of the typically elongate pyroxene grains seen. D) Spinel grains visible in olivine rims of S75, the hybrid experiment with the doped synthetic composition. Although more common in S75, due to the presence of V in the sample, similar spinel grains were observed in the other hybrid experiments. The exsolved spinel in olivine rims is morphologically different from the spinel in the glass, appearing as elongate rather than equant grains. E) Spinel grains along olivine margins in S75. F) Plagioclase and a silica polymorph in S58. Although both grains appear dark, the

silica phase has finer grains and appears to be twinned. Silica is also concentrated around vesicle margins.

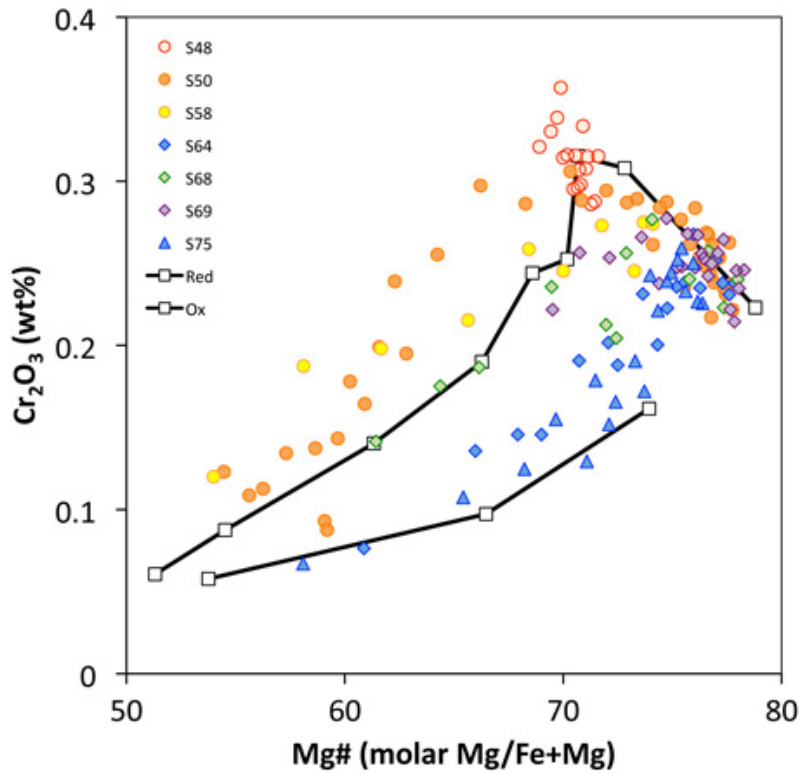


**Figure 3.2:** Cr<sub>2</sub>O<sub>3</sub> vs Mg# for olivine profiles from Tissint experiments. Olivine compositions from the isothermal experiments of Castle and Herd (2017) are shown for reference (black squares), with the upper curve being reducing and the lower curve oxidizing conditions. Circles represent cooling rate experiments performed under reducing conditions (S48: 1375-1225°C, S50: 1375-1100°C, S58:1375-1000°C; Castle and Herd, 2017). Diamonds represent hybrid experiments (S64 was previously reported in Castle and Herd, 2017). The triangles are S75, the repeat of the original hybrid experiment (S64) with the doped synthetic composition. Each data point represents the average of three adjacent points, sorted by Mg#, to help minimize analytical scatter.

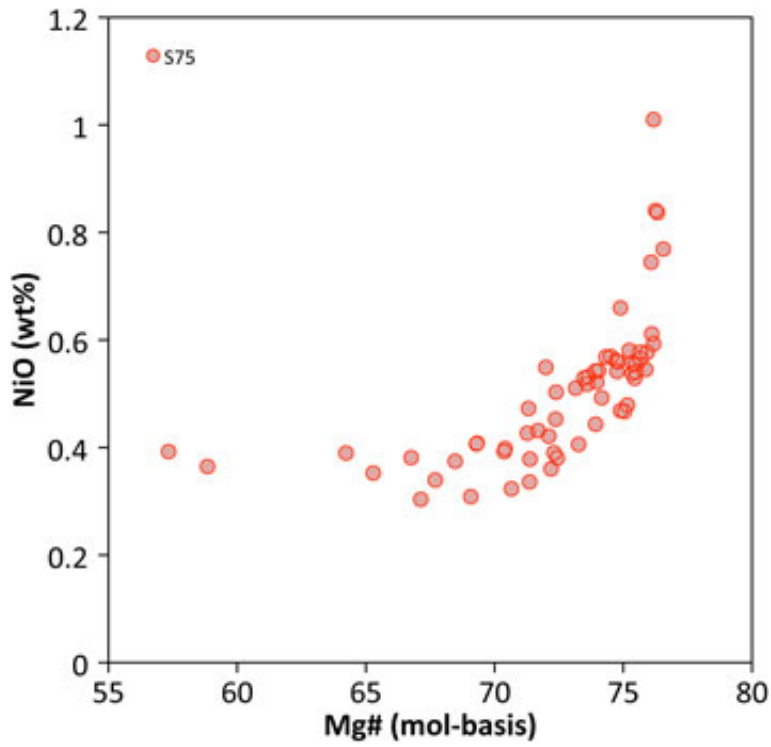


**Figure 3.3:** Variation between Ni content and Mg# in S75 olivine. The rapid drop in Ni out from the core of olivine is consistent with typical compatible element behavior. Analytical error estimates based on counting statistics are smaller than points shown. No averaging has been performed.

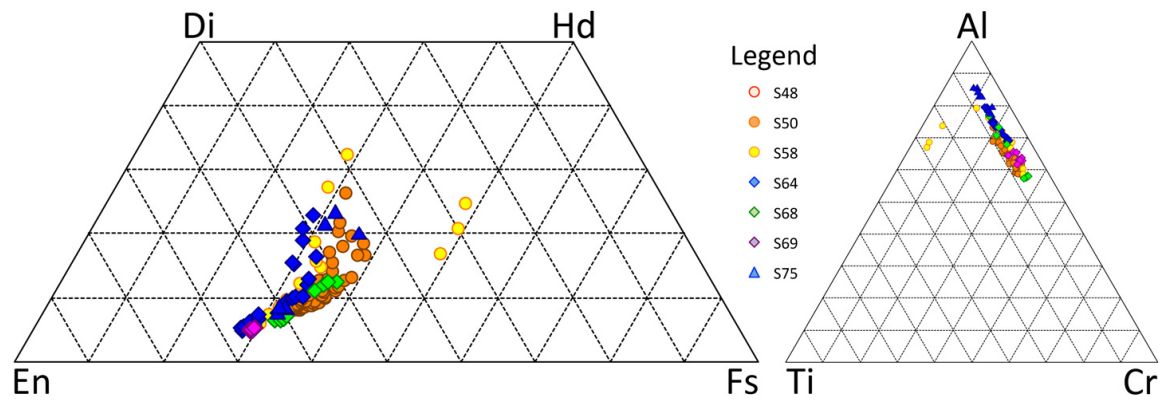


**Figure 3.4:** Pyroxene compositional range from reducing (circles) and hybrid (diamond) cooling rate experiments (S75, triangles). The range is relatively limited, and mostly temperature dependent.

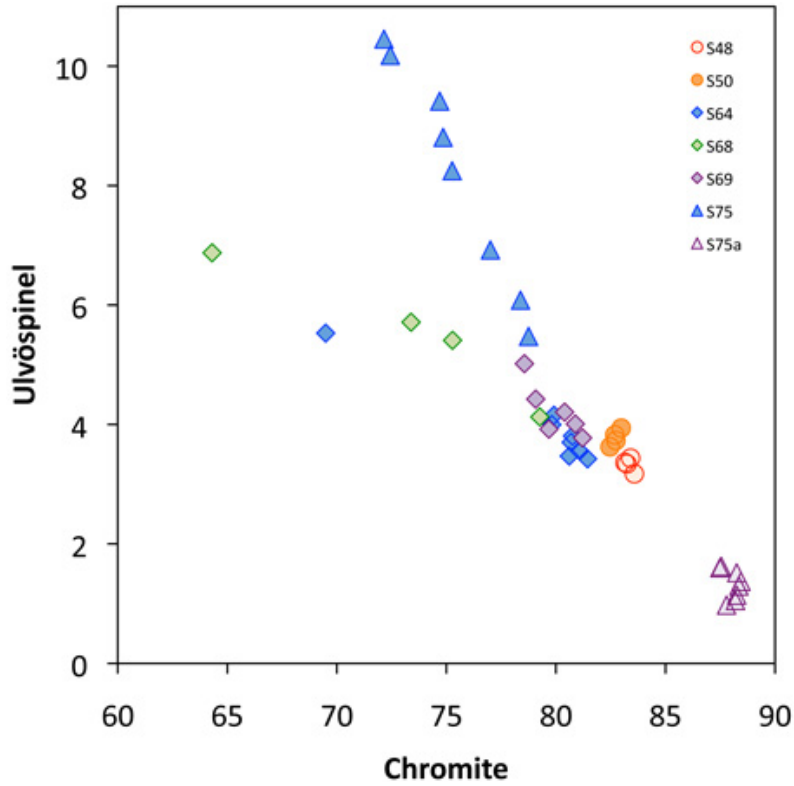


**Figure 3.5:** Spinel compositional range from reducing (circles) and hybrid (diamonds) cooling rate experiments. Chromite was calculated as molar  $\text{Cr} / (\text{Ti}/2 + \text{Cr} + \text{Al})$  and ulvöspinel was calculated as molar  $\text{Ti}/2 / (\text{Ti}/2 + \text{Cr} + \text{Al})$ , both shown in percent. In the case of S75 (triangles) the fractions were calculated both neglecting V (S75) and incorporating V as though it were Cr (S75a); neglecting V fails to account for  $\sim 1/3$  of the total cations in the spinel.

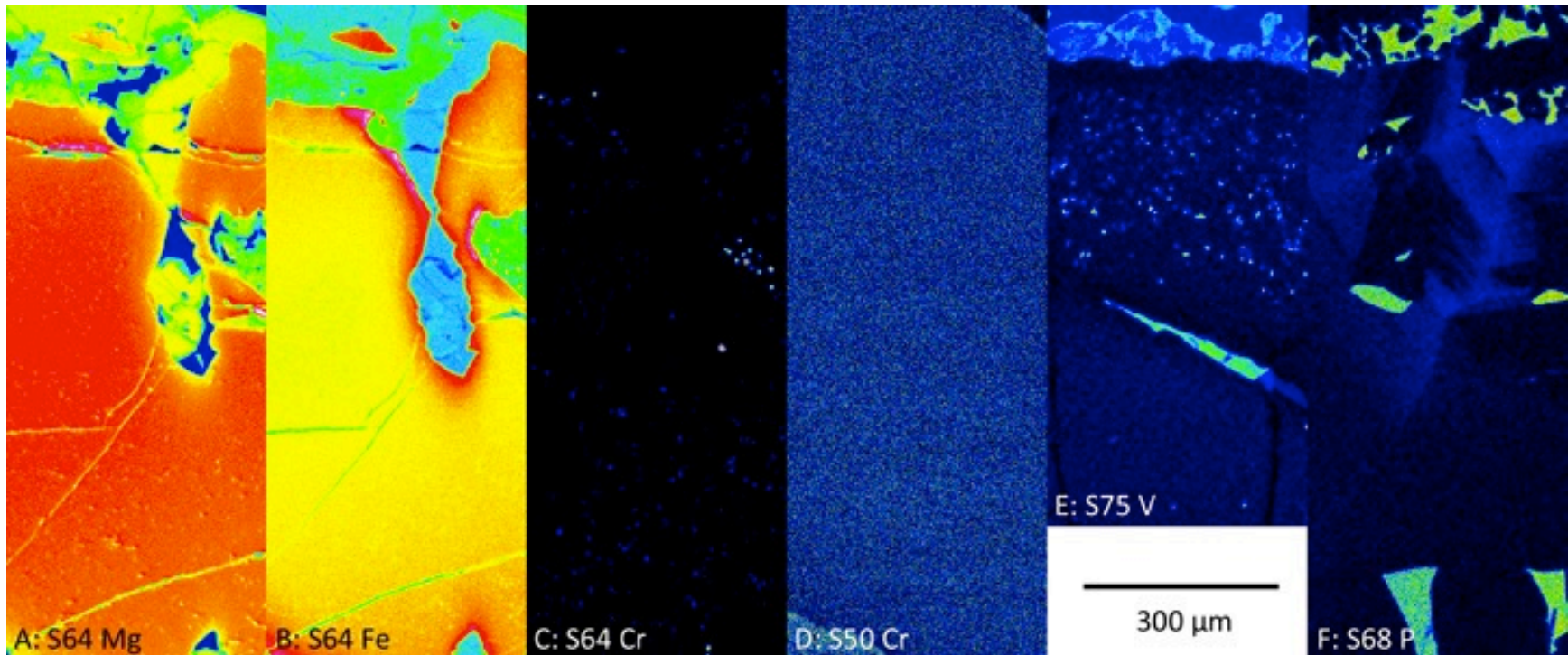


**Figure 3.6:** Selected x-ray maps of olivines from hybrid and reducing cooling rate experiments. A) Mg map of S64 olivine, showing a decrease from core to rim. B) Fe map of S64 olivine (the same location as A,C), showing an increase from core to rim. C) Cr map of S64 olivine (the same location as A,B). The brightest spots are chromites in the glass, but the blue spots located throughout the olivine grain are small (<1  $\mu\text{m}$ ) spinel grains exsolved from olivine. D) Cr map of S50, the reducing cooling rate experiment over the same temperature range as most of the hybrid experiments (1375-1100°C). Note the lack of higher-concentration regions, indicating a uniformity of Cr in the olivine profile. The olivine rim is in the lower left corner of the figure; the core is in the upper right. E) V map of S75. Bright spots are spinel grains (2-10  $\mu\text{m}$ , elongate) exsolved from the olivine rim. The rim is the upper half, the core is the lower half; the bright margin at the top is a mixture of pyroxene and glass. F) P map of S68 olivine showing feathered zoning. Variations in P concentration do not vary with any other element. See Appendix 2 for the full set of x-ray maps for both hybrid and reducing cooling rate experiments.

## **Chapter 4: Partial Melting of the Zoned Eucrite Northwest Africa 7035: Implications for Eucrite Petrogenesis**

### **4.1 Introduction**

The howardite, eucrite, and diogenite (HED) meteorite suite is a group of related achondrite meteorite types. Diogenites are ultramafic rocks, ranging from orthopyroxenites to dunites (e.g. Beck and McSween Jr, 2010), and are typically interpreted as either early cumulates from the eucritic source magmas (e.g. Fowler et al., 1994; Fowler et al., 1995; Shearer et al., 1997), or the mantle residuum remaining after eucrite extraction (e.g. Stolper, 1975, 1977). Eucrites are basalts and gabbros, and are believed to represent the crust of a differentiated asteroid (e.g. Duke and Silver, 1967). Howardites are impact breccias composed of a mixture of eucrites and diogenites, often with additional xenolithic material (e.g. CM chondrite fragments or meteoritic iron). Some howardites are samples of regolith of the HED parent body, preserving evidence of interaction with the solar wind (Warren et al., 2009), but all are commonly believed to represent the impact breccia on the outermost portion of the body (e.g. Fuhrman et al., 1982). The HED parent body is widely assumed to be the asteroid 4 Vesta, based on reflectance spectroscopy from both ground-based (Larson and Fink, 1975; McCord et al., 1970) and orbital observations (De Sanctis et al., 2012).

The focus of this study is the petrogenesis of eucrite basalts, particularly with regard to complications from the range of chemical compositions they represent. Eucrites are defined as igneous meteorites, with or without subsequent brecciation, composed primarily of a subequal mixture of low-Ca clinopyroxene (pigeonite) and anorthitic plagioclase (Duke and Silver, 1967). Most eucrites, commonly referred to as ‘typical’ eucrites, have undergone a degree of metamorphism that removed all evidence of chemical zonation in the pyroxene (Takeda and Graham, 1991; Yamaguchi et al., 1996). Typical eucrites are divided into two groups, the cumulate eucrites (CE) and the basaltic (sometimes referred to as “non-cumulate”) eucrites. In major-elements, cumulate eucrites appear complementary to the basaltic eucrites (Hewins and Newsom, 1988), however, the

high concentration of incompatible trace-elements (ITEs; e.g. Y, Ti, REEs) in cumulate eucrites suggests that they originate from different magma bodies (Pun et al., 1997), although the ITE content may also be the result of a trapped melt component masked by metamorphic re-equilibration (Treiman, 1996, 1997). There are three chemical types within the basaltic eucrites (e.g. Ahrens, 1970; Hewins and Newsom, 1988): the main group trend (MGT) which is the most common eucrite composition and is believed to represent the primitive eucritic magma (Ruzicka et al., 1997), typified by the composition of the Juvinas eucrite (e.g. Barrat et al., 2007); the Nuevo Laredo trend (NLT), named for the Nuevo Laredo eucrite, which is a ferroan extension of the MGT and is believed to represent magmas fractionated from the MGT (Stolper, 1977); and the Stannern trend (ST), named for the Stannern eucrite, which is enriched in ITEs but has a major-element composition indistinguishable from the MGT. There is a modern consensus that both eucrites and diogenites result from the crystallization of a magma ocean on the HED parent body (Grove and Bartels, 1992; Mandler and Elkins-Tanton, 2013; Righter and Drake, 1997) and that most were metamorphosed as a result of slow cooling (Takeda and Graham, 1991; Yamaguchi et al., 1996). The metamorphic overprinting, along with the potential to incorporate trapped magma into the metamorphosed mineral compositions (Pun and Papike, 1995, 1996; Pun et al., 1997; Treiman, 1996, 1997), makes it difficult to trace the igneous evolution of the eucrites.

One of the major unresolved questions is how the ST eucrites are related to the MGT (Mittlefehldt and Lindstrom, 2003). It is difficult to generate an ITE enrichment in a magma body without also altering the major-element composition of the melt, which is exactly what needs to have happened to generate the ST from a MGT composition magma ocean. One plausible explanation of the ITE enrichment is heterogeneity of the source magma, but studies of the geochemical and isotopic homogeneity of eucrites conflict with this idea (Wiechert et al., 2004). To date, the most successful model for the origin of the ST is that increasing degrees of ITE enrichment are the result of incorporation of progressively larger amounts of a low-degree partial melt from a preexisting eucritic crust (Barrat et al., 2007). A primary goal of this study is to test this model using experimental petrology methods.

Northwest Africa (NWA) 7035, the main sample studied and presented here, is one of several known examples of a eucrite with zoned pyroxenes (referred to here as ‘zoned eucrites,’ and elsewhere as ‘unequilibrated eucrites’). Other zoned eucrites include Pasamonte (e.g. Miyamoto et al., 1985) and a number of the Yamato meteorites (e.g. Y-74159, Y-74450, and Y75011; Pun and Papike, 1996), and are most frequently described as small (<1 cm) lithic fragments in polymict breccias. Zoned eucrites are divided into three chemical trends based on chemical zoning in pyroxene (Miyamoto et al., 1985; Pun and Papike, 1996; Takeda and Graham, 1991; Takeda et al., 1983): the Ca-Fe-Mg trend, also referred to as the Pasamonte trend, where the pyroxene increases substantially in Wo as it decreases in Mg#; the Fe-Mg trend where, although there is a progressive enrichment in Wo, the dominant zoning is a progressive decrease in Mg#; and the Fe-Ca trend that approximates the exsolution trend of a typical eucrite with low Wo cores and high Wo rims. Some zoned eucrites exhibit evidence of metasomatization, where progressive alteration from a Ca-Fe-Mg-rich fluid (magmatic or aqueous) creates Fe-rich rims around cracks in pyroxene at low degrees of alteration (Barrat et al., 2011); higher degrees of this alteration can result in fayalite veins with minor troilite, secondary anorthite inclusions in Fe-rich veins, and even reverse zoning in pyroxenes where Fe-rich cores zone to more magnesian rims (Barrat et al., 2011; Mittlefehldt and Lindstrom, 1997; Roszjar et al., 2011; Takeda et al., 1994; Takeda et al., 1983; Treiman and Drake, 1985).

To understand some of the complexities of igneous processes on the HED parent body, experiments on unaltered samples of eucritic crust are warranted. Typical eucrites, although ubiquitous as meteoritic samples, are the products of extensive metamorphism (Takeda and Graham, 1991; Yamaguchi et al., 1996), and as such are unlikely to be samples that interacted with the early stages of evolution of a magma ocean. A zoned eucrite, NWA 7035, was selected for study because it is representative of what we might expect from a lava flow that was once part of the primitive eucritic crust of the HED parent body. Having escaped extensive reheating or metamorphism, NWA 7035 has preserved the geochemical record of its petrogenesis. Further, NWA 7035 has not been modified by metasomatism, or terrestrial weathering, and, although the meteorite is classified as monomict (Ruzicka et al., 2014), the sample obtained for study shows no

evidence of brecciation, making NWA 7035 one of the most pristine, unaltered, igneous samples yet obtained from the HED parent body.

Using typical eucrites, rather than zoned eucrites, to generate partial melts is unlikely to result in a partial melt that can generate the incompatible trace-element enrichment required without altering other chemical systems. A major difference between typical and zoned eucrites is that the trace-element content of typical eucrites is redistributed across the sample by metamorphism (Treiman, 1996, 1997), whereas in zoned eucrites it is likely to be concentrated in the mesostasis. Even though a low degree partial melt from a typical eucrite is likely to be less ferroan than the same degree partial melt from a zoned eucrite, the lower ITE concentration of the melt from a typical eucrite would require a higher fraction of the partial melt to generate the ITE enrichment of the ST, making it more likely that other chemical components would be disturbed by mixing a partial melt from a typical eucrite.

## 4.2 Methods

Experiments were performed in 1-bar GERO vertical-tube gas-mixing furnaces at the High Temperature Planetary Petrology Laboratory at the University of Alberta (UAlberta). Redox conditions were controlled with a CO-CO<sub>2</sub> gas mixture monitored in the effluent and calibrated using a zirconia cell suspended in a remote DelTech reference furnace at constant temperature. Redox potential of the zirconia cell was calculated using the Gas.Bas program (Jurewicz et al., 1993) which uses the Nernst equation to calculate the oxygen fugacity. Oxygen fugacity was calculated relative to the iron-wüstite buffer of O'Neill (1988) to be IW-1, that is one log unit below the iron-wüstite oxygen buffer; highly reducing conditions were used as some eucrites contain metal in igneous assemblages (see Mittlefehldt, 2015 for additional discussion). Experimental charges consisted of tiles cut from a polished slab of the NWA 7035 eucrite (University of Alberta Meteorite Collection specimen MET11633/1) and individually massed at between 161.8 and 137.1 mg each. Tile size was chosen to be larger than the typical pyroxene grain size in an attempt to capture the range of compositions in NWA 7035 in each tile. Cutting was done using a Buehler IsoMet low speed saw with a Buehler IsoMet

20HC wafering blade dedicated to use with achondrites; cuts were performed dry to enable collection of the tailings for bulk chemical analysis. Samples were suspended in furnaces by Re-wire to minimize Fe loss, similar to the method of Borisov and Jones (1999); samples were held to the sample assembly by wire wrapping. All experiments were performed isothermally, and all but one sample were held at temperature for 1 week; the exception was a 24 hr experiment performed to assess the effect of experimental duration (Table 4.1).

A single thin section of NWA 7035 from the type specimen was obtained for description and analysis. Initial backscatter electron (BSE) imaging of this thin section was performed by electron microprobe analysis (EMPA) on the University of Washington JEOL 733 superprobe; further imaging was performed on the University of Alberta (UAlberta) JEOL 8900. Sample tiles were imaged on the Zeiss Sigma 300 VP field emission scanning electron microscope (SEM) at UAlberta, operating in low-vacuum mode (which obviates the need for carbon coating) before use in partial melting experiments. Samples recovered from partial melting experiments were embedded in epoxy, sectioned, and analyzed by EMPA on the UAlberta JEOL 8900. Chemical analyses on thin sections and experimental run products were carried out on olivine (Ol), pyroxene (Px), spinel (Sp), ilmenite (Ilm), and glass (Gl). Calibration was performed using well-characterized standards. Elemental analysis included: Si, Ti, Al, Cr, Fe, Mn, Mg, Ca, Na, K, P, and S; a subset of pyroxenes and experimental glasses were also analyzed for V, Ni, and Zr. Glass analyses were performed using a 5-10  $\mu\text{m}$  beam diameter, otherwise a focused ( $< 1 \mu\text{m}$ ) beam was utilized. All analyses were performed using an accelerating voltage of 20 kV and a beam current of 20 nA. Elements were analyzed for 60 sec on peak and 30 sec each for high and low backgrounds; in one series, P was counted on two spectrometers, effectively doubling the count time.

The bulk composition of NWA 7035 was determined using inductively coupled plasma mass spectrometry (ICP-MS) at UAlberta using a Perkin Elmers Elan 6000 dual sector mass spectrometer in dual detector mode. The bulk powder analyzed was a mixture of 283.0 mg of cutting tailings from generating experimental tiles and 206.3 mg of crushed sample tiles, both combined and ground under acetone in an agate mortar and pestle. Two roughly 200 mg splits were each progressively digested in a heated (130°C)

mixture of HF and HNO<sub>3</sub>, then HCl and HNO<sub>3</sub>, and finally placed in solution with concentrated HNO<sub>3</sub>. The acid suspended sample was diluted with DI H<sub>2</sub>O for analysis (1.0 mL sample solution, 0.1 mL conc. HNO<sub>3</sub>, 0.1 mL internal standard solution, 8.8 mL DI H<sub>2</sub>O). All acids utilized were trace metal grade. Instrument flow rate was approximately 1 mL/min. Measurements were performed with 35 sweeps per reading, and repeated 3 times per split. Dwell times were 10 ms for Na, K, Cu, Zn, and Sr, and 20 ms for the remainder. In, Bi, and Sc were used as internal standards. The ICP RF power was 1300 W. Blanks were subtracted after the internal standard correction. 4 point calibration curves were used (0, 0.25, 0.50, and 1.00 ppm for Na, Ca, Mg, Fe, K, and P; 0, 0.005, 0.010, and 0.020 ppm for the other elements). Typical count rates for the method utilized are between 150,000 and 200,000 cps for 10 ppb Pb. The USGS reference material GSP-2 was used as a secondary standard.

In-situ analysis of glass and mineral trace-element compositions were performed using laser ablation sourced ICP-MS (LA-ICP-MS). Samples were ablated using a NuWave UP-213 Nd:YAG laser using either a 40 or 30  $\mu\text{m}$  spot size; the smaller spot size was only used for the lower temperature experiments where melt glass pockets were small. A 5 Hz pulse rate at 80% power resulted in a fluence of approximately 8 J/cm<sup>2</sup> for the 40  $\mu\text{m}$  spot size (14 J/cm<sup>2</sup> for 30  $\mu\text{m}$ ). Ablated material was passed through an Ar ICP using He as a carrier gas, running at 0.5 L/min with 4 mL/min N<sub>2</sub> gas added to improve analytical sensitivity. Mass analysis was performed using an iCAP Q quadrupole mass spectrometer from Thermo Scientific. Data reduction was performed using Iolite V 3.4. Mass numbers for analyzed elements are: Si (29), Ca (43), Sc (45), Ti (48 & 49), V (51), Cr (52), Co (59), Ni (60), Sr (88), Y (89), Zr (90), Nb (93), Mo (95), La (139), Ce (140), Pr (141), Nd (146), Sm (147), Eu (153), Gd (157), Tb (159), Dy (163), Ho (165), Er (166), Tm (169), Yb (172), Lu (175), and Hf (178 & 179). Count durations were approximately 30 sec/point. Calibration was performed using NIST SRM 614 and checked using NIST SRM 612. Each set of unknown analyses was bracketed by NIST analyses (both 612 and 614) to monitor instrument drift. Both Si and Ca were used separately as internal standards and the resulting abundances are within reasonable agreement; Ca was used for the reported glass values. Reported errors in trace-element abundances are 2 standard errors.

Melt glass compositions were further vetted to remove analyses with evidence of significant mineral inclusion along with the glass composition. As the experimentally produced glass has a higher REE content than either the typical pyroxene or plagioclase analyzed in NWA 7035, this was accomplished by selecting the set of analyses with the highest REE content from the glass analyses in each experiment. A full list of the trace-element analyses can be found in Appendix 3; only the highest REE content glass analyses were utilized here.

Trace-element compositions of natural pyroxenes were reduced differently from the glass data. As Ca is highly variable in the measured pyroxenes, and further complicated by exsolution, using Ca as an internal standard would require either a model to estimate the pyroxene composition as a function of position, or a specific EMPA measurement of each individual LA-ICP-MS spot before trace-element analysis; both methods are likely to introduce systematic errors. To avoid the complications of Ca, Si was used as the internal standard. A consistent Si content (22.94 wt%) was used in the reduction of trace-element data for all pyroxene analyses. Although the Si atoms per formula unit (APFU) of the measured pyroxenes was nearly constant (1.96 APFU with a standard deviation of 0.016 APFU for 225 measured pyroxene compositions), the wt% Si does vary with composition, ranging between 24.8 and 21.3 wt%, which introduces a maximum systematic error of  $\pm 7.6\%$  (relative). This error will vary primarily with Mg#, and was neglected as it is small relative to the analytical uncertainty for the majority of compositions analyzed.

### **4.3 Results**

Northwest Africa 7035 is an igneous meteorite composed primarily of low-Ca clinopyroxene (pigeonite) with lesser amounts of anorthitic plagioclase and minor silica (Fig. 4.1). Pyroxene preserves extensive igneous zoning, spanning a range of En from higher than cumulate eucrites to lower than Nuevo Laredo trend basaltic eucrites (approximately En<sub>58</sub> to En<sub>27</sub> at low Wo content, respectively; Mayne et al., 2009), the range of the typical (that is, unzoned) eucrites (Fig. 1.13). Pyroxene grains have shallowly inclined extinction, consistent with pigeonite, and show a single exsolution

direction in each grain, likely (001) based on the direction of elongation although no work was performed to verify crystallographic direction. Exsolution was not apparent in BSE images of NWA 7035. Plagioclase grains are acicular and concentrated near pyroxene rims. Both plagioclase and the silica polymorph show mottled extinction under cross-polarized light, consistent with partial disruption during a shock event. Although none were present in either the experimental samples or the thin section, shock-melt veins were observed in the hand sample. There is no indication of terrestrial weathering in the samples of NWA 7035 obtained for study, in spite of it having been a desert find. Minor phases in NWA 7035 include fayalite, troilite, spinel, and ilmenite.

The chemical zoning pattern of pyroxenes in NWA 7035 is consistent with the Ca-Mg-Fe trend of zoned eucrites, sometimes referred to as the Pasamonte trend after the meteorite where it was first described (Fig. 4.2). Within Pasamonte, two pyroxene trends were observed, one where the trend peaks in Wo-content before the lowest Mg# compositions (type 1), and one where the Mg# trend halts as the sample increases in Wo content (type 2) (Miyamoto et al., 1985). Although both trends are commonly observed in Ca-Mg-Fe trend eucrites, only type 1 was observed in NWA 7035; this may be the result of the extensiveness of zoning in NWA 7035, which ends in the metastable pyroxferroite composition (with the resulting mineral breakdown texture) that is more ferroan than previously observed in zoned eucrites (e.g. Mayne et al., 2016; Pun and Papike, 1996). On the high Mg# end, NWA 7035 cores have an Mg# indistinguishable from Pasamonte, but less magnesian than many of the Yamato eucrites (Pun and Papike, 1996). There is a substantial variation in the relation between Mg# and Wo content from pyroxene grain to pyroxene grain, resulting in a wide scatter in the core-to-rim profiles of pyroxenes in the meteorite. NWA 7035 shows no evidence of the metasomatism common to zoned eucrites.

Of the seven partial melting experiments, discernable melt glass was observed in all but one (Table 4.1). Melt was observed in the lowest temperature experiment (1000°C), albeit restricted to regions with a specific mineralogy, and in very low amounts; melt was not observed in the next higher temperature experiment (1010°C) likely due to NWA 7035's mineralogical heterogeneity and the low degree of melting

achieved. Representative mineral major- and trace-element compositions were determined for comparison with melt glass compositions (Tables 4.2 and 4.3).

The whole-rock trace-element composition of NWA 7035 was determined by solution ICPMS for comparison with melt glass compositions and to aid in classifying NWA 7035 relative to more typical eucrites (Table 4.4). In terms of CI-normalized REE content, the bulk composition of NWA 7035 is intermediate between the Juvinas and Stannern bulk compositions, and nearly identical to Nuevo Laredo (Barrat et al., 2007); NWA 7035 has a higher Sc content than Nuevo Laredo, consistent with the more ferroan pyroxene composition (and likely trapped glass component) of the most evolved portions of NWA 7035.

A coherent sequence of events in the melting process can be inferred from petrography of the melting experiments. Melt initiates in regions that contain mixtures of fayalite, plagioclase, silica, and pyroxene (Fig. 4.3a), and may involve oxide phases (spinel and ilmenite). Of the silicate phases, fayalite is the first phase to become largely absent from experiments with increasing temperature, not being observed in the 1060°C sample (E). Oxide phases are difficult to track, as large (>10  $\mu\text{m}$ ) inclusions are uncommon in NWA 7035, but both ilmenite and spinel were observed in an anomalously oxide-rich area of melt in the 1020°C experiment (F); their absence in higher temperature experiments may either be due to melting or their relative scarcity. Oxides are not critical to melt generation as an anomalously oxide-rich region of the 1000°C experiment (A) does not show evidence of melt glass. Even the lowest-temperature experiments show evidence of melt infiltration into plagioclase and silica laths, resulting in a speckled texture in BSE images (e.g. Fig. 4.3a, b, and d). As the melt fraction increases, and melt pockets become interconnected, plagioclase laths break up into small crystals that scatter into the melt (Fig. 4.3b). Silica laths similarly break up into smaller euhedral crystals, but at a coarser scale than the plagioclase. Plagioclase is present in both of the highest temperature melting experiments (1100°C, C & G), but silica is absent in the longer duration experiment (G). In all experiments, there is evidence of melt infiltration into pyroxene grains along cracks (Fig. 4.3c), and there is some evidence of melt infiltration along crystallographic surfaces. At all temperatures, there is evidence that pyroxene has been modified by interaction with the melt, resulting in a substantially more

homogeneous and ferroan composition away from areas of melting; this melt infiltration can also be seen as wetting of the interfaces between pyroxene and plagioclase at low temperature (Fig. 4.3d).

Fayalite occurs in two different assemblages in NWA 7035. The most common occurrence is in pyroxferroite, or metastable ferri-pigeonite, breakdown textures as part of the fine-grained intergrowth of fayalite, silica, and augite (Fig. 4.4b). Coarser fayalite is also present in a high-Fe mesostasis near pyroxene rims, where it is intergrown with pyroxene, plagioclase, silica, and spinel (Fig. 4.4a). The fayalite in these two occurrences is likely to be chemically different: the fayalite resulting from breakdown of the metastable phase would inherit its composition from the phase from which it crystallized; the fayalite formed in the mesostasis is likely to inherit the ITE content of any trapped melt (e.g. Treiman, 1996, 1997). The fayalite formed from mineral breakdown is too fine-grained to analyze by EMPA, and both were too fine-grained to be analyzed for trace-elements by LA-ICP-MS, so, although theoretically reasonable, the expected difference in fayalite composition could not be experimentally verified.

The petrography of NWA 7035 was significantly modified by the heating experiments, as can be seen in the example of variation in fayalite textures. Although rarely present as coarse grains ( $>10\ \mu\text{m}$ ) in the natural sample, fayalite is present as moderate to coarse grains in areas associated with the first melts (see Fig. 4.1, 4.3-4.4). A plausible explanation for the occurrence of coarser fayalite in the experimentally heated samples is that fayalite, whether from metastable mineral breakdown or from the mesostasis, coarsens over the course of experimental heating; alternatively, a fayalite-rich assemblage may not have been imaged due to sample heterogeneity, although this possibility seems unlikely given the extensive imaging of samples pre-heating.

The rare earth element content of all partial melts is substantially higher than the bulk composition of Stannern (Barrat et al., 2007), allowing for the possibility that the incompatible trace-element enrichment of the Stannern Trend may be caused by incorporation of partial melts of pre-existing eucritic crust (Fig. 4.5).

#### **4.4 Discussion**

#### *4.4.1 Major-element geochemical description of melting*

To a first order, the progressive increase of melting can be visualized as a sequential removal of pyroxene zoning as the melt incorporates the pyroxene from rim to core. Visually, this can be demonstrated by plotting the Ca-Mg-Fe content of the melt on a pyroxene quadrilateral along with the remaining zoned pyroxene compositions (Fig. 4.6a). The melt composition starts equivalent to a very high Fe pyroxene in the augite stability field; as melting progresses the composition becomes somewhat more calcic, but the principal progression is to higher Mg#. Complementary to the liquid trend, the remnant pyroxene zoning halts at progressively higher Mg# with increasing degree of partial melting. Unlike the profiles measured in the thin section, pyroxene profiles from experimental charges show a linear trend on the pyroxene quadrilateral with a constant slope increase in Wo with decreasing Mg#; the variability of the Wo component seems to be concentrated in the rim of the pyroxenes, proximal to where they contact the liquid. This may be explained by a preferential melting of the high-Ca end member of the pigeonite exsolution, as suggested by the gradual increase in the liquid Ca content, despite the general trend of the pyroxene profiles decreasing in Ca content towards pyroxene cores. In terms of the minor-elements, the progression of the melt composition towards higher Al content, rather than towards higher Cr content like the zoning in pyroxene cores, shows the involvement of plagioclase. The minor-element ternary diagram (Fig. 4.6b) also demonstrates that there is not a significant involvement of oxides: if spinel or ilmenite were involved in the early melting, we would expect a higher Ti abundance over Al; further, spinel involvement should result in a significant Cr abundance; however, the liquid plots along the Ti-Al join at all degrees of melting (Fig. 4.6b).

The CIPW norm shows a melt progression consistent with our inferences from petrography (Cross et al., 1902; Pruseth, 2009a, b). At all stages of melting pyroxene (the sum of hypersthene and diopside from the norm) dominates the liquid composition, but the fraction of pyroxene involved is the highest in the lowest degrees of melting (Fig. 4.7). From petrography, it is apparent that both fayalite and silica are involved in the earliest melt, however, the initial melting appears to involve both in a ratio

stoichiometrically equivalent to pyroxene. The norm shows that even at the lowest degree of melting some plagioclase is involved. The normative fraction of plagioclase increases, relative to pyroxene, as the total fraction of melt increases; similarly, the total fraction of silica (quartz) in the norm increases with increased melting. The norm shows a decreasing ratio of clinopyroxene to orthopyroxene as melt fraction increases, consistent with both the progressive melting of pyroxene zones and a preferential incorporation of the high-Ca member of the pyroxene exsolution in early stages of melting. The norm calculates an ilmenite component to the melt, apparently contradicting our earlier inference that oxides are largely absent from the melt; however, the fraction is small (6.7% at highest), and can mostly be accounted for by the Ti component of both natural pyroxene and plagioclase.

To examine the validity and applicability of our experiments, we compared our results with existing projections from crystallization experiments performed on typical eucrites. Stolper (1975, 1977) projected the evolution of a fractionating eucritic melt, based on either equilibrium or fractional crystallization, by determining the phase diagram for eucrite magmas. The phase relationships he determined should still apply, whether the system reaches equilibrium or not. As the Stolper experiments are the theoretical reverse of our melting experiments, our results should plot backwards along these projections towards the parental melt composition (Fig. 4.8). To help visualize the system, Stolper (1975, 1977) employed a variant of the CIPW norm as follows (all in molar units): Silica ( $\text{SiO}_2 - 0.5*[\text{FeO} + \text{MgO} + \text{MnO}] - 5*[\text{Na}_2\text{O} + \text{K}_2\text{O}] - \text{Al}_2\text{O}_3 - \text{CaO}$ ); Anorthite ( $\text{Al}_2\text{O}_3 - \text{Na}_2\text{O} - \text{K}_2\text{O}$ ); Fayalite ( $0.5*[\text{FeO} + \text{MnO}]$ ); Forsterite ( $0.5*\text{MgO}$ ); Wollastonite ( $\text{CaO} + \text{K}_2\text{O} + \text{Na}_2\text{O} - \text{Al}_2\text{O}_3$ ); Albite ( $2*\text{Na}_2\text{O}$ ); Orthoclase ( $2*\text{K}_2\text{O}$ ). On the silica, forsterite, fayalite projection, the melt glass compositions plot along an extension of Stolper's projected fractionation curve for a silica-saturated system, suggesting that our melt is consistent with his projection. The highest-temperature melt, where silica is nearly depleted, begins to diverge from the projected silica-saturated melt line towards more typical eucrite compositions; it is likely that at higher degrees of melt the melt composition would progress towards the typical parental melt compositions.

Although we have ignored it to this point, there is a substantial kinetic control on the melt composition. Only one experiment was held at a shorter duration than the others

(C: 1100°C, 1 day). The effect is that in every representation of the melt composition used here, composition C plots proximal to the longer-duration melt E (1060°C, 1 week). The offset between the two experiments at the highest temperature (C: 1 day, G: 1 week; 1100°C for both) is consistent with a lower degree of plagioclase incorporated into the melting. This suggests that pyroxene melts more rapidly than plagioclase, and that the longer the melt is kept in contact with the source rock the larger the plagioclase component incorporated into the melting will be; consequently, there is a kinetic effect on the composition of melt formed based on how rapidly the melt is separated from the source rock. This may impact trace-element models of eucrite melting as, for example, Sc partitions very differently for plagioclase ( $D_{Sc} = 0.016$ ) and pyroxene ( $D_{Sc} = 1.4$ ) equilibrating with melt (Aigner-Torres et al., 2007; McKay and Weill, 1976).

#### *4.4.2 Trace-element description of melting and the Stannern trend*

Previous work attempted to generate the Stannern trend eucrite compositions from a primitive main group trend magma by assimilating a low-degree partial melt of pre-existing eucritic crust in a computational model (Barrat et al., 2007). The calculated melt compositions are based on partition coefficients from the literature and low degrees of partial melting (5%, 10% and 15%) resulting in a significant enrichment of ITEs (see the discussion and references in Barrat et al., 2007, for more details on the calculation). The shape of the REE curves is broadly similar between the calculated and experimentally derived ones (Fig. 4.5). In terms of REE abundance, partial melt A (1000°C) is roughly double the concentration of the calculated 5% partial melt, melt F (1020°C) is intermediate between 5% and 10% partial melts, and melt B (1040°C) is highly similar to the 15% partial melt. No attempt was made to estimate the degrees of partial melt represented by each of the experimental samples due to the likelihood that sample heterogeneity would bias any such estimate. The compositional similarity of the calculated and experimentally-derived melts suggests that the experimentally-derived melts can be reasonably applied into the previous magma mixing models rather than representing fundamentally different melts.

It is possible to generate a melt with a Stannern-like REE content by mixing any of the observed partial melts with the Juvinas bulk composition (Fig. 4.9). For each partial melt composition, a mixture of closest approach was calculated by minimizing the square of the difference between the mixture composition and Stannern for all REEs, excluding Eu. The proportional drop in REE content with an increased fraction of partial melting requires a commensurate increase in the fraction of partial melt incorporated into the Juvinas-like magma to generate a Stannern-like REE content, starting at only ~5% for partial melt A (1000°C), but becoming nearly 70% by partial melts G and C (both 1100°C). The closest match to the Stannern REE curve is calculated for the intermediate temperature melts (F, B, E; 1020-1060°C). Mismatch is due to changes in the slope of the REE curve; as temperature increases the La/Lu ratio decreases, from 2.74 for partial melt A to 1.19 for G and 1.03 for C. If Stannern were formed from mixing with a very low-degree partial melt, like A, then we would expect it to have a higher La/Lu; similarly, mixing with a higher degree partial melt generates an increasingly flat REE curve.

Among the other trace-elements, Sc is commonly used in eucrites as a proxy for magmatic evolution as increasing Sc correlates well with decreasing Mg# in typical eucrites (Mittlefehldt and Lindstrom, 2003). All of the partial melts of NWA 7035 have a higher Sc content than the Juvinas bulk composition, so although each of the melts can generate a magma with a Stannern-like REE content by mixing with the Juvinas bulk composition, there will be a concurrent increase in the Sc content, conflicting with the observation that ST magmas are highly similar to the MGT in Sc (Fig. 4.10). The effect is minimal for partial melt A, as the fraction of melt required is very low, but it would be very difficult to extract such a low degree of partial melt from the host rock as it exists only in small, isolated, pockets. It may be possible to find a eucritic composition that does not show the same enrichment in Sc during melting, as the Sc content of the melt is strongly dependent on the ratio of plagioclase to pyroxene involved in the melting; if such a composition exists it is likely to have a higher plagioclase content than NWA 7035.

A kinetic factor, previously discussed in terms of the major-element composition of the melts, is also apparent in the trace-element compositions. Both samples C and G were heated to 1100°C, and although both melts have a similar REE content, the shorter

duration of heating for sample C resulted in a substantial increase in the Sc content of the melt. This is consistent with the earlier observation that less plagioclase is involved in melting over the shorter duration experiment, as pyroxene has a substantially higher Sc content than plagioclase. This kinetic factor presents an alternative mechanism to counter the increase in Sc: rather than requiring a bulk composition with a higher plagioclase to pyroxene ratio, a longer equilibration time before melt extraction may result in the lower Sc content in the partial melt by allowing more plagioclase to participate in the melting. In this scenario, longer equilibration times before melt extraction are required to account for the Sc content of the ST eucrites based on our modeling.

An advantage to experimentally producing melt glasses is the existence of a robust major-element composition. Using the melt glass compositions, a major-element mixing model can be constructed using the trace-element model as a guide (Fig. 4.11). Mixing of even 5% melt A into the Juvinas bulk composition, the amount required to match the REE content of Stannern, will result in a substantial drop in Mg#, from 40.6 to 38.6. This change in Mg# is ~25% of the difference between Juvinas and Nuevo Laredo (Mg# 32.7) (Barrat et al., 2007), the approximate range of all typical basaltic eucrites. Using higher melt fraction compositions will exacerbate the decrease in Mg#; although the Mg# of the melt decreases with increased melting fraction, the proportion of melt required to generate the required ITE enrichment also increases, resulting in a net decrease in Mg# as temperature of the partial melt increases. The decrease in Mg# would be further enhanced by incorporation of a fractional crystallization component into the mixing model (e.g. Barrat et al., 2007; after DePaolo, 1981) as both the magma mixing (“assimilation”) and fractional crystallization processes will drive the magma to lower Mg# when using the experimentally derived partial melts as assimilants. A ferroan shift in major-element composition is incompatible with the observed major-element compositions of ST magmas, casting doubt on the viability of partial melts to generate the ITE enrichment of the ST eucrites.

A potential mechanism to create a partial melt without the large shift in Mg# encountered by melting of NWA 7035 would be to generate modest degree partial melts from a zoned cumulate eucrite. Although low degree partial melts would still be ferroan, as the degree of partial melting increases the Mg# of a melt of a cumulate eucrite would

also rapidly increase, albeit at much higher temperature. The ITE content of cumulate eucrites is believed to be controlled by the fraction of melt trapped during petrogenesis (Treiman, 1997), so it may be possible to generate a similar ITE enrichment to a moderate degree partial melt of NWA 7035 (e.g. experiments E, G, or C) with a more magnesian liquid composition. To test this hypothesis, partial melting experiments on a zoned eucrite with either a substantially higher Mg# in pyroxene cores, or significantly larger magnesian pyroxene cores (consistent with slow cooling and pyroxene accumulation), than NWA 7035 should be performed. A consequence of this change in sample is that the temperatures of partial melting would increase. A difficulty in this model, assuming that a liquid with both the ITE enrichment and Mg# necessary to generate the ST can be generated, will be to explain why cumulate compositions would be preferentially incorporated (a.k.a. why we don't see the ferroan enhancement expected from the results here by incorporating a usual zoned eucrite composition) and why the degree of partial melting that balances the ITE enrichment with the lack of shift in Mg# is preferentially assimilated.

#### *4.4.3 Metasomatism*

Although not the intended goal of this study, the observations of partial melting results may offer some insight into the nature of the fluids that metasomatized some eucrites and howardites. Previous work has described a number of potential fluids, ranging from aqueous fluids (Barrat et al., 2011; Warren et al., 2014), to S-rich vapors (Zhang et al., 2013), to Fe-rich dry vapors (Schwartz and McCallum, 2005). To be clear, the metasomatization we are discussing is the formation of Fe-rich rims on pyroxene, often associated with troilite veins, with progressively increasing degrees of metasomatization forming fayalite veins, and ultimately resulting in Fe-rich veins with anorthite inclusions within broader regions of Al-depletion, as described by Barrat et al. (2011), not the formation of quartz veins (Treiman et al., 2004) or other metasomatic processes inferred for the HED parent body (e.g. impact-driven fluid alteration from impact of primitive chondritic material, Warren et al., 2014). Silicate magma has been deemed unlikely by previous workers based on various observed chemical shifts in the

metasomatism (e.g. broad Al depletion, Barrat et al., 2011; or different Fe/Mn ratios from the host, Mittlefehldt and Lindstrom, 1997).

Petrographic observations of metasomatized pyroxene along fractures in experiments on NWA 7035 (Fig. 4.12) are consistent with the petrography described by Barrat et al. (2011) and others (Roszjar et al., 2009; Takeda et al., 1983; Warren, 2002). In most of our experiments, from the lowest-temperature melting (A: 1000°C) to the highest (G: 1100°C) there is evidence of metasomatic aureoles around melt-infilled cracks in pyroxene, but especially in B (1040°C) Fe-rich pyroxene surrounds a melt vein that contains anorthitic plagioclase, fayalite, and troilite; this is essentially the petrography described for the highest degree of metasomatization. In all experiments – representing all stages of melting – troilite veins have formed preferentially along melt-filled fractures in pyroxene. Although more detailed analysis is required to compare these experimental results to veins in natural samples, our results are highly suggestive that magmatic infiltration of low-degree partial melts from other eucrite compositions may be responsible for the metasomatization observed in some eucrites and eucritic clasts in howardites.

#### **4.5 Conclusions**

Partial melting experiments have demonstrated that low degrees of partial melts of a zoned eucrite can generate the incompatible trace-element enrichment required to generate the Stannern trend by mixing such a partial melt with a main group trend (Juvinas-like) magma. However, our results have difficulty reconciling the Sc and major-element (e.g. Mg#) compositions of such a melt. The Sc enrichment of a partial melt may be decreased by a longer equilibration time before melt extraction than performed in laboratory experiments because plagioclase, which has a lower Sc content, is kinetically slow to melt. Alternatively, a more plagioclase-rich composition may result in a lower Sc enrichment in a partial melt. The ferroan nature of the partial melts could potentially be overcome by using a more magnesian composition for generating the partial melt; however, the anticipated changes to the Mg# of the mixed magma remains an outstanding issue with the model. The ability to closely approximate a Stannern-like rare earth

element pattern from mixtures of the Juvinas bulk composition with partial melts of NWA 7035 over a wide range of degrees of melting warrants further experimentation to determine if the issues with Sc and Mg# can be overcome with other eucrite compositions.

**Table 4.1:** Experimental parameters, melt observations

Name	Mass (mg)	Temp. (°C)	Duration	Melting notes
NWA 7035 A	140.3	1000	1 week	Minor melting
NWA 7035 B	161.8	1040	1 week	Melt pockets
NWA 7035 C	138.0	1100	1 day	Interconnected melt
NWA 7035 D	161.8	1010	1 week	No evidence of melting
NWA 7035 E	137.2	1060	1 week	Interconnected melt
NWA 7035 F	148.8	1020	1 week	Wetting of plagioclase edges
NWA 7035 G	137.1	1100	1 week	Interconnected melt

† All samples were held at IW-1

**Table 4.2:** Average glass compositions from partial melting experiments

	NWA 7035 A		NWA 7035 B		NWA 7035 C	
n	15		24		18	
SiO <sub>2</sub>	41.6	±0.2	46.9	±0.1	49.8	±0.1
TiO <sub>2</sub>	3.55	±0.02	2.6	±0.06	1.62	±0.04
Al <sub>2</sub> O <sub>3</sub>	6.15	±0.07	8.48	±0.03	9.53	±0.09
Cr <sub>2</sub> O <sub>3</sub>	0.016	±0.003	0.061	±0.004	0.132	±0.004
FeO	32.3	±0.1	26.63	±0.06	23.6	±0.2
MnO	0.726	±0.009	0.992	±0.005	0.624	±0.005
MgO	0.34	±0.01	1.28	±0.02	2.42	±0.03
CaO	10.93	±0.07	9.94	±0.02	10.13	±0.02
Na <sub>2</sub> O	0.47	±0.01	0.712	±0.006	0.737	±0.009
K <sub>2</sub> O	0.389	±0.008	0.294	±0.007	0.129	±0.002
P <sub>2</sub> O <sub>5</sub>	2.22	±0.07	0.39	±0.01	0.165	±0.005
SO <sub>3</sub>	1.47	±0.05	0.04	±0.02	0.046	±0.006
Total	100.1	±0.2	98.3	±0.2	98.86	±0.06
Mg#	1.84	±0.08	7.9	±0.1	15.5	±0.2
n	2		12		30*	
Sc	34.0	±0.8	39	±1	36.1	±0.1
V	4.4	±0.7	14	±1	21.3	±0.2
Co	3	±1	8	±1	4.37	±0.03
Ni	8.2	±0.3	3.3	±0.8	1.2	±0.1
Sr	161	±6	104	±3	94.5	±0.3
Y	280	±10	73	±2	36.8	±0.2
Zr	950	±30	200	±0	105.3	±0.5
Nb	62	±1	17.3	±0.7	8.50	±0.05
Mo	0.1	±0.1	0.47	±0.05	0.44	±0.02
La	73	±3	15.3	±0.5	6.28	±0.04
Ce	177	±6	38	±1	15.61	±0.05
Pr	25	±1	5.5	±0.2	2.34	±0.01
Nd	128	±3	28	±1	12.43	±0.06
Sm	37	±1	9.1	±0.4	4.03	±0.03
Eu	2.54	±0.09	1.25	±0.03	0.899	±0.006
Gd	45	±2	11.2	±0.4	5.27	±0.04
Tb	7.0	±0.3	1.91	±0.07	0.922	±0.006
Dy	48	±1	13.3	±0.4	6.62	±0.03
Ho	9.8	±0.06	2.86	±0.09	1.44	±0.009
Er	26.6	±0.9	8.5	±0.3	4.26	±0.03
Tm	3.5	±0.2	1.21	±0.04	0.63	±0.006
Yb	21.4	±0.6	8.1	±0.3	4.31	±0.03
Lu	2.76	±0.09	1.19	±0.04	0.631	±0.006
Hf	20.7	±0.4	6	±0.3	2.88	±0.02

	NWA 7035 E		NWA 7035 F		NWA 7035 G	
n	18		14		16	
SiO <sub>2</sub>	49.7	±0.05	44.2	±0.4	50.34	±0.04
TiO <sub>2</sub>	1.82	±0.02	3.5	±0.06	1.359	±0.009
Al <sub>2</sub> O <sub>3</sub>	9.3	±0.02	7.3	±0.1	10.47	±0.02
Cr <sub>2</sub> O <sub>3</sub>	0.096	±0.004	0.034	±0.003	0.131	±0.005
FeO	24.45	±0.04	29.2	±0.3	21.5	±0.03
MnO	0.644	±0.002	1.065	±0.009	0.586	±0.003
MgO	1.784	±0.006	0.73	±0.03	3.02	±0.01
CaO	9.889	±0.009	10.25	±0.07	10.18	±0.02
Na <sub>2</sub> O	0.764	±0.006	0.6	±0.01	0.75	±0.004
K <sub>2</sub> O	0.194	±0.002	0.356	±0.005	0.1197	±0.0009
P <sub>2</sub> O <sub>5</sub>	0.223	±0.006	0.57	±0.02	0.157	±0.003
SO <sub>3</sub>	0.061	±0.012	0.5	±0.1	0.011	±0.002
Total	98.92	±0.06	98.2	±0.3	98.64	±0.05
Mg#	11.51	±0.04	4.3	±0.2	20.04	±0.09
n	25*		3		10	
Sc	34.1	±0.1	39.5	±0.9	32.6	±0.2
V	16.8	±0.3	8.1	±0.3	25.7	±0.6
Co	3.07	±0.1	5	±0.5	3.46	±0.04
Ni	0.7	±0.06	2.3	±0.7	1.8	±0.5
Sr	103.1	±0.3	125	±1	94.8	±0.2
Y	53.6	±0.4	121	±2	35.5	±0.1
Zr	165	±2	388	±8	109.7	±0.3
Nb	13.1	±0.1	35.6	±0.7	8.36	±0.04
Mo	0.18	±0.01	0.18	±0.03	0.37	±0.02
La	10.86	±0.07	26.1	±0.3	6.64	±0.03
Ce	26.3	±0.2	67.0	±0.4	16.55	±0.06
Pr	3.90	±0.03	9.82	±0.07	2.45	±0.01
Nd	20.3	±0.1	49.4	±0.4	12.8	±0.1
Sm	6.46	±0.05	15.3	±0.2	4.22	±0.05
Eu	1.143	±0.007	1.76	±0.05	0.926	±0.008
Gd	8.22	±0.06	19.1	±0.3	5.3	±0.05
Tb	1.426	±0.007	3.21	±0.05	0.919	±0.008
Dy	10.00	±0.06	23.097	±0.003	6.58	±0.07
Ho	2.10	±0.01	4.94	±0.05	1.4	±0.01
Er	6.09	±0.03	14.2	±0.2	4.11	±0.02
Tm	0.879	±0.005	1.96	±0.01	0.583	±0.006
Yb	5.67	±0.03	12.7	±0.2	3.87	±0.04
Lu	0.827	±0.006	1.91	±0.05	0.578	±0.005
Hf	4.56	±0.07	10.4	±0.3	3.03	±0.02

† Oxides are reported in wt%, elements in ppm (µg/g)

\* The number of analyses performed on La for samples C and E were less than for other trace-elements, 12 and 11 respectively.

**Table 4.3:** NWA 7035 mineral compositions

Mineral	Pyroxene	Pyroxene	Pyroxene	Pyroxene
Sub	High-Mg	High-Wo	High-Fe	Ferripigeonite
n	7	11	7	39
SiO <sub>2</sub>	52.1 ±0.4	49.4 ±0.1	47.3 ±0.1	46.93 ±0.08
TiO <sub>2</sub>	0.16 ±0.02	0.45 ±0.01	0.7 ±0.05	0.444 ±0.006
Al <sub>2</sub> O <sub>3</sub>	1.3 ±0.1	1.38 ±0.05	0.87 ±0.04	0.315 ±0.006
Cr <sub>2</sub> O <sub>3</sub>	0.75 ±0.05	0.69 ±0.03	0.2 ±0.03	0.032 ±0.004
FeO	20.5 ±0.1	23.9 ±0.3	37.6 ±0.1	42.74 ±0.06
MnO	0.75 ±0.009	0.829 ±0.009	1.07 ±0.02	1.46 ±0.01
MgO	21 ±0.2	10.3 ±0.3	4 ±0.3	2.29 ±0.05
CaO	3.11 ±0.08	12.7 ±0.3	8.4 ±0.4	5.81 ±0.04
Na <sub>2</sub> O	0.031 ±0.005	0.1 ±0.01	0.044 ±0.008	0.023 ±0.002
K <sub>2</sub> O	<MDL	<MDL	<MDL	<MDL
Total	99.7 ±0.3	99.7 ±0.1	100.22 ±0.09	100.04 ±0.09
Mg#	64.6 ±0.6	43 ±1	16 ±1	8.7 ±0.2
En	60.4 ±0.5	31.4 ±0.8	13 ±1	7.5 ±0.2
Fs	33.1 ±0.2	40.9 ±0.7	68 ±1	78.8 ±0.2
Wo	6.4 ±0.2	27.7 ±0.7	19.4 ±0.9	13.7 ±0.1

Mineral	Spinel	Ilmenite	Olivine	Plagioclase
n	3	3	13	5
SiO <sub>2</sub>	0.027 ±0.004	0.008 ±0.005	30.6 ±0.2	47.3 ±0.1
TiO <sub>2</sub>	30.73 ±0.04	52.2 ±0.1	0.127 ±0.007	0.05 ±0.02
Al <sub>2</sub> O <sub>3</sub>	1.94 ±0.02	0.162 ±0.008	0.026 ±0.002	32.84 ±0.09
Cr <sub>2</sub> O <sub>3</sub>	5.4 ±0.02	0.46 ±0.01	0.057 ±0.008	0.004 ±0.003
FeO	58.81 ±0.07	45 ±0.06	61.6 ±0.5	0.8 ±0.2
MnO	1.088 ±0.006	1.191 ±0.004	2.08 ±0.06	0.019 ±0.006
MgO	0.54 ±0.02	0.58 ±0.02	5.1 ±0.5	0.16 ±0.02
CaO	0.2 ±0.02	0.11 ±0.02	0.85 ±0.02	17.38 ±0.06
Na <sub>2</sub> O	<MDL	<MDL	0.011 ±0.004	1.82 ±0.02
K <sub>2</sub> O	<MDL	<MDL	<MDL	0.13 ±0.01
P <sub>2</sub> O <sub>5</sub>	<MDL	<MDL	<MDL	0.1 ±0.01
Total	98.75 ±0.08	99.7 ±0.1	100.5 ±0.2	100.6 ±0.1
Mg#	1.6 ±0.05	2.25 ±0.08	13 ±1	
E1	63.8 ±0.1		13 ±1	83.4 ±0.4
E2	23.6 ±0.1		87 ±1	15.8 ±0.2
E3	12.6 ±0.1			0.76 ±0.06

<sup>†</sup> MDL stands for method detection limit. All oxides are in wt%. End members and Mg#s were calculated on a molar basis. Spinel: E1=ulvöspinel, E2=chromite, E3=spinel; olivine: E1=forsterite, E2=fayalite; plagioclase: E1=anorthite, E2=albite, E3=orthoclase.

**Table 4.4:** NWA 7035 bulk composition from solution ICP-MS

	MDL	Split 1	Split 2	Average
Li	0.05	10.7	9.61	10.16
Na	0.5	5291	4809.4	5050.2
P	5	483	435	459
K	6	667	635	651
Sc	0.01	41.66	37.48	39.57
Ti	0.09	5581.69	5337.4	5459.54
V	0.05	44	42.1	43.05
Cr	0.05	1869.05	1780.77	1824.91
Mn	0.03	4161.83	3986.93	4074.38
Co	0.03	9.18	8.45	8.82
Ni*	0.06	90.10	48.85	69.47
Cu	0.03	411.92	378.42	395.17
Zn	0.08	2.96	2.73	2.84
Ga	0.01	1.88	1.77	1.83
Ge	0.02	0.2	0.18	0.19
As	0.06	1.59	1.36	1.47
Rb	0.04	1.1	0.96	1.03
Sr	0.03	82.13	78	80.06
Y	0.02	21.84	21.24	21.54
Nb*	0.04	6.88	5.9	6.39
Mo	0.02	0.34	0.36	0.35
Pd	0.01	2.3	2.21	2.25
Sn	0.06	97.13	87.53	92.33
Sb	0.01	3.23	3.53	3.38
Ba	0.03	50.36	48.84	49.6
La	0.03	4.55	4.33	4.44
Ce	0.03	11.64	11.12	11.38
Pr	0.04	1.79	1.65	1.72
Nd	0.03	8.35	8.22	8.29
Sm	0.04	2.62	2.58	2.6
Eu	0.03	0.77	0.72	0.75
Gd	0.03	3.44	3.45	3.45
Tb	0.03	0.64	0.58	0.61
Dy	0.04	4.1	3.92	4.01
Ho	0.02	0.9	0.84	0.87
Er	0.04	2.56	2.39	2.48
Yb	0.05	2.38	2.29	2.33
Lu**	0.04	0.38	0.33	0.35
Re	0.03	4.85	5.11	4.98
Pb	0.03	0.7	0.61	0.65

† All units are ppm ( $\mu\text{g/g}$ ). MDL is the estimated method detection limit.

\* Ni and Nb had very high internal variation between the analyses, so the average value should be treated as suspect.

\*\* Lu had a low percent recovery in the analysis of the standard material (GSP-2; 65% recovery), so the result may be suspect.

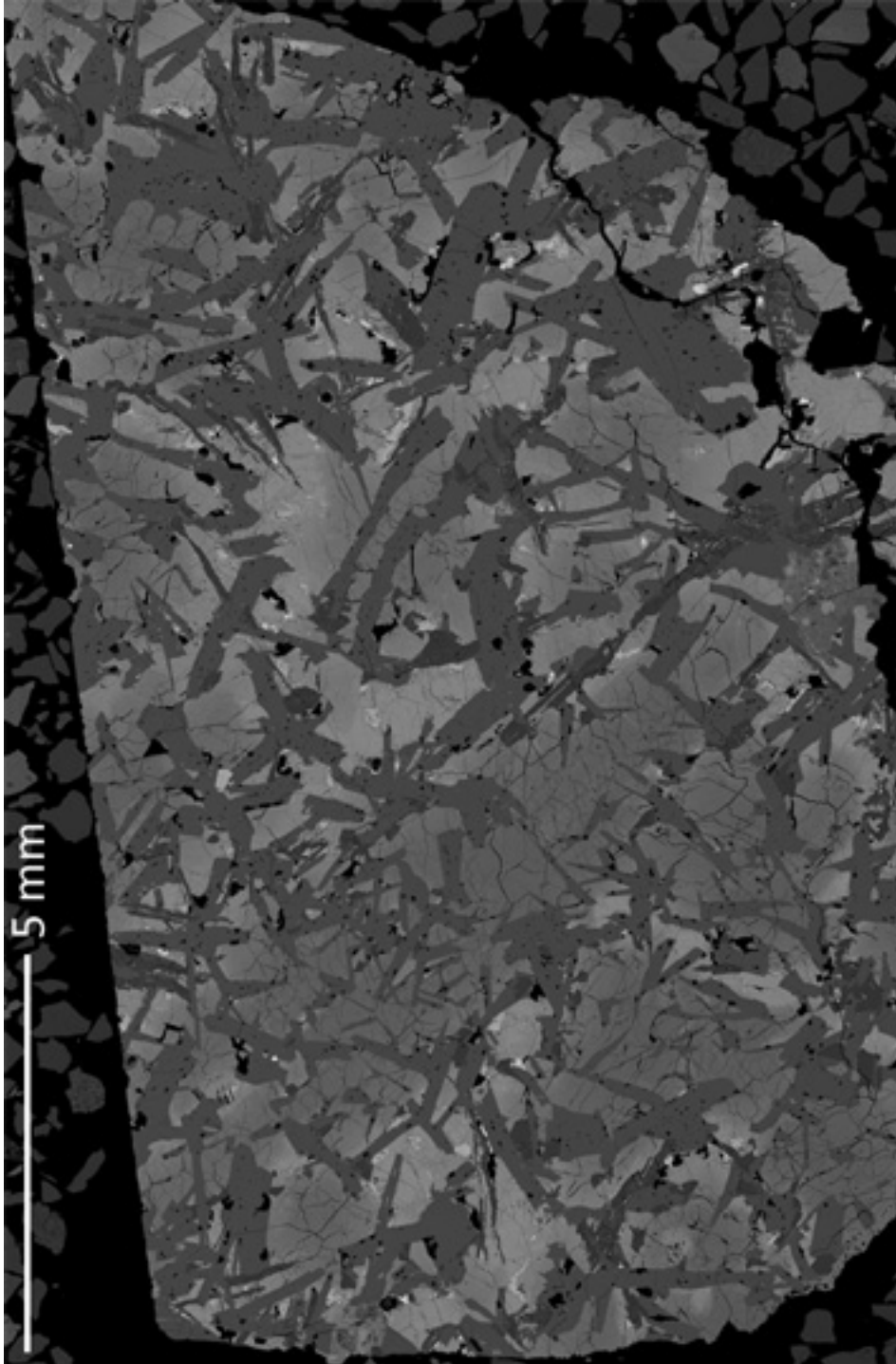


**Figure 4.1:** BSE photo mosaic of NWA 7035 thin section. The darker of the two lath-shaped minerals is a silica polymorph, the brighter is anorthitic plagioclase. The zoned mineral is low-Ca clinopyroxene (pigeonite). The bright gray mineral is fayalite, typically in regions of mesostasis (fayalite, silica, anorthite, pyroxene intergrowths). Rare white spots are oxides, typically spinel.

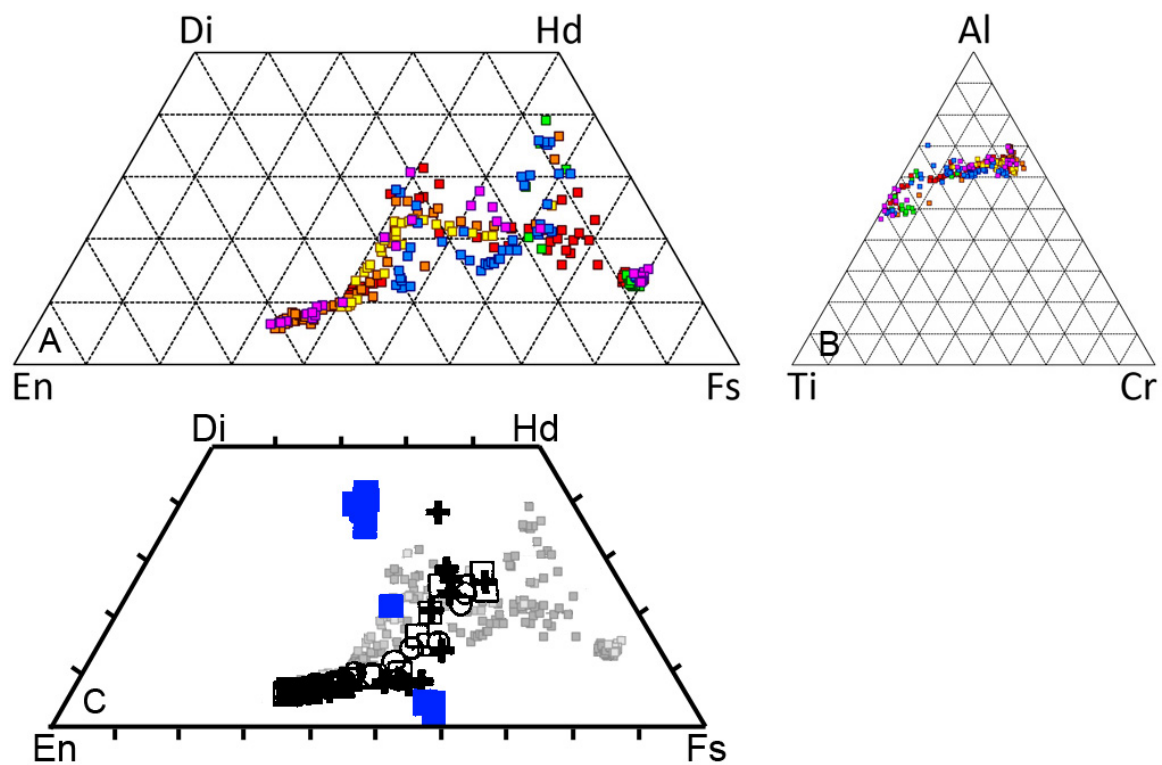


**Figure 4.2:** A: Pyroxene compositions from traverses of NWA 7035 in major elements and B: minor elements. Each color represents a separate traverse of a different pyroxene grain. Increasing Mg# on the Al-Ti-Cr diagram proceeds from left to right. C: Reference compositions of pyroxene zoning in Pasamonte (black) and pyroxene exsolution in Juvinas (blue) from Pun and Papike (1996); NWA 7035 pyroxene is shown in gray for comparison.

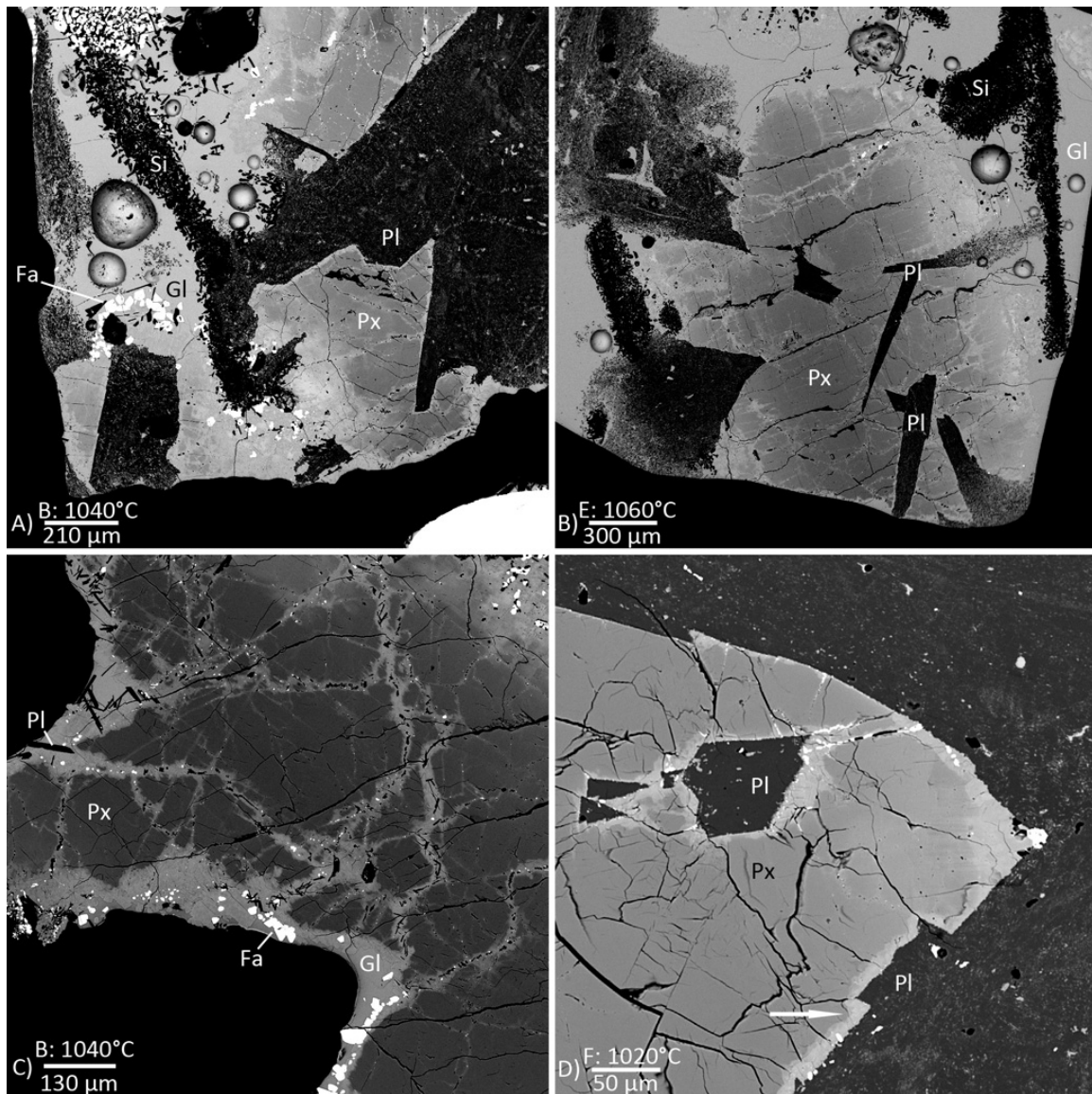


**Figure 4.3:** BSE images of several features observed in melting experiments. A) Melt initiation in a region surrounding fayalite in sample B, 1040°C (upper left). B) Pyroxene laths breaking up into smaller crystals as melt infiltrates in sample E, 1060°C (upper right). C) Melt infiltration along cracks in pyroxene crystals in sample B (lower left). Note that melt is originating from the two regions with bright fayalite grains, in the upper right corner and along the lower/left edge. D) Melt wetting along the plagioclase-pyroxene interface in sample F, 1020°C (lower right). Note that progressive alteration of pyroxene to a brighter (higher-Fe) composition occurs away from the interface. Also note that melt infiltration of plagioclase is visible in A, B, and D. Labels are plagioclase (Pl), pyroxene (Px), fayalite (Fa), glass (Gl), and an unspecified silica polymorph (Si). The arrow in D points to ferroan alteration of pyroxene from wetting of the plagioclase-pyroxene boundary.

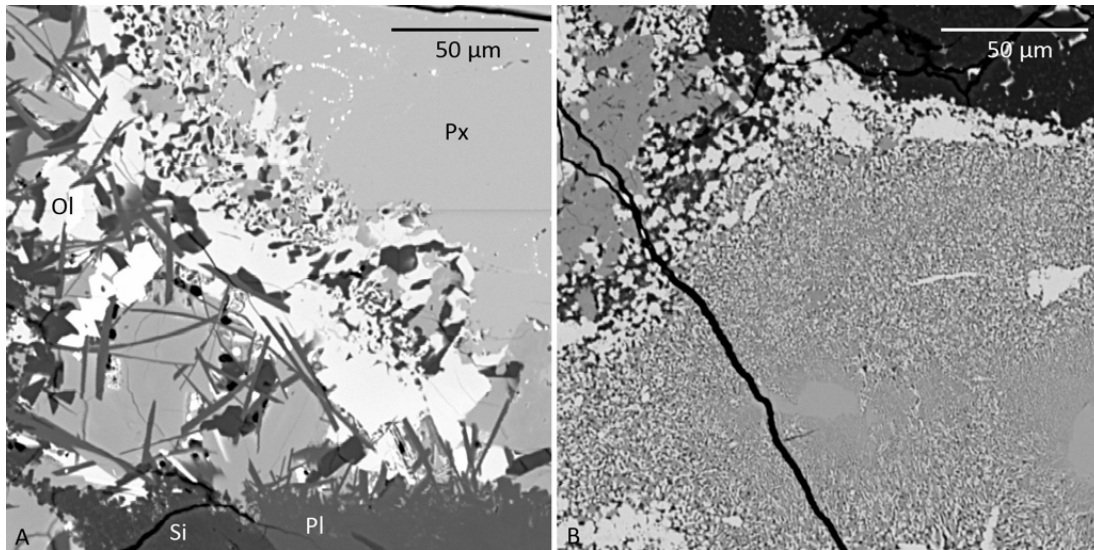


**Figure 4.4:** A: High-Fe mesostasis in NWA 7035 located near ferroan pyroxene rims. B: Fine-grained intergrowth of fayalite, anorthite, ferroan-augite, silica, and oxides resulting from breakdown of a metastable ferripigeonite or pyroxferite composition. Fayalite is found in both areas, but is substantially finer-grained in the mineral breakdown texture. Most of the ITE content of NWA 7035 is expected to originate from the mesostasis.

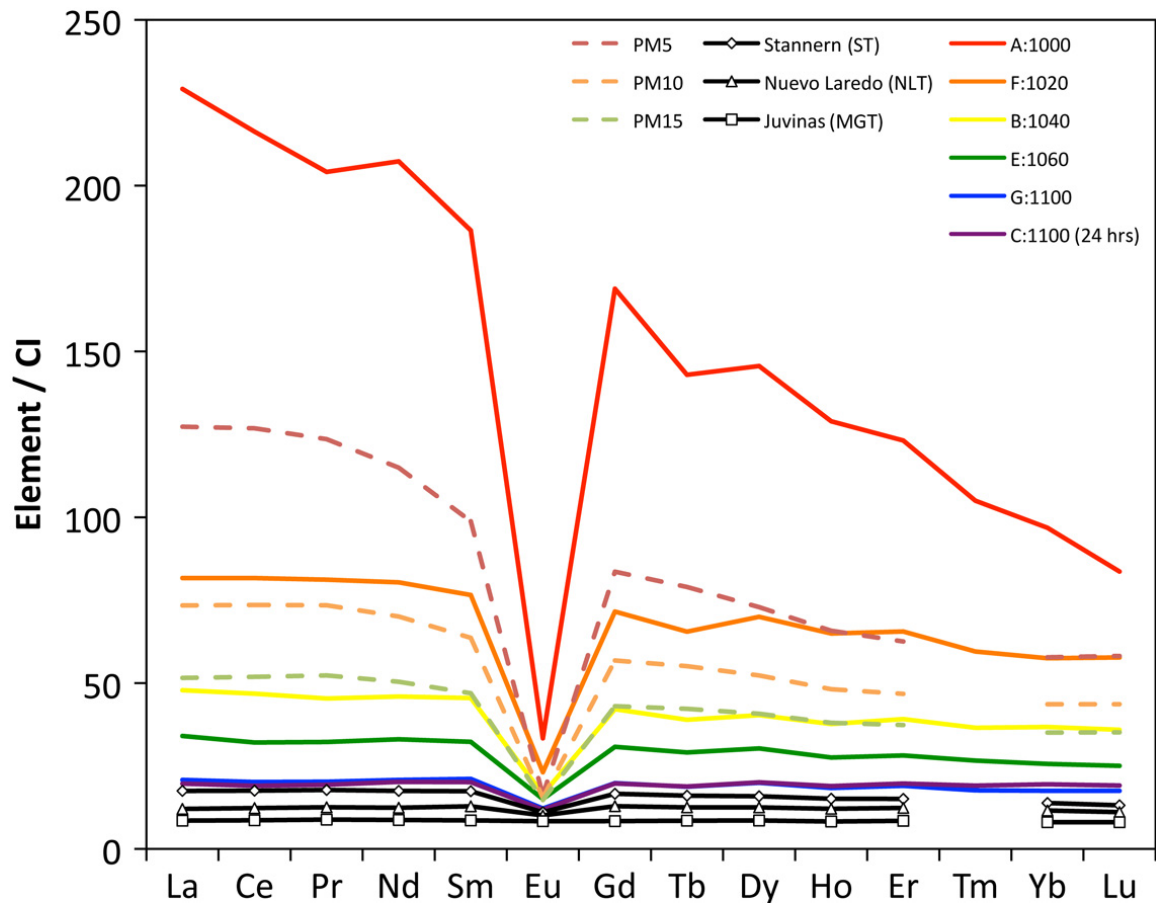


**Figure 4.5:** Rare earth element trends of each of the experimentally derived partial melts (solid colors, lower REE abundance with higher temperature). The calculated partial melt compositions from Barrat et al. (2007) for 5, 10, and 15% partial melts are included for comparison (dashed). The whole rock REE abundance for Juvinas (squares), Stannern (diamonds), and Nuevo Laredo (triangles), representative meteorites of the MGT, ST, and NLT compositions respectively, are also included for comparison (Barrat et al., 2007).

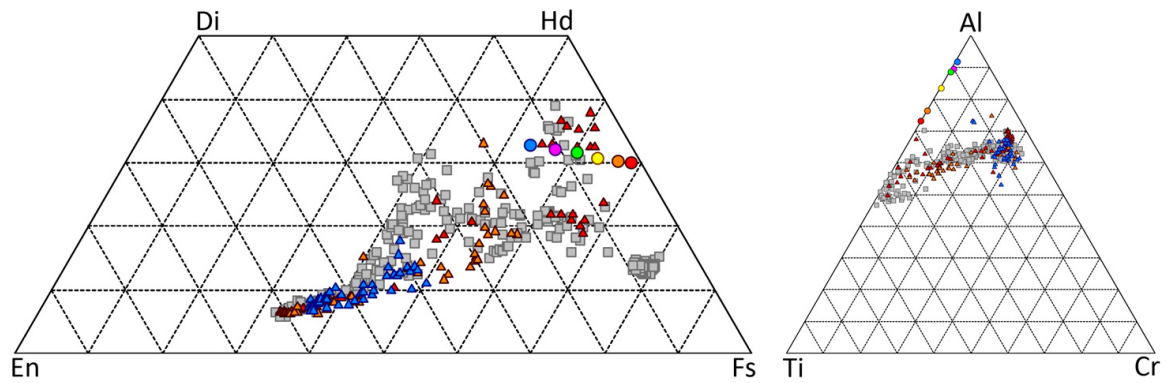


**Figure 4.6:** Pyroxene compositional ranges from three experiments (triangles) in both major and minor-elements (blue, G, 1100°C; orange, F, 1040°C; red, A, 1000°C). Glass compositions are also included (circles) based on the same colors, and including all experiments (yellow, B, 1020°C; green, C, 1060°C; purple, C, 1100°C with a shorter hold time). Colors correspond to increasing temperature from red (1000°C) to blue (1100°C) with purple as the shorter duration 1100°C experiment (C). Pyroxenes measured in the thin section of NWA 7035 are shown for comparison of compositional ranges (gray squares).

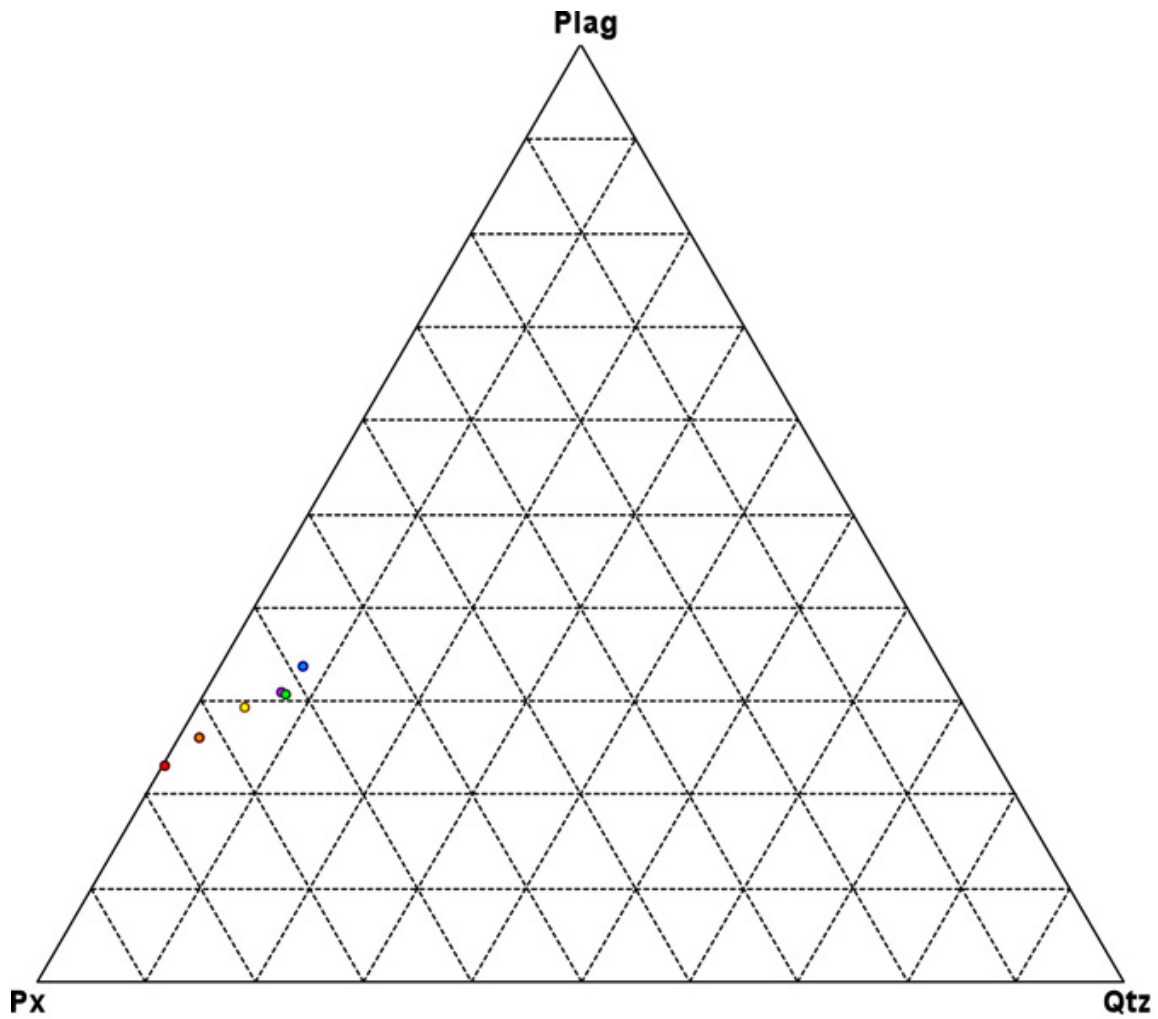


**Figure 4.7:** CIPW norm projection of the melt composition with increasing degree of melting (red to blue) for normative plagioclase (anorthite + albite + orthoclase), pyroxene (diopside + hypersthene), and quartz. The trend suggests that the melting starts dominated by normative pyroxene, although this may actually be fayalite mixing with the silica during initial melting. As melting increases, the trend is towards an increasing fraction of both plagioclase and silica participating in the melting. The shorter duration experiment (C – 1100°C, 1 day; purple) is nearly indistinguishable from the longer duration experiment at the next lower temperature (E – 1060°C, 1 week; green) in this projection.

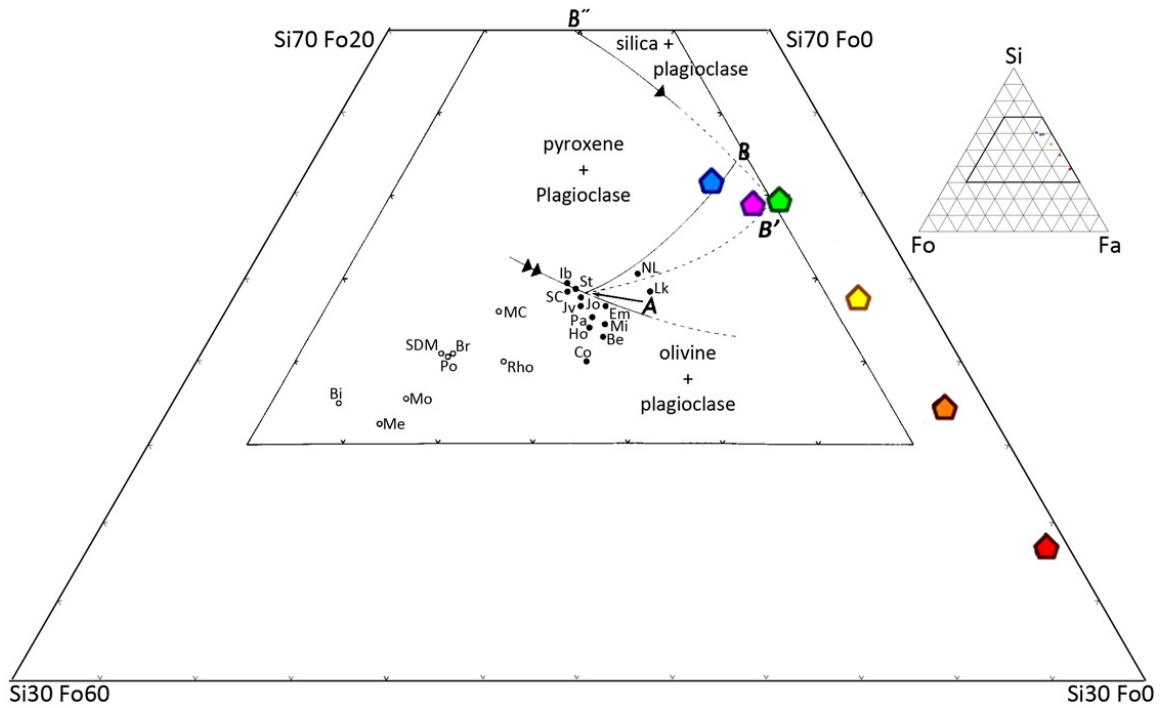


**Figure 4.8:** Stolper's projection of the silica, forsterite, and fayalite components of eucritic melts (see text for projection details), modified from Stolper (1977). Composition A is both the eutectic composition for partial melting of an olivine-plagioclase-pyroxene composition, and the average basaltic eucrite composition. B and B' are the projected equilibrium and fractional crystallization paths of an evolving magma from composition A; B'' is the silica-saturated curve. Pentagons are the projected magma compositions from partial melting experiments, colored for increasing temperature (red: A, 1000°C to blue: G, 1100°C; purple is the shorter duration C, 1100°C). Magma compositions plot along an extension of the silica-saturated crystallization curve (B''), consistent with the presence of silica in residuum of all experiments. Basaltic eucrites (black circles) are the bulk compositions of Béréba (Be), Cachari (Ca), Emmaville (Em), Haraiya (Ha), Ibitira (Ib), Jonzac (Jo), Juvinas (Jv), Lakangaon (Lk), Millbillillie (Mb), Nuevo Laredo (NL), Pasamonte (Pa), Sioux County (SC), and Stannern (St). Cumulate eucrites (white circles) are the bulk compositions of Binda (Bi), Brient (Br), Medanitos (Me), Moama (Mo), Moore County (MC), Pomozdino (Po), and Serra de Magé (SDM). See Stolper (1977) Table 2 for the sources of the bulk data and the averaging performed for plotting.

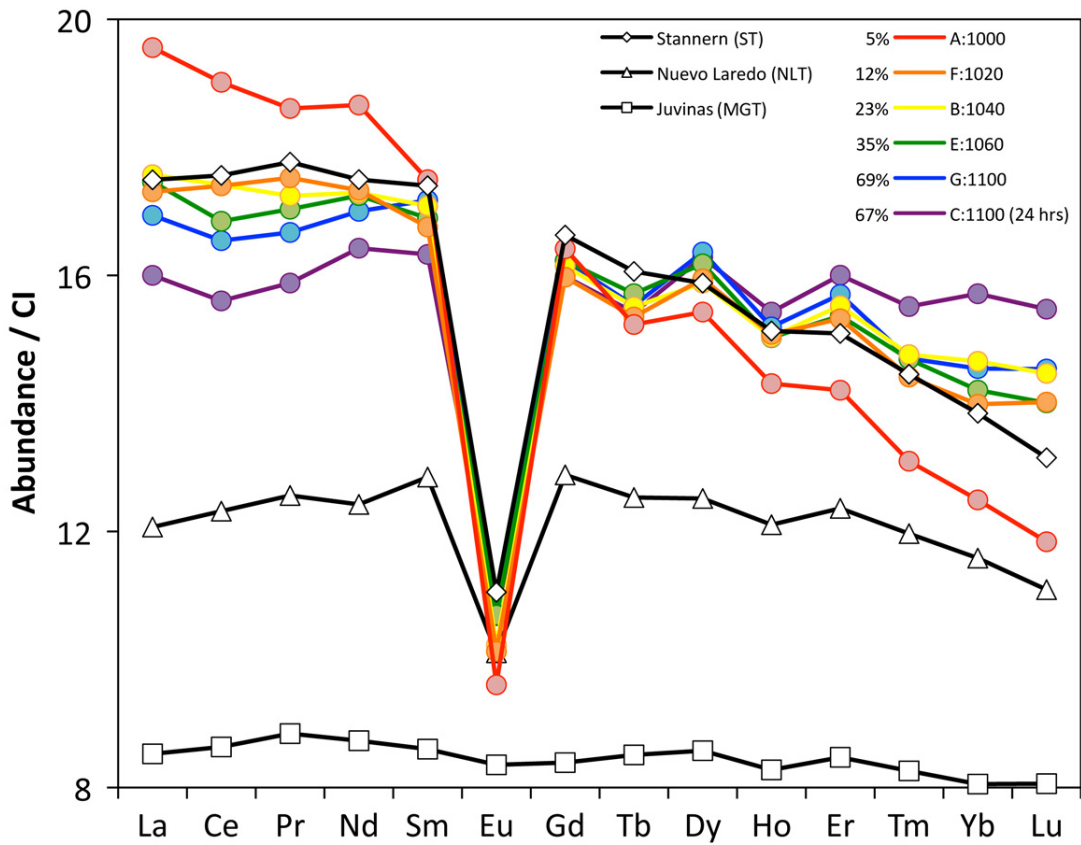


**Figure 4.9:** Best-fit rare earth element compositions for mixtures of the experimentally derived melt compositions with the Juvinas bulk composition to generate a Stannern-like composition (solid colors). Stannern (diamonds), Juvinas (squares), and Nuevo Laredo (triangles) are shown for reference (Barrat et al., 2007). Note that only the middle REEs are well matched for most melt compositions, and that the depth of the Eu anomaly is lower for Stannern than for the calculated mixtures. Percent of the experimentally derived melt composition required to generate the REE curve is indicated in the legend.

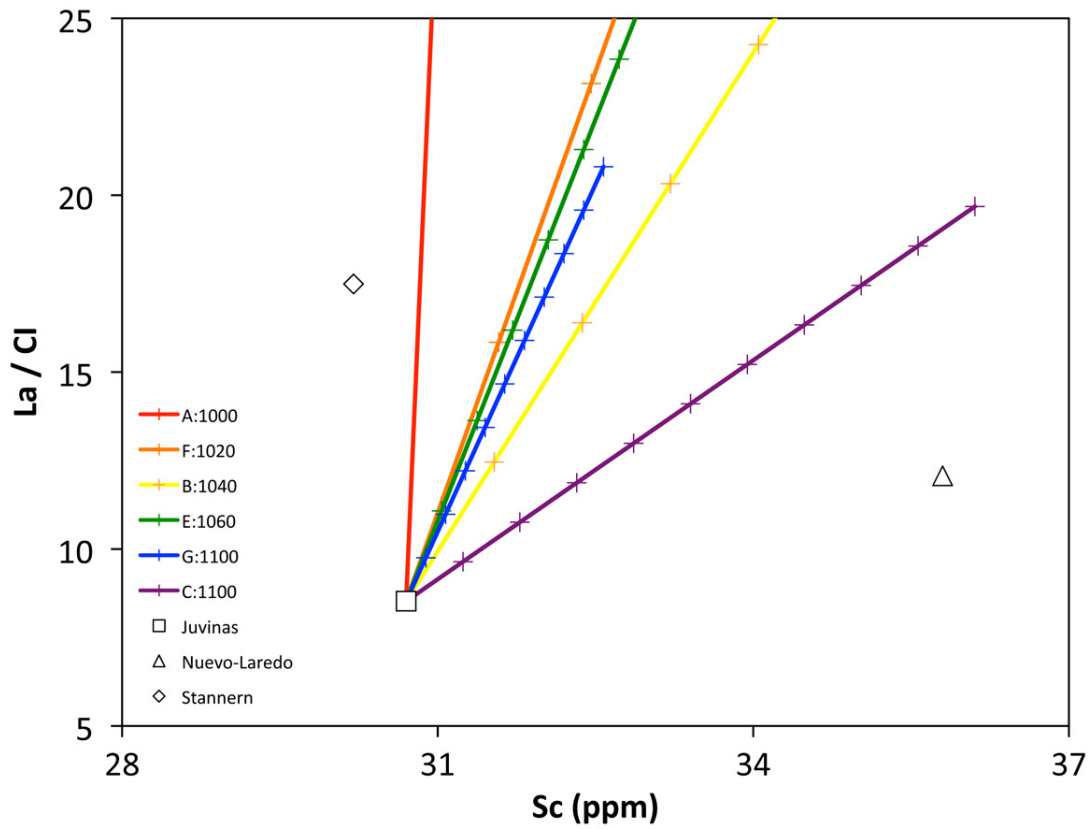


**Figure 4.10:** Partial mixing models for the experimentally-derived melt compositions with the Juvinas bulk composition of Barrat et al. (2007). La is normalized to an average CI chondrite composition. Note that the melt compositions for C and G are substantially different in La/Sc space, demonstrating the impact that equilibration times has on melt composition. Tic marks appear every 10% and terminate at melt compositions.

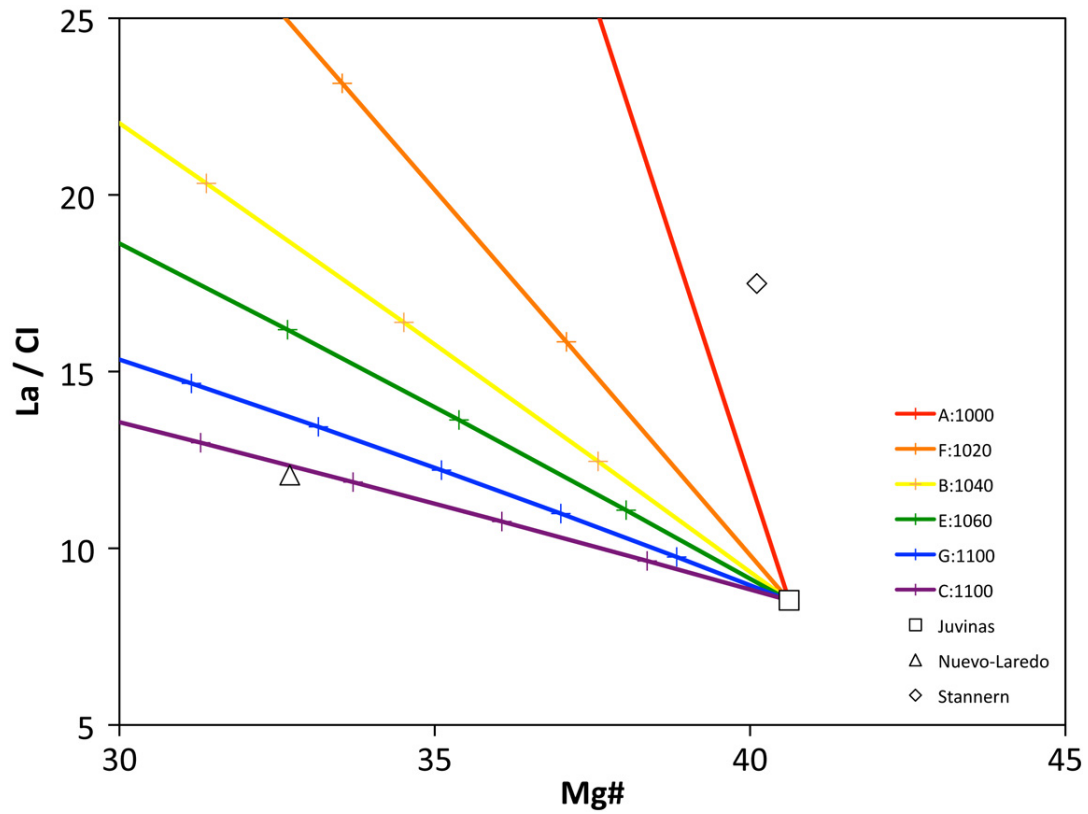


**Figure 4.11:** Partial mixing models for experimentally-derived melt compositions with the Juvinas bulk composition of Barrat et al. (2007). La is normalized to an average CI chondrite composition. Experimental glass compositions allow major-element modeling, unlike most calculated melt compositions where major-elements are difficult to constrain. Note that the difference between C and G shows the effect of increased equilibration time, shifting the mixing curve both up and to the left (higher La, more ferroan). Tic marks appear every 10%.

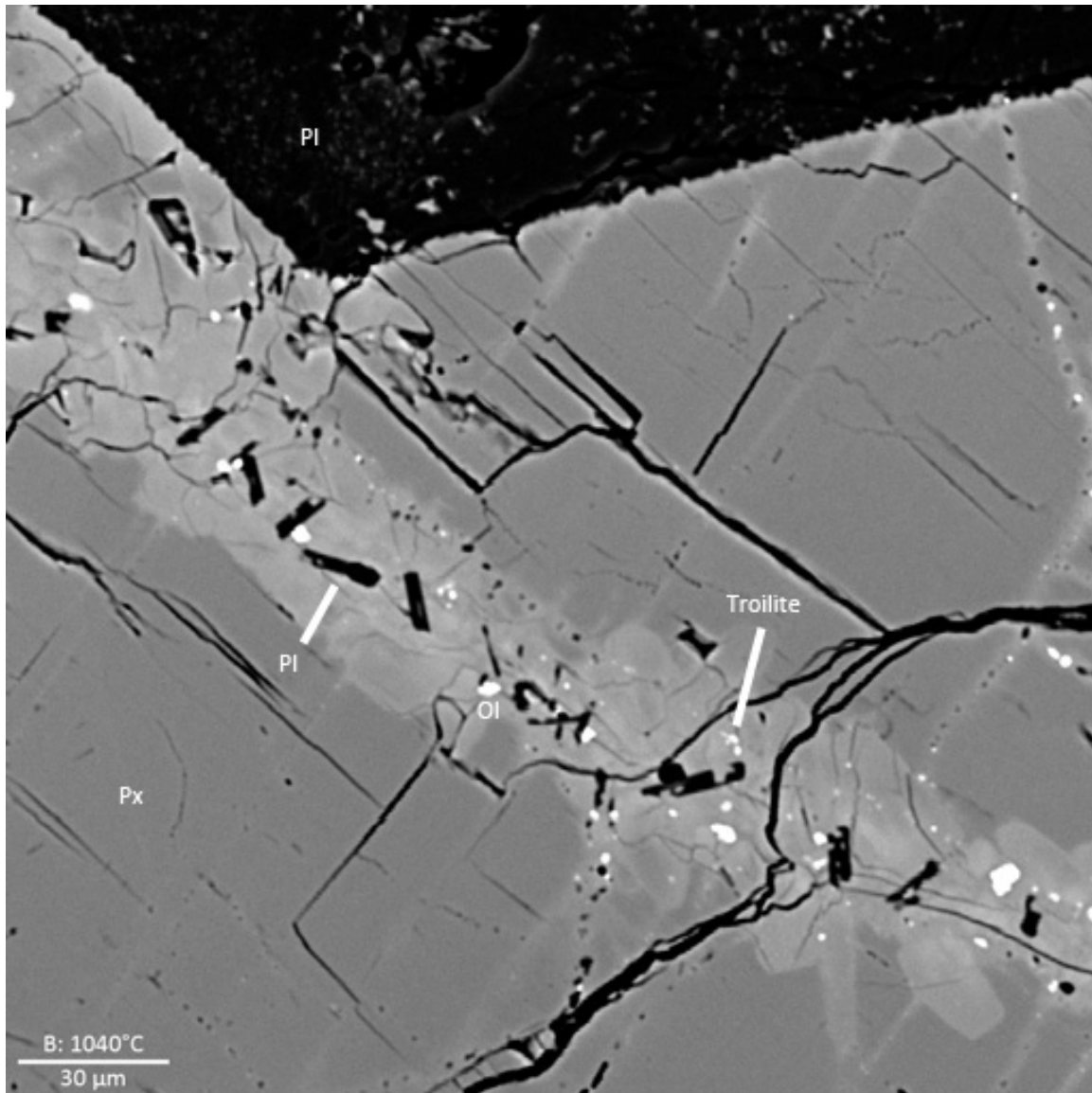


**Figure 4.12:** BSE photomicrograph of a Fe-rich vein and surrounding metasomatized pyroxene in experiment B (1040°C). The dark mineral, visible as both the large grain at the top and small euhedral crystals throughout, is plagioclase. The brightest minerals are fayalite and troilite, with troilite typically the smaller of the two. There is some indication that fluid infiltration may preferentially occur along high-Ca exsolution surfaces, as well as along fractures, as indicated by the brighter contrast along flat surfaces in the pyroxene.

## **Chapter 5: Summary, Conclusions, and Further Study**

### **5.1 Summary, and questions for further study of the Tissint meteorite**

The experimental investigation in Ch. 2 & 3 has had several significant impacts. First, by demonstrating a change in  $fO_2$  that was larger than can be rationalized by auto-oxidation in a depleted shergottite, we have disproven the hypothesis that volatiles are present only in the enriched reservoir of Mars. Secondly, we have shown that some shergottites from different textural types can be related by fractional crystallization processes, but further, that not all shergottites from within a textural type can be related by the same. Thirdly, we have demonstrated that spinel can exsolve from olivine due to an oxidation event, as is known to have occurred in at least four shergottites, and that in so doing it overprints the profile of Cr in the olivine.

One future research project based on the oxidation-induced exsolution of spinel from olivine is to perform a more detailed study of the phenomenon. A combination of a higher-resolution imaging technique, like transmission electron microscopy (TEM), with an X-ray diffraction (XRD) technique, like micro-XRD or synchrotron XRD, to determine the structural distribution of elements could enable us to derive a more detailed chemical reaction for the exsolution by elucidating the changes in oxidation state, and structural rearrangement, involved. This could be of benefit not just to the study of shergottites, where this phenomenon was observed in this study, but also to other meteorite types where exsolution of spinel has been inferred from petrography of a number of mineral phases (e.g. exsolution of spinel from pyroxenes in eucrites).

A second future research project is into the variable cooling rates inferred from phenocryst and groundmass assemblages in the Tissint meteorite. Olivine phenocrysts within Tissint have large, compositionally homogeneous, cores, indicative of a very slow cooling rate that allowed equilibrium, or nearly equilibrium, crystallization of olivine from the liquid (Balta et al., 2015; Basu Sarbadhikari et al., 2016). This is mantled by a more rapidly changing rim, although some of the olivine in the rim is still known to be in compositional equilibrium with the early-formed olivine-spinel-pyroxene mineral

assemblage. If the inferred gas-escape mechanism for oxidation is correct, then this portion of the olivine rim should have formed before the eruption or emplacement event that allowed gas escape, suggesting an intermediate cooling rate. Finally, the groundmass has a much finer grained texture, consistent with a relatively rapid cooling rate. None of the experiments performed have addressed either different, or variable, cooling rates, and so no interpretations have been made about the effect a variable cooling rate would have on the compositions of minerals produced by experiment. This is worth addressing as mineral growth kinetics are a known complication in petrogenesis, and have been demonstrated to be important factors in several of the processes invoked in the studies presented here (e.g. peritectic resorption, mineral exsolution, spinel nucleation, plagioclase formation, etc...).

A third research project, complemented by the second, would be to investigate the occurrence of feathered zoning of P in olivine. Feathered zoning of P has been observed in a few olivine-phyric shergottites (e.g. Tissint, Basu Sarbadhikari et al., 2016), but its origin is unclear. Observing feathered P zoning in olivine in a single hybrid experiment, but not in others, suggests either that the feathered P zoning only occurs occasionally (or is only observable in specific structural orientations) and that the olivine grains were under-sampled in x-ray data, or that the single experiment hit on the exact conditions under which it formed. Further study should begin by repeating the experiment to verify that forming the feathered P zone was not a low-probability event, but due to the experimental parameters; if successful, variants of the experiment should be performed to outline the conditions under which the zone forms in an attempt to determine its origin.

## **5.2 Summary, and questions for further study of eucrites**

The partial melting experiments on a zoned eucrite, NWA 7035, have proven fruitful thus far. It is intriguing that a wide range of partial melts can be mixed with the bulk composition of Juvinas to produce the rare earth element trend of Stannern, potentially relating the Stannern trend to the main group trend as discussed by Barrat et al. (2007), although the mismatch with Sc and Mg# requires a further explanation. The observation of experimentally-produced textures reminiscent of metasomatic textures

observed in natural samples suggests that metasomatism on the HED parent body may be by low-degree partial melts of eucritic material, rather than an aqueous or S-rich fluid (e.g. Barrat et al., 2011).

There are two avenues for further experimental research into the origin of the Stannern trend from this work. This first has already been directly proposed in Ch. 4: identifying a different, more magnesian, zoned eucrite composition to repeat these experiments with to see if a more magnesian melt can be produced. The second is to generate a range of partial melt compositions from typical eucrites to investigate how the melt composition changes if a metamorphosed composition is utilized. Although typical eucrites are not consistent with what we would expect in a pristine eucritic crust, they may be more representative of a deep crustal section that has been buried by successive eruptions and heated to near solidus conditions. Similarly, expanding the existing set of experiments on NWA 7035 by further varying the equilibration times may also help reconcile the Sc and Mg# composition of the melt with the Stannern trend, as longer durations should increase the involvement of plagioclase, lowering the Sc content of the melt, and allow pyroxene to further equilibrate with the melt as larger zones are metasomatized, potentially also lowering the Mg# of the melt.

The observed metasomatization of pyroxene in heated samples of NWA 7035 needs further characterization. A higher resolution technique should be utilized to measure the composition of mineral inclusions within the high-Fe veins for comparison with meteorite observations. The chemical shift in the host pyroxene composition also needs to be characterized to enable comparison with veins observed in the meteorite record. Finally, longer-duration experiments should be performed to determine if textures consistent with high-degree metasomatism from other meteorites can be experimentally generated.

## References

- CT Server Fe-Ti oxide [ctserver.ofm-research.org/OxideGeothrm/OxideGeothrm.php](http://ctserver.ofm-research.org/OxideGeothrm/OxideGeothrm.php)  
CT Server Ol-Px-Sp [ctserver.ofm-research.org/Olv\\_Spn\\_Opx/index.php](http://ctserver.ofm-research.org/Olv_Spn_Opx/index.php)
- Agee C. B. and Draper D. S. (2004) Experimental constraints on the origin of Martian meteorites and the composition of the Martian mantle. *Earth and Planetary Science Letters* **224**(3-4), 415-429.
- Agee C. B., Wilson N. V., McCubbin F. M., Ziegler K., Polyak V. J., Sharp Z. D., Asmerom Y., Nunn M. H., Shaheen R., Thiemens M. H., Steele A., Fogel M. L., Bowden R., Glamoclija M., Zhang Z., and Elardo S. M. (2013) Unique Meteorite from Early Amazonian Mars: Water-Rich Basaltic Breccia Northwest Africa 7034. *Science* **339**(6121), 780-785.
- Ahrens L. H. (1970) The composition of stony meteorites (VII) the special significance of eucrites Stannern and Nuevo Laredo in lunar-meteorite comparative studies. *Earth and Planetary Science Letters* **9**(4), 341-344.
- Aigner-Torres M., Blundy J., Ulmer P., and Pettke T. (2007) Laser Ablation ICPMS study of trace element partitioning between plagioclase and basaltic melts: an experimental approach. *Contributions to Mineralogy and Petrology* **153**(6), 647-667.
- Asimow P. D. and Ghiorso M. S. (1998) Algorithmic modifications extending MELTS to calculate subsolidus phase relations. *American Mineralogist* **83**(9-10), 1127-1132.
- Bacon C. R. and Hirschmann M. M. (1988) Mg/Mn partitioning as a test for equilibrium between coexisting Fe-Ti oxides. *American Mineralogist* **73**(1-2), 57-61.
- Ballhaus C., Berry R. F., and Green D. H. (1991) High pressure experimental calibration of the olivine-orthopyroxene-spinel oxygen geobarometer: implications for the oxidation state of the upper mantle. *Contributions to Mineralogy and Petrology* **107**(1), 27-40.
- Balta J. B., Sanborn M. E., Udry A., Wadhwa M., and McSween H. Y. (2015) Petrology and trace element geochemistry of Tissint, the newest shergottite fall. *Meteoritics & Planetary Science* **50**(1), 63-85.
- Barrat J. A., Blichert-Toft J., Gillet P., and Keller F. (2000) The differentiation of eucrites: The role of in situ crystallization. *Meteoritics & Planetary Science* **35**(5), 1087-1100.
- Barrat J. A., Gillet P., Sautter V., Jambon A., Javoy M., Göpel C., Lesourd M., Keller F., and Petit E. (2002a) Petrology and chemistry of the basaltic shergottite North West Africa 480. *Meteoritics & Planetary Science* **37**(4), 487-499.
- Barrat J. A., Jambon A., Bohn M., Gillet P. h., Sautter V., Göpel C., Lesourd M., and Keller F. (2002b) Petrology and chemistry of the Picritic Shergottite North West Africa 1068 (NWA 1068). *Geochimica et Cosmochimica Acta* **66**(19), 3505-3518.

- Barrat J. A., Yamaguchi A., Bunch T. E., Bohn M., Bollinger C., and Ceuleneer G. (2011) Possible fluid-rock interactions on differentiated asteroids recorded in eucritic meteorites. *Geochimica et Cosmochimica Acta* **75**(13), 3839-3852.
- Barrat J. A., Yamaguchi A., Greenwood R. C., Bohn M., Cotten J., Benoit M., and Franchi I. A. (2007) The Stannern trend eucrites: Contamination of main group eucrite magmas by crustal partial melts. *Geochimica et Cosmochimica Acta* **71**, 4108-4124.
- Basu Sarbadhikari A., Babu E. V. S. S. K., Vijaya Kumar T., and Chennaoui Aoudjehane H. (2016) Martian meteorite Tissint records unique petrogenesis among the depleted shergottites. *Meteoritics & Planetary Science* **51**(9), 1588-1610.
- Basu Sarbadhikari A., Day J. M. D., Liu Y., Rumble III D., and Taylor L. A. (2009) Petrogenesis of olivine-phyric shergottite Larkman Nunatak 06319: Implications for enriched components in martian basalts. *Geochimica et Cosmochimica Acta* **73**(7), 2190-2214.
- Beck A. W. and McSween Jr H. Y. (2010) Diogenites as polymict breccias composed of orthopyroxenite and harzburgite. *Meteoritics & Planetary Science* **45**(5), 850-872.
- Beck A. W., Mittlefehldt D. W., McSween Jr H. Y., Rumble Iii D., Lee C.-T. A., and Bodnar R. J. (2011) MIL 03443, a dunite from asteroid 4 Vesta: Evidence for its classification and cumulate origin. *Meteoritics & Planetary Science* **46**(8), 1133-1151.
- Becker R. H. and Pepin R. O. (1984) The case for a martian origin of the shergottites: nitrogen and noble gases in EETA79001. *Earth and Planetary Science Letters* **69**, 225-242.
- Berry A. J. and O'Neill H. S. C. (2004) A XANES determination of the oxidation state of chromium in silicate glasses. *American Mineralogist* **89**(5-6), 790-798.
- Blinova A. and Herd C. D. K. (2009) Experimental study of polybaric REE partitioning between olivine, pyroxene and melt of the Yamato 980459 composition: Insights into the petrogenesis of depleted shergottites. *Geochimica et Cosmochimica Acta* **73**(11), 3471-3492.
- Bogard D. and Johnson P. (1983) Martian gases in an Antarctic meteorite? *Science* **221**, 651-654.
- Bogard D. D. and Garrison D. H. (2003) <sup>39</sup>Ar-<sup>40</sup>Ar ages of eucrites and thermal history of asteroid 4 Vesta. *Meteoritics & Planetary Science* **38**(5), 669-710.
- Bogard D. D., Nyquist L. E., and Johnson P. (1984) Noble gas contents of shergottites and implications for the Martian origin of SNC meteorites. *Geochimica et Cosmochimica Acta* **48**(9), 1723-1739.
- Borg L. E., Brennecka G. A., and Symes S. J. (2016) Accretion timescale and impact history of Mars deduced from the isotopic systematics of martian meteorites. *Geochimica et Cosmochimica Acta* **175**, 150-167.
- Borg L. E. and Draper D. S. (2003) A petrogenetic model for the origin and compositional variation of the martian basaltic meteorites. *Meteoritics & Planetary Science* **38**(12), 1713-1731.
- Borg L. E., Nyquist L. E., Taylor L. A., Wiesmann H., and Shih C.-Y. (1997) Constraints on Martian differentiation processes from Rb-Sr and Sm-Nd isotopic analyses

- of the basaltic shergottite QUE 94201. *Geochimica et Cosmochimica Acta* **61**(22), 4915-4931.
- Borg L. E., Nyquist L. E., Wiesmann H., Shih C.-Y., and Reese Y. (2003) The age of Dar al Gani 476 and the differentiation history of the martian meteorites inferred from their radiogenic isotopic systematics. *Geochimica et Cosmochimica Acta* **67**(18), 3519-3536.
- Borisov A. and Jones J. H. (1999) An evaluation of Re, as an alternative to Pt, for the 1 bar loop technique; an experimental study at 1400 degrees C. *American Mineralogist* **84**(10), 1528-1534.
- Brennecka G. A., Borg L. E., and Wadhwa M. (2014) Insights into the Martian mantle: The age and isotopics of the meteorite fall Tissint. *Meteoritics & Planetary Science* **49**(3), 412-418.
- Bridges J. C. and Warren P. H. (2006) The SNC meteorites: basaltic igneous processes on Mars. *Journal of the Geological Society* **163**(2), 229-251.
- Buening D. K. and Buseck P. R. (1973) Fe-Mg lattice diffusion in olivine. *Journal of Geophysical Research* **78**(29), 6852-6862.
- Cartwright J. A., Ott U., Mittlefehldt D. W., Herrin J. S., Herrmann S., Mertzman S. A., Mertzman K. R., Peng Z. X., and Quinn J. E. (2013) The quest for regolithic howardites. Part 1: Two trends uncovered using noble gases. *Geochimica et Cosmochimica Acta* **105**(0), 395-421.
- Castle N. and Herd C. D. K. (2014) Observational and Experimental Results for Tissint Magma Formation: The Story Thus Far. In *Lunar and Planetary Science Conference*, pp. 2334.
- Castle N. and Herd C. D. K. (2017) Experimental petrology of the Tissint meteorite: Redox estimates, crystallization curves, and evaluation of petrogenetic models. *Meteoritics & Planetary Science*, n/a-n/a.
- Chakraborty S. (1997) Rates and mechanisms of Fe-Mg interdiffusion in olivine at 980°–1300°C. *Journal of Geophysical Research: Solid Earth* **102**(B6), 12317-12331.
- Chennaoui Aoudjehane H., Avice G., Barrat J.-A., Boudouma O., Chen G., Duke M. J. M., Franchi I. A., Gattacceca J., Grady M. M., Greenwood R. C., Herd C. D. K., Hewins R., Jambon A., Marty B., Rochette P., Smith C. L., Sautter V., Verchovsky A., Weber P., and Zanda B. (2012) Tissint Martian Meteorite: A Fresh Look at the Interior, Surface, and Atmosphere of Mars. *Science* **338**(6108), 785-788.
- Clayton R. N. and Mayeda T. K. (1983) Oxygen isotopes in eucrites, shergottites, nakhlites, and chassignites. *Earth and Planetary Science Letters* **62**(1), 1-6.
- Cross W., Iddings J. P., Pirsson L. V., and Washington H. S. (1902) A Quantitative Chemico-Mineralogical Classification and Nomenclature of Igneous Rocks. *The Journal of Geology* **10**(6), 555-690.
- De Sanctis M. C., Ammannito E., Capria M. T., Tosi F., Capaccioni F., Zambon F., Carraro F., Fonte S., Frigeri A., Jaumann R., Magni G., Marchi S., McCord T. B., McFadden L. A., McSween H. Y., Mittlefehldt D. W., Nathues A., Palomba E., Pieters C. M., Raymond C. A., Russell C. T., Toplis M. J., and Turrini D. (2012) Spectroscopic Characterization of Mineralogy and Its Diversity Across Vesta. *Science* **336**(6082), 697-700.

- Debaille V., Brandon A. D., Yin Q. Z., and Jacobsen B. (2007) Coupled  $^{142}\text{Nd}$ - $^{143}\text{Nd}$  evidence for a protracted magma ocean in Mars. *Nature* **450**(7169), 525-528.
- DePaolo D. J. (1981) Trace element and isotopic effects of combined wallrock assimilation and fractional crystallization. *Earth and Planetary Science Letters* **53**(2), 189-202.
- Duke M. B. and Silver L. T. (1967) Petrology of eucrites, howardites and mesosiderites. *Geochimica et Cosmochimica Acta* **31**(10), 1637-1665.
- Dundas C., Keszthelyi L., Jaeger W., and Milazzo M. (2016) Tilted-Facet Terrain of Elysium Planitia, Mars. In *Lunar and Planetary Science Conference*, pp. 2334.
- Filiberto J., Chin E., Day J. M. D., Franchi I. A., Greenwood R. C., Gross J., Penniston-Dorland S. C., Schwenzer S. P., and Treiman A. H. (2012) Geochemistry of intermediate olivine-phyric shergottite Northwest Africa 6234, with similarities to basaltic shergottite Northwest Africa 480 and olivine-phyric shergottite Northwest Africa 2990. *Meteoritics & Planetary Science* **47**(8), 1256-1273.
- Filiberto J. and Dasgupta R. (2011)  $\text{Fe}^{2+}$ -Mg partitioning between olivine and basaltic melts: Applications to genesis of olivine-phyric shergottites and conditions of melting in the Martian interior. *Earth and Planetary Science Letters* **304**(3-4), 527-537.
- Fowler G. W., Papike J. J., Spilde M. N., and Shearer C. K. (1994) Diogenites as asteroidal cumulates: Insights from orthopyroxene major and minor element chemistry. *Geochimica et Cosmochimica Acta* **58**(18), 3921-3929.
- Fowler G. W., Shearer C. K., Papike J. J., and Layne G. D. (1995) Diogenites as asteroidal cumulates: insights from orthopyroxene trace element chemistry. *Geochimica et Cosmochimica Acta* **59**(14), 3071-3084.
- Fuhrman M., Papike J. J., and Ridings R. (1982) Howardites and polymict eucrites: Regolith samples from the eucrite parent body - Petrology of Bholgati, Bununu, Kapoeta, and ALHA 76005. In *Lunar and Planetary Science Conference Proceedings* (ed. R. B. Merrill), pp. 1257-1279.
- Ghiorso M. and Sack O. (1991) Fe-Ti oxide geothermometry: thermodynamic formulation and the estimation of intensive variables in silicic magmas. *Contributions to Mineralogy and Petrology* **108**(4), 485-510.
- Ghiorso M. S. and Evans B. W. (2008) Thermodynamics of Rhombohedral Oxide Solid Solutions and a Revision of the Fe-Ti Two-Oxide Geothermometer and Oxygen-Barometer. *American Journal of Science* **308**(9), 957-1039.
- Ghiorso M. S. and Sack R. O. (1995) Chemical mass transfer in magmatic processes IV. A revised and internally consistent thermodynamic model for the interpolation and extrapolation of liquid-solid equilibria in magmatic systems at elevated temperatures and pressures. *Contributions to Mineralogy and Petrology* **119**(2), 197-212.
- Goodrich C. A., Herd C. D. K., and Taylor L. A. (2003) Spinels and oxygen fugacity in olivine-phyric and lherzolithic shergottites. *Meteoritics & Planetary Science* **38**(12), 1773-1792.
- Greenwood R. C., Burbine T. H., Miller M. F., and Franchi I. A. (2016) Melting and differentiation of early-formed asteroids: The perspective from high precision oxygen isotope studies. *Chemie der Erde - Geochemistry*.

- Greenwood R. C., Franchi I. A., Jambon A., and Buchanan P. C. (2005) Widespread magma oceans on asteroidal bodies in the early Solar System. *Nature* **435**(7044), 916-918.
- Gross J., Filiberto J., Herd C. D. K., Daswani M. M., Schwenzer S. P., and Treiman A. H. (2013) Petrography, mineral chemistry, and crystallization history of olivine-phyric shergottite NWA 6234: A new melt composition. *Meteoritics & Planetary Science* **48**(5), 854-871.
- Gross J., Treiman A. H., Filiberto J., and Herd C. D. K. (2011) Primitive olivine-phyric shergottite NWA 5789: Petrography, mineral chemistry, and cooling history imply a magma similar to Yamato-980459. *Meteoritics & Planetary Science* **46**(1), 116-133.
- Grove T. L. and Bartels K. S. (1992) The relation between diogenite cumulates and eucrite magmas. In *Lunar and Planetary Science Conference Proceedings*, pp. 437-445.
- Gualda G. A. R., Ghiorso M. S., Lemons R. V., and Carley T. L. (2012) Rhyolite-MELTS: a Modified Calibration of MELTS Optimized for Silica-rich, Fluid-bearing Magmatic Systems. *Journal of Petrology*.
- Hale V. P. S., McSween Jr H. Y., and McKay G. A. (1999) Re-evaluation of intercumulus liquid composition and oxidation state for the Shergotty meteorite. *Geochimica et Cosmochimica Acta* **63**(9), 1459-1470.
- Hanson B. and Jones J. H. (1998) The systematics of Cr<sup>3+</sup> and Cr<sup>2+</sup> partitioning between olivine and liquid in the presence of spinel. *American Mineralogist* **83**(7), 669-684.
- Herd C. D., Dwarzski R. E., and Shearer C. K. (2009) The behavior of Co and Ni in olivine in planetary basalts: An experimental investigation. *American Mineralogist* **94**(2-3), 244-255.
- Herd C. D. K. (2003) Oxygen fugacity of olivine-phyric martian basalts and the components within the mantle and crust of Mars. *Meteoritics and Planetary Science* **38**, 1793-1805.
- Herd C. D. K. (2006) Insights into the redox history of the NWA 1068/1110 martian basalt from mineral equilibria and vanadium oxybarometry. *American Mineralogist* **91**(10), 1616-1627.
- Herd C. D. K. (2008) Basalts as Probes of Planetary Interior Redox State. *Reviews in Mineralogy and Geochemistry* **68**(1), 527-553.
- Herd C. D. K., Borg L. E., Jones J. H., and Papike J. J. (2002a) Oxygen fugacity and geochemical variations in the martian basalts: implications for martian basalt petrogenesis and the oxidation state of the upper mantle of Mars. *Geochimica et Cosmochimica Acta* **66**(11), 2025-2036.
- Herd C. D. K., Duke M. J. M., Bryden C. D., and Pearson D. G. (2013) Tissint Among the Shergottites: Parental Melt Composition, Redox State, La/Yb and V/Sc. *LPSC XLIV* **1719**, 2683.
- Herd C. D. K., Schwandt C. S., Jones J. H., and Papike J. J. (2002b) An experimental and petrographic investigation of Elephant Moraine 79001 lithology A: Implications for its petrogenesis and the partitioning of chromium and vanadium in a martian basalt. *Meteoritics and Planetary Science* **37**, 987-1000.

- Herd C. D. K., Treiman A. H., McKay G. A., and Shearer C. K. (2004) The behavior of Li and B during planetary basalt crystallization. *American Mineralogist* **89**(5-6), 832-840.
- Hewins R. and Newsom H. (1988) Igneous activity in the early solar system. *Meteorites and the early solar system* **1**, 73-101.
- Hewins R. H., Zanda B., Humayun M., Nemchin A., Lorand J.-P., Pont S., Deldicque D., Bellucci J. J., Beck P., Leroux H., Marinova M., Remusat L., Göpel C., Lewin E., Grange M., Kennedy A., and Whitehouse M. J. (2016) Regolith breccia Northwest Africa 7533: Mineralogy and petrology with implications for early Mars. *Meteoritics & Planetary Science*, n/a-n/a.
- Hsu W. and Crozaz G. (1997) Mineral chemistry and the petrogenesis of eucrites: II. Cumulate eucrites. *Geochimica et Cosmochimica Acta* **61**(6), 1293-1302.
- Humayun M., Nemchin A., Zanda B., Hewins R. H., Grange M., Kennedy A., Lorand J. P., Göpel C., Fieni C., Pont S., and Deldicque D. (2013) Origin and age of the earliest Martian crust from meteorite NWA 7533. *Nature* **503**(7477), 513.
- Iishi K., Kadomi M., and Okamoto K. (1989) Synthesis of laihunite by heating Fe-Mn olivine in air. *Neues Jahrbuch für Mineralogie Monatshefte*(6), 245-254.
- Martian Meteorites <http://www.imca.cc/mars/martian-meteorites.htm>
- Irving A. J., Kuehner S. M., Herd C. D. K., Gellissen M., Korotev R. L., Puchtel I., Walker R. J., Lapen T., and Rumble D. (2010) Petrologic, Elemental and Multi-Isotopic Characterization of Permafic Olivine-Phyric Shergottite Northwest Africa 5789: A Primitive Magma Derived from Depleted Martian Mantle. In *Lunar and Planetary Science Conference*, pp. 1547.
- Ito M. and Ganguly J. (2006) Diffusion kinetics of Cr in olivine and <sup>53</sup>Mn-<sup>53</sup>Cr thermochronology of early solar system objects. *Geochimica et Cosmochimica Acta* **70**(3), 799-809.
- Jurewicz A. J. G., Mittlefehldt D. W., and Jones J. H. (1993) Experimental partial melting of the Allende (CV) and Murchison (CM) chondrites and the origin of asteroidal basalts. *Geochimica et Cosmochimica Acta* **57**(9), 2123-2139.
- Jurewicz A. J. G., Mittlefehldt D. W., and Jones J. H. (1995) Experimental partial melting of the St. Severin (LL) and Lost City (H) chondrites. *Geochimica et Cosmochimica Acta* **59**(2), 391-408.
- Kiefer W. S. (2003) Melting in the martian mantle: Shergottite formation and implications for present-day mantle convection on Mars. *Meteoritics & Planetary Science* **38**(12), 1815-1832.
- Kleine T., Mezger K., Münker C., Palme H., and Bischoff A. (2004) <sup>182</sup>Hf-<sup>182</sup>W isotope systematics of chondrites, eucrites, and martian meteorites: Chronology of core formation and early mantle differentiation in Vesta and Mars. *Geochimica et Cosmochimica Acta* **68**(13), 2935-2946.
- Kring D. A., Gleason J. D., Swindle T. D., Nishiizumi K., Caffee M. W., Hill D. H., Jull A. J. T., and Boynton W. V. (2003) Composition of the first bulk melt sample from a volcanic region of Mars: Queen Alexandra Range 94201. *Meteoritics and Planetary Science* **38**, 1833-1848.
- Kushiro I. (1968) Compositions of magmas formed by partial zone melting of the earth's upper mantle. *Journal of Geophysical Research* **73**(2), 619-634.

- Larson H. P. and Fink U. (1975) Infrared spectral observations of asteroid 4 Vesta. *Icarus* **26**(4), 420-427.
- Laul J. C., Smith M. R., Wänke H., Jagoutz E., Dreibus G., Palme H., Spettel B., Burghelle A., Lipschutz M. E., and Verkoeteren R. M. (1986) Chemical systematics of the shergotty meteorite and the composition of its parent body (Mars). *Geochimica et Cosmochimica Acta* **50**(6), 909-926.
- Longhi J. and Pan V. (1989) The parent magmas of the SNC meteorites. In *19th Lunar and Planetary Science Conference Proceedings* (ed. G. Ryder), pp. 451-464.
- Lugmair G. and Shukolyukov A. (1998) Early solar system timescales according to <sup>53</sup>Mn-<sup>53</sup>Cr systematics. *Geochimica et Cosmochimica Acta* **62**(16), 2863-2886.
- Lugmair G. and Shukolyukov A. (2001) The Leonard Award Address: Presented 2000 August 30, Chicago, Illinois, USA: Early solar system events and timescales. *Meteoritics & Planetary Science* **36**(8), 1017-1026.
- Mandler B. E. and Elkins-Tanton L. T. (2013) The origin of eucrites, diogenites, and olivine diogenites: Magma ocean crystallization and shallow magma chamber processes on Vesta. *Meteoritics & Planetary Science* **48**(11), 2333-2349.
- Mattioli G. S. and Wood B. J. (1988) Magnetite activities across the MgAl<sub>2</sub>O<sub>4</sub>-Fe<sub>3</sub>O<sub>4</sub> spinel join, with application to thermobarometric estimates of upper mantle oxygen fugacity. *Contributions to Mineralogy and Petrology* **98**(2), 148-162.
- Mayne G. R., McSween Jr. H. Y., McCoy T. J., and Gale A. (2009) Petrology of the unbrecciated eucrites. *Geochimica et Cosmochimica Acta* **73**, 794-819.
- Mayne R. G., Smith S. E., and Corrigan C. M. (2016) Hiding in the howardites: Unequilibrated eucrite clasts as a guide to the formation of Vesta's crust. *Meteoritics & Planetary Science*, n/a-n/a.
- McCord T. B., Adams J. B., and Johnson T. V. (1970) Asteroid Vesta: Spectral Reflectivity and Compositional Implications. *Science* **168**(3938), 1445-1447.
- McCoy T. J., Corrigan C. M., and Herd C. D. K. (2011) Combining meteorites and missions to explore Mars. *Proceedings of the National Academy of Sciences* **108**(48), 19159-19164.
- McCoy T. J., Taylor G. J., and Keil K. (1992) Zagami: Product of a two-stage magmatic history. *Geochimica et Cosmochimica Acta* **56**(9), 3571-3582.
- McCubbin F. M., Hauri E. H., Elardo S. M., Vander Kaaden K. E., Wang J., and Shearer C. K. (2012) Hydrous melting of the martian mantle produced both depleted and enriched shergottites. *Geology* **40**(8), 683-686.
- McKay G. A. and Weill D. F. (1976) Petrogenesis of KREEP. In *Lunar and Planetary Science Conference Proceedings* (ed. D. C. Kinsler), pp. 2427-2447.
- McKay G. A. and Weill D. F. (1977) KREEP petrogenesis revisited. In *Lunar and Planetary Science Conference Proceedings* (ed. R. B. Merrill), pp. 2339-2355.
- McSween H. Y., Binzel R. P., De Sanctis M. C., Ammannito E., Prettyman T. H., Beck A. W., Reddy V., Le Corre L., Gaffey M. J., McCord T. B., Raymond C. A., Russell C. T., and the Dawn Science T. (2013) Dawn; the Vesta-HED connection; and the geologic context for eucrites, diogenites, and howardites. *Meteoritics & Planetary Science* **48**(11), 2090-2104.
- McSween H. Y., Jr. (1994) What we have learned about Mars from SNC meteorites. *Meteoritics* **29**, 757-779.

- McSween H. Y. and Treiman A. H. (1998) Martian meteorites. *Reviews in Mineralogy and Geochemistry* **36**(1), 6.1-6.53.
- McSween Jr H. Y. and Jarosewich E. (1983) Petrogenesis of the Elephant Moraine A79001 meteorite: Multiple magma pulses on the shergottite parent body. *Geochimica et Cosmochimica Acta* **47**(8), 1501-1513.
- Metzler K., Bobe K. D., Palme H., Spettel B., and Stöckhert D. (1995) Thermal and impact metamorphism on the HED parent asteroid. *Planetary and Space Science* **43**(3-4), 499-525.
- Mikouchi T., Miyamoto M., and McKay G. A. (1998) Mineralogy of Antarctic basaltic shergottite QUE94201: Similarities to EETA7900 1 (Lithology B) martian meteorite. *Meteoritics and Planetary Science* **33**, 181-189.
- Mittlefehldt D. W. (2005) Ibitira: A basaltic achondrite from a distinct parent asteroid and implications for the Dawn mission. *Meteoritics & Planetary Science* **40**(5), 665-677.
- Mittlefehldt D. W. (2015) Asteroid (4) Vesta: I. The howardite-eucrite-diogenite (HED) clan of meteorites. *Chemie der Erde - Geochemistry* **75**(2), 155-183.
- Mittlefehldt D. W. and Lindstrom M. M. (1997) Magnesian basalt clasts from the EET 92014 and Kapoeta howardites and a discussion of alleged primary magnesian HED basalts. *Geochimica et Cosmochimica Acta* **61**(2), 453-462.
- Mittlefehldt D. W. and Lindstrom M. M. (2003) Geochemistry of eucrites: genesis of basaltic eucrites, and Hf and Ta as petrogenetic indicators for altered antarctic eucrites. *Geochimica et Cosmochimica Acta* **67**(10), 1911-1934.
- Mittlefehldt D. W., McCoy T. J., Goodrich C. A., and Kracher A. (1998) Non-chondritic meteorites from asteroidal bodies. *Reviews in Mineralogy and Geochemistry* **36**(1), 4.1-4.195.
- Miyamoto M., Duke M. B., and McKay D. S. (1985) Chemical zoning and homogenization of Pasamonte-type pyroxene and their bearing on thermal metamorphism of a howardite parent body. In *Lunar and Planetary Science Conference Proceedings*, pp. C629-C635.
- Mysen B. r. O. (1983) The structure of silicate melts. *Annual Review of Earth and Planetary Sciences* **11**, 75.
- Nielsen R. L., Forsythe L. M., Gallahan W. E., and Fisk M. R. (1994) Major- and trace-element magnetite-melt equilibria. *Chemical Geology* **117**(1-4), 167-191.
- Nyquist L. E., Bogard D., Takeda H., Bansal B., Wiesmann H., and Shih C. Y. (1997) Crystallization, recrystallization, and impact-metamorphic ages of eucrites Y792510 and Y791186. *Geochimica et Cosmochimica Acta* **61**(10), 2119-2138.
- Nyquist L. E., Bogard D. D., Shih C. Y., Park J., Reese Y. D., and Irving A. J. (2009a) Concordant Rb-Sr, Sm-Nd, and Ar-Ar ages for Northwest Africa 1460: A 346 Ma old basaltic shergottite related to "lherzolithic" shergottites. *Geochimica et Cosmochimica Acta* **73**(14), 4288-4309.
- Nyquist L. E., Kleine T., Shih C. Y., and Reese Y. D. (2009b) The distribution of short-lived radioisotopes in the early solar system and the chronology of asteroid accretion, differentiation, and secondary mineralization. *Geochimica et Cosmochimica Acta* **73**(17), 5115-5136.

- Nyquist L. E., Reese Y., Wiesmann H., Shih C. Y., and Takeda H. (2003) Fossil  $^{26}\text{Al}$  and  $^{53}\text{Mn}$  in the Asuka 881394 eucrite: evidence of the earliest crust on asteroid 4 Vesta. *Earth and Planetary Science Letters* **214**(1-2), 11-25.
- Nyquist L. E., Takeda H., Bansal B. M., Shih C. Y., Wiesmann H., and Wooden J. L. (1986) Rb-Sr and Sm-Nd Internal Isochron Ages of a Subophitic Basalt Clast and a Matrix Sample from the Y75011 Eucrite. *J. Geophys. Res.* **91**(B8), 8137-8150.
- O'Neill H. S. (1987) Quartz-fayalite-iron and quartz-fayalite-magnetite equilibria and the free energy of formation of fayalite ( $\text{Fe}_2\text{SiO}_4$ ) and magnetite ( $\text{Fe}_3\text{O}_4$ ). *American Mineralogist* **72**(1-2), 67-75.
- O'Neill H. S. C. (1988) Systems Fe-O and Cu-O: thermodynamic data for the equilibria Fe-'FeO', Fe-Fe<sub>3</sub>O<sub>4</sub>, 'FeO'-Fe<sub>3</sub>O<sub>4</sub>, Fe<sub>3</sub>O<sub>4</sub>-Fe<sub>2</sub>O<sub>3</sub>, Cu-Cu<sub>2</sub>O, and Cu<sub>2</sub>O-CuO from emf measurements. *Am. Mineral* **73**, 470-486.
- Oeser M., Dohmen R., Horn I., Schuth S., and Weyer S. (2015) Processes and time scales of magmatic evolution as revealed by Fe-Mg chemical and isotopic zoning in natural olivines. *Geochimica et Cosmochimica Acta* **154**, 130-150.
- Ott U. (1988) Noble gases in SNC meteorites: Shergotty, Nakhla, Chassigny. *Geochimica et Cosmochimica Acta* **52**(7), 1937-1948.
- Owen T. (1992) The composition and early history of the atmosphere of Mars. *Mars*, 818-834.
- Owen T., Biemann K., Rushneck D., Biller J., Howarth D., and Lafleur A. (1977) The composition of the atmosphere at the surface of Mars. *Journal of Geophysical Research* **82**(28), 4635-4639.
- Papike J. J., Karner J. M., and Shearer C. K. (2005) Comparative planetary mineralogy: Valence state partitioning of Cr, Fe, Ti, and V among crystallographic sites in olivine, pyroxene, and spinel from planetary basalts. *American Mineralogist* **90**(2-3), 277-290.
- Papike J. J., Karner J. M., Shearer C. K., and Burger P. V. (2009) Silicate mineralogy of martian meteorites. *Geochimica et Cosmochimica Acta* **73**(24), 7443-7485.
- Pepin R. O. and Carr M. H. (1992) Major issues and outstanding questions. *Mars*, 120-143.
- Peslier A. H., Hnatyshin D., Herd C. D. K., Walton E. L., Brandon A. D., Lapen T. J., and Shafer J. T. (2010) Crystallization, melt inclusion, and redox history of a Martian meteorite: Olivine-phyric shergottite Larkman Nunatak 06319. *Geochimica et Cosmochimica Acta* **74**(15), 4543-4576.
- Pruseth K. L. (2009a) Calculation of the CIPW norm: New formulas. *Journal of Earth System Science* **118**(1), 101-113.
- Pruseth K. L. (2009b) MATNORM: Calculating NORM using composition matrices. *Computers & Geosciences* **35**, 1785-1788.
- Pun A. and Papike J. J. (1995) Ion microprobe investigation of exsolved pyroxenes in cumulate eucrites: Determination of selected trace-element partition coefficients. *Geochimica et Cosmochimica Acta* **59**(11), 2279-2289.
- Pun A. and Papike J. J. (1996) Unequilibrated eucrites and the equilibrated Juvinas eucrite; pyroxene REE systematics and major, minor, and trace element zoning. *American Mineralogist* **81**(11-12), 1438-1451.

- Pun A., Papike J. J., and Layne G. D. (1997) Subsolidus REE partitioning between pyroxene and plagioclase in cumulate eucrites: An ion microprobe investigation. *Geochimica et Cosmochimica Acta* **61**(23), 5089-5097.
- Quitté G., Birck J.-L., and Allègre C. J. (2000) 182Hf-182W systematics in eucrites: the puzzle of iron segregation in the early solar system. *Earth and Planetary Science Letters* **184**(1), 83-94.
- Rapp J. F., Draper D. S., and Mercer C. M. (2013) Anhydrous liquid line of descent of Yamato-980459 and evolution of Martian parental magmas. *Meteoritics & Planetary Science* **48**(10), 1780-1799.
- Righter K. and Drake M. J. (1997) A magma ocean on Vesta: Core formation and petrogenesis of eucrites and diogenites. *Meteoritics & Planetary Science* **32**(6), 929-944.
- Righter K., Leeman W. P., and Hervig R. L. (2006) Partitioning of Ni, Co and V between spinel-structured oxides and silicate melts: Importance of spinel composition. *Chemical Geology* **227**(1-2), 1-25.
- Roeder P. L. and Reynolds I. (1991) Crystallization of Chromite and Chromium Solubility in Basaltic Melts. *Journal of Petrology* **32**(5), 909-934.
- Roszjar J., Metzler K., Bischoff A., Barrat J.-A., Geisler T., Greenwood R. C., Franchi I. A., and Klemme S. (2011) Thermal history of Northwest Africa 5073--A coarse-grained Stannern-trend eucrite containing cm-sized pyroxenes and large zircon grains. *Meteoritics & Planetary Science* **46**(11), 1754-1773.
- Roszjar J., Metzler K., Bischoff A., Greenwood R., and Franchi I. (2009) Northwest Africa (NWA) 5073-An Eucritic Basalt with cm-sized Pyroxenes. *Meteoritics and Planetary Science Supplement* **72**, 5202.
- Rubin A. E., Warren P. H., Greenwood J. P., Verish R. S., Leshin L. A., Hervig R. L., Clayton R. N., and Mayeda T. K. (2000) Los Angeles: The most differentiated basaltic martian meteorite. *Geology* **28**(11), 1011-1014.
- Ruzicka A., Grossman J. N., and Garvie L. (2014) The Meteoritical Bulletin, No. 100, 2014 June. *Meteoritics & Planetary Science* **49**(8), E1-E101.
- Ruzicka A., Snyder G. A., and Taylor L. A. (1997) Vesta as the howardite, eucrite and diogenite parent body: Implications for the size of a core and for large-scale differentiation. *Meteoritics & Planetary Science* **32**(6), 825-840.
- Sack R. O. and Ghiorso M. S. (1989) Importance of considerations of mixing properties in establishing an internally consistent thermodynamic database: thermochemistry of minerals in the system Mg<sub>2</sub>SiO<sub>4</sub>-Fe<sub>2</sub>SiO<sub>4</sub>-SiO<sub>2</sub>. *Contributions to Mineralogy and Petrology* **102**(1), 41-68.
- Sack R. O. and Ghiorso M. S. (1991a) Chromian spinels as petrogenetic indicators; thermodynamics and petrological applications. *American Mineralogist* **76**(5-6), 827-847.
- Sack R. O. and Ghiorso M. S. (1991b) An internally consistent model for the thermodynamic properties of Fe-Mg-titanomagnetite-aluminate spinels. *Contributions to Mineralogy and Petrology* **106**(4), 474-505.
- Sack R. O. and Ghiorso M. S. (1994a) Thermodynamics of multicomponent pyroxenes: I. Formulation of a general model. *Contributions to Mineralogy and Petrology* **116**(3), 277-286.

- Sack R. O. and Ghiorso M. S. (1994b) Thermodynamics of multicomponent pyroxenes: II. Phase relations in the quadrilateral. *Contributions to Mineralogy and Petrology* **116**(3), 287-300.
- Sack R. O. and Ghiorso M. S. (1994c) Thermodynamics of multicomponent pyroxenes: III. Calibration of  $\text{Fe}^{2+}(\text{Mg})$ -1,  $\text{TiAl}_2(\text{MgSi}_2)$ -1,  $\text{TiFe}_2\text{Fe}^{3+}(\text{MgSi}_2)$ -1,  $\text{AlFe}_3(\text{MgSi})$ -1,  $\text{NaAl}(\text{CaMg})$ -1,  $\text{Al}_2(\text{MgSi})$ -1 and  $\text{Ca}(\text{Mg})$ -1 exchange reactions between pyroxenes and silicate melts. *Contributions to Mineralogy and Petrology* **118**(3), 271-296.
- Schiller M., Baker J. A., and Bizzarro M. (2010)  $^{26}\text{Al}$ - $^{26}\text{Mg}$  dating of asteroidal magmatism in the young Solar System. *Geochimica et Cosmochimica Acta* **74**(16), 4844-4864.
- Schreiber H. D. and Haskin L. A. (1976) Chromium in basalts: Experimental determination of redox states and partitioning among synthetic silicate phases. In *7th Lunar and Planetary Science Conference Proceedings* (ed. R. B. Merrill), pp. 1221-1259.
- Schwartz J. M. and McCallum I. S. (2005) Comparative study of equilibrated and unequilibrated eucrites: Subsolvus thermal histories of Haraiya and Pasamonte. *American Mineralogist* **90**(11-12), 1871-1886.
- Scott E. R. D., Greenwood R. C., Franchi I. A., and Sanders I. S. (2009) Oxygen isotopic constraints on the origin and parent bodies of eucrites, diogenites, and howardites. *Geochimica et Cosmochimica Acta* **73**(19), 5835-5853.
- Shearer C. K., Aaron P. M., Burger P. V., Guan Y., Bell A. S., and Papike J. J. (2013) Petrogenetic linkages among  $\text{fO}_2$ , isotopic enrichments-depletions and crystallization history in Martian basalts. Evidence from the distribution of phosphorus in olivine megacrysts. *Geochimica et Cosmochimica Acta* **120**(0), 17-38.
- Shearer C. K., Burger P., and Papike J. J. (2010) Petrogenetic relationships between diogenites and olivine diogenites: Implications for magmatism on the HED parent body. *Geochimica et Cosmochimica Acta* **74**(16), 4865-4880.
- Shearer C. K., Burger P. V., Papdce J. J., Borg L. E., Irving A. J., and Herd C. (2008) Petrogenetic linkages among Martian basalts: Implications based on trace element chemistry of olivine. *Meteoritics & Planetary Science* **43**(7), 1241-1258.
- Shearer C. K., Fowler G. W., and Papike J. J. (1997) Petrogenetic models for magmatism on the eucrite parent body: Evidence from orthopyroxene in diogenites. *Meteoritics & Planetary Science* **32**(6), 877-889.
- Sio C. K. I., Dauphas N., Teng F.-Z., Chaussidon M., Helz R. T., and Roskosz M. (2013) Discerning crystal growth from diffusion profiles in zoned olivine by in situ Mg-Fe isotopic analyses. *Geochimica et Cosmochimica Acta* **123**, 302-321.
- Stolper E. (1975) Petrogenesis of eucrite, howardite and diogenite meteorites. *Nature* **258**(5532), 220-222.
- Stolper E. (1977) Experimental petrology of eucritic meteorites. *Geochimica et Cosmochimica Acta* **41**(5), 587-611.
- Stolper E. and McSween Jr H. Y. (1979) Petrology and origin of the shergottite meteorites. *Geochimica et Cosmochimica Acta* **43**(9), 1475-1498.

- Stolper E., McSween Jr H. Y., and Hays J. F. (1979) A petrogenetic model of the relationships among achondritic meteorites. *Geochimica et Cosmochimica Acta* **43**(4), 589-602.
- Symes S. J. K., Borg L. E., Shearer C. K., and Irving A. J. (2008) The age of the martian meteorite Northwest Africa 1195 and the differentiation history of the shergottites. *Geochimica et Cosmochimica Acta* **72**(6), 1696-1710.
- Takeda H. and Graham A. L. (1991) Degree of equilibration of eucritic pyroxenes and thermal metamorphism of the earliest planetary crust. *Meteoritics* **26**, 129-134.
- Takeda H., Mori H., and Bogard D. D. (1994) Mineralogy and <sup>39</sup>Ar-<sup>40</sup>Ar age of an old pristine basalt: Thermal history of the HED parent body. *Earth and Planetary Science Letters* **122**(1-2), 183-194.
- Takeda H., Wooden J. L., Mori H., Delaney J. S., Prinz M., and Nyquist L. E. (1983) Comparison of Yamato and Victoria Land polymict eucrites: A view from mineralogical and isotopic studies. *Journal of Geophysical Research: Solid Earth* **88**(S01), B245-B256.
- Treiman A. H. (1996) The perils of partition: Difficulties in retrieving magma compositions from chemically equilibrated basaltic meteorites. *Geochimica et Cosmochimica Acta* **60**(1), 147-155.
- Treiman A. H. (1997) The parent magmas of the cumulate eucrites: A mass balance approach. *Meteoritics & Planetary Science* **32**(2), 217-230.
- Treiman A. H. and Drake M. J. (1985) Basaltic volcanism on the eucrite parent body: petrology and chemistry of the polymict eucrite ALHA80102. *Journal of Geophysical Research* **90**, 619.
- Treiman A. H., Gleason J. D., and Bogard D. D. (2000) The SNC meteorites are from Mars. *Planetary and Space Science* **48**, 1213-1230.
- Treiman A. H., Lanzirotti A., and Xirouchakis D. (2004) Ancient water on asteroid 4 Vesta: evidence from a quartz veinlet in the Serra de Mag<sup>√</sup>© eucrite meteorite. *Earth and Planetary Science Letters* **219**(3,À4), 189-199.
- Usui T., McSween Jr H. Y., and Floss C. (2008) Petrogenesis of olivine-phyric shergottite Yamato 980459, revisited. *Geochimica et Cosmochimica Acta* **72**(6), 1711-1730.
- Wadhwa M. (2001) Redox State of Mars' Upper Mantle and Crust from Eu Anomalies in Shergottite Pyroxenes. *Science* **291**(5508), 1527-1530.
- Wadhwa M., McSween Jr H. Y., and Crozaz G. (1994) Petrogenesis of shergottite meteorites inferred from minor and trace element microdistributions. *Geochimica et Cosmochimica Acta* **58**(19), 4213-4229.
- Walton E. L., Irving A. J., Bunch T. E., and Herd C. D. K. (2012) Northwest Africa 4797: A strongly shocked ultramafic poikilitic shergottite related to compositionally intermediate Martian meteorites. *Meteoritics & Planetary Science* **47**(9), 1449-1474.
- Walton E. L., Kelley S. P., and Herd C. D. K. (2008) Isotopic and petrographic evidence for young Martian basalts. *Geochimica et Cosmochimica Acta* **72**(23), 5819-5837.

- Warren P. (2002) Northwest Africa 1000: a new eucrite with maskelynite, unequilibrated pyroxene crisscrossed by fayalite-rich veins, and Stannern-like geochemistry. In *Lunar and Planetary Science Conference*, pp. 1147.
- Warren P. H., Kallemeyn G. W., Huber H., Ulf-Møller F., and Choe W. (2009) Siderophile and other geochemical constraints on mixing relationships among HED-meteorite breccias. *Geochimica et Cosmochimica Acta* **73**, 5918-5943.
- Warren P. H., Kallemeyn G. W., and Kyte F. T. (1999) Origin of planetary cores: evidence from highly siderophile elements in martian meteorites. *Geochimica et Cosmochimica Acta* **63**(13-14), 2105-2122.
- Warren P. H., Rubin A. E., Isa J., Gessler N., Ahn I., and Choi B.-G. (2014) Northwest Africa 5738: Multistage fluid-driven secondary alteration in an extraordinarily evolved eucrite. *Geochimica et Cosmochimica Acta* **141**, 199-227.
- Wiechert U. H., Halliday A. N., Palme H., and Rumble D. (2004) Oxygen isotope evidence for rapid mixing of the HED meteorite parent body. *Earth and Planetary Science Letters* **221**(1-4), 373-382.
- Wilkening L. L. (1973) Foreign inclusions in stony meteorites, I. Carbonaceous chondritic xenoliths in the Kapoeta howardite. *Geochimica et Cosmochimica Acta* **37**(8), 1985-1989.
- Wilson L. and Keil K. (1996) Volcanic eruptions and intrusions on the asteroid 4 Vesta. *J. Geophys. Res.* **101**(E8), 18927-18940.
- Wones D. R. and Gilbert M. C. (1969) The fayalite-magnetite-quartz assemblage between 600 and 800 C. *Am. J. Sci* **267**, 480-488.
- Wood B. (1991) Oxygen Barometry of Spinel Peridotites. *Reviews in Mineralogy* **25**.
- Yamaguchi A., Taylor G. J., and Keil K. (1996) Global Crustal Metamorphism of the Eucrite Parent Body. *Icarus* **124**(1), 97-112.
- Zhang A.-C., Wang R.-C., Hsu W.-B., and Bartoschewitz R. (2013) Record of S-rich vapors on asteroid 4 Vesta: Sulfurization in the Northwest Africa 2339 eucrite. *Geochimica et Cosmochimica Acta* **109**, 1-13.

## **Appendix 1 – Supplemental information from Tissint experimental petrology**

This appendix is the supplemental information included in the publication of Ch. 2 (Castle and Herd, 2017). The tables are primarily related to mineral compositions from isothermal experiments.

**Table A1.1:** Calculated modal abundances from isothermal experiments at QFM-3.2

Run	Temp	Ol	Px	Sp	Pl	Gl
S38	1375	NP	NP	NP	NP	100.0%
S45	1363	1.0%	NP	NP	NP	99.0%
S42	1280	18.2%	NP	NP	NP	81.8%
S44	1250	23.0%	NP	NP	NP	77.0%
S54	1240	17.5%	9.6%	0.08%	NP	72.8%
S46	1225	16.5%	16.5%	0.06%	NP	66.9%
S40	1200	19.7%	20.2%	0.15%	NP	60.0%
S39	1140	24.2%	38.2%	0.08%	NP	37.5%
S49	1100	23.2%	55.6%	0.03%	7.2%	13.8%
S55	1078	16.2%	66.1%	0.47%	11.8%	5.4%

All values reported are wt% of system based on mass balance

NP indicates phase not present in experimental charge

**Table A1.2:** Calculated modal abundances from isothermal experiments at QFM-1

Run	Temp	Ol	Px	Sp	Pl	Gl
S63	1275	17.3%	NP	0.33%	NP	82.4%
S60	1200	14.3%	36.8%	0.27%	NP	48.7%
S62	1100	3.6%	82.9%	0.71%	3.1%	9.7%

All values reported are wt% of system based on mass balance

NP indicates phase not present in experimental charge

Temp is in °C

**Table A1.3:** Isothermal experiment average chromite analysis

	S54	S46	S40	S39	S49
Temp	1240	1225	1200	1140	1100
$fO_2$	-3.2	-3.2	-3.2	-3.2	-3.2
n	24	21	15	5	12
SiO <sub>2</sub>	0.8 ±0.4	0.33 ±0.07	0.6 ±0.1	0.49 ±0.07	0.60 ±0.09
TiO <sub>2</sub>	1.28 ±0.08	1.24 ±0.02	2.18 ±0.08	2.42 ±0.06	3.1 ±0.3
Al <sub>2</sub> O <sub>3</sub>	7.78 ±0.09	7.8 ±0.1	7.58 ±0.07	9.6 ±0.2	7.7 ±0.4
Cr <sub>2</sub> O <sub>3</sub>	55.2 ±0.6	55.7 ±0.3	52.7 ±0.4	49.0 ±0.4	49.7 ±0.8
FeO	26.1 ±0.1	26.37 ±0.04	28.8 ±0.1	30.0 ±0.1	32.3 ±0.2
MnO	0.471 ±0.003	0.476 ±0.003	0.480 ±0.004	0.490 ±0.004	0.462 ±0.007
MgO	7.01 ±0.03	6.71 ±0.03	6.3 ±0.1	5.28 ±0.07	3.98 ±0.09
CaO	0.3 ±0.1	0.22 ±0.04	0.28 ±0.03	0.33 ±0.04	0.31 ±0.03
Na <sub>2</sub> O	0.009 ±0.002	0.006 ±0.002	0.009 ±0.003	0.014 ±0.008	0.020 ±0.005
K <sub>2</sub> O	0.001 ±0.001	0.001 ±0.001	0.003 ±0.001	ND	0.001 ±0.001
P <sub>2</sub> O <sub>5</sub>	0.007 ±0.004	0.004 ±0.001	0.008 ±0.003	0.007 ±0.005	0.018 ±0.008
Total	98.9 ±0.2	98.9 ±0.2	99.0 ±0.2	97.6 ±0.3	98.1 ±0.1
Mg#	32.4 ±0.2	31.2 ±0.1	28.1 ±0.6	23.9 ±0.3	18.0 ±0.4
Cr#	82.6 ±1.4	82.7 ±1.4	82.3 ±1.0	77.4 ±2.0	81.2 ±3.9

	S63	S60	S62
Temp	1275	1200	1100
$fO_2$	-1	-1	-1
n	11	8	13
SiO <sub>2</sub>	0.193 ±0.006	0.17 ±0.02	0.20 ±0.02
TiO <sub>2</sub>	1.05 ±0.03	1.65 ±0.09	1.4 ±0.3
Al <sub>2</sub> O <sub>3</sub>	7.6 ±0.1	9.7 ±0.2	6.7 ±0.3
Cr <sub>2</sub> O <sub>3</sub>	51.2 ±0.4	45.7 ±0.5	46.7 ±1.2
FeO	31.0 ±0.2	34.8 ±0.3	39.8 ±0.7
MnO	0.439 ±0.005	0.45 ±0.01	0.431 ±0.006
MgO	7.61 ±0.03	6.00 ±0.03	3.24 ±0.03
CaO	0.09 ±0.02	0.20 ±0.01	0.17 ±0.01
Na <sub>2</sub> O	0.019 ±0.005	0.015 ±0.004	0.016 ±0.005
K <sub>2</sub> O	0.004 ±0.002	0.002 ±0.001	0.002 ±0.001
P <sub>2</sub> O <sub>5</sub>	0.005 ±0.002	0.004 ±0.002	0.008 ±0.003
Total	99.2 ±0.1	98.7 ±0.2	98.7 ±0.1
Mg#	30.5 ±0.2	23.5 ±0.2	12.7 ±0.3
Cr#	81.8 ±1.6	75.9 ±1.9	82.4 ±3.9

All values are weight percents, except Mg# and Cr# which were calculated on a molar basis

Errors reported are 1s standard errors derived from EMPA

$fO_2$  is reported relative to the QFM buffer

Temp is in °C

**Table A1.4:** Isothermal experiment average titanomagnetite analysis

	S49	S55	S62
Temp	1100	1078	1100
$fO_2$	-3.2	-3.2	-1
n	7	9	7
SiO <sub>2</sub>	0.42 ±0.05	0.24 ±0.03	0.30 ±0.04
TiO <sub>2</sub>	6.5 ±0.5	16.0 ±0.2	13.0 ±0.2
Al <sub>2</sub> O <sub>3</sub>	10.8 ±0.5	6.8 ±0.1	7.9 ±0.2
Cr <sub>2</sub> O <sub>3</sub>	39.4 ±1.1	25.1 ±0.4	20.4 ±0.3
FeO	34.9 ±0.5	45.5 ±0.4	51.7 ±0.4
MnO	0.494 ±0.006	0.503 ±0.009	0.484 ±0.006
MgO	4.7 ±0.1	4.2 ±0.1	3.8 ±0.1
CaO	0.28 ±0.04	0.27 ±0.02	0.33 ±0.03
Na <sub>2</sub> O	0.018 ±0.008	0.011 ±0.004	0.012 ±0.004
K <sub>2</sub> O	0.004 ±0.002	0.003 ±0.001	0.003 ±0.002
P <sub>2</sub> O <sub>5</sub>	0.007 ±0.004	0.006 ±0.002	0.012 ±0.004
Total	97.5 ±0.2	98.62 ±0.08	98.0 ±0.3
Mg#	19.3 ±0.6	14.1 ±0.4	11.7 ±0.4
Cr#	71.0 ±4.0	71.1 ±1.7	63.3 ±1.7

All values are weight percents, except Mg# and Cr# which were calculated on a molar basis

Errors reported are 1s standard errors derived from EMPA

$fO_2$  is reported relative to the QFM buffer

Temp is in °C

**Table A1.5:** Isothermal experiment average olivine analysis

	S45		S52		S42		S44		S54	
Temp	1363		1362		1280		1250		1240	
$fO_2$	-3.2		-3.2		-3.2		-3.2		-3.2	
n	8		8		5		5		12	
SiO <sub>2</sub>	37.96	±0.04	38.42	±0.08	37.01	±0.09	36.74	±0.02	37.59	±0.04
TiO <sub>2</sub>	0.005	±0.003	0.007	±0.003	0.005	±0.005	0.017	±0.004	0.010	±0.002
Al <sub>2</sub> O <sub>3</sub>	0.040	±0.005	0.041	±0.002	0.050	±0.007	0.038	±0.007	0.033	±0.002
Cr <sub>2</sub> O <sub>3</sub>	0.22	±0.01	0.24	±0.01	0.308	±0.009	0.32	±0.01	0.253	±0.005
FeO	19.76	±0.04	20.30	±0.02	24.33	±0.03	26.10	±0.07	26.68	±0.02
MnO	0.419	±0.008	0.445	±0.007	0.511	±0.009	0.54	±0.01	0.562	±0.003
MgO	41.19	±0.10	40.51	±0.06	36.55	±0.09	35.3	±0.2	35.23	±0.04
CaO	0.232	±0.005	0.273	±0.003	0.276	±0.002	0.295	±0.006	0.296	±0.003
Na <sub>2</sub> O	0.014	±0.005	0.015	±0.005	0.012	±0.006	0.013	±0.006	0.005	±0.002
K <sub>2</sub> O	0.003	±0.002	0.001	±0.001	0.002	±0.002	ND		0.001	±0.001
P <sub>2</sub> O <sub>5</sub>	0.05	±0.01	0.06	±0.02	0.24	±0.04	0.07	±0.04	0.07	±0.02
Total	99.92	±0.10	100.3	±0.1	99.3	±0.1	99.4	±0.2	100.72	±0.05
Mg#	78.8	±0.2	78.1	±0.1	72.8	±0.2	70.7	±0.4	70.2	±0.1

	S46		S40		S39		S49		S55	
Temp	1225		1200		1140		1100		1078	
$fO_2$	-3.2		-3.2		-3.2		-3.2		-3.2	
n	14		11		11		10		8	
SiO <sub>2</sub>	37.1	±0.2	36.6	±0.2	36.2	±0.2	35.1	±0.1	34.8	±0.1
TiO <sub>2</sub>	0.012	±0.004	0.022	±0.005	0.034	±0.005	0.049	±0.006	0.049	±0.005
Al <sub>2</sub> O <sub>3</sub>	0.037	±0.003	0.13	±0.10	0.041	±0.006	0.045	±0.005	0.036	±0.004
Cr <sub>2</sub> O <sub>3</sub>	0.244	±0.010	0.190	±0.007	0.14	±0.01	0.088	±0.009	0.061	±0.009
FeO	28.00	±0.09	29.47	±0.07	33.21	±0.08	38.4	±0.1	40.3	±0.4
MnO	0.580	±0.008	0.615	±0.005	0.655	±0.004	0.696	±0.008	0.72	±0.01
MgO	34.31	±0.09	32.5	±0.2	29.55	±0.07	25.83	±0.07	23.8	±0.3
CaO	0.334	±0.005	0.415	±0.005	0.455	±0.008	0.465	±0.008	0.43	±0.01
Na <sub>2</sub> O	0.013	±0.003	0.007	±0.003	0.008	±0.003	0.018	±0.004	0.021	±0.005
K <sub>2</sub> O	0.002	±0.001	0.003	±0.001	0.002	±0.001	0.002	±0.001	0.004	±0.002
P <sub>2</sub> O <sub>5</sub>	0.05	±0.02	0.11	±0.02	0.11	±0.02	0.12	±0.02	0.20	±0.03
Total	100.65	±0.09	100.0	±0.3	100.4	±0.2	100.8	±0.1	100.47	±0.09
Mg#	68.6	±0.3	66.3	±0.4	61.3	±0.2	54.5	±0.2	51.3	±0.9

	S63		S60		S62	
Temp	1275		1200		1100	
$fO_2$	-1		-1		-1	
n	9		8		9	
SiO <sub>2</sub>	37.83	±0.08	36.94	±0.05	35.6	±0.1
TiO <sub>2</sub>	0.012	±0.003	0.008	±0.003	0.032	±0.006
Al <sub>2</sub> O <sub>3</sub>	0.050	±0.006	0.048	±0.006	0.048	±0.004
Cr <sub>2</sub> O <sub>3</sub>	0.16	±0.01	0.10	±0.01	0.058	±0.008
FeO	23.60	±0.04	29.42	±0.04	38.5	±0.6
MnO	0.525	±0.008	0.612	±0.007	0.69	±0.01
MgO	37.55	±0.07	32.71	±0.08	25.1	±0.5
CaO	0.252	±0.003	0.358	±0.005	0.43	±0.02
Na <sub>2</sub> O	0.008	±0.006	0.024	±0.007	0.011	±0.005
K <sub>2</sub> O	0.001	±0.001	0.002	±0.001	ND	
P <sub>2</sub> O <sub>5</sub>	0.10	±0.04	0.08	±0.02	0.13	±0.01
Total	100.08	±0.07	100.3	±0.1	100.65	±0.09
Mg#	73.9	±0.2	66.5	±0.2	53.8	±1.4

All values are weight percents, except Mg# which was calculated on a molar basis

Errors reported are 1s standard errors derived from EMPA

$fO_2$  is reported relative to the QFM buffer

Temp is in °C

**Table A1.6:** Isothermal experiment average pyroxene analysis

	S54		S46		S40		S39		S49	
Temp	1240		1225		1200		1140		1100	
$fO_2$	-3.2		-3.2		-3.2		-3.2		-3.2	
n	12		14		11		21		10	
SiO <sub>2</sub>	54.38	±0.03	54.50	±0.04	54.08	±0.06	52.68	±0.09	51.4	±0.4
TiO <sub>2</sub>	0.081	±0.002	0.092	±0.003	0.131	±0.005	0.24	±0.01	0.6	±0.2
Al <sub>2</sub> O <sub>3</sub>	0.492	±0.009	0.58	±0.02	0.71	±0.02	1.16	±0.06	2.3	±0.5
Cr <sub>2</sub> O <sub>3</sub>	0.57	±0.01	0.59	±0.01	0.63	±0.01	0.71	±0.04	0.46	±0.07
FeO	16.27	±0.02	17.10	±0.09	17.77	±0.08	18.0	±0.2	19.5	±0.7
MnO	0.516	±0.003	0.540	±0.006	0.589	±0.007	0.631	±0.007	0.63	±0.02
MgO	28.06	±0.03	25.7	±0.3	24.7	±0.2	19.9	±0.3	17.1	±0.9
CaO	1.734	±0.008	2.05	±0.01	3.03	±0.05	7.8	±0.4	9.2	±1.1
Na <sub>2</sub> O	0.009	±0.002	0.015	±0.003	0.026	±0.004	0.068	±0.005	0.2	±0.1
K <sub>2</sub> O	0.001	±0.001	0.003	±0.001	0.001	±0.001	0.002	±0.001	0.004	±0.002
P <sub>2</sub> O <sub>5</sub>	0.003	±0.001	0.008	±0.002	0.011	±0.004	0.014	±0.002	0.2	±0.1
Total	102.11	±0.06	101.2	±0.2	101.68	±0.06	101.19	±0.05	101.5	±0.1
Mg#	75.5	±0.1	72.9	±0.9	71.2	±0.6	66.3	±1.3	61.0	±3.9
En	73.0	±0.3	69.9	±1.0	67.0	±1.2	55.9	±3.1	49.3	±6.9
Wo	3.24	±0.02	4.00	±0.06	5.9	±0.1	15.7	±0.9	19.1	±2.7

	S55		S60		S62	
Temp	1078		1200		1100	
$fO_2$	-3.2		-1		-1	
n	20		8		9	
SiO <sub>2</sub>	51.0	±0.2	53.62	±0.06	51.6	±0.3
TiO <sub>2</sub>	0.48	±0.03	0.115	±0.008	0.26	±0.03
Al <sub>2</sub> O <sub>3</sub>	1.9	±0.1	0.97	±0.06	1.6	±0.2
Cr <sub>2</sub> O <sub>3</sub>	0.46	±0.03	0.52	±0.02	0.44	±0.06
FeO	21.1	±0.4	18.1	±0.1	21.7	±0.3
MnO	0.68	±0.01	0.61	±0.01	0.67	±0.02
MgO	17.9	±0.7	24.7	±0.1	18.3	±0.3
CaO	7.0	±0.7	2.48	±0.05	6.2	±0.4
Na <sub>2</sub> O	0.067	±0.005	0.014	±0.003	0.006	±0.002
K <sub>2</sub> O	0.003	±0.001	0.002	±0.001	0.000	±0.000
P <sub>2</sub> O <sub>5</sub>	0.06	±0.01	0.006	±0.003	0.022	±0.008
Total	100.6	±0.1	101.2	±0.1	100.9	±0.1
Mg#	60.3	±2.8	70.9	±0.5	60.1	±1.4
En	51.6	±5.9	67.4	±1.5	52.4	±3.9
Wo	14.4	±1.7	4.87	±0.11	12.8	±0.9

All values are weight percents, except Mg#, En, and Wo, which were calculated on a molar basis

Errors reported are 1s standard errors derived from EMPA

$fO_2$  is reported relative to the QFM buffer

Temp is in °C

**Table A1.7:** Isothermal experiment average plagioclase analysis

	S49	S55	S62
Temp	1100	1078	1100
$fO_2$	-3.2	-3.2	-1
n	12	10	11
SiO <sub>2</sub>	52.1 ±0.2	53.9 ±0.3	45.3 ±0.2
TiO <sub>2</sub>	0.064 ±0.006	0.074 ±0.008	0.031 ±0.003
Al <sub>2</sub> O <sub>3</sub>	29.7 ±0.1	28.5 ±0.2	33.7 ±0.2
Cr <sub>2</sub> O <sub>3</sub>	0.019 ±0.006	0.013 ±0.005	0.005 ±0.003
FeO	0.98 ±0.03	1.10 ±0.05	1.49 ±0.03
MnO	0.034 ±0.004	0.028 ±0.004	0.036 ±0.005
MgO	0.02 ±0.01	ND	ND
CaO	13.43 ±0.08	12.4 ±0.2	19.55 ±0.07
Na <sub>2</sub> O	3.77 ±0.05	4.29 ±0.09	0.179 ±0.007
K <sub>2</sub> O	0.009 ±0.003	0.030 ±0.002	0.001 ±0.001
P <sub>2</sub> O <sub>5</sub>	0.028 ±0.005	0.051 ±0.006	0.035 ±0.005
Total	100.2 ±0.2	100.31 ±0.08	100.3 ±0.2
An	79.7 ±1.1	76.1 ±1.9	99.2 ±3.9
Ab	20.3 ±0.3	23.8 ±0.6	0.82 ±0.03

All values are weight percents, except An and Ab which were calculated on a molar basis

Errors reported are 1s standard errors derived from EMPA

$fO_2$  is reported relative to the QFM buffer

Temp is in °C

**Table A1.8:** Isothermal experiment average glass analyses

	S38	S43	S45	S52	S42
Temp	1375	1363	1363	1362	1280
$fO_2$	-3.2	-3.2	-3.2	-3.2	-3.2
n	16	16	10	8	8
SiO <sub>2</sub>	47.65 ±0.04	47.60 ±0.04	48.08 ±0.03	47.46 ±0.07	49.56 ±0.02
TiO <sub>2</sub>	0.676 ±0.007	0.668 ±0.005	0.68 ±0.01	0.708 ±0.008	0.790 ±0.005
Al <sub>2</sub> O <sub>3</sub>	5.39 ±0.01	5.60 ±0.02	5.57 ±0.02	5.666 ±0.009	6.50 ±0.01
Cr <sub>2</sub> O <sub>3</sub>	0.38 ±0.01	0.375 ±0.006	0.38 ±0.01	0.376 ±0.009	0.390 ±0.010
FeO	21.99 ±0.03	22.07 ±0.02	21.55 ±0.04	21.56 ±0.03	21.67 ±0.04
MnO	0.552 ±0.005	0.551 ±0.005	0.555 ±0.008	0.538 ±0.008	0.561 ±0.008
MgO	16.16 ±0.03	16.15 ±0.04	15.92 ±0.05	14.77 ±0.02	11.59 ±0.04
CaO	7.35 ±0.01	7.36 ±0.01	7.54 ±0.02	7.80 ±0.02	8.80 ±0.02
Na <sub>2</sub> O	0.133 ±0.004	0.187 ±0.005	0.055 ±0.007	0.91 ±0.02	0.51 ±0.01
K <sub>2</sub> O	0.006 ±0.001	0.006 ±0.001	ND	0.007 ±0.002	0.006 ±0.002
P <sub>2</sub> O <sub>5</sub>	0.348 ±0.008	0.345 ±0.007	0.285 ±0.009	0.047 ±0.008	0.445 ±0.004
Total	100.65 ±0.05	100.91 ±0.07	100.6 ±0.1	99.8 ±0.1	100.81 ±0.07
Mg#	56.7 ±0.1	56.6 ±0.1	56.8 ±0.2	55.0 ±0.1	48.8 ±0.2

	S44	S54	S46	S40	S39
Temp	1250	1240	1225	1200	1140
$fO_2$	-3.2	-3.2	-3.2	-3.2	-3.2
n	12	9	10	8	17
SiO <sub>2</sub>	50.19 ±0.04	48.64 ±0.06	48.50 ±0.04	49.16 ±0.05	48.96 ±0.04
TiO <sub>2</sub>	0.862 ±0.006	0.911 ±0.008	0.96 ±0.01	1.047 ±0.007	1.32 ±0.01
Al <sub>2</sub> O <sub>3</sub>	6.88 ±0.02	7.322 ±0.008	7.79 ±0.02	8.46 ±0.01	11.02 ±0.02
Cr <sub>2</sub> O <sub>3</sub>	0.400 ±0.007	0.330 ±0.008	0.31 ±0.01	0.22 ±0.01	0.105 ±0.006
FeO	21.14 ±0.03	21.48 ±0.03	21.83 ±0.04	20.74 ±0.05	18.77 ±0.03
MnO	0.549 ±0.004	0.563 ±0.003	0.55 ±0.01	0.512 ±0.008	0.450 ±0.004
MgO	10.41 ±0.02	10.01 ±0.07	9.33 ±0.05	8.02 ±0.03	5.91 ±0.01
CaO	9.27 ±0.02	9.99 ±0.04	10.41 ±0.01	10.97 ±0.02	11.39 ±0.01
Na <sub>2</sub> O	0.337 ±0.008	0.117 ±0.003	0.157 ±0.007	0.77 ±0.01	1.43 ±0.01
K <sub>2</sub> O	0.007 ±0.002	0.005 ±0.002	0.002 ±0.002	0.013 ±0.001	0.019 ±0.002
P <sub>2</sub> O <sub>5</sub>	0.425 ±0.008	0.533 ±0.008	0.524 ±0.009	0.62 ±0.01	0.859 ±0.005
Total	100.47 ±0.07	99.90 ±0.09	100.38 ±0.05	100.53 ±0.06	100.24 ±0.07
Mg#	46.7 ±0.1	45.4 ±0.3	43.2 ±0.2	40.8 ±0.2	35.9 ±0.1

	S49	S55	S63	S60	S62
Temp	1100	1078	1275	1200	1100
$fO_2$	-3.2	-3.2	-1	-1	-1
n	8	12	11	11	11
SiO <sub>2</sub>	45.0 ±0.2	40.3 ±0.3	49.33 ±0.04	47.50 ±0.05	40.1 ±0.2
TiO <sub>2</sub>	2.83 ±0.03	4.44 ±0.07	0.795 ±0.007	1.064 ±0.008	3.89 ±0.05
Al <sub>2</sub> O <sub>3</sub>	10.29 ±0.03	8.68 ±0.08	6.38 ±0.01	8.66 ±0.02	9.07 ±0.09
Cr <sub>2</sub> O <sub>3</sub>	0.088 ±0.008	0.064 ±0.007	0.213 ±0.010	0.107 ±0.006	0.033 ±0.005
FeO	20.2 ±0.1	21.4 ±0.3	21.55 ±0.03	21.90 ±0.04	24.93 ±0.06
MnO	0.45 ±0.01	0.490 ±0.009	0.559 ±0.007	0.543 ±0.009	0.507 ±0.006
MgO	4.77 ±0.03	4.53 ±0.09	11.68 ±0.04	8.22 ±0.01	3.8 ±0.1
CaO	11.31 ±0.03	12.26 ±0.09	8.87 ±0.02	11.29 ±0.01	13.22 ±0.07
Na <sub>2</sub> O	1.50 ±0.03	1.26 ±0.03	0.176 ±0.004	0.024 ±0.003	0.042 ±0.005
K <sub>2</sub> O	0.037 ±0.002	0.043 ±0.004	0.001 ±0.001	0.002 ±0.001	0.001 ±0.001
P <sub>2</sub> O <sub>5</sub>	2.19 ±0.05	5.1 ±0.1	0.485 ±0.006	0.719 ±0.007	3.47 ±0.08
Total	98.6 ±0.2	98.5 ±0.3	100.03 ±0.05	100.04 ±0.08	99.11 ±0.05
Mg#	29.6 ±0.3	27.4 ±0.6	49.1 ±0.2	40.08 ±0.09	21.5 ±0.8

All values are weight percents, except Mg# which was calculated on a molar basis

Errors reported are 1s standard errors derived from EMPA

$fO_2$  is reported relative to the QFM buffer

Temp is in °C

**Table A1.9:** Cooling rate experiment average glass analyses

	S48	S50	S58	S64
Temp	1225	1100	1000	1100
$fO_2$	-3.2	-3.2	-3.2	Hybrid
n	8	8	10	9
SiO <sub>2</sub>	49.64 ±0.04	50.7 ±0.1	42.0 ±0.5	49.87 ±0.08
TiO <sub>2</sub>	0.863 ±0.008	1.26 ±0.01	4.11 ±0.10	1.33 ±0.01
Al <sub>2</sub> O <sub>3</sub>	6.84 ±0.03	10.0 ±0.1	7.2 ±0.1	10.75 ±0.03
Cr <sub>2</sub> O <sub>3</sub>	0.397 ±0.010	0.10 ±0.01	0.008 ±0.004	0.051 ±0.009
FeO	21.38 ±0.04	20.21 ±0.07	30.9 ±0.6	20.60 ±0.07
MnO	0.569 ±0.007	0.516 ±0.007	0.60 ±0.01	0.495 ±0.008
MgO	9.68 ±0.03	3.42 ±0.04	0.28 ±0.02	3.41 ±0.02
CaO	9.47 ±0.01	12.02 ±0.01	11.06 ±0.04	12.12 ±0.02
Na <sub>2</sub> O	0.081 ±0.004	0.056 ±0.005	0.038 ±0.004	0.070 ±0.002
K <sub>2</sub> O	0.006 ±0.003	0.006 ±0.002	0.006 ±0.002	0.003 ±0.001
P <sub>2</sub> O <sub>5</sub>	0.36 ±0.01	0.481 ±0.008	2.29 ±0.07	0.488 ±0.008
Total	99.28 ±0.06	98.8 ±0.1	98.53 ±0.07	99.18 ±0.08
Mg#	44.7 ±0.1	23.2 ±0.3	1.6 ±0.1	22.8 ±0.1

All experimental runs were set to cool from 1375°C to the listed temperature at 1°C/hr. Due to the offset between furnace set temperature and sample temperature, achieved cooling rates were between 1.0-0.9°C/hr (see Tbl. 1)

CO-CO<sub>2</sub> gas mixture to control  $fO_2$  was set for the midpoint temperature, meaning that actual  $fO_2$  changed over the course of the experiment (see Fig. 2)

The hybrid experiment was initially set to QFM-3.2 from 1375°C-1200°C, then increased to QFM-1 from 1200°C-1100°C

All values are weight percents, except Mg# which was calculated on a molar basis

Errors reported are 1s standard errors derived from EMPA

$fO_2$  is reported relative to the QFM buffer

Temp is in °C

**Table A1.10:** Example Tissint mineralogy and olivine-spinel-pyroxene geothermometer/oxybarometer results

Phase	Olivine	Pyroxene	Spinel	Spinel	Spinel
SiO <sub>2</sub>	38.06	54.04	0.17	0.16	0.18
TiO <sub>2</sub>	0.00	0.07	0.80	0.89	0.83
Al <sub>2</sub> O <sub>3</sub>	0.07	0.56	6.31	6.49	6.97
Cr <sub>2</sub> O <sub>3</sub>	0.12	0.47	57.82	58.46	55.82
V <sub>2</sub> O <sub>5</sub>	0.00	NA	0.49	0.49	0.50
FeO	27.76	16.27	30.18	29.42	30.23
MnO	0.56	0.56	0.47	0.52	0.51
NiO	0.07	0.00	0.02	0.06	0.00
MgO	34.36	24.41	3.58	4.15	3.75
CaO	0.27	2.89	0.08	0.04	0.10
Na <sub>2</sub> O	0.10	0.07	0.00	0.00	0.04
K <sub>2</sub> O	0.02	0.00	0.00	0.00	0.00
P <sub>2</sub> O <sub>5</sub>	NA	NA	0.00	0.01	0.00
Total	101.37	99.35	99.92	100.66	98.92
Mg#	63.2	67.5	14.1	16.3	14.7
Cr#			86.0	85.8	84.3
$fO_2$			-3.51	-3.12	-3.72
Temp			979	997	1055

Calculations were all performed on the computational thermodynamics server (ct.server) using the Ol-Sp-Px geothermometer/oxybarometer calculator

The same silicate compositions were used with each spinel for the calculation. Spinel compositions were randomly chosen here to show a range of  $fO_2$  results

NA indicates the element was not analyzed

All  $fO_2$  values are reported relative to the QFM buffer

Temp is in °C

**Table A1.11:** Example Tissint mineralogy and titanomagnetite-ilmenite geothermometer/oxybarometer results

Phase	Spinel	Ilmenite	Spinel	Ilmenite	Spinel	Ilmenite
SiO <sub>2</sub>	0.09	0.07	0.13	0.30	0.10	0.02
TiO <sub>2</sub>	21.67	51.44	31.75	50.40	23.27	52.41
Al <sub>2</sub> O <sub>3</sub>	3.56	0.09	1.19	0.12	2.82	0.13
Cr <sub>2</sub> O <sub>3</sub>	14.92	0.30	0.43	0.22	13.33	0.29
V <sub>2</sub> O <sub>5</sub>	0.51	0.09	0.07	0.06	0.38	0.09
FeO	55.25	44.70	62.09	44.93	56.76	44.03
MnO	0.72	0.73	0.67	0.85	0.67	0.70
NiO	0.00	0.01	0.00	0.02	0.00	0.02
MgO	1.53	2.10	0.75	1.25	1.56	2.33
CaO	0.11	0.13	0.46	0.31	0.11	0.10
Na <sub>2</sub> O	0.00	0.01	0.05	0.04	0.00	0.00
K <sub>2</sub> O	0.00	0.00	0.00	0.00	0.00	0.01
Total	98.36	99.67	97.59	98.48	99.00	100.12
Mg#	3.7	6.1	1.6	3.7	3.7	6.8
Cr#	73.8	69.1	19.7	55.9	76.0	60.0
$f_{O_2}$		-0.81		-1.42		-1.99
Temp		1135		1324		930

Calculations were all performed on the computational thermodynamics server (ct.server) using the two oxide geothermometer/oxybarometer calculator

Each pair was vetted for Mg-Mn equilibrium using the method from Bacon and Hirschmann (1988) (see text, Fig. A1.1). These three pairs were randomly chosen to show a range of  $f_{O_2}$  results

All  $f_{O_2}$  values are reported relative to the QFM buffer

Temp is in °C

**Table A1.12:** Laboratory-GTOB comparison

Run	n	Experimental		Calculated		Offset	
		Temp	$fO_2$	Temp	$fO_2$	Temp	$fO_2$
S54	9	1240	-3.2	1397 ±5	-3.48 ±0.35	157.31	-0.24
S46	16	1225	-3.2	1399 ±8	-3.44 ±0.13	171.81	-0.20
S40	10	1200	-3.2	1357 ±10	-3.31 ±0.33	156.58	-0.09
S49	8	1100	-3.2	1273 ±16	-3.40 ±0.23	172.53	-0.16
S49a	7	1100	-3.2	1293 ±29	-3.04 ±0.35	192.61	0.20
S57	7	1100	-3.2	1265 ±5	-3.02 ±0.23	164.72	0.22
S55a	8	1078	-3.2	1196 ±19	-2.36 ±0.18	118.11	0.88
S60	7	1200	-1.0	1359 ±6	-1.33 ±0.18	159.50	-0.33
S62	11	1100	-1.0	1181 ±24	-1.32 ±0.59	81.29	-0.32
S62a	10	1100	-1.0	1126 ±23	-0.96 ±0.21	26.07	0.04

Laboratory temperature measurement was calibrated with an Au standard, and is accurate to within <1°C

Laboratory  $fO_2$  measurement was performed with a ZrO<sub>2</sub> half-cell in a remote furnace. Reproducible to approximately 0.1 log units

All  $fO_2$  values are reported relative to the QFM buffer

'a' on a run number denotes titanomagnetite (rather than chromite) analysis

Mismatch is calculated relative to laboratory settings: positive values indicate that the calculated value exceeds the laboratory setting

Temp is in °C

**Table A1.13:** Cr partitioning behavior calculated from experimental olivine and glass

Experimental				Calculations				
Run	Temp	$fO_2$	$D_{Cr}$	NBO/T	$D_{Cr(III)}$	$D_{Cr(II)}$	$Cr^{2+}/Cr^{3+}$	$D_{Cr}$
S38	1375	-3.2	N/A	1.85	0.57	0.62	0.85	0.59
S43	1363	-3.2	N/A	1.84	0.57	0.64	0.91	0.60
S45	1363	-3.2	0.58	1.80	0.59	0.64	0.91	0.61
S52	1362	-3.2	0.63	1.77	0.60	0.64	0.91	0.62
S42	1280	-3.2	0.79	1.56	0.68	0.79	1.49	0.75
S44	1250	-3.2	0.79	1.46	0.72	0.86	1.80	0.81
S54	1240	-3.2	0.76	1.49	0.71	0.89	1.92	0.83
S46	1225	-3.2	0.78	1.47	0.72	0.93	2.13	0.86
S40	1200	-3.2	0.87	1.37	0.76	1.00	2.53	0.93
S39	1140	-3.2	1.34	1.16	0.84	1.21	3.91	1.13
S49	1100	-3.2	1.00	1.43	0.73	1.39	5.34	1.28
S55	1078	-3.2	0.94	2.05	0.49	1.50	6.39	1.36
Clc*	1375	-1.0	N/A	1.85	0.57	0.62	0.23	0.58
S63	1275	-1.0	0.76	1.56	0.68	0.81	0.41	0.72
S60	1200	-1.0	0.91	1.43	0.73	1.00	0.68	0.84
S62	1100	-1.0	1.76	1.93	0.54	1.39	1.43	1.04

N/A denotes where an experimentally based calculation cannot be performed due to a lack of olivine composition. In the case of Clc and S38 no olivine was present. In the case of S43 olivine was too thin to analyze by EMPA

$D_{Cr}$  calculations were performed using the method from Hanson and Jones (1998)

Clc is a calculated value based on the initial liquid composition (S38) and set  $fO_2$

All quantities were calculated on a molar basis

All  $fO_2$  values are reported relative to the QFM buffer

Temp is in °C

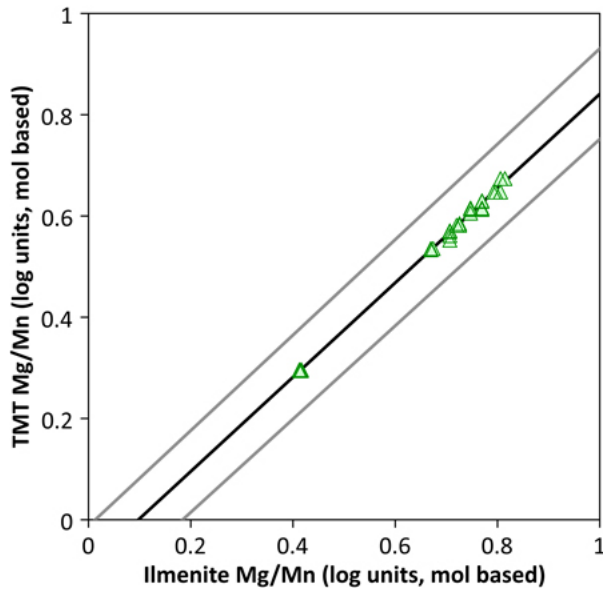


**Figure A1.1:** Comparison between oxide pairs (green) and the equilibrium model of Bacon and Hirschmann (1988) for Mg-Mn equilibrium (black), with a  $1\sigma$  error envelope (gray). All 29 oxide pairs used in this study to evaluate the late-stage  $fO_2$  of the Tissint meteorite are shown.

## **Appendix 2 – X-Ray maps from cooling rate experiments**

This appendix is the full set of X-ray maps generated from cooling rate (hybrid and reducing) experiments on the Tissint synthetic composition. A subset were included for specific discussion in Ch.3.

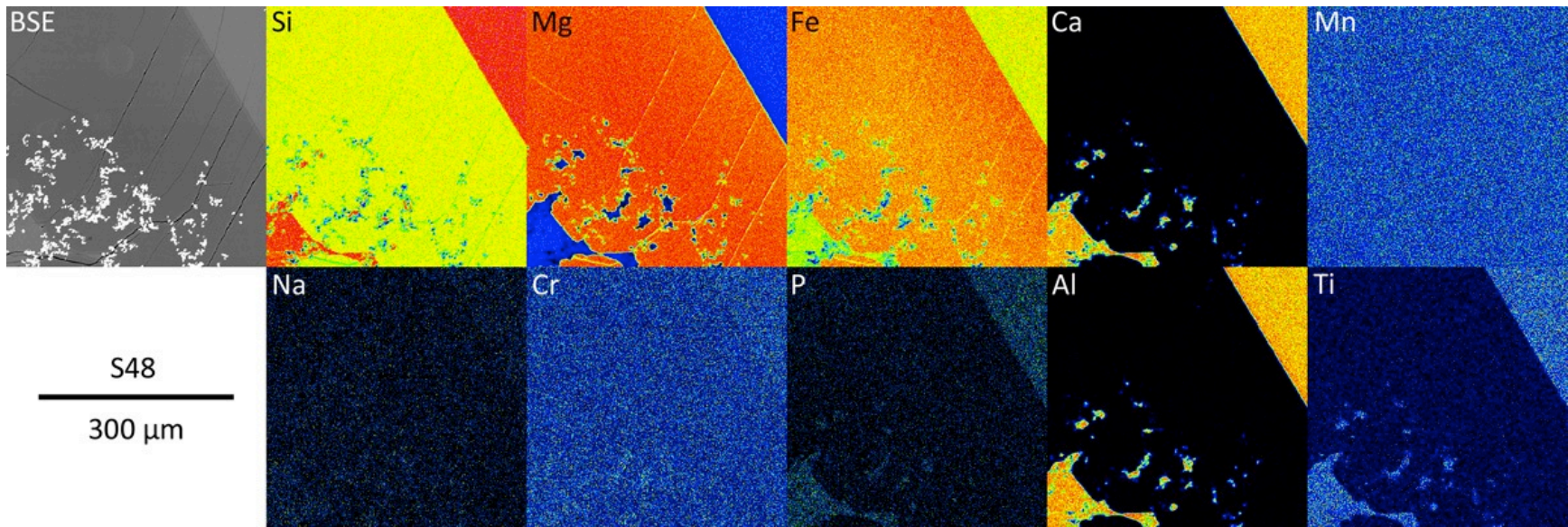


**Figure A2.1:** X-Ray maps of an olivine grain in S48, the cooling rate experiment under reducing conditions from 1375-1225°C.

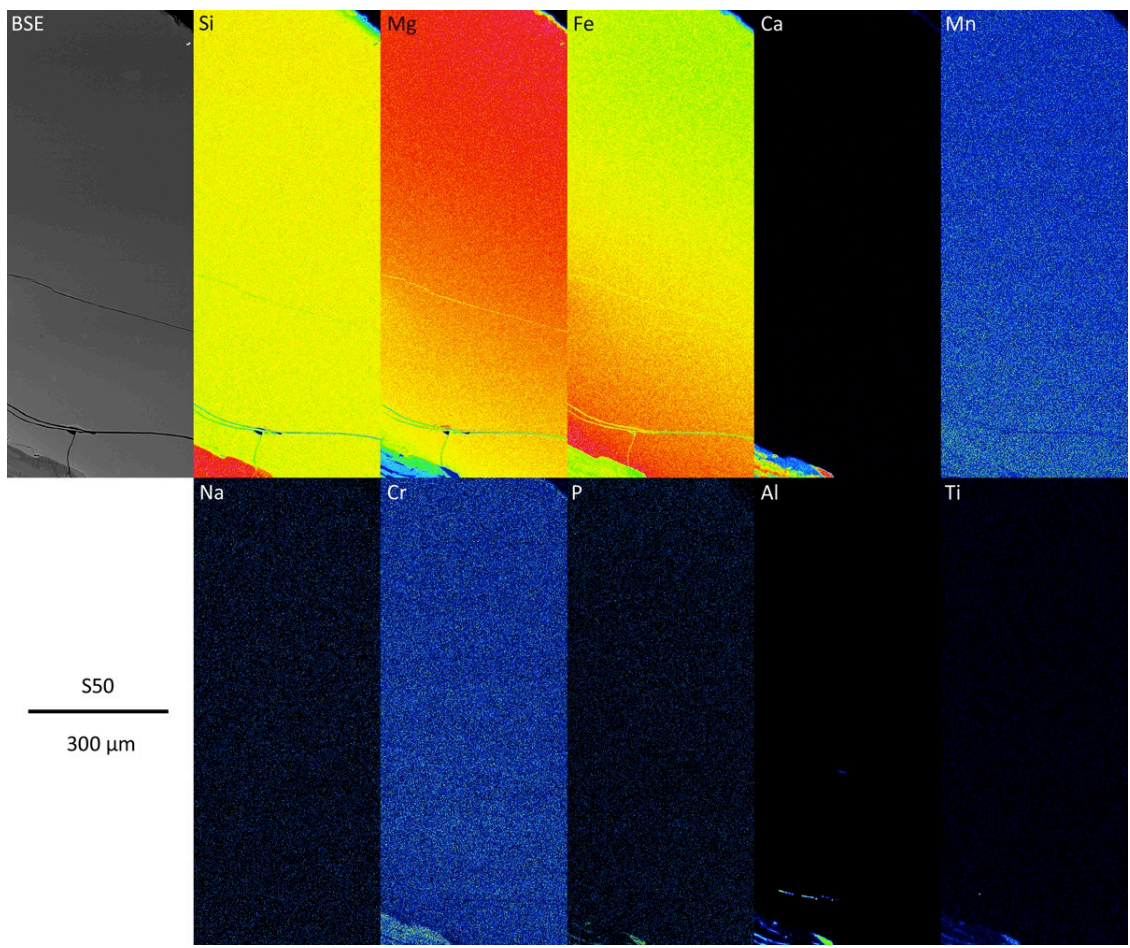


**Figure A2.2:** X-Ray maps of an olivine grain in S50, the cooling rate experiment under reducing conditions from 1375-1100°, oxidized at 1150°C.

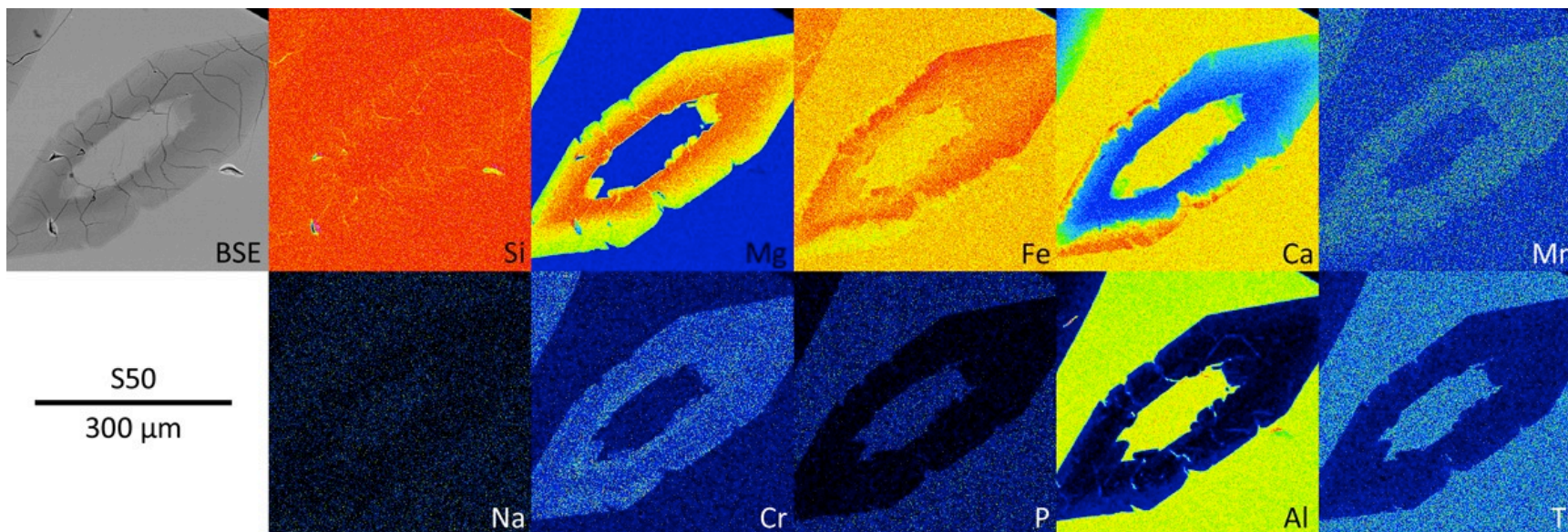


**Figure A2.3:** X-Ray maps of a pyroxene grain in S50, the cooling rate experiment under reducing conditions from 1375-1100°C. This series was collected on a pyroxene grain, rather than centered on an olivine grain as the rest of the figures in this appendix.

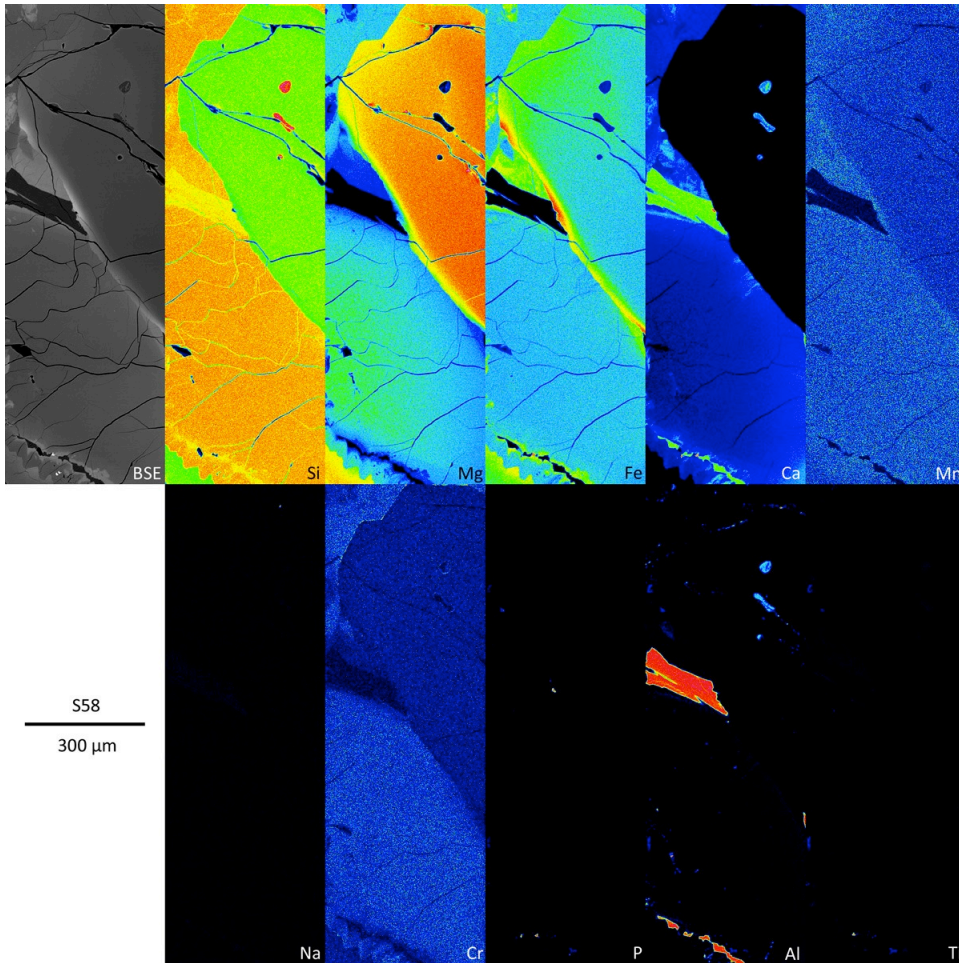


**Figure A2.4:** X-Ray maps of a mixture of olivine and pyroxene grains in S58, the cooling rate experiment under reducing conditions from 1375-1000°C.

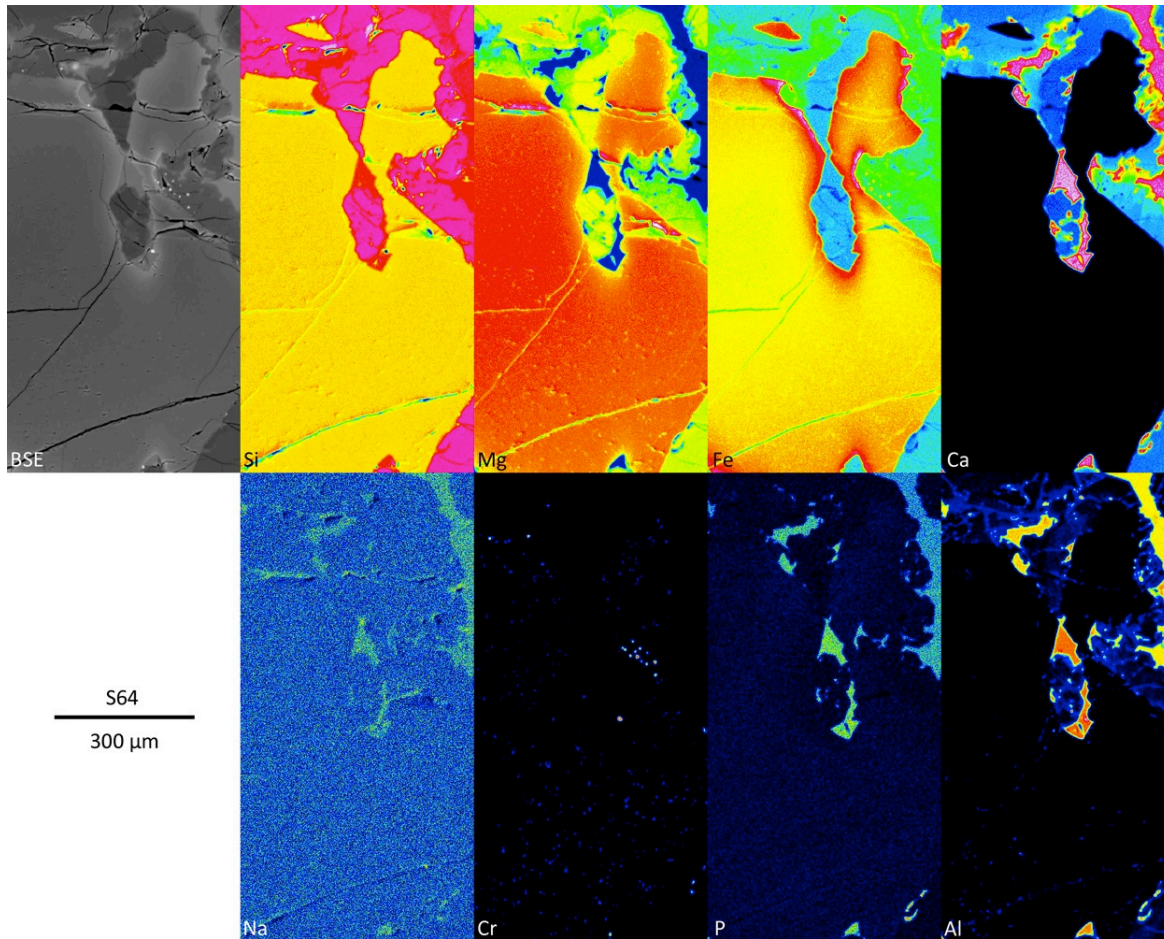


**Figure A2.5:** X-Ray maps of an olivine grain in S64, the hybrid cooling rate experiment from 1375-1100°, oxidized at 1200°C.

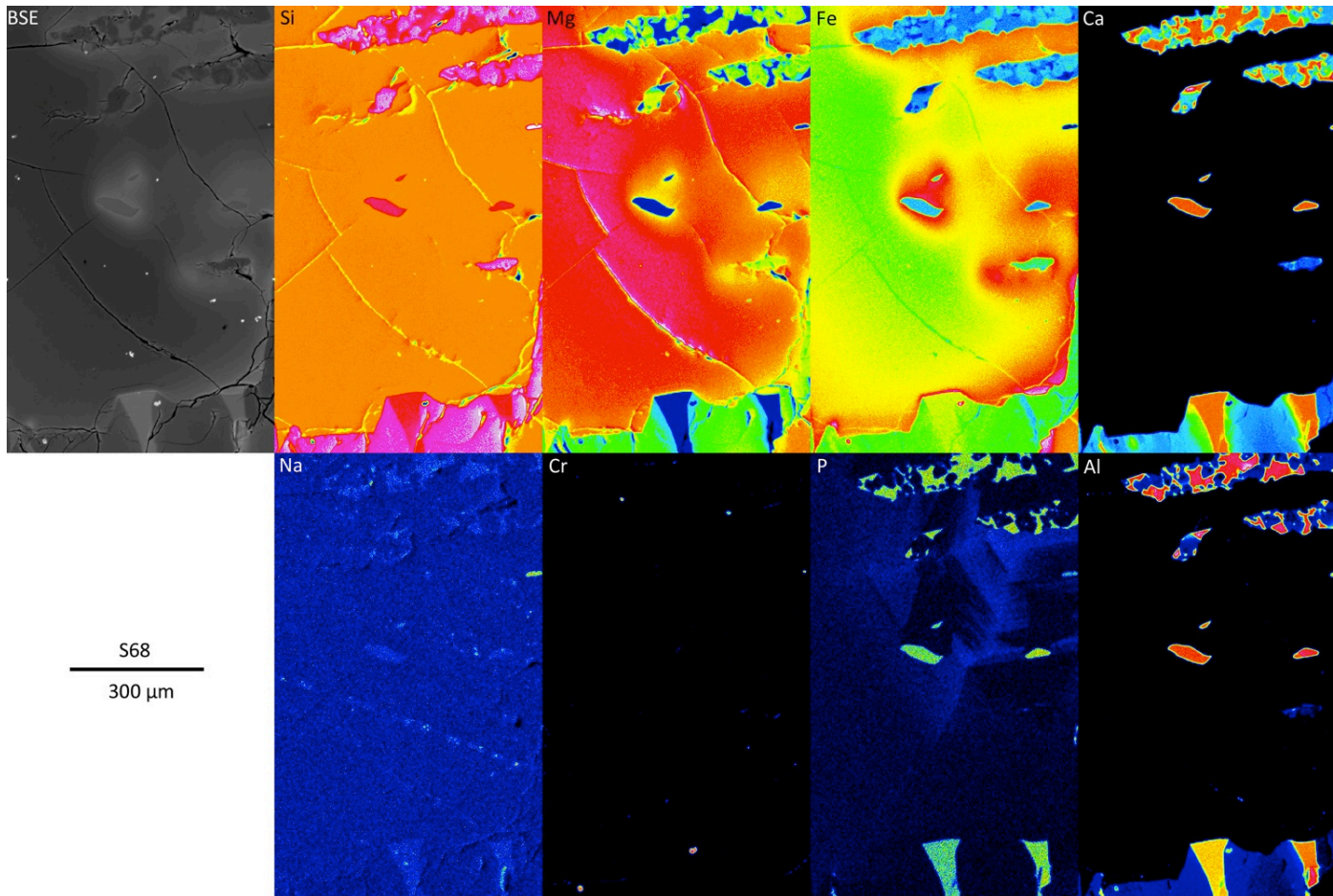


**Figure A2.6:** X-Ray maps of an olivine grain in S68, the hybrid cooling rate experiment from 1375-1100°, oxidized at 1150°C.

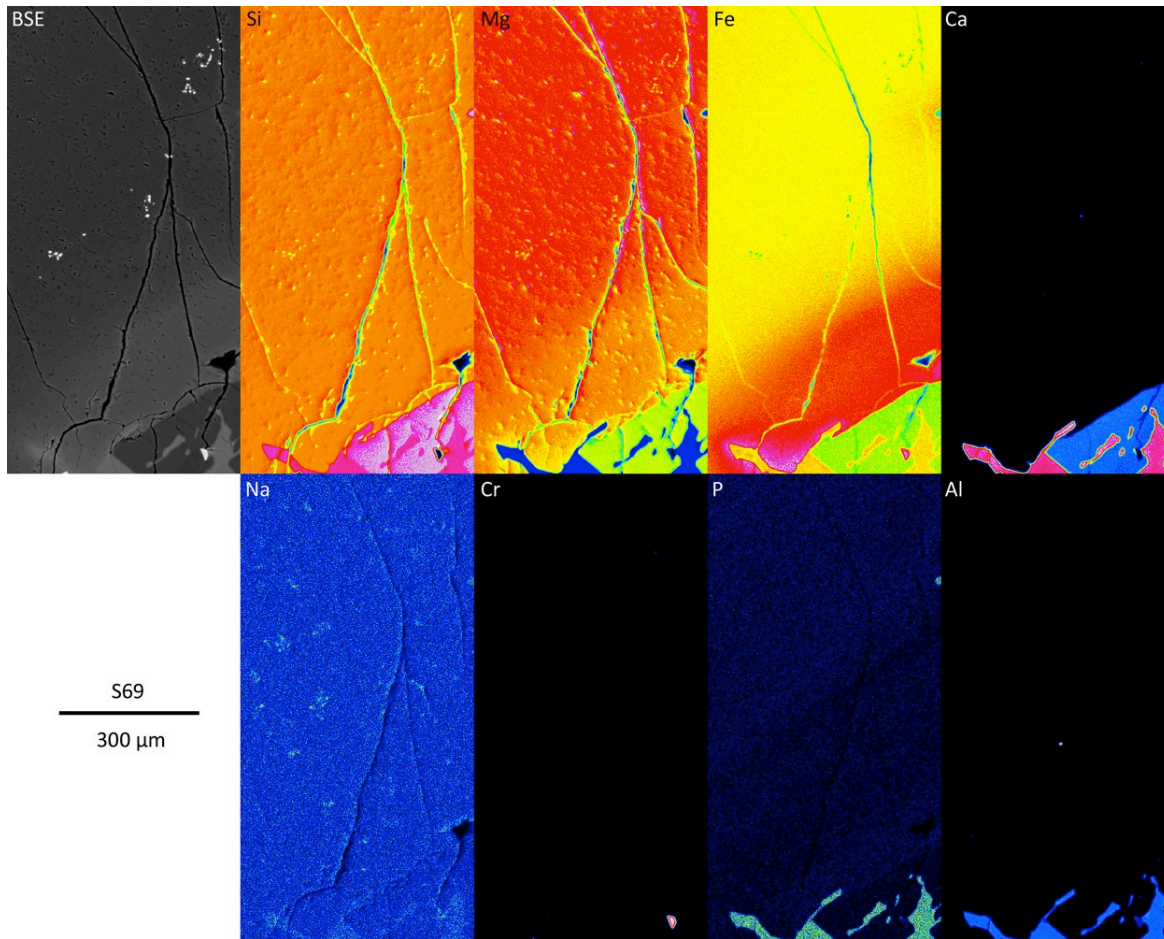


**Figure A2.7:** X-Ray maps of an olivine grain in S69, the hybrid cooling rate experiment from 1375-1200°, oxidized at 1200°C, then held for 24 hrs.

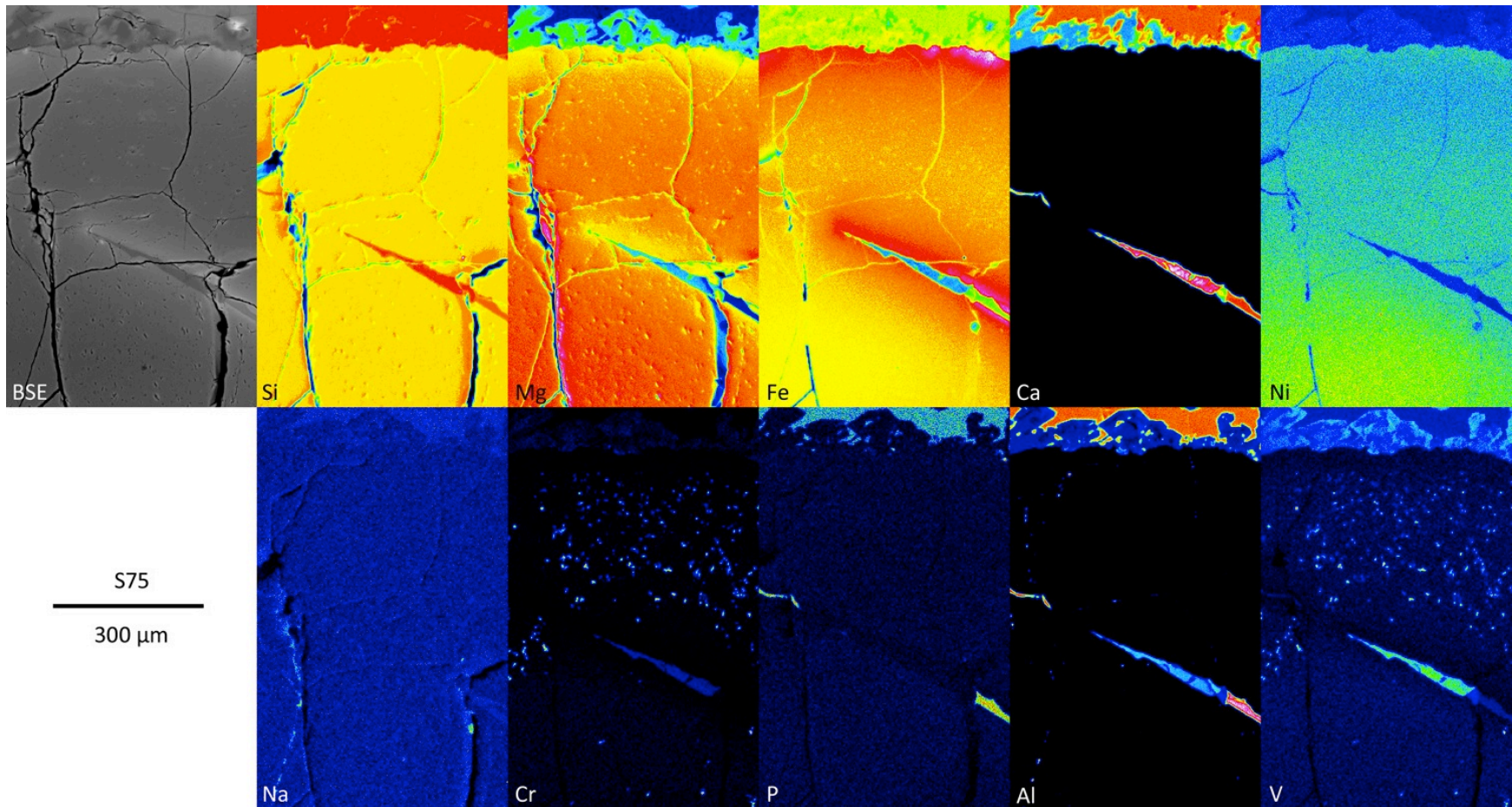


**Figure A2.8:** X-Ray maps of an olivine grain in S75, a hybrid cooling rate experiment from 1375-1100°, oxidized at 1200°C. This experiment was performed using a synthetic composition doped with 1% each NiO and V<sub>2</sub>O<sub>5</sub>.

### **Appendix 3 – NWA 7035 glass trace-element compositions**

This appendix is the full list of trace-element compositions from experimental glasses. The variability of trace-element compositions is likely due to minerals included in the glass analysis during laser ablation. As the glass has the highest rare earth element content in each sample the highest REE content analysis population was chosen for further analysis in Ch.4 – these compositions are all denoted as “1” in each set (e.g. A1).

**Table A3.1:** Full collection of trace-element compositions measured in glasses from partial melting of NWA 7035

	A1		A2	A3		A4	
n	2		1	2		2	
Sc	34	±0.8	44.9	49.3	±1	90	±20
Ti	24450	±750	12610	6100	±500	6000	±1000
V	4.4	±0.7	12.1	13.7	±0.06	4	±1
Cr	170	±10	530	580	±3	150	±80
Co	3.4	±0	2.8	2.7	±0.1	14	±6
Ni	8.2	±0.3	19.7	0	±3	20	±10
Sr	161	±6	76	31	±6	16	±5
Y	280	±10	130	41	±7	100	±3
Zr	950	±30	460	110	±30	90	±30
Nb	62	±1	28	5	±2	6	±2
Mo	0.1	±0.1	0.1	0.08	±0.02	0.6	±0.2
La	73	±3	33	7	±2	5	±2
Ce	177	±6	82	19	±5	14	±4
Pr	25	±1	12	2.9	±0.7	2.3	±0.7
Nd	128	±3	61	16	±4	14	±4
Sm	37	±1	19	6	±1	5.4	±0.8
Eu	2.54	±0.09	1.38	0.46	±0.07	0.42	±0.08
Gd	45	±2	23	7	±1	8	±1
Tb	7	±0.3	3.9	1.2	±0.2	1.8	±0.1
Dy	48	±1	26	8	±2	15	±0.3
Ho	9.8	±0.06	5.22	1.6	±0.3	3.7	±0.1
Er	26.6	±0.9	14.7	4.5	±0.7	14	±1
Tm	3.5	±0.2	1.9	0.6	±0.1	2.3	±0.2
Yb	21.4	±0.6	11.6	4	±0.5	20	±1
Lu	2.76	±0.09	1.63	0.58	±0.05	3.3	±0.2
Hf	20.7	±0.4	12.2	3.5	±0.9	2.4	±1.0

	A5	B1	B2	C
n	2	12	2	30
Sc	27.4 ±0.3	39 ±1	17 ±1	36.1 ±0.1
Ti	2000 ±600	15800 ±500	6800 ±800	11500 ±100
V	2.09 ±0.07	14 ±1	5.8 ±0.6	21.3 ±0.2
Cr	79 ±5	530 ±50	180 ±20	880 ±10
Co	2.1 ±0.01	8 ±1	2.2 ±0.3	4.37 ±0.03
Ni	0.2 ±0.2	3.3 ±0.8	1.7 ±0.6	1.2 ±0.1
Sr	16 ±3	104 ±3	140 ±9	94.5 ±0.3
Y	70 ±10	73 ±2	33 ±4	36.8 ±0.2
Zr	100 ±30	230 ±10	110 ±10	105.3 ±0.5
Nb	3 ±1	17.3 ±0.7	8.1 ±0.9	8.5 ±0.05
Mo	0.15 ±0.04	0.47 ±0.05	0.31 ±0.02	0.44 ±0.02
La	4 ±1	15.3 ±0.5	7.1 ±0.9	6.28 ±0.04
Ce	12 ±4	38 ±1	18 ±2	15.61 ±0.05
Pr	2 ±0.6	5.5 ±0.2	2.6 ±0.3	2.34 ±0.01
Nd	12 ±3	28 ±1	14 ±2	12.43 ±0.06
Sm	5 ±1	9.1 ±0.4	4.3 ±0.5	4.03 ±0.03
Eu	0.35 ±0.01	1.25 ±0.03	1.18 ±0.02	0.899 ±0.006
Gd	8 ±1	11.2 ±0.4	5.1 ±0.6	5.27 ±0.04
Tb	1.6 ±0.3	1.91 ±0.07	0.9 ±0.1	0.922 ±0.006
Dy	12 ±2	13.3 ±0.4	6.3 ±0.8	6.62 ±0.03
Ho	2.8 ±0.5	2.86 ±0.09	1.3 ±0.2	1.44 ±0.009
Er	9 ±2	8.5 ±0.3	3.8 ±0.6	4.26 ±0.03
Tm	1.3 ±0.2	1.21 ±0.04	0.55 ±0.04	0.63 ±0.006
Yb	9 ±2	8.1 ±0.3	3.6 ±0.4	4.31 ±0.03
Lu	1.3 ±0.3	1.19 ±0.04	0.51 ±0.05	0.631 ±0.006
Hf	3.3 ±0.8	6.0 ±0.3	3 ±0.3	2.88 ±0.02

	E1		E2		F1		F2	
n	25		4		3		2	
Sc	34.1	±0.1	34.6	±0.3	39.5	±0.9	43	±5
Ti	12660	±40	10940	±60	24600	±200	19000	±1000
V	16.8	±0.3	15.8	±0.1	8.1	±0.3	7	±1
Cr	624	±6	602	±4	280	±10	300	±100
Co	3.07	±0.1	4.11	±0.03	5	±0.5	11	±8
Ni	0.7	±0.06	1.1	±0.1	2.3	±0.7	2	±1
Sr	103.1	±0.3	100.3	±0.4	125	±1	123	±7
Y	53.6	±0.4	44	±0.2	121	±2	105	±3
Zr	165	±2	126.6	±0.6	388	±8	298	±2
Nb	13.11	±0.1	9.7	±0.1	35.6	±0.7	22.3	±0.8
Mo	0.18	±0.01	0.36	±0.03	0.18	±0.03	0.6	±0.2
La	10.86	±0.07	8.25	±0.08	26.1	±0.3	20.3	±0.6
Ce	26.3	±0.2	20.5	±0.2	67	±0.4	52	±2
Pr	3.9	±0.03	3.04	±0.02	9.82	±0.07	7.5	±0.3
Nd	20.3	±0.1	16.2	±0.1	49.4	±0.4	39	±2
Sm	6.46	±0.05	5.2	±0.2	15.3	±0.2	11.8	±0.7
Eu	1.143	±0.007	1.05	±0.007	1.76	±0.05	1.61	±0.04
Gd	8.22	±0.06	6.5	±0.08	19.1	±0.3	15.7	±0.9
Tb	1.426	±0.007	1.15	±0.02	3.21	±0.05	2.8	±0.2
Dy	10	±0.06	8.1	±0.1	23.097	±0.003	19.6	±0.3
Ho	2.1	±0.01	1.68	±0.02	4.94	±0.05	4.13	±0.06
Er	6.09	±0.03	4.9	±0.1	14.2	±0.2	12.2	±0.2
Tm	0.879	±0.005	0.72	±0.01	1.96	±0.01	1.76	±0.06
Yb	5.67	±0.03	4.6	±0.03	12.7	±0.2	11.42	±0.09
Lu	0.827	±0.006	0.709	±0.007	1.91	±0.05	1.83	±0.07
Hf	4.56	±0.07	3.41	±0.03	10.4	±0.3	8.42	±0.03

	F3		F4		G1		G2	
n	4		2		10		3	
Sc	46	±7	27	±7	32.6	±0.2	27.1	±0.9
Ti	21000	±1000	10600	±900	8150	±30	7800	±300
V	7.4	±0.8	4.1	±0.1	25.7	±0.6	21.3	±0.8
Cr	300	±50	150	±20	930	±90	700	±20
Co	11	±5	2.5	±0.4	3.46	±0.04	2.71	±0.04
Ni	3	±1	1.1	±0.2	1.8	±0.5	5.2	±0.5
Sr	121	±5	100	±40	94.8	±0.2	94.5	±0.8
Y	90	±3	70	±10	35.5	±0.1	28.2	±0.9
Zr	262	±2	175	±2	109.7	±0.3	85	±3
Nb	22.3	±0.6	14	±2	8.36	±0.04	7.1	±0.3
Mo	0.38	±0.05	0.2	±0.08	0.37	±0.02	0.35	±0.04
La	17.7	±0.3	11.6	±0.2	6.64	±0.03	0	±0
Ce	44.7	±0.5	30.3	±0.3	16.55	±0.06	13.7	±0.3
Pr	6.54	±0.02	4.36	±0.01	2.45	±0.01	1.98	±0.07
Nd	33.6	±0.4	22.9	±0.9	12.8	±0.1	10.4	±0.2
Sm	10.3	±0.2	7.1	±0.5	4.22	±0.05	3.27	±0.02
Eu	1.43	±0.04	1.15	±0.1	0.926	±0.008	0.83	±0.03
Gd	13.4	±0.2	9.7	±1	5.3	±0.05	4.11	±0.09
Tb	2.24	±0.06	1.7	±0.2	0.919	±0.008	0.73	±0.01
Dy	16.2	±0.7	12	±2	6.58	±0.07	5.1	±0.2
Ho	3.5	±0.1	2.6	±0.4	1.4	±0.01	1.12	±0.03
Er	10.5	±0.4	8	±1	4.11	±0.02	3.2	±0.1
Tm	1.53	±0.09	1.1	±0.3	0.583	±0.006	0.47	±0.01
Yb	10.4	±0.6	8	±2	3.87	±0.04	3.1	±0.2
Lu	1.6	±0.1	1.1	±0.3	0.578	±0.005	0.43	±0.02
Hf	7.1	±0.2	4.81	±0.02	3.03	±0.02	2.41	±0.09

G3	
n	6
Sc	17.6 ±0.5
Ti	4200 ±100
V	13.4 ±0.4
Cr	410 ±10
Co	1.65 ±0.07
Ni	1.2 ±0.5
Sr	94.4 ±0.3
Y	15.9 ±0.5
Zr	47 ±2
Nb	3.8 ±0.2
Mo	0.2 ±0.01
La	0 ±0
Ce	7.4 ±0.2
Pr	1.08 ±0.04
Nd	5.8 ±0.2
Sm	1.77 ±0.06
Eu	0.7 ±0.02
Gd	2.4 ±0.1
Tb	0.39 ±0.01
Dy	2.8 ±0.1
Ho	0.61 ±0.03
Er	1.8 ±0.07
Tm	0.26 ±0.01
Yb	1.68 ±0.06
Lu	0.25 ±0.01
Hf	1.28 ±0.05